Spin-charge conversion in 2D materials and van der Waals heterostructures

Khasan Abdukayumov

THÈSE

Pour obtenir le grade de

DOCTEUR DE L'UNIVERSITÉ GRENOBLE ALPES

École doctorale : PHYS - Physique
Spécialité : Physique de la Matière Condensée et du Rayonnement
Unité de recherche : Spintronique et Technologie des Composants

Conversion spin-charge dans les matériaux 2D et les hétérostructures de van der Waals

Spin-charge conversion in 2D materials and van der Waals heterostructures

Présentée par :

Khasan ABDUKAYUMOV

Direction de thèse :

Matthieu JAMET DIRECTEUR DE RECHERCHE, CEA CENTRE DE GRENOBLE	Directeur de thèse
Céline VERGNAUD INGENIEUR CHERCHEUR, CEA - GRENOBLE - INAC	Co-encadrante de thèse

Rapporteurs :

FREDERIC TEPPE
DIRECTEUR DE RECHERCHE, CNRS DELEGATION OCCITANIE EST
PIERRE RENUCCI
PROFESSEUR DES UNIVERSITES, INSA LYON

Thèse soutenue publiquement le **23 avril 2024**, devant le jury composé de :

LISA MICHEZ, PROFESSEURE DES UNIVERSITES, AIX-MARSEILLE UNIVERSITE	Présidente
FREDERIC TEPPE, DIRECTEUR DE RECHERCHE, CNRS DELEGATION OCCITANIE EST	Rapporteur
PIERRE RENUCCI, PROFESSEUR DES UNIVERSITES, INSA LYON	Rapporteur
BRUNO DLUBAK, CHARGE DE RECHERCHE, CNRS DELEGATION ILE-DE-FRANCE SUD	Examinateur
LAURENT RANNO, MAITRE DE CONFERENCES HDR, UNIVERSITE GRENOBLE ALPES	Examinateur

Invités :

SUKHDEEP DHILLON
DIRECTEUR DE RECHERCHE, CNRS DELEGATION PARIS CENTRE

Résumé

Après la première exfoliation du graphène en 2004, de nombreux autres matériaux 2D ont été étudiés pour diverses applications, notamment la spintronique, un domaine qui exploite le degré de liberté du spin des électrons par opposition à la charge en électronique. La pierre angulaire de la spintronique fondamentale est le phénomène d'interconversion entre un courant de spin et un courant de charge, plus connu sous le nom de conversion spin-charge (SCC). Les matériaux 2D sont caractérisés par une faible interaction de van der Waals (vdW) entre les couches, ce qui permet de relâcher la contrainte d'accord de paramètre de maille pour l'épitaxie et de produire des hétérostructures vdW complexes. Cela peut également offrir de nouvelles plates-formes de croissance difficilement accessibles aux matériaux 3D conventionnels et, en raison des faibles liaisons vdW, les films produits peuvent être transférés sur un autre substrat. En outre, les matériaux 2D présentent une structure de bande dépendant de l'épaisseur et diverses hétérostructures peuvent être formées, ce qui ouvre la voie à un grand nombre de nouvelles applications en spintronique. Cependant, la plupart des recherches actuelles sont basées sur des flocons exfoliés dont la taille ne dépasse pas quelques dizaines de µm, ce qui limite les possibilités d'intégration. Dans cette thèse, je présente la croissance sur de grandes surfaces de matériaux 2D de haute qualité et d'hétérostructures vdW par épitaxie par jets moléculaires (EJM) et j'étudie les effets SCC par émission THz spintronique sondée par spectroscopie THz dans le domaine temporel. Tout d'abord, des hétérostructures CoFeB/$PtSe_2$ avec une épaisseur variable de $PtSe_2$ ont été étudiées et une transition de l'effet Rashba-Edelstein inverse dans quelques monocouches (ML) à l'effet Hall de spin inverse dans des films plus épais a été observée. C'est la première fois qu'un matériau présente une telle transition. Le second système était une bicouche $PtSe_2$/$MoSe_2$ dans laquelle nous avons observé une bande électronique hybridée présentant une texture de spin opposée à celle de $PtSe_2$. Nous avons ainsi pu démontrer la possibilité d'inverser le signe de l'effet Rashba-Edelstein inverse en insérant une seule couche de $MoSe_2$, ce qui ouvre une nouvelle voie pour moduler l'intensité et le signe de la SCC dans les hétérostructures vdW avec un contrôle à l'échelle de la monocouche. Enfin, la SCC dans quelques couches de $PtSe_2$/$MoSe_2$ a été étudiée en fonction d'un champ électrique externe variable ou rémanent par effet de proximité avec un matériau ferroélectrique 3D. En effet, cette hétérostructure vdW est semi-conductrice avec une efficacité de SCC possiblement plus grande dans les bandes électroniques loin du niveau de Fermi accessibles par l'application d'un champ électrique. Ces résultats nous incitent à explorer davantage le monde des matériaux 2D par divers moyens, tels que les champs électriques, et à rapprocher les matériaux 2D des applications dans le domaine de la spintronique.

Abstract

After the first-time successful exfoliation of graphene in 2004 many more 2D materials have been studied for various applications, including spintronics, a field that exploits the spin degree of freedom of electrons as opposed to the charge in electronics. The cornerstone of fundamental spintronics is the spin current-charge current interconversion phenomena, shortly known as spin-charge conversion (SCC). 2D materials are characterized by weak van der Waals (vdW) interaction between the layers, thus, relaxing the lattice-matching requirement for the epitaxy, enabling to grow complex vdW heterostructures. This can also offer new growth platforms not easily accessible by conventional 3D materials, and, due to the weak nature of the vdW forces, grown films can be transferred onto another substrate. Moreover, 2D materials show thickness dependent band structure and various heterostructures can be formed, opening a vast number of possibly new physics for spintronic applications that can be explored. However, most of the current research is based on exfoliated flakes that are at most tens of μm in size, limiting their possible implementation for applications. In this thesis, I present large-area growth of high quality 2D materials and vdW heterostructures by molecular beam epitaxy (MBE) and study SCC effects by spintronic THz emission probed by THz time domain spectroscopy. First, CoFeB/$PtSe_2$ heterostructures with varying the thickness of $PtSe_2$ were studied and a transition from the inverse Rashba-Edelstein effect in a few monolayers (ML) to the inverse spin Hall effect in thicker films was observed. This is the first time a material showed such a transition. The second system was $PtSe_2$/$MoSe_2$ bilayer where we observed a hybridized electronic band showing an opposite spin texture to that of $PtSe_2$. By this, we could demonstrate the possibility to reverse the sign of the inverse Rashba-Edelstein effect by inserting a single $MoSe_2$ layer opening a new route to modulate SCC intensity and sign in vdW heterostructures with monolayer control. Finally, SCC in few layer $PtSe_2$/$MoSe_2$ was investigated as a function of an external electric field either variable or remanent by proximity with a 3D ferroelectric material. Indeed, this vdW heterostructure is semiconducting with possibly larger SCC efficiency in electronic bands far from the Fermi level accessible through the application of an electric field. Those findings push us to explore the world of 2D materials even more by various means, such as electric fields, and bring 2D materials closer to spintronic device applications.

Contents

Acronyms

1D - one-dimensional
2D - two-dimensional
3D - three-dimensional
3TM - Three Temperature Model
AC - Alternating Current
AFM - Atomic Force Microscopy
AHE - Anomalous Hall Effect
AMR - Anisotropic Magnetoresistance
ARPES - Angle-Resolved Photo-Electron Spectroscopy
BFO - Bismuth ferrite, $BiFeO_3$
BLG - Bilayer graphene
CBM - Conduction Band Minimum
CCD - Charge coupled display
CPW - Co-planar waveguide
CVD - Chemical Vapor Deposition
DC - Direct Current
DFT - Density Functional Theory
DI - De-ionized
DOS - Density of States
EDOS - Electronic Density of States
EOS - Electro-optical sampling
EPR - Electron Paramagnetic Resonance
FF - Far-field
FFT - Fast Fourier Transform
FIB - Focused Ion Beam
FM - Ferromagnet
FMR - Ferromagnetic resonance
FvdM - Franck-van der Merwe
FWHM - Full Width at Half Maximum
HAADF - High-angle annular dark-field
HM - Heavy metal
HOPG - Highly oriented pyrolytic graphite
HWHM - Half width at half maximum
IR - Infra-red
IREE - Inverse Rashba Edelstein effect
IRIG - Institut de recherche interdisciplinaire de Grenoble
ISHE - Inverse spin Hall effect
LEED - Low energy electron diffraction
LL - Laser lithography
LLG - Landau-Lifshitz-Gilbert
LNO - Lithium niobate, $LiNbO_3$
MBE - Molecular beam epitaxy
MFP - Mean-free path
ML - Monolayer
MLG - Monolayer graphene
MOKE - Magneto-optical Kerr effect
MR - Magnetoresistance
MRAM - Magnetic random access memory
NF - Near-field
NIR - Near infra-red
NM - Non-magnetic
OHE - Ordinary Hall effect
PAW - Projector augmented wave
PBE - Perdew-Burke-Ernzerhof
PBN - Pyrolytic boron nitride
PCB - Printed circuit board
PFM - Piezo force microscopy
PFT - Peak-force tapping
PLD - Pulsed laser deposition
PMA - Perpendicular magnetic anisotropy
PMMA - Polymethyl methacrylate
QCM - Quartz crystal microbalance
QL - Quintuple layer
REE - Rashba-Edelstein effect
RHEED - Reflection high energy electron diffraction
SCC - Spin-charge conversion
SHE - Spin Hall effect
SK - Stranski-Krastanov
SOC - Spin-orbit coupling
SOT - Spin-orbit torques

SP - Spin pumping
SSE - Spin-Seebeck effect
ST - Spin-transfer
STE - Spintronic THz emission
STEM - Scanning Transmission electron microscopy
STM - Scanning tunneling microscopy
STS - Scanning tunneling spectroscopy
TEM - Transmission electron microscopy
THz-TDS - THz time-domain spectroscopy
TI - Topological insulator
TM - Tapping mode
TMD - Transition metal dicholcogenide
UHV - Ultra-high vacuum
UV - Ultra violet
VASP - Vienna ab initio simulation package
VBE - Valence band edge
VBM - Valence band maximum
vdP - van der Pauw
vdW - van der Waals
vdWE - van der Waals epitaxy
VHE - valley Hall effect
VNA - Vector network analyser
VW - Volmer-Weber
XMCD - X-ray magnetic circular dichroism
XPS - X-ray photoelectron spectroscopy
XRD - X-ray diffraction
XRR - X-ray reflectivity

Introduction

Spintronics exploits the spin of electrons, instead of the charge, to process and store information that aims at reducing the energy consumption of in devices. Various physical phenomena are involved in the generation, manipulation, and detection of spin currents in materials. The dependence of the electrical resistivity of a material on the relative direction of the magnetic field and injected current is known as anisotropic magnetoresistance. Other hallmark magnetoresistive effects include tunneling magnetoresistance (TMR) [1] and giant magnetoresistance (GMR), the latter yielded in a Nobel Prize in Physics for Albert Fert in 2007. These two effects accelerated the integration of spintronic devices in data processing and storage technology.

Hall effect is the most historical demonstration of manipulation of electrons by external fields where the electron trajectory is bent by the Lorentz force [2]. This is manifested in the form of transverse electrical potential change inside the material. Other concepts were further discovered such as the anomalous Hall (AHE) and spin Hall (SHE) effects to name a couple of them. In the former, a contribution to the potential change comes from the magnetization of a magnetic material and in the latter the electrons trajectory is locked into its spin state in the presence of spin-orbit coupling (SOC). Conventional 3-dimensional (3D) materials, such as, Pt and W, have been well studied for generating transverse spin currents by the spin Hall effect, however, intermixing with other elements during sputtering is unavoidable in these materials which could be detrimental and reduce the effects. On the other hand, lattice matching with the substrate is extremely important to obtain high quality epitaxial (grains are aligned with the substrate structure) thin film crystals.

Since the first successful exfoliation and physical study of atomically thin graphene in 2004 [3], the research of 2D materials has exploded. Due to the van der Waals (vdW) nature of the interaction between the layers, the lattice matching requirement is relaxed and it is even possible to grow the thin films on one substrate and transfer onto another with wet or dry chemistry techniques. Among 2D materials, transition metal dichalcogenides offer novel electronic properties and modulation approaches, such as, thickness dependent ($PtSe_2$, WSe_2, $MoSe_2$, on the order of 0.1-1 eV) and twists angle dependent (on the order of 10 meV) band gap. This could allow more precise control as it does not introduce disorder into the system unlike the conventional doping techniques. Moreover, strong spin-orbit coupling and various crystal symmetries give a new playground to explore this class of materials for spintronic applications. On top of that, heterostructures of vdW materials can be formed that can host new electronic bands at the vdW interface to be explored theoretically and experimentally.

Up to now, most of the studies of 2D materials for SCC have been carried out on exfoliated flakes with the size of a few hundred micrometers at most or lacked a thorough structural analysis that could hinder their potential implementation in industrial applications. In this thesis, I present several advanced characterizations of 2D van der Waals heterostructures.

Chapter 1 lays a theoretical solid base for understanding the physics of the spin-charge conversion (SCC) phenomena in ferromagnet (FM)/non-magnet (NM) heterostructures, such as inverse spin Hall effect (ISHE) and inverse Rashba-Edelstein effect (IREE). Next, I focus on physical experiments employed to study the

effects, first, with spin-pumping by Ferromagnetic resonance (FMR), then, with THz- time domain spectroscopy (TDS) which is based on ultrafast demagnetization of FM layer and injection of superdiffusive spin current into the NM layer.

Chapter 2 focuses on the tools that made the experiments possible, the most important one being molecular beam epitaxy (MBE). I also discuss the particular case of MBE for van der Waals (vdW) materials growth: van der Waals epitaxy (vdWE). The introduction of the characterization tools, such as, reflection high energy diffraction (RHEED), x-ray diffraction (XRD), and THz-TDS optical bench, is presented.

Chapter 3 studies the thickness dependent transition of SCC phenomena in $PtSe_2$ by THz-TDS which is carried out in collaboration with Martin Micica and Sukhdeep Dhillon at the Laboratoire de Physique at the Ecole Normale Supérieure. In this study, we prepared $PtSe_2$ layers on graphene/SiC by vdWE and sputtered CoFeB on top and found a transition from IREE (in the semiconducting regime of 1-3 ML) to ISHE (in the semimetallic regime of >5 ML). A theoretical explanation is provided by Fatima Ibrahim, Libor Vojacek, and Mair Chshiev from SPINTEC that showed that inversion symmetry breaking in the 1 ML regime due to the graphene substrate is essential to induce Rashba-type spin-splitting in $PtSe_2$. This study was published in Advanced Materials in January 2024 [4].

In Chapter 4, we studied SCC in $PtSe_2$/$MoSe_2$ bilayer based on the theoretical work of Xiang et al [5] that predicted large and electric-field adjustable Rashba-type spin splitting. We then prepared the bilayer stucture by vdWE and capped with Se. The preliminary spin-resolved Angle-resolved photoelectron spectroscopy (ARPES) study indeed shows the hybridized Rashba-like bands with spin polarization that was opposite to that previously shown in $PtSe_2$ MLs. This observation was also confirmed by SCC experiments by THz-TDS where we obtained opposite emitted THz electric field polarization. This chapter also presents successful transfer of the bilayer from mica onto SiO_2/Si to be able to apply a backgate voltage and modulate the Fermi level position that preserves the crystal quality of the film.

Chapter 5 is about the perspectives in the study of vdW heterostructures, first, on $PtSe_2$/$MoSe_2$ heterostructures transferred on a ferroelectric substrate to modulate the spin-split bands which is also being studied by THz-TDS in collaboration with Oliver Paull at the Laboratoire Albert Fert in Palaiseau. A second work is based on the theoretical findings of Sattar et al [6] that predicted large Rashba-type spin-splitting in heterostructures of $PtSe_2$ and Bi_2Se_3. For this experiments we collaborated with Sylvain Massebeau and Henri Jaffrès at the Laboratoire Albert Fert in Palaiseau which consisted of photon energy dependent study of SCC by THz-TDS.

To sum up, this doctoral thesis demonstrates that 2D materials can offer tunable physical properties for applications in spintronics, in particular, for spin-charge interconversion which is promising for spintronic THz emitters and SOT-MRAMs.

Conferences and Publications

List of Conferences and Schools attended

European School of Magnetism (ESM) 6-17 September, 2021 in Cluj-Napoca, Romania, a poster presentation on Spin-charge interconversion in 2D transition metal diselenides.

Graphene 2021 26-29 October, 2021, in Grenoble, France, a poster presentation on Spin-charge interconversion in 2D transition metal diselenides.

European workshop on epitaxial graphene and 2D materials (eweg2D) 24-28 May, 2022, in St. Moritz, Switzerland, an oral presentation on Spin-charge interconversion in 2D transition metal diselenides.

20éme Colloque Louis Néel (CLN) 28 June-1 July, in 2022, Obernay, France, a poster on Spintronic THz emission from $PtSe_2$.

Joint European Magnetic Symposia 2022 (JEMS2022) 24-29 July, 2022, in Warsaw, Poland, an oral presentation on Spin-charge interconversion in 2D transition metal diselenides.

9th Materials with Novel Electronic Properties (MaNEP) Winter School 15-20 January, 2023, in Saas-Fee, Switzerland, no presentation session organized.

International Conference on Magnetism, INTERMAG2023 15-19 May, 2023, in Sendai, Japan, an oral presentation in Spintronic THz emission in 2D-$PtSe_2$.

List of Publications

Ferromagnetism and Rashba Spin–Orbit Coupling in the Two-Dimensional (V,Pt)Se_2 Alloy - Authors: E. Vélez-Fort, A. Hallal, R. Sant, T. Guillet, K. Abdukayumov, A. Marty, C. Vergnaud, J.-F. Jacquot, D. Jalabert, J. Fujii, I. Vobornik, J. Rault, N. B. Brookes, D. Longo, P. Ohresser, A. Ouerghi, J.-Y. Veuillen, P. Mallet, H. Boukari, H. Okuno, M. Chshiev, F. Bonell, and M. Jamet.

ACS Appl. Electron. Mater. 2022, 4, 1, 259-268

Angular dependence of the interlayer coupling at the interface between two-dimensional materials 1T-$PtSe_2$ and graphene - Authors: P. Mallet, F. Ibrahim, K. Abdukayumov, A. Marty, C. Vergnaud, F. Bonell, M. Chshiev, M. Jamet, and J-Y. Veuillen.

Phys. Rev. Materials 7, L121001, 2023

Atomic-Layer Controlled Transition from Inverse Rashba–Edelstein Effect to Inverse Spin Hall Effect in 2D $PtSe_2$ Probed by THz Spintronic Emission - Authors: K. Abdukayumov, M. Mičica, F. Ibrahim, L. Vojáček, C. Vergnaud, A. Marty, J.-Y. Veuillen, P. Mallet, I. G. de Moraes, D. Dosenovic, S. Gambarelli, V. Maurel, A. Wright, J. Tignon, J. Mangeney, A. Ouerghi, V. Renard, F. Mesple, J. Li, F. Bonell, H. Okuno, M. Chshiev, J.-M. George, H. Jaffrès, S. Dhillon, M. Jamet.

Advanced Materials 2024, 2304243

Chapter 1

Theoretical Background

1.1 Magnetism

In Solid State Physics textbook, Ashcroft and Mermin define the magnetization density, $M(H)$, as [7]

$$M(H) = -\frac{1}{V}\frac{\partial E_o(H)}{\partial H} \tag{1.1}$$

where V is the volume of the quantum-mechanical system, H uniform magnetic field, $E_0(H)$ is the ground state energy, H the applied magnetic field field. This equation is valid for $T = 0$ K. At a finite temperature, the magnetization density is defined as the thermal equilibrium average of the magnetization density of each excited state of energy $E_n(H)$:

$$M(H,T) = \frac{\Sigma_n M_n(H) e^{-E_n/k_B T}}{\Sigma_n e^{-E_n/k_B T}} \tag{1.2}$$

with

$$M_n(H) = -\frac{1}{V}\frac{\partial E_n(H)}{\partial H} \tag{1.3}$$

in the thermodynamic form:

$$M = -\frac{1}{V}\frac{\partial F}{\partial H} \tag{1.4}$$

F being the magnetic Helmholtz free energy, defined by the fundamental statistical mechanical rule:

$$e^{-F/k_B T} = \Sigma_n e^{-E_n(H)/k_B T} \tag{1.5}$$

And we define the susceptibility as

$$\chi = \frac{\partial M}{\partial H} = -\frac{1}{V}\frac{\partial^2 F}{\partial H^2} \tag{1.6}$$

Magnetism arises for example, from the arrangement of electron spins in a material in certain ordered configurations that give a net spontaneous magnetization. The mechanism responsible for this arrangement is the exchange coupling of the neighbouring spins. We can distinguish two origins of magnetism: the first is from moving electric charge, generating Oersted field, and the other is intrinsically from matter in the absence of electric current. In the latter, magnetism is in the electron itself, or more specifically, in the spin

quantum number. The first experience of humans with magnetism was with magnetite, a type of ferromagnet, as there's non-zero magnetic field emanating from the material under a critical temperature, T_c.

Further investigations of magnetism in materials yielded the other types of magnetic ordering and the reaction of materials to external magnetic fields. Although, one common feature of magnetic response of all materials is repelling the external magnetic field, also known as diamagnetism, it is not equally strong in all materials and some materials have additional contributions. For example, as mentioned above, some materials show spontaneous non-zero magnetization where the ferromagnetic/paramagnetic configuration of the spins overcomes the diamagnetic contribution, hence, the material is attracted to the external magnetic field.

In an atom, magnetism can emerge from the electron spin moment, s as well as the orbital moment, l, with μ_s and μ_l being their magnetic moments, respectively:

$$\mu_{\mathbf{s}} = -\frac{g_s \mu_B s}{\hbar} \tag{1.7}$$

and

$$\mu_{\mathbf{l}} = -\frac{g_l \mu_B l}{\hbar} \tag{1.8}$$

where $|s| = \frac{\hbar}{2}$ ($\hbar$ is the reduced Planck's constant), μ_B is the Bohr magneton ($\mu_B = 9.27 \times 10^{-27}$ J/T), g_s and g_l are the Landé factors of the spin and orbital moments, respectively, with $g = 2$ for a free electron. From the equation above, we can see that the spin moment (orbital moment) and the magnetic moment have opposite signs. Thus, in magnetotransport, the majority magnetic moment $\mathbf{m}^{\uparrow}$ corresponds to the majority spin moment $\mathbf{s}^{\Downarrow}$, and the minority magnetic moment $\mathbf{m}^{\downarrow}$ corresponds to the minority spin moment $\mathbf{s}^{\Uparrow}$. This convention is adopted from The Basics of electron transport in spintronics by V. Baltz [8].

For an atom to have a magnetic moment it must contain unpaired electrons. This reasoning can be extended up to the level of a material, i.e. ensemble of 10^{24} atoms/cm^3 atoms where, electrons do not belong to a single atom but participate in chemical bonding, leading to a compensation of magnetic moments. Nevertheless, in ferromagnetic materials, the electronic band structure is dominated by one type of spins (up or down), giving a net non-zero magnetic moment as discussed in the next paragraph.

1.1.1 Magnetic orders

In some elements and compounds depending on the crystal structure, magnetic structures can arise. Some have a non-zero net magnetization, they exhibit a spin split band structure, while some others, in spite of the ordering of the electron spins in a certain manner, do not exhibit a net magnetization, those are called antiferromagnets without spin split states in the band structure as the spins form a structure that cancel out each other. Recently, a new type of magnetic ordering was discovered showing spin-split bands without net magnetization. They received the name of alter-magnets, though it is not unanimously accepted and a topic of intense debate, and I will not talk about this magnetic ordering as its theory is still under development, neither will I talk about ferrimagnets and antiferromagnets since these materials were not considered in this PhD work.

Ferromagnetism

In ferromagnetic order, spin up and down populations are not equal and a net magnetic moment sets in. In terms of electronic band structure, they can have insulating or metallic character. However, there have been many attempts to find semiconducting ferromagnets at room temperature but without success. Depending

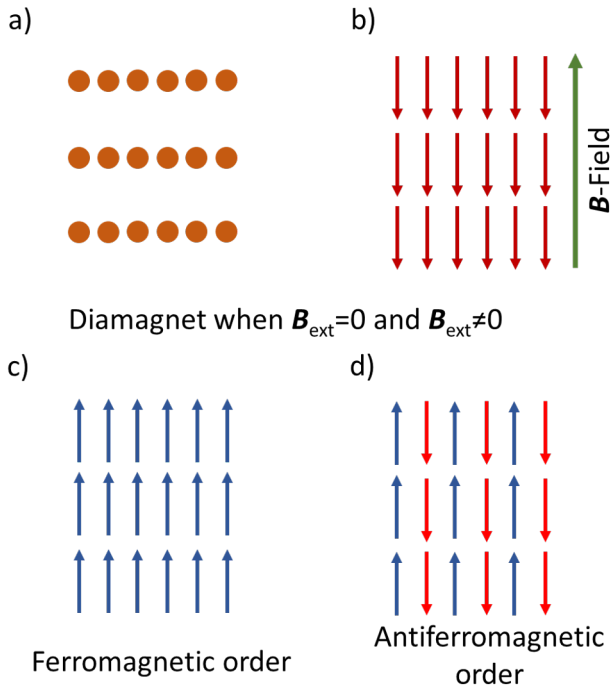

Figure 1.1: Schematics of some possible magnetic orderings in materials. Diamagnet in a) the absence and b) the presence of an external magnetic field. c) ferromagnet and d) antiferromagnet.

on which band of electrons carries the magnetic moment, we can differentiate itinerant and Ising magnetism for conduction and valence band electrons, respectively.

Heisenberg model

The Heisenberg model of ferromagnetism gives a quantum mechanical approach to the magnetic behaviour of materials via exchange interactions. The Hamiltonian $\mathscr{H}$ of the Heisenberg model is given as:

$$\mathscr{H} = \frac{1}{2}\Sigma_{i,j} J_{ij} \mathbf{S}_i \mathbf{S}_j \tag{1.9}$$

Here J_{ij} is the exchange constant, $\mathbf{S_i}$ and $\mathbf{S_j}$ are the spin operators at sites i and j respectively. Since this model considers exchange interaction only between nearest neighbours. For J_{ij}<0 spins with parallel alignment show a minimum in energy, leading to a ferromagnetic order. Whereas for J_{ij}>0 the spins tend to align anti-parallel to each other, which is an antiferromagnetic order. The model, as mentioned above, is based on isotropic exchange interactions. Those interactions originate from Coulomb repulsion and Pauli exclusion principle. The Heisenberg ferromagnetism is typically observed in insulators or metals with localized magnetic moments.

Itinerant Ferromagnetism

The itinerant ferromagnetism model, initially formulated by Bloch in 1929 for metals and semi-metals, provides a theoretical framework for understanding the magnetic behaviour of these materials. At its core, the model involves the concept of a Fermi sphere in momentum space, which is populated by conduction

electrons. Each momentum value within the Fermi sphere can accommodate two electrons, one of spin up and one of spin down. If an exchange interaction exists between these two electrons, they tend to align their spins in a parallel configuration. However, this alignment is prohibited by the Pauli exclusion principle, thus, one of the electrons has to occupy a higher energy level. Consequently, the system experiences an increase in kinetic energy, denoted as ΔK.

In essence, there exists a competition between two energy contributions: the exchange interaction, which seeks to minimize the overall energy by aligning the electron spins, and the kinetic energy, which is increased when one electron occupies a higher energy state due to the Pauli exclusion principle. If the energy decrease resulting from spin alignment surpasses ΔK, the electron spins align, leading to the emergence of itinerant ferromagnetism within the material.

Subsequently, Stoner proposed a fundamental model (referred to as the Stoner theory) that incorporates an effective exchange field acting on itinerant electrons, without explicitly considering the origin of the exchange interaction in metals [9]. The Stoner theory was subsequently verified computationally and found to be in agreement with certain experimental observations. In both the Bloch and Stoner theories, the origin of ferromagnetism can be ascribed to the interplay between exchange energy, which reduces the system's energy, and kinetic energy, which elevates the system's energy. The final expression for the ferromagnetic condition can be written as:

$$I\rho(E_F) > 1 \tag{1.10}$$

Here, I represents the average exchange interaction energy, and $\rho(E_F)$ denotes the electronic density of states (EDOS) at the Fermi level. According to the Stoner condition, metals with a higher value of EDOS at the Fermi level or those possessing a stronger exchange interaction tend to exhibit ferromagnetic behaviour. Specifically, metals with d-band electrons are more likely to be ferromagnetic due to their significantly higher EDOS in the d-band region. Conversely, metals with s-band and p-band electrons have lower EDOS at the Fermi level, leading to paramagnetic or diamagnetic properties. It should be noted that while this trend applies to many d-band metals, it is not universally applicable, and the Stoner model gives a qualitative representation rather than a complete quantitative explanation.

In itinerant ferromagnets, the magnetic moments are carried by delocalized electrons, which is characteristic of the type of ferromagnetism observed in metals.

1.1.2 Magnetism in thin films and 2D materials

Since the first successful exfoliation of graphene, a gapless semiconductor with large electron mobility [11], new physical properties have been added to the family of 2D materials, for example superconducting ($NbSe_2$), semiconducting (WSe_2 and $MoSe_2$), metallic (VSe_2), with magnetic ordering missing in this class of materials. As mentioned above, magnetic ordering persists up to a certain temperature, T_c, after that thermal fluctuations are too strong and they destroy the order. The dimensionality of the system plays an important role on the efficiency of thermal fluctuations to kill magnetic ordering [10]. In 3D magnets the phase transition can take place at a finite temperature, whereas 1D magnets can keep magnetic ordering only at T=0 K [12]. 2D magnets are in between 3D and 1D magnets, thus, the preservation of magnetic ordering in 2D systems depends on the physical quantity called *spin dimensionality*, n. Spin dimensionality is determined by the physical parameters of the system, such as magnetic anisotropy. A simple representation of the spin dimensionality in 2D systems is shown in Fig. 1.2 for n=1, 2, and 3 (adapted from Gibertini et al [10]). According to the Mermin-Wagner-Hohenberg theorem, due to finite-range interactions, magnetic ordering in 2D systems with the spin dimensionality equal to 3 is destroyed by thermal fluctuations at a finite temperature [13], [14]. The Heisenberg model [15] falls into n=3 where spins can be oriented isotropically.

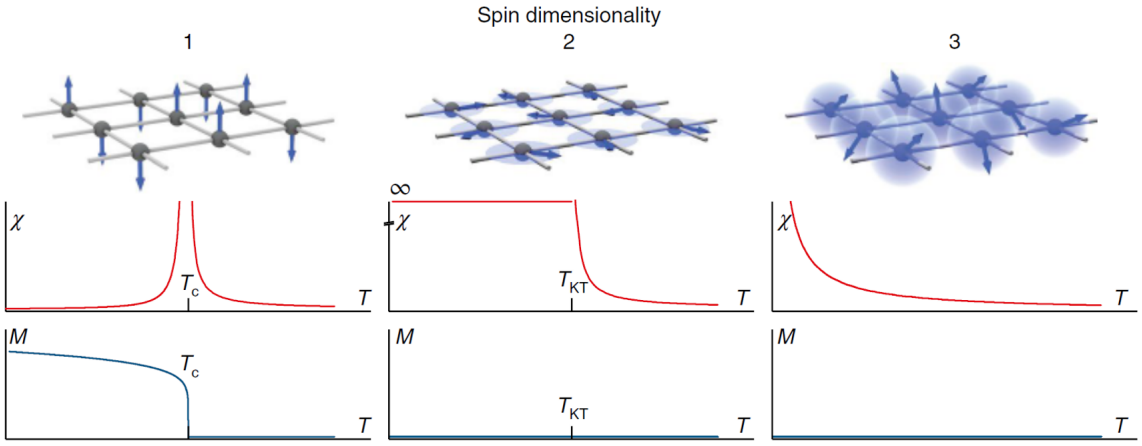

Figure 1.2: Representation of possible spin orientation for three distinct spin dimensionalities with the corresponding temperature dependence of the susceptibility, χ, and magnetization, M [10].

In the case of a continuous symmetry (or isotropy), spin waves destroy magnetic ordering down to T=0 K. In the Ising model, n=1, the anisotropy of the system surpasses thermal fluctuations, thus, allowing magnetic ordering at a finite temperature. Finally, the XY model, n=2, is described by the lack of conventional transition to long-range order, but the susceptibility abruptly changes at the critical temperature associated with the onset of topological order, known as Kosterlitz-Thouless temperature, T_{KT}. Below T_{KT}, a quasi-long-range ordering emerges.

In practice, real materials behave differently than those three idealized cases which requires a case-by-case interpretation. However, the presence of magnetic anisotropy is the key to establish magnetic ordering in 2D systems.

Finally, ferromagnetism was discovered in 2017 in CrI_3 [16], the first 2D ferromagnet with a T_c of 60 K and out-of-plane easy axis. CrI_3 is a semiconductor with a bandgap of around 1 eV, its low T_c hinders it from using it in practical devices. Other van der Waals ferromagnets include Fe_3GeTe_2 [17], Fe_5GeTe_3 [18], and $CrTe_2$ [19]. Although, Fe_3GeTe_2 and Fe_5GeTe_3 are similar compounds chemically, they show distinct magnetic properties: Fe_3GeTe_2 has PMA with a Curie temperature of 130 K in the monolayer limit [17], while Fe_5GeTe_3 has in-plane magnetic anisotropy with a T_c of 229 K in the bilayer structure, and multilayers show a T_c close to room temperature [18].

1.2 Spin charge interconversion

1.2.1 Spin current and charge current

Before introducing spin-charge current interconversion effects, we have to define what spin and charge currents are in the first place. A charge current describes in a Brownian motion of electrons, the net charge movement in a certain direction crossing a surface S per unit time t:

$$J_c = \frac{e}{S}\frac{dN}{dt} \tag{1.11}$$

with N being the number of charges. As non-magnetic metals do not exhibit spin polarized band structure, charge currents in these metals do not show any spin polarization. However, the density of states at the Fermi level in ferromagnetic metals is spin polarized, an electric current in ferromagnets is also spin

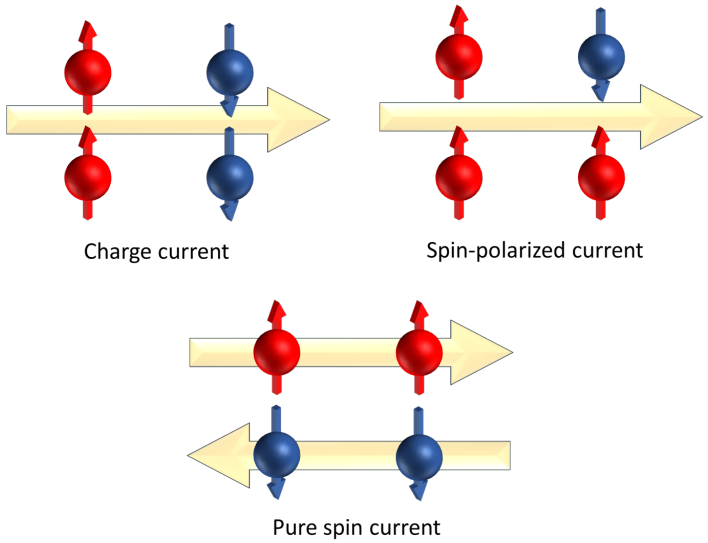

Figure 1.3: Distinction between spin current and charge current. The horizontal arrows show the direction of a charge carrier movement.

polarized:

$$J_{\Uparrow(\Downarrow)} = \frac{h}{2e}\frac{e}{S}\frac{dN_{\Uparrow(\Downarrow)}}{dt} \tag{1.12}$$

$\Uparrow$ and $\Downarrow$ meaning spin-up and spin-down, respectively, and the factor $\frac{h}{2e}\frac{e}{S}$ means there is a flow of angular momentum. In this situation, the total charge current is given by:

$$J_c = J_{\Uparrow} + J_{\Downarrow} \tag{1.13}$$

and the corresponding spin current is given by

$$J_s = J_{\Uparrow} - J_{\Downarrow} \tag{1.14}$$

Spin diffusion length

When spin polarized electrons are injected into a material, they can keep their spin polarization only up to a certain length before it vanishes. This length is referred to as the spin diffusion length, λ_s. Figure 1.4 gives a graphical representation of the spin diffusion length, including the spin flip length, l_{sf}, being the mean distance between two spin-flipping collisions. The mean free path λ_t is defined as the mean distance between two electron scattering events.

Unlike charge currents, spin currents are not conserved. Indeed, there is a finite length, l_{sf} - mean distance between spin-flipping collisions involving the spin-orbit coupling - beyond which the spin current vanishes. The relationship between the spin-flip length l_{sf} and the spin diffusion length λ_s is given by:

$$\lambda_s = \sqrt{D\tau_{sf}} = \sqrt{(1/3)\lambda_t v_F \tau_{sf}} = \sqrt{(1/3)\lambda_t l_{sf}} \tag{1.15}$$

D being the diffusion constant, τ_{sf} the mean time between spin-flipping events, v_F the Fermi velocity

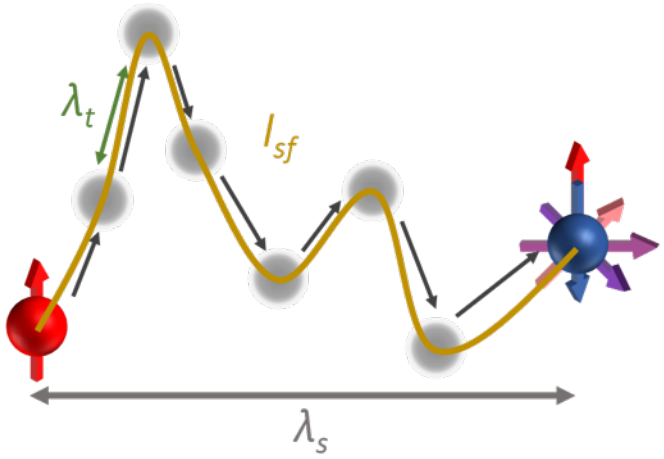

Figure 1.4: A representation of λ_s and l_{sf} showing the electron spin is flipping after a certain distance into a material.

[20].

Spin current polarization

Depending on the relative amount of $J_{\Uparrow}$ and $J_{\Downarrow}$, a current can be divided into three major categories: charge current, spin-polarized current, and pure spin current with no net charge current (Fig.1.3). If we define P as the spin polarization with the formula

$$P = \frac{J_{\Uparrow} - J_{\Downarrow}}{J_{\Uparrow} + J_{\Downarrow}}, \tag{1.16}$$

then a charge current could be assigned to $P = 0$, a pure spin current to $P = 1$, and a spin polarized current to $0 < P < 1$.

Another important aspect of spin currents is how they flow inside various metals. Spin-up polarized electrons, for example, 'see' much less resistance (or less scattering events) inside a magnetic film with 'up' oriented magnetization than spin-down electrons, and the opposite is true for the case of spin-down electrons. This phenomenon is referred to as the 'two-current conduction' model [21] and is depicted in Fig.1.5 with red electrons seeing less resistance in the $FM1$ and then seeing more resistance in $FM2$.

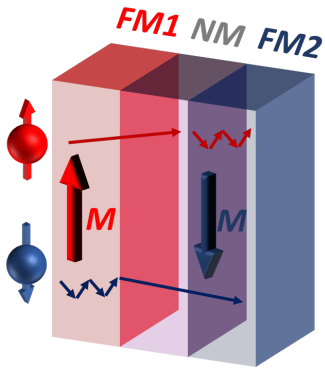

Figure 1.5: A sketch of two resistance channels for spin-up and spin-down electrons.

1.2.2 Generation of spin currents

Typical non-magnetic metals, such as Cu and Au, have electronic band structure with equal density of states for both spin up and spin down at the Fermi level, as shown in Fig.1.6a), i.e. the spin polarization is equal to zero, $P = 0$. Thus, in non-magnetic metals, it is not possible to produce spin-polarized current. On the other hand, ferromagnetic metals show imbalance of electron spins at the Fermi level, as shown in Fig. 1.6b). This means that metallic ferromagnets can generate spin polarized currents.

Now, if we consider a non-magnetic/ferromagnetic bilayer, it is possible to inject electrically a spin polarized current from the latter to the former. This, however, modifies the spin density of the non-magnetic metal, (Fig.1.6c), inducing a net magnetization $\delta\mathbf{M}$, due to spin accumulation at the interface. However, as mentioned earlier, spin polarization is not a conservative quantity: due to scattering events in the non-magnet, the spin polarization of the current vanishes after a certain depth of λ_s, the spin diffusion length. Thus, $\delta\mathbf{M}$ is only contained in the vicinity of the interface with the ferromagnet.

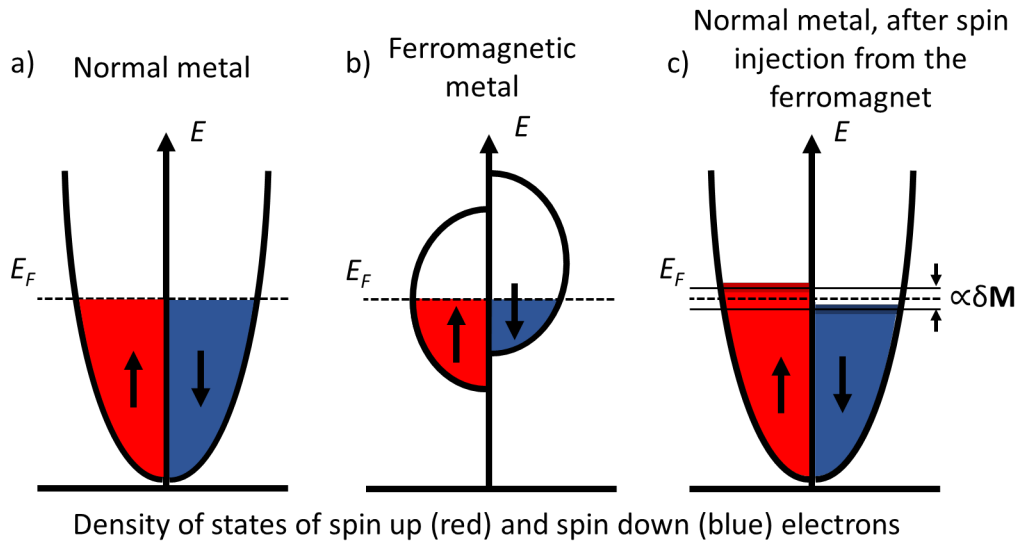

Figure 1.6: Spin density of states of a) normal metal and b) ferromagnetic metal, c) a change in the spin density of the normal metal after the current injection from the ferromagnetic metal that induces spin accumulation and a net magnetization δ_M in the former.

1.2.3 Hall effects

The Hall effect is named after Edwin Hall who discovered it in 1879 [2]. As shown in Fig.1.7a), the Hall effect is based on the production of a Hall voltage, along the y direction, due to the Lorentz force when a longitudinal current ($\mathbf{j_x}$) is applied along a wire made of any material in the presence of a perpendicular magnetic field $\mathbf{B}$ along z. Charge carriers (of charge $q = +e$ and velocity $\mathbf{v}$) are submitted to the following force:

$$\mathbf{F}_L = q\mathbf{E} + q\mathbf{v} \times \mathbf{B} \tag{1.17}$$

They are then deflected on one side of the wire and since the wire has a limited width, they start accumulating only on this side, building up an electric field $\mathbf{E}_{xy}$ which opposes further carriers to be deflected. The built-up transverse field is proportional to the resultant Hall voltage, V_H, and it is perpendicular to both the

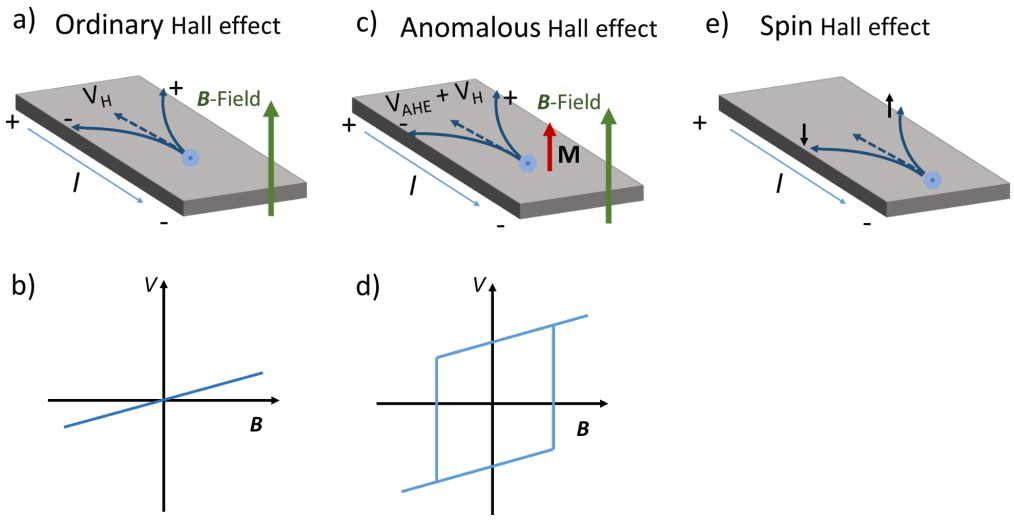

Figure 1.7: Hall effects. a) Ordinary Hall effect (OHE) and b) the measured graph corresponding to OHE, c) anomalous Hall effect (AHE) and b) the measured hysteresis loop corresponding to AHE, e) spin Hall effect (SHE) which cannot be directly measured as it does not produce any transverse voltage.

applied current and the magnetic field directions. xy in $\mathbf{E}_{xy}$ means that the electric field is in the y direction and generated by a current in the x direction.

In this type of measurements, two quantities are of interest: ρ_H and $\mathbf{E}_{xy}$. ρ_H is the ratio between the electric field along the wire and the current density as a function of the applied magnetic field:

$$\rho_H = \frac{E_{xx}}{j_x} \tag{1.18}$$

It is also referred to as the transverse magnetoresistance. $\mathbf{E}_{xy}$ is the transverse field and it is proportional to the applied magnetic field and the electrical current as it is generating a force opposite to the Lorentz force. The relation between those parameters is given by the Hall coefficient:

$$R_H = \frac{E_{xy}}{j_x B} \tag{1.19}$$

It should be noted that since $\mathbf{E}_{xy}$ is along $-y$, R_H is negative. $\mathbf{E}_{xy}$ will be along $+y$ for positive charge carriers. Hence, in semiconductors, Hall measurements play an important role as the sign of R_H depends on the type of carriers. By measuring the Hall field, one can know the type of the majority charge carriers. After further simplification, the Hall coefficient becomes:

$$R_H = -\frac{1}{nq} \tag{1.20}$$

for metal or n-doped semiconductors, and

$$R_H = \frac{1}{pq} \tag{1.21}$$

for p-doped semiconductors, n and p being the (positive) electrons and holes densities, respectively. Hence, Hall measurements also allow to determine the carrier concentration in semiconductors. In order to measure the strength of the Hall effect, one can define the Hall angle or Hall efficiency ϕ_H as

$$\phi_H = \arctan\left(\frac{E_{xy}}{E_{xx}}\right) \tag{1.22}$$

where $\mathbf{E}_{xx}$ is the longitudinal electric field which is parallel to the electrical current. It corresponds to the angle of deflection of an electron by the applied or any intrinsic magnetic field. It also allows to normalize the data. We have defined the ordinary Hall effect but there are several other types of Hall effects like the Anomalous Hall effect (AHE), the Spin Hall effect (SHE) or the Valley Hall effect (VHE), to name a few.

Anomalous Hall effect

The Hall effect in ferromagnets is different from that in non-magnetic materials in a way that it has an additional contribution. In short, the transverse resistivity ρ_{xy} in a ferromagnet consists of two parts,

$$\rho_{xy} = R_o \mu_o H + R_s \mu_o M \tag{1.23}$$

where H is the applied magnetic field, M is the spontaneous magnetization, R_s the anomalous Hall coefficient. The first term describes the ordinary Hall effect (OHE). In bulk metallic ferromagnets, the electrons density is very high and the second term is usually much larger than the first one [22], leading to the following approximation:

$$\rho_{xy} = R_s \mu_o M \tag{1.24}$$

The origins of AHE are not fully understood yet. In this paragraph, we focus on its origin due to the spin-orbit interaction which is typical for itinerant ferromagnetic materials. Karplus et al. show that the AHE is due to the action of spin-orbit coupling on electron spins [23]. More precisely, due to the spin-orbit interaction, stationary states will become asymmetric in terms of scattering direction (left or right). Therefore, an applied electric field results in an electric current that is perpendicular to both the electric field and spontaneous magnetization, or the electron spin polarization. Smit et al. propose that the electron scattering probability depends on its momentum and its spin (skew scattering) [24],[25]. This creates a net transverse spin polarized current. In a side note, they use the term Spontaneous Hall effect, instead of AHE, as it is possible to measure a Hall signal in the absence of an external magnetic field, hence the term 'spontaneous'. Berger describes another scattering mechanism called side-jump which occurs in the presence of a point-like defects, such as in alloys [26]. AHE is a widely used as an indirect measurement technique of thin films magnetization.

Spin Hall effect

The spin Hall effect is described by the spin dependent scattering of charged particles in the presence of a longitudinal electric field, creating transverse spin voltage, or spin accumulation at the sample edges. This phenomenon is observed even in the absence of magnetic field or magnetic material since it is due to quantum mechanical and the relativistic effect called spin-orbit coupling (SOC): due to SOC the spin of an electron is coupled to its momentum. The contributions to the SHE can be divided into two major groups: intrinsic and extrinsic. The intrinsic effect originates from spin-orbit interactions and the Berry curvature, while the extrinsic effects come from impurities, defects or other spin dependent scattering mechanisms which can enhance or modify SHE [27]. Since the number of spin up and spin down electrons in non-magnetic materials is the same, SHE cannot generate a transverse Hall voltage, it only causes spin accumulation at the two edges of the sample due to the circulation of a pure spin current. To compare materials regarding their efficiencies to convert a charge current into a spin current and vice versa, a term called the spin Hall angle,

θ_{SH}, which is a dimensionless quantity is introduced. In theory, it is related to the charge current, $\mathbf{j}_c$, and spin current, $\mathbf{j}_s$ via the following equation:

$$\mathbf{j}_c = \theta_{SH}\mathbf{j}_s \times \hat{\sigma} \tag{1.25}$$

$\hat{\sigma}$ being the spin polarization unit vector. θ_{SH} can be expressed as:

$$\theta_{SH} = \frac{j_s}{j_c} \tag{1.26}$$

This effect is well observed in materials with high atomic number, Z, such as Pt, W, and alloys of those, AuW for example. The physical mechanisms giving rise to the SHE are similar to those giving rise to the AHE: SHE also has intrinsic and extrinsic contributions. The intrinsic one is observed in the absence external sources of scattering, such as impurities or disorders, in other words, it originates from the band structure; moreover, it is insensitive to the scattering time, τ. In this case the off-diagonal terms in the resistivity matrix are non-zero and spin-dependent due to the Berry curvature that links the band structure to the anomalous contribution to the velocity in the presence of an electric field [28],[29]. We can see in Fig. 1.8a) that in the presence of an electric field, the electrons are deflected to opposite directions depending on their spins. Pt is a good example of a material with a strong intrinsic spin Hall contribution [30].

The extrinsic contributions are divided into two types: side-jump (Fig.1.8b) [31] and skew scattering (Fig.1.8c) [32]. Those were actually proposed as possible explanations for the off-diagonal non-zero terms in the resistivity matrix in the case of AHE. Thus, the scattering events in the presence of SOC are a possible origin of AHE in ferromagnets and SHE in paramagnets [33]. It is possible to tune the spin Hall angle by playing with the impurity concentration of the film.

In the side-jump scattering, the electron is scattered into opposite direction when approaching and leaving the impurity proximity due to the opposing electric field contributions. During this scattering event, the electron keeps its k-vector, depending on its spin it deflects to the right or left. In the case of the skew scattering, though, the electrons are deflected by the presence of an impurity, which changes the k-vector direction before and after the scattering event, depending on the spin state of an electron [34].

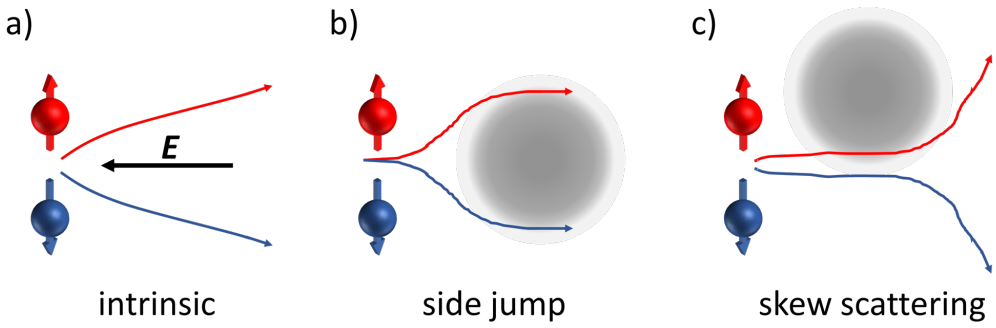

Figure 1.8: Responsible mechanisms for AHE and SHE. a) intrinsic, b) side-jump, and c) skew scattering. The grey area can be a defect or other scattering point.

It is not easy to measure the Spin Hall effect of materials as pure spin currents do not generate any voltage. Thus, other techniques have been developed to measure the manifestation of the SHE rather than the SHE itself like spin-orbit torques or spin Hall magnetoresistance in FM/SHE material bilayers [35].

Inverse Spin Hall effect

Following the Onsager principle, there is an opposite effect of the SHE called the inverse spin Hall effect (ISHE) where a spin current is converted into a charge current. In theory, the ISHE is easier to detect than the SHE as it produces a charge current and measurable potential difference in the sample.

The important step is the generation of a spin current or spin-polarized current to inject into the material. Ferromagnets are known to have spin polarized electrons at the Fermi level, the next challenge is to inject those electrons into the material. One proposed technique was to use a FM/NM bilayer, as mentioned previously, to inject a spin current by Spin pumping at the ferromagnetic resonance when the magnetization of the ferromagnet is excited in the GHz frequency range. When this oscillation is damped, it relaxes by emitting angular momentum in the form of a spin current. The injected spin current is converted into a charge current in the presence of SOC in the NM material. The process was experimentally demonstrated at room temperature by Saitoh et al. [36].

1.2.4 Magnetoresistance

Magnetoresistance (MR) is the change of resistance of a conductor under the influence of an applied magnetic field. Usually, MR and Hall effect are probed simultaneously, and, in an ideal case, they should not interfere with each other. There are several types of MR: ordinary MR in all materials due to the Lorentz force leading to a parabolic dependence of the resistance with respect to the field, the Giant MR in FM/NM/FM multilayers [37], Anisotropic MR observed in FM layers [38], and sometimes MR due to quantum effects such as weak localization or anti-localization effects [39]. MR can offer valuable insight into the origins of physical properties from a fundamental point of view. Applications of various MR effects include, but not limited to, magnetic recording and magnetic field sensors.

Anisotropic Magnetoresistance

Anisotropic magnetoresistance (AMR) is a phenomenon observed in ferromagnetic materials where the electrical resistance depends on the angle between the direction of the current flow and the magnetization orientation, as shown in Fig. 1.9. This effect arises due to the anisotropic scattering of electrons in the presence of SOC.

The AMR effect can be described by the following equation:

$$\begin{aligned} \Delta R_{AMR} &= R_{\parallel} - R_{\perp} \\ R(\theta) &= R_{\perp} + \Delta R_{AMR} \cos^2 \theta \end{aligned} \tag{1.27}$$

where ΔR_{AMR} is the change of resistance, $R_{\parallel}$ and $R_{\perp}$ are the resistances with the magnetization parallel and perpendicular to the current direction, and θ is the angle between the magnetization direction and the current direction.

In this equation, the $\cos^2 \theta$ term indicates that the resistance is maximum when the magnetization is perpendicular to the current direction, $\theta = 90^\circ$, and minimum when the magnetization is parallel to the current direction, $\theta = 0^\circ$. The change in resistance, ΔR_{AMR}, provides a measure of the AMR effect.

The AMR effect can also be quantified by the AMR ratio (AMR%), which represents the relative change in resistance. It is given by:

$$AMR \tag{1.28}$$

This ratio provides a measure of the sensitivity of the material to changes in the magnetization direction.

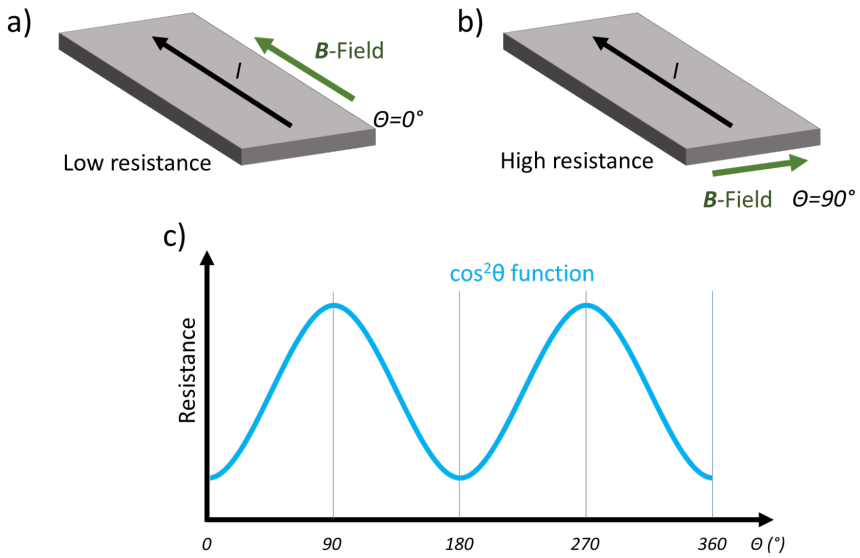

Figure 1.9: AMR measurement geometry for a) $\theta = 0°$ and b) $\theta = 90°$, θ being the angle between the in plane current direction and the in-plane applied **B**-field. c) angular dependence of the resistance under saturating **B**-field.

1.2.5 Spin-charge interconversion phenomena at surfaces and interfaces

Due to the distinct symmetries at surfaces and interfaces and in the bulk, the electron band structure is modified in the former case. In a bulk crystal with inversion symmetry: $E(\uparrow,k) = E(\uparrow,-k)$ and for a non-magnetic material, time reversal symmetry holds and gives: $E(\uparrow,k) = E(\downarrow,-k)$ which leads to spin degeneracy: $(E(\uparrow,k) = E(\downarrow,k))$. In the case of a surface or an interface, the inversion symmetry is broken, leading to an effective out-of-plane electric field. This in turn creates an effective in plane magnetic field, B_{eff}, lifting the spin degeneracy. This additional term can be described by the Rashba Hamiltonian:

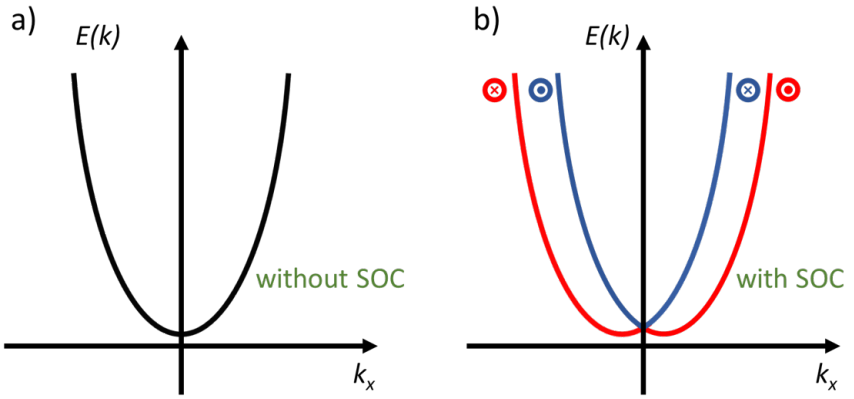

Figure 1.10: Rashba spin splitting of the band structure in a) the absence and b) the presence of SOC.

$$\mathscr{H}_{Rashba} = \alpha_R(\sigma \times \mathbf{p}) \cdot \mathbf{z} \tag{1.29}$$

Here α_R is the Rashba coefficient, σ is the Pauli matrix, $\mathbf{p}$ is the electron momentum. The Rashba effect is responsible for the coupling between the electron spin and its momentum, thus, lifting the spin degeneracy.

It gives two energy bands with opposite spin chiralities at surfaces and interfaces:

$$E_{\uparrow(\downarrow)} = \frac{\hbar^2 k^2}{2m^*} + (-)\alpha_R k \tag{1.30}$$

Fig 1.10 a shows a parabolic band structure with degenerate spins in the absence of SOC and Fig. 1.10b) the spin-split bands due to the Rashba contribution as a consequence of SOC. This effect was observed experimentally on the Au (111) surface by ARPES [40]. The details of the ARPES technique are given in the Experimental Background Chapter.

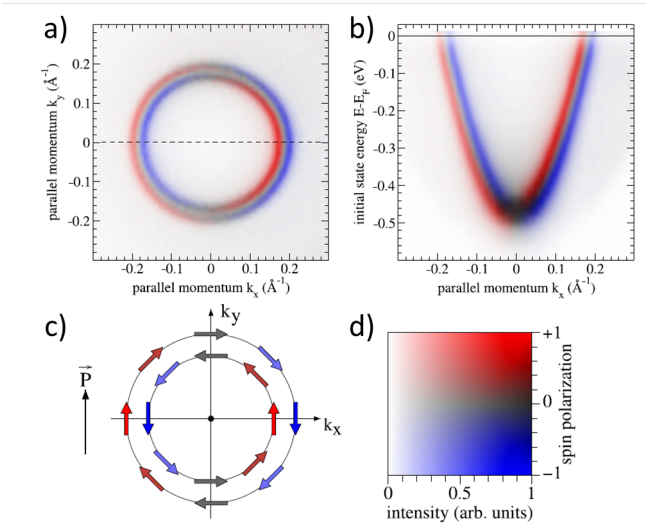

Figure 1.11: Experimental observation of Rashba spin-split states on the Au(111) surface by ARPES showing clear spin-splitting in the band structure [40].

When we look at the band structure at a constant energy (Fig. 1.12a), dashed line), we can see the resulting spin texture in the k_x-k_y plane as shown in Fig. 1.12.b) where there are two Fermi contours with opposite spin chiralities. By injecting a current density $\mathbf{j}_c$ along $-x$ (as shown in Fig. 1.12c), the corresponding electric field E is defined by the Ohm's law as: $\mathbf{j}_c = \sigma\mathbf{E}$ (with the electrical conductivity σ), in turn, a Coulomb force $\mathbf{F}_{Coul} = -e\mathbf{E}$ acts on the electrons. We can also write the Coulomb force as $\mathbf{F}_{Coul} = \frac{d\mathbf{p}}{dt}$ (Newton's principle of dynamics). From quantum mechanics, we know that $\mathbf{p} = \hbar\mathbf{k}$. Thus, when a charge current $\mathbf{j}_c$ is injected in a time period of Δt, it shifts the Fermi surface by $\Delta\mathbf{k}$:

$$\Delta\mathbf{k} = \frac{e\Delta t\mathbf{j}}{\hbar\sigma} = \frac{e\tau\mathbf{j}}{\hbar\sigma} \tag{1.31}$$

τ being the momentum scattering time which is around *ps* for semiconductors.

Hence, when a current density $\mathbf{j}_c$ is injected in the direction $-x$, a shift of the Fermi contour occurs by $\Delta\mathbf{k}$. This, in turn, leads to an accumulation of spins (shown in the shaded area of Fig.1.12c). Since this accumulation occurs in both contours with opposite chiralities, they partially cancel out, leaving spin accumulation coming from the larger Fermi contour. In other words, the injected charge current is converted into a spin accumulation at the surface/interface.

This spin accumulation due to the REE can be utilized, for example, in a bilayer with a ferromagnet: a spin current can flow into the ferromagnet by diffusion of the spin accumulation from the interface. The conversion 'efficiency' of a 2D charge current into a 3D spin current is denoted as:

$$q_{EE} = \frac{j_s^{3D}}{j_c^{2D}} \tag{1.32}$$

It has the unit of an inverse length and high q_{EE} values mean strong conversion.

Inverse Rashba-Edelstein effect

Referring back to Fig 1.12 b where the spin texture is shown when there is no spin current is injected in the material. The injection of a spin current, for example from the ferromagnetic layer, perpendicular to the surface creates an out-of-equilibrium spin density $< \delta S >$. This in turn shifts the Fermi contours by $\Delta\mathbf{k}$. Combining this shift with equation 1.29, a two-dimensional charge current is created (Fig 1.12d). In this case, a 2D charge current is created from a 3D spin current, and the conversion 'efficiency' is defined as the inverse Rashba-Edelstein length with the formula:

$$\lambda_{IREE} = \frac{j_c^{2D}}{j_s^{3D}} \tag{1.33}$$

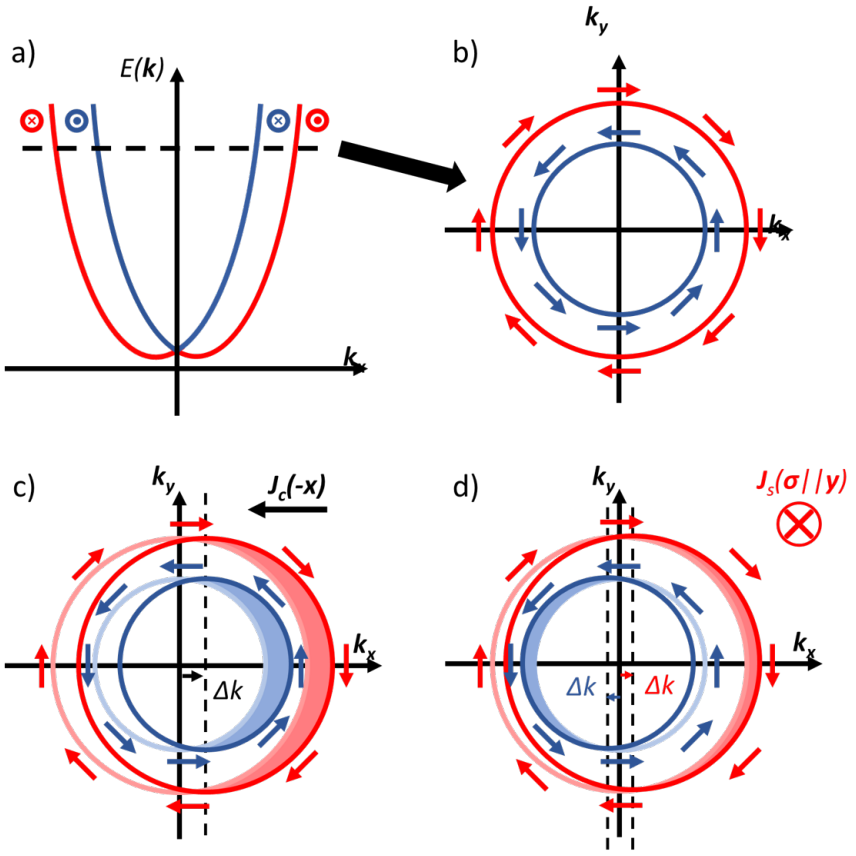

Figure 1.12: Cross-section of spin split bands (a) and corresponding spin texture at a given energy (b). This could result in Rashba Edelstein effect (c) and Inverse Rashba Edelstein Effect (d). Adapted from Guillet [41].

Calculating the spin-charge conversion efficiency at Rashba Interfaces

A phenomenological approach to calculate spin-charge conversion efficiencies at Rashba interfaces is given in Sanchez et al [42]. As presented previously, Rashba spin textures contain two opposite chiralities, one at higher k-values than the other. Now, when there is a conversion at one contour, the conversion at the other texture partially compensate it. To better calculate the efficiencies, the spin densities of the majority, δS_+, and minority, δS_-, contours have to be taken into account: $< \delta S >= \delta S_+ + \delta S_-$. The two spin densities also have distinct spin relaxation times and Fermi wave-vectors while they share the same Fermi energy, hence Fermi velocity. To obtain the Rashba splitting, one can write α_R [33]:

$$\begin{aligned} k_{F+} - k_{F-} &= \frac{m^*}{\hbar^2}\alpha_R \\ \delta S_\pm &= \frac{m^*}{e2\hbar k_{F\pm}} J_\pm \\ J_c^{2D} &= \frac{q\alpha_R}{\hbar} < \delta S > \end{aligned} \tag{1.34}$$

with q being the carrier charge. Combining equations 1.33 and 1.34, we obtain:

$$\lambda_{IREE} = \frac{\alpha_R \tau}{\hbar} \tag{1.35}$$

From this equation, we deduce that high λ_{IREE} values are obtained in systems with either high Rashba spin-orbit splitting, α_R, or long spin relaxation time, τ.

Comparing the efficiencies of ISHE and IREE

It is worth noting that the unit of the conversion efficiency of ISHE is dimensionless while the one of IREE has a unit of length. Also, the conversion in ISHE takes place on a distance comparable to the spin diffusion length, λ_s, we can thus compare the IREE length with the spin Hall angle, θ_{SH}, through the equation:

$$\lambda_{IREE} \approx \lambda_s \theta_{SH} \tag{1.36}$$

1.3 Ferromagnetic resonance and spin pumping

1.3.1 Ferromagnetic resonance

The concept of magnetization precession in a ferromagnetic crystal was first developed by the Soviet physicists Lev Landau and Evgeny Lifshitz back in 1935 [43] which was further updated by Gilbert in 1955 when he included the damping term [44] in the Landau-Lifshitz equation (which is now called Landau-Lifshitz-Gilbert, LLG, equation). In the following, I will present the magnetization precession equations under resonance conditions.

LLG equation

First, we can discuss the pioneering Landau-Lifshitz equation which gives the relation between the magnetization vector, $\mathbf{M}$ (its norm is the saturated magnetization, M_s), and the effective applied magnetic field, $\mathbf{H}_{eff}$:

$$\frac{d\mathbf{M}}{dt} = -\frac{g\mu_B}{\hbar}\mathbf{M} \times \mu_0\mathbf{H}_{eff} \tag{1.37}$$

g being the Landé factor (2<g<2.2 for a ferromagnet), μ_B the Bohr magneton, and μ_0 the vacuum permeability. As a remainder:

$$\mathbf{H}_{eff} = \mathbf{H}_0 + \mathbf{H}_D + \mathbf{H}_k \tag{1.38}$$

$\mathbf{H}_0$ being the external applied field, $\mathbf{H}_D$ the demagnetizing field, $\mathbf{H}_k$ the anisotropy field.

A simple explanation of the Landau-Lifshitz equation is again given by Noel [33], and can be summarized as follows:

The effective field, $\mu_0\mathbf{H}_{eff}$, tends to align the moments $\boldsymbol{\mu}$ in the ferromagnet along its direction through the action of a torque $\boldsymbol{\tau}$:

$$\boldsymbol{\tau} = \boldsymbol{\mu} \times \mu_0\mathbf{H}_{eff} \tag{1.39}$$

And, by definition, the torque applied by the effective field is equal to the derivative of the angular momentum, $\mathbf{J}$:

$$\boldsymbol{\tau} = \frac{d\mathbf{J}}{dt} \tag{1.40}$$

Moreover, the magnetic moment and the angular momentum are linked through the gyromagnetic ratio, $\gamma = \frac{g\mu_B}{\hbar}$:

$$\boldsymbol{\mu} = -\gamma\mathbf{J} \tag{1.41}$$

So far, $\boldsymbol{\mu}$ was for a single atom, now we can replace it by the magnetization vector $\mathbf{M}$ (being the density of magnetic moments in the ferromagnet) of the whole material, giving the Landau-Lifshitz equation.

The Landau-Lifshitz equation implies that the precession goes on perpetually, without any process to damp the precession. Landau and Lifshitz added a small damping term, λ, that takes into account various scattering events (electron-magnon scattering, magnon-phonon scattering, etc.) leading to the following equation:

$$\frac{d\mathbf{M}}{dt} = -\gamma\mathbf{M} \times \mu_0\mathbf{H}_{eff} - \lambda\mathbf{M} \times (\mathbf{M} \times \mathbf{H}_{eff}) \tag{1.42}$$

Then, for a large damping, Gilbert proposed a modification for the above equation in 1955 [44] to have the damping term proportional to the derivative of the magnetization vector. In other words, if the precession is rapid, i.e. the magnetization vector is changing fast, then the damping is also strong. This, in turn, slows down the precession, which also decreases the damping in the negative feedback loop. The damping term, a dimensionless parameter, is denoted as α, and the resulting Landau-Lifshitz-Gilbert equation becomes:

$$\frac{d\mathbf{M}}{dt} = -\gamma\mathbf{M} \times \mu_0\mathbf{H}_{eff} + \frac{\alpha}{M_s}\mathbf{M} \times \frac{d\mathbf{M}}{dt} \tag{1.43}$$

Fig.1.14 summarizes the difference of magnetization precessions with and without the damping term in the LL and LLG equations, respectively.

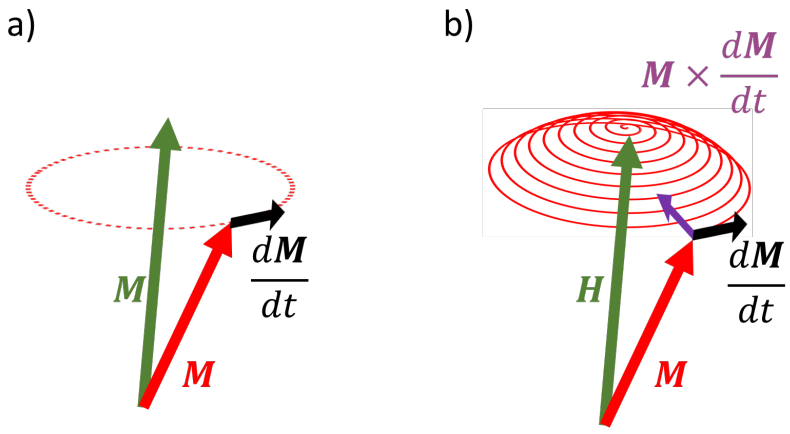

Figure 1.13: Representation of LLG equation a) with and b) without a damping term.

Ferromagnetic resonance

Resonance is an important phenomenon in physics where the amplitude of oscillation of a system is greatly enhanced at specific frequencies of external excitations. In ferromagnets, the resonance frequency of the magnetization vector is in the GHz range, depending on the applied external field. In the following paragraphs, we summarize the resonance conditions for ferromagnetic thin films.

As discussed in the previous sections, the precessional motion of the magnetization vector around the effective external field can be well described by the Landau-Lifshitz equation. Now, we will separate the magnetization and the field vectors into static and dynamic components:

$$\begin{aligned} \mathbf{M}_{tot} &= \mathbf{M}_0 + \mathbf{m}(\mathbf{r},t) \\ \mathbf{H}_{tot} &= \mathbf{H}_{eff} + \mathbf{h}(\mathbf{r},t) \end{aligned} \tag{1.44}$$

here $\mathbf{M}_0$ and $\mathbf{H}_{eff}$ are the static components; and $\mathbf{m}(\mathbf{r},t)$ and $\mathbf{h}(\mathbf{r},t)$ are the dynamic components of the magnetization and effective field, respectively.

$\mathbf{m}$ and $\mathbf{h}$ are usually two orders of magnitude smaller than $\mathbf{M}_0$ and $\mathbf{H}_{eff}$, thus, $\mathbf{m}$ and $\mathbf{h}$ can be treated as perturbations to the total magnetization and magnetic field.

To make the vectorial calculations easier, we redefine the magnetization and magnetic field vectors with unit vectors:

$$\begin{aligned} \mathbf{M}_0 &= M_0\mathbf{y} \\ \mathbf{H}_{eff} &= H_{eff}\mathbf{y} \end{aligned} \tag{1.45}$$

Now, introducing these perturbations into the Landau-Lifshitz equation gives:

$$\frac{d\mathbf{m}(\mathbf{r},t)}{dt} = -\mu_B \frac{1}{\hbar}(M_0\mathbf{y} \times \mu_0\mathbf{h}(\mathbf{r},t) + \mathbf{m}(\mathbf{r},t) \times \mu_0 H_{eff}\mathbf{y}) \tag{1.46}$$

And writing $\mathbf{m}$ and $\mathbf{h}$ in the frequency domain as $\mathbf{m}(\omega)e^{i(\omega t)}$ and $\mathbf{h}(\omega)e^{i(\omega t)}$ allows to linearise the previous equation as:

$$i\omega\mathbf{m} = -\frac{g\mu_B}{\hbar}\mathbf{y} \times (M_0\mathbf{h} - \mu_0 H_{eff}\mathbf{m}) \tag{1.47}$$

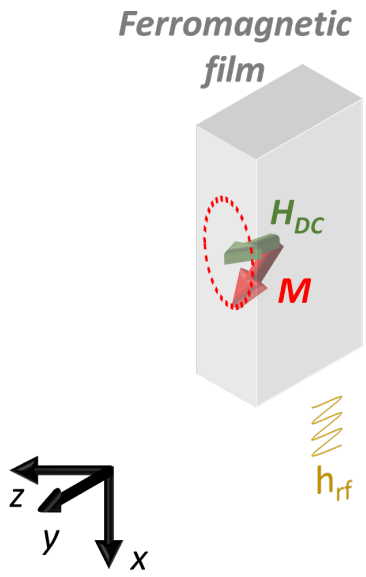

Figure 1.14: Ferromagnetic resonance sketch including the coordinate system adopted in the derivation of the equations.

Projecting this equation on the coordinate axis yields:

$$\begin{aligned} i\omega m_x &= \frac{g\mu_B}{\hbar}(\mu_0 M_0 h_z - \mu_0 H_{eff} m_z) \\ i\omega m_y &= 0 \\ i\omega m_z &= \frac{g\mu_B}{\hbar}(-\mu_0 M_0 h_x - \mu_0 H_{eff} m_x) \end{aligned} \tag{1.48}$$

With the Polder susceptibility tensor, it is possible to link the magnetization with the external magnetic field, as $\mathbf{m} = \overleftrightarrow{\chi}\mathbf{h}$, with the tensor being:

$$\overleftrightarrow{\chi} = \begin{pmatrix} \chi' & i\chi'' \\ -i\chi'' & \chi' \end{pmatrix} \tag{1.49}$$

Combining the previous two equations, we obtain:

$$\chi' = \frac{M_0 H_{eff}(\frac{g\mu_B}{\hbar})^2}{(\frac{g\mu_B}{\hbar})^2 H_{eff}^2 - \omega^2}; \chi'' = \frac{\omega M_0 \frac{g\mu_B}{\hbar}}{(\frac{g\mu_B}{\hbar})^2 H_{eff}^2 - \omega^2} \tag{1.50}$$

Since the susceptibility of a material defines how strong its response is to a magnetic field, we have to find its maximum value which means when the denominator equals zero:

$$\omega_{res} = (\frac{g\mu_B}{\hbar})\mu_0 H_{eff} \tag{1.51}$$

This equation is indeed different from the Kittel formula [45] which takes into account the demagnetizing field.

In the thin film limit, the demagnetizing tensor relates the demagnetizing field to the magnetization through, $\mathbf{H}_D = \overleftrightarrow{N}\mathbf{M}_{tot}$:

$$\mathbf{H}_D = \begin{pmatrix} N_x & 0 & 0 \\ 0 & N_y & 0 \\ 0 & 0 & N_z \end{pmatrix} \begin{pmatrix} m_x \\ M_s \\ m_z \end{pmatrix} \tag{1.52}$$

For an in-plane field in an infinite film, it yields $N_x = N_y = 0$ and $N_z = 1$. Now we can include the damping and demagnetizing field into the Polder susceptibility given above for the imaginary part:

$$\chi'' = \frac{-\alpha(\frac{\omega}{\gamma})\mu_0 M_s((\mu_0 M_s + \mu_0 H_0 + \mu_0 H_k)^2 + (\frac{\omega}{\gamma})^2)}{(\mu_0^2(M_s + H_0 + H_k) * (H_0 + H_k) - (\frac{\omega}{\gamma})^2) + (\alpha(\frac{\omega}{\gamma})(\mu_0 M_s + 2(\mu_0 H_0 + H_k))^2)} \tag{1.53}$$

The resonance condition corresponds to the Kittel formula:

$$\omega_{res} = \frac{g\mu_B}{\hbar}\mu_0\sqrt{(M_s + H_0 + H_k)(H_0 + H_k)} \tag{1.54}$$

The absorption of the microwave power by the ferromagnetic film is proportional to χ'' and close to the resonance, it exhibits a Lorentzian shape as a function of the applied field:

$$\chi'' = \frac{A_{sym}\Delta H^2}{\Delta H^2 + (H_{eff} - H_{res})^2} \tag{1.55}$$

A_{sym} being the amplitude of the Lorentzian, ΔH the half width at half maximum (HWHM). The relation between the Gilbert damping, α, and ΔH is given by $\mu_0\Delta H = \frac{\alpha\omega}{\gamma}$; the absorbed power is given by $P_{abs} = \omega\chi'' h_{rf}^2$, thus, is directly proportional to the square of the rf magnetic field.

There could be asymmetric contributions to the Lorentzian shape of the FMR signal, possibly due to eddy currents in the metallic heterostructures. For this reason, we can write down the total signal as the sum of symmetric and asymmetric components:

$$\chi'' = A_{sym}\frac{\Delta H^2}{\Delta H^2 + (H_{eff} - H_{res})^2} + B_{asym}\frac{\Delta H(H_{eff} - H_{res})}{\Delta H^2 + (H_{eff} - H_{res})^2} \tag{1.56}$$

In this manuscript, I will discuss FMR results obtained either in a cavity setup at $\mathscr{X}$-frequency with field modulation or in a broadband setup with Au-waveguides at various GHz frequencies. The detailed description of each setup can be found in the experimental methods chapter.

To detect the FMR signal we use a lock-in technique which gives the signal in the form of the first order derivative of the Lorentzian signal (see Fig. 1.15). To fit the experimental curve we use the following equation:

$$\frac{d\chi''}{dH} = -2A_{sym}\frac{\Delta H^2(H_{eff} - H_{res})}{(\Delta H^2 + (H_{eff} - H_{res})^2)^2} + 2B_{asym}\frac{\Delta H(H_{eff} - H_{res})^2}{(\Delta H^2 + (H_{eff} - H_{res})^2)^2} - B_{asym}\frac{\Delta H}{(\Delta H^2 + (H_{eff} - H_{res})^2} \tag{1.57}$$

The fit is used to extract important parameters from the FMR signal, such as, H_{res}, ΔH, and ΔH_{pp}; and the relation between the last two is: $\Delta H_{pp} = \frac{2}{\sqrt{3}}\Delta H$. ΔH_{pp} is an important quantity as it is related to the Gilbert damping in the LLG equation:

$$\mu_0\Delta H_{pp} = \frac{2}{\sqrt{3}}\frac{\alpha\omega}{\gamma} \tag{1.58}$$

However, this is a simplistic picture of the linewidth (ΔH_{pp}). There could be additional effects contributing to the linewidth broadening, such as, inhomogeneity in the crystal, magnetic anisotropy, etc., which

modifies the above equation to:

$$\mu_0 \Delta H_{pp} = \frac{2}{\sqrt{3}} \frac{\alpha \omega}{\gamma} + \mu_0 \Delta H_0 \tag{1.59}$$

ΔH_0 being the supposed broadening at 0 GHz frequency. To find this value, broadband experiments have to be carried out at various frequencies to plot ΔH_{pp} as a function of the frequency. This gives a linear dependence, extrapolating this to 0 GHz gives the ΔH_0 value.

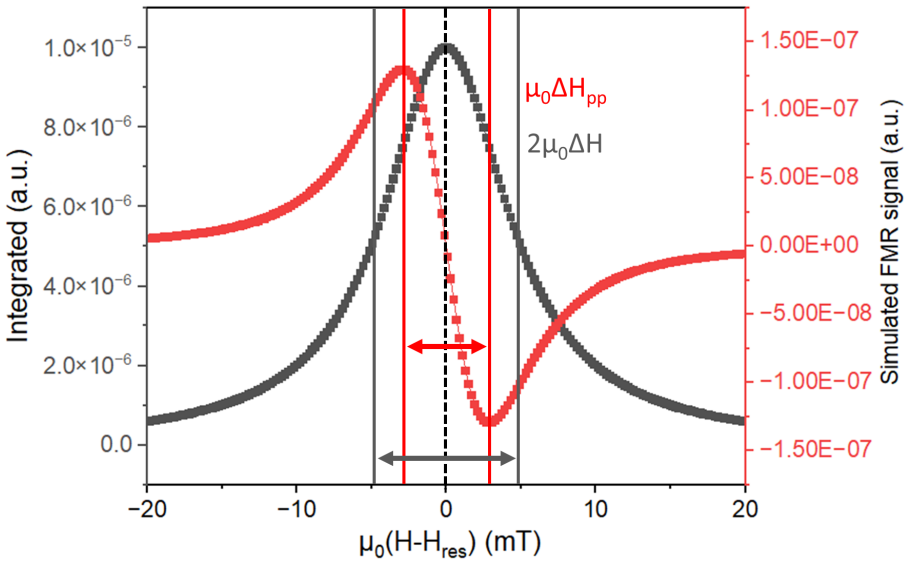

Figure 1.15: FMR signal showing the HWHM of the Lorentzian.

Broadband and in cavity FMR

Most of the FMR experiments were carried out in a resonant microwave cavity. Unlike the broadband setup which is described in the Experimental Methods chapter, it is not possible to modulate the frequency in the resonant cavity. The resonant cavity we used was a MS5 loop-gap resonator at X band (9.8 GHz) operating in a pseudo- TE_{102} mode [33]. The resonant cavity gives better signal-to-noise ratio than the broadband setup thanks to the isolation from the outside radiation sources, also we can obtain other important physical quantities, such as, M_s, H_k, and the damping parameter, α by measuring the full angular dependence of the resonance field.

A Brucker EPR 300E setup was used to obtain the ferromagnetic resonance in cavity. The sample is inserted in the center of the cavity where the rf field, h_{rf}, is maximized. The angle between the normal of the sample surface and the applied DC magnetic field is defined as θ_H, which can be adjusted with a goniometer.

The resonance condition for each angle is given by the Smit-Beljers equation [46], [47], [48] that is based on the minimization of the free energy density in the ferromagnetic film, F:

$$(\frac{\omega}{\gamma})^2 = \frac{1}{\mu_0 M_s^2 sin^2\theta} \left[\frac{\partial^2 F}{\partial \theta^2} \frac{\partial^2 F}{\partial \phi^2} - \left(\frac{\partial^2 F}{\partial \theta \partial \phi} \right)^2 \right] \tag{1.60}$$

θ and ϕ being the polar and azimuthal angles, respectively. The derivatives are calculated at the equilibrium angles θ_M and ϕ_M defined when the magnetization direction satisfies: $\partial F/\partial \theta$=0 and $\partial F/\partial \phi$=0. For an

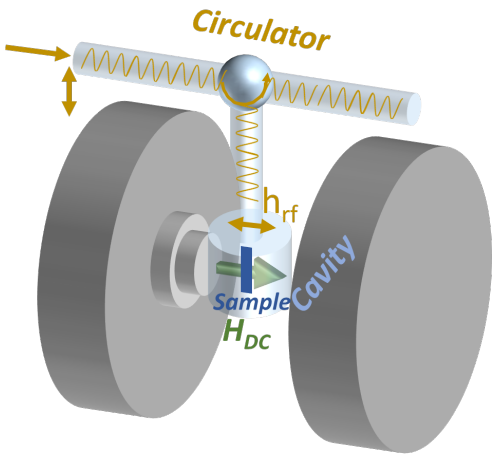

Figure 1.16: Illustration of the setup used for spin pumping using FMR. The cavity is located in between the two coils of the electromagnet.

out-of-plane angular-dependence, only the polar angle θ is modulated, the azimuthal angle ϕ is fixed. Now we can write the free energy density, F, as the sume of the Zeeman energy, demagnetization energy, and the uniaxial magnetic anisotropy energy:

$$F = -\mu_0 \mathbf{M} \cdot \mathbf{H} + \frac{\mu_0}{2} M_s^2 cos^2\theta_M + K_u cos^2\theta_M \tag{1.61}$$

K_u is defined as the perpendicular uniaxial magnetic anisotropy energy, $K_u = \frac{\mu_0 H_u M_s}{2}$, and H_u is the corresponding anisotropy field. For an out-of-plane angular dependence in the yz plane, $\mathbf{M}$ and $\mathbf{H}$ are given by:

$$\begin{aligned} \mathbf{M} &= M[sin\theta_M cos\phi_M \mathbf{x} + sin\theta_M sin\phi_M \mathbf{y} + cos\phi_M \mathbf{z}] \\ \mathbf{H} &= H_{DC}[sin\theta_H \mathbf{y} + cos\theta_H \mathbf{z}] \end{aligned} \tag{1.62}$$

Then, the expression of the free energy density becomes:

$$F = -\mu_0 M_s H_{DC}(sin\theta_M sin\phi_M sin\theta_H + cos\theta_M cos\theta_H) + \frac{\mu_0}{2}(M_s + H_u) M_s cos^2\theta_M \tag{1.63}$$

Combining the conditions of vanishing derivatives in 1.60 and the free energy expression in 1.63, we obtain the equilibrium condition:

$$\begin{aligned} 2H_{DC} sin(\theta_M - \theta_H) &= M_{seff} sin2\theta_M \\ \phi_M &= \pi/2 \end{aligned} \tag{1.64}$$

M_{seff} being the effective magnetization taking into account the anisotropy $M_{seff} = M_s + H_u$. 1.60 can now be written as:

$$\left(\frac{\omega}{\gamma}\right)^2 = \mu_0^2 \left[H_D C cos(\theta_M - \theta_H) - M_{seff} cos^2\theta_M\right] \left[H_{DC} cos(\theta_M - \theta_H) - M_{seff} cos2\theta_M\right] \tag{1.65}$$

Using the equation above, one can extract the effective magnetization, magnetic anisotropy, and g-factor (gyromagnetic ratio) from the out-of-plane angular dependence.

1.3.2 Spin pumping by ferromagnetic resonance

There are various methods to study spin-charge interconversion phenomena which giving rise to (inverse) spin Hall and (inverse) Rashba-Edelstein effects. The methods include Spin-Transfer FMR (ST-FMR), second harmonic Hall measurements, spin pumping by FMR (SP-FMR), spintronic THz emission (STE), etc. The first two study charge to spin conversion, while the latter two study spin to charge conversion.

SP-FMR is based on the technique of FMR that has been discussed earlier where the magnetization of the ferromagnet is excited to resonance by GHz waves. The concept of injecting spins into another material from the ferromagnet at the resonance condition was first conceptualized by Silsbee and Johnson [49] in 1980s. The spin pumping theory was then developed by Tserkovniak in 2002 [50]. The experimental proof was given later in 2006 by Saitoh [36] by measuring the voltage resulting from spin to charge conversion in platinum. Following those results, spin pumping by ferromagnetic resonance has become a well-established technique to study spin to charge conversion phenomena and determine the spin diffusion length and, more importantly, the spin Hall angle, θ_{SH}, and the inverse Rashba-Edelstein length, λ_{IREE}.

Spin injection

Spin injection from a magnetic material into a non-magnetic material can be understood as the inverse effect to spin torque. According to the description given by Berger and Slonczewski [51], when a spin current from the non-magnetic material is injected into a magnetic material, a transfer of angular momentum occurs to the latter via the s-d exchange [33]. This leads to the precession of the magnetization vector, and if sufficient angular momentum is provided by the non-magnetic layer, the magnetization vector can switch to the opposite direction. To account for the additional torque on the magnetization, originating from the non-magnetic layer in the form of angular moment transfer, Berger and Slonczewski added a term in the Landau-Lifschitz-Gilbert (making it Landau-Lifschitz-Gilbert-Slonczewski) equation:

$$\frac{d\mathbf{M}}{dt} = -\gamma\mu_0\mathbf{M}\times\mathbf{H}_{eff} + \frac{\alpha}{M_s}\mathbf{M}\times\frac{d\mathbf{M}}{dt} + \tau_{Sloncz} \tag{1.66}$$

On the contrary, when the magnetization is precessing due to, for example, ferromagnetic resonance excitation at the GHz frequency, the magnetic layer loses angular momentum into the non-magnetic layer in the form of a spin current, $J_{s,pumping}$. For this reason, spin pumping at ferromagnetic resonance comes from angular momentum loss, and contributes to the damping parameter, α, by $\Delta\alpha$. This requires the next modification to the LLG equation: the damping term, α, should be divided into to two. The first one is for the ferromagnetic layer only (that gives α_{ref}), and the second is for the ferromagnetic/non magnetic bilayer giving $\alpha_{tot} = \alpha_{ref} + \Delta\alpha$:

$$\frac{d\mathbf{M}}{dt} = -\gamma\mu_0\mathbf{M}\times\mathbf{H}_{eff} + \frac{\alpha_{ref}}{M_s}\mathbf{M}\times\frac{d\mathbf{M}}{dt} + \frac{\Delta\alpha}{M_s}\mathbf{M}\times\frac{d\mathbf{M}}{dt} \tag{1.67}$$

However, for some ferromagnetic/non-magnetic interfaces, one has to consider another mechanism called spin memory loss [52]. In the case of Pt/Py, this effect is negligible.

Spin current

A high quality interface between the ferromagnetic and the non-magnetic layers ensures efficient spin injection at ferromagnetic resonance, large damping and Δ_α values, implying enhanced spin injection by

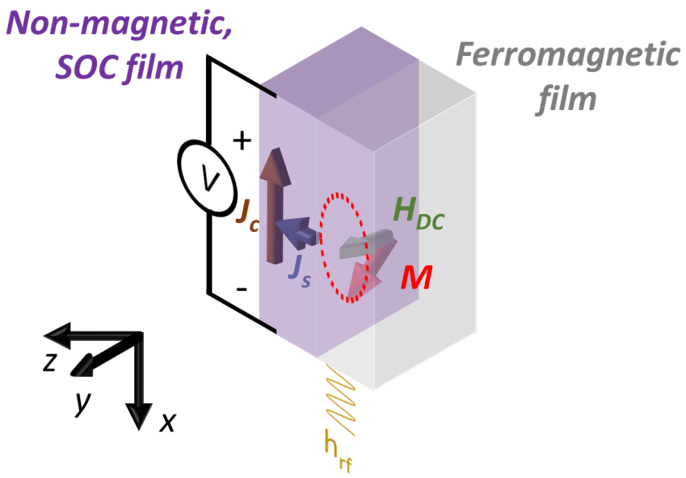

Figure 1.17: Sketch of the spin injection in SP-FMR experiments. The injected spin current is converted into a charge current by ISHE, leading to the formation of a potential difference at the sample ends which can be measured in open circuit conditions.

spin pumping, as presented in the model of Tserkovnyak et al. [50]:

$$\begin{aligned} \mathbf{J}_{s,0}^{pump} &= \frac{\hbar}{4\pi}\frac{Re(g^{\uparrow\downarrow})}{M_s^2}\mathbf{M}\times\frac{d\mathbf{M}}{dt}\left(\frac{2e}{\hbar}\right) \\ \Delta\alpha &= \frac{g\mu_B}{4\pi M_s t_{FM} Re(g^{\uparrow\downarrow})} \end{aligned} \tag{1.68}$$

with $g^{\uparrow\downarrow}$ being the spin mixing conductance standing for global spin current transmission, t_{FM} being the ferromagnetic layer thickness.

The injected spin current can be reabsorbed by the ferromagnetic layer in particular when the thickness of NM is less than the spin diffusion length, mainly due to the reflection back at the NM/vacuum interface. Considering the effect of this back-flow on the spin current and spin mixing conductance, we can write down their effective expressions:

$$\begin{aligned} J_s &= J_{s,0}^{pump}\left(1-e^{\frac{-2t_{NM}}{\lambda_s}}\right) \\ g_{eff}^{\uparrow\downarrow} &= g^{\uparrow\downarrow}\left(1-e^{\frac{-2t_{NM}}{\lambda_s}}\right) \end{aligned} \tag{1.69}$$

The factor two is due to the back and forth trajectory of the electrons, while $e^{\frac{-2t_{NM}}{\lambda_s}}$ represents the exponential decrease of the spin population in the NM.

The equation of the spin current is given to be dependent on the derivative of the magnetization, meaning that it is an AC current. The measured charge current arising from the spin-to-charge conversion of the spin pumped signal is in DC. This DC current is obtained by integrating over the whole precession of the magnetization vector giving:

$$J_{s,DC}^{pump} = \frac{\omega}{2\pi}\int_0^{\frac{2\pi}{\omega}}\frac{\hbar}{2}\frac{Re(g_{eff}^{\uparrow\downarrow})}{M_s^2}\mathbf{M}\times\frac{d\mathbf{M}}{dt}\left(\frac{2e}{\hbar}\right)\mathrm{d}t. \tag{1.70}$$

All the physical quantities in this equation do not change with time, except for the magnetization. Thus, to accurately estimate the DC spin current, one has to know the exact trajectory of the magnetization vector.

In homogeneously magnetized samples, restricting the calculation to a small precession cone angle approximation, the LLG equation can be linearized. The next step is to calculate the magnetization components along x, y, and z which requires the exact expression of the Polder tensor and resonance conditions for each angle in the equations 1.64 and 1.65. Then, we obtain the magnetization components along x and z:

$$\begin{aligned} M_x(t) &= \frac{\mu_0 M_s h_{rf}\gamma\left[2\alpha\omega cos\omega t + \left(\mu_0 M_s\gamma sin^2(\theta_M + \sqrt{(\mu_0 M_s\gamma sin^2\theta_M)^2+4\omega^2}\right) sin\omega t\right]}{2\alpha\omega\sqrt{(\mu_0 M_s\gamma sin^2\theta_M)^2+4\omega^2}} \\ M_z(t) &= \frac{\mu_0 M_s h_{rf}\gamma cos\omega t}{\alpha\sqrt{(\mu_0 M_s\gamma sin^2\theta_M)^2+4\omega^2}} \end{aligned} \tag{1.71}$$

Those two equations and the small angle approximation giving $\frac{dM_y}{dt} = 0$, yield the expression for the spin current:

$$J_{s,pump} = \frac{Re\cdot g^{\uparrow\downarrow}\cdot\gamma^2\cdot h\cdot h_{rf}^2}{16\pi^2\alpha^2}\left(\frac{\mu_0 M_s\gamma sin^2\theta_M + \sqrt{(\mu_0 M_s\gamma sin^2\theta_M)^2+4\omega^2}}{(4\pi M_s\gamma sin^2\theta_M)^2+4\omega^2}\right)\left(\frac{2e}{\hbar}\right) \tag{1.72}$$

The above equation implies that the injected spin current is proportional to the absorbed microwave power at resonance (linearly dependent on h_{rf}^2), thus to the out-of-equilibrium magnetization and the field dependence exhibits a Lorentzian shape as χ''. The injected spin current is given in units of $A\cdot m^{-2}\cdot T^{-2}$. The above equation can also give the angular dependence of ISHE and IREE as explained in the next subsection.

1.3.3 Charge current measurements

After establishing the principles of spin current generation and injection into a non-magnetic thin film, the next step is to measure the converted charge current. In open circuit conditions, the current is measured as a voltage drop thanks to a nanovoltmeter with much larger impedance (GOhm) than the sample one (500 Ohm). The injected spin current from the FM is polarized along the y axis and is injected into the heavy metal (HM or SOC material). Due to SOC (in the bulk and/or at the interface), the spin current current is converted into a charge current either by the ISHE or IREE and flows along the x axis creating an electric field $\mathbf{E}$. This electric field creates a current equal, in open circuit conditions, in amplitude but opposite to the current generated by the ISHE (or the IREE):

$$\mathbf{J}_c(x) = -\sigma\mathbf{E} \tag{1.73}$$

σ being the conductivity of the sample. The sample is approximated to a wire due to its dimensions (length=2.4 mm and width=0.4 mm), therefore we can write that $||\mathbf{E}|| = V_{sp}/L$. Due to the spin to charge conversion mechanism, the measured voltage shows a Lorentzian shape. Moreover, following symmetry relations, it changes sign when the magnetic field or the stacking order is reversed. From the previous equation, we can simply calculate the total charge current produced with the Ohm's law:

$$I_c = \frac{V_{sp}}{R} \tag{1.74}$$

R being the total resistance of the sample.

As the sample is never ideally placed inside the cavity, the absorbed rf power can vary as we rotate the sample inside the cavity. Thus, we have to normalize the obtained voltage (and by the rf power current) to obtain a better picture of conversion, showing the signal in the unit of $\mu V/T^2$. In the MS5 3loop-2gap cavity,

we can determine the rf field amplitude using the cavity quality factor (Q) and the microwave power (P):

$$h_{rf} = 0.2\sqrt{\frac{PQ}{500}} \tag{1.75}$$

Conversion efficiency

In spin-to-charge conversion experiments, we aim at estimating physical quantities that can give information on conversion efficiencies. Such quantities are the spin Hall angle, θ_{SH}, the spin diffusion length, λ_s, or the inverse Edelstein length, λ_{IREE}. The inverse Rashba-Edelstein length is given by:

$$\lambda_{IREE} = \frac{J_c^{2D}}{J_{s,pump}^{3D}} = \frac{J_c}{W \cdot J_{s,pump}^{3D} sin\theta_M} \tag{1.76}$$

For the ISHE, we have to take into account the spin diffusion length and the spin current as a function of the distance from the FM/SOC material interface can be defined as:

$$J_s(z) = J_{s,pump} \frac{sinh(\frac{t_N - z}{\lambda_s})}{sinh(\frac{t_N}{\lambda_s})} \tag{1.77}$$

t_N being the thickness of the non-magnetic material, $J_{s,pump}$ is the spin current density at the interface due spin injection by spin pumping at the FMR. This spin current is then converted into a charge current by the ISHE: $\mathbf{J}_c^{ISHE} = \theta_{SH}\mathbf{J}_s(z) \times \sigma$. To calculate the total charge current along x, we have to integrate along z:

$$J_c = W \int_0^{t_N} \theta_{SH} \left(\mathbf{J_s}(z) \times \sigma\right) \cdot \mathbf{x} dz \tag{1.78}$$

Combining equations 1.76 and 1.77 into the 1.78, we obtain:

$$J_c = W \theta_{SH} \lambda_s sin\theta_M J_{s,pump} tanh(\frac{t_N}{2\lambda_s}) \tag{1.79}$$

In summary, we can write the relation between the charge current and the thickness of the films, $I_c \propto tanh(\frac{t_N}{2\lambda_s})$.

1.4 Study of spin-to-charge conversion using ultrafast phenomena

The control of magnetization in thin films has been the cornerstone of spintronics: from stray fields for in-plane recording, to transfer of angular momentum through spin currents in SOT-MRAMs. For applications, the faster the switching, the better it is. However, until 1996 the study of ultrafast electronic relaxation processes occurring in metallic materials with the help of femtosecond optical pulses was lacking contributions from magnetic effects. The pioneering work was conducted by Beaurepaire et al [53], where they observed ultrafast demagnetization of a ferromagnetic nickel film using optical and magneto-optical pump-probe techniques. Later, follow up experiments by other groups found the existence of spin currents, with the debating nature of whether it is diffusive or ballistic. From an application point of view for ultrafast recording, it was important to understand the dynamics of these spin currents. However, by means of magneto-optical techniques, it is not possible to directly measure spin currents, as they only measure (de)magnetization dynamics. The three-temperature model tells us that there is a transfer of angular momentum from the electron system to the phonon system meaning that de- and re-magnetization dynamics are not described by spin current dynamics. Thus, traditional magneto-optical techniques are not suitable to study

spin current dynamics. There are, however, other techniques to study spin current by means of magnetization reversal that would require elaborate sample processing steps which would add complexity to the interpretation of the dynamics. Moreover, the existing electronics are not able to detect signals in the THz regime. To circumvent this issue, Battiato et al proposed [54],[55] to use the inverse spin Hall effect. Spin-to-charge conversion by the ISHE was observed by spin pumping at the ferromagnetic resonance in static conditions at the Fermi level. During my PhD, I used the opposite approach: I used spintronic THz emission to study spin-to-charge conversion mechanisms in novel 2D van der Waals materials since measuring the conversion effects using the conventional spin pumping technique was made difficult by the sample preparation step (due to the van der Waals nature of the materials). THz-TDS does not require any sample preparation step, whereas for spin pumping experiments samples have to be diced into bars of 0.4 mm by 2.4 mm to minimize the effect of the microwave electric field in the cavity, THz-TDS measurements can be done on as grown heterostructures.

In the following sections, I will give a brief introduction to the history of ultrafast demagnetization backed up with experimental evidence, the creation of superdiffusive spin currents, and how these transient spin currents create transient charge currents giving rise to the THz radiation. of the ultrafast phenomena in ferromagnets and their heterostructures with heavy metals.

1.4.1 Briefly about THz and THz emitters

THz radiation is situated in between microwaves and infrared radiation, consisting of frequencies ranging between 0.3 THz and 30 THz, as shown in Fig. 1.18. Microwaves, infrared and visible radiations are widely used in electronics and photonics, but not many viable THz emitters are in the market. On the other hand, water molecules absorb THz electromagnetic fields, strongly reducing their intensity.

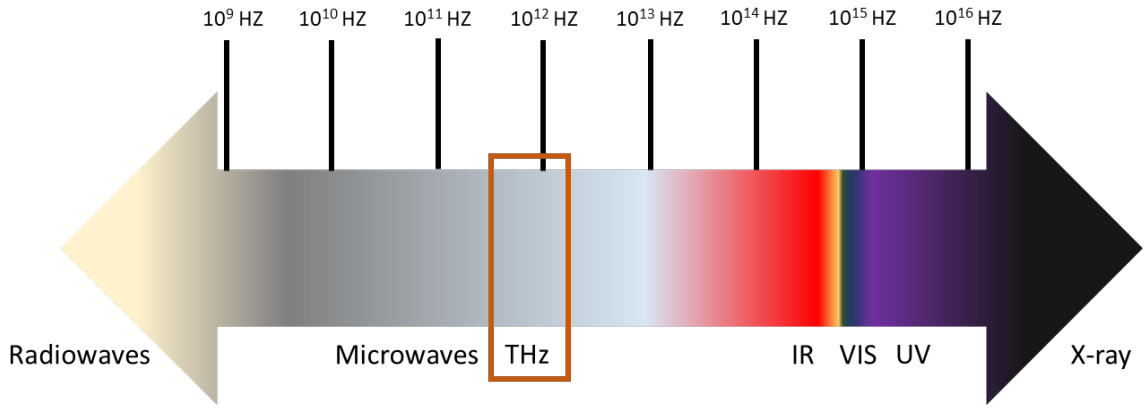

Figure 1.18: THz radiation range in the eletromagnetic spectrum.

In solid state physics, there are two main sources of THz radiation that are based on charges (electrons and holes in semiconductors) or on spin current dynamics (spintronic THz emitters) and the foundations of the emission obeys the Maxwell's equations:

$$\begin{aligned} \text{Maxwell-Gauss} \quad & \nabla \cdot \mathbf{E} = \rho/\varepsilon_0 \\ \text{Maxwell-Thomson} \quad & \nabla \cdot \mathbf{B} = 0 \\ \text{Maxwell-Faraday} \quad & \nabla \times \mathbf{E} = -\partial \mathbf{B}/\partial t \\ \text{Maxwell-Ampere} \quad & \nabla \times \mathbf{B} = \mu_0 j_c + \mu_0 \varepsilon_0 \partial \mathbf{E}/\partial t \end{aligned} \tag{1.80}$$

The magnetic induction can be defined as: $\mathbf{B} = \mu_0(\mathbf{H}+\mathbf{M})$. The output THz field, consisting of electric ($\mathbf{E}(t)$) and magnetic ($\mathbf{B}(t)$) fields, may have two distinct origins: (i) the emergence of a charge current $\mathbf{J}_c(t)$ in the sub-picosecond time scale (above 1 THz) acting as the source of the electric dipolar radiation; (ii) time varying magnetization $\mathbf{M}(t)$ also at the sub-picosecond time scales, resulting in magnetic dipolar radiation. This PhD has been about the first case and it allows to understand spin-charge conversion phenomena.

Near-field expressions

When dealing with THz emitters, we have to separately consider the near-field and far-field emissions [56], [57]. In near-field emission the electric field $\mathbf{E}^{NF}$ corresponds to the one at the vicinity of the nanometer thick emitter, while in the far-field emission the electric field $\mathbf{E}^{FF}$ represents the radiated electric field at the detector level, a few tens of centimeters away from the actual emitter. The electric fields are proportional to each other $\mathbf{E}^{NF} \propto \mathbf{E}^{FF}$.

In the former case, we can define the electric field as:

$$E^{NF}_{THz}(\omega) \propto eZ(\omega)\theta_{SH}l_{sf}j^{2D}_s(\omega), \quad \text{in the time domain:} \quad E^{NF}_{THz}(t) \propto j_c(t) \tag{1.81}$$

hence, it is directly proportional to the charge current. Here, $Z(\omega)$ is the THz impedance and j^{2D}_s is the spin current density. On the other hand, the magnetic dipolar radiation is

$$E^{NF}_{THz}(\omega) \propto -\frac{i\omega n_{THz}d_{FM}}{c}Z(\omega)M(\omega) \quad \text{and in the time domain:} \quad E^{NF}_{THz}(t) \propto \frac{\partial M(t)}{\partial t} \tag{1.82}$$

n_{THz} being the THz refractive index, d_{FM} thickness of the ferromagnet. The equation above shows that the magnetic dipolar radiation is due to the time-dependent magnetization dynamics. In spintronic THz emitters, the spin-injection based THz emission is much stronger than the one based on magnetization dynamics.

Far-field expressions

In the far-field case, we can write down the integrated output power in the free space as:

$$P_{THz} = \int_{\Omega} \varepsilon E^2(r,t)cdS \tag{1.83}$$

$\Omega = 4\pi R_0^2$ being the integrated surface (the surface of a sphere with radius R_0 being the distance to the source of emission).

$$P_{THz} \simeq \frac{Tn_{NIR}\lambda^2_{rel}S^2_{NIR}}{4\pi\varepsilon_0 c^3}\left(\frac{\partial j_c(t)}{\partial t}\right)^2 = \frac{Tn_{NIR}\lambda^2_{rel}S^2_{NIR}\omega^2}{4\pi\varepsilon_0 c^3}j_c^2 \tag{1.84}$$

$T = t^2$ is the effective transmission coefficient of NIR, n_{NIR} is the refractive index at near infrared, S_{NIR} is the pump spot size resulting in the charge current $I_c = j_c S_{NIR}$, ω the oscillation frequency and λ_{rel} the relaxation length in the active material (λ_s for ISHE or λ_{IREE} for IREE). Taking into account the integrated output power $P_{THz} = \varepsilon_0 E^2_{THz}\Omega_c$, the far-field electric field is proportional to the time derivative of the charge current times the effective THz impedance, Z_{eff}:

$$E^{FF}_{THz}(t) \propto Z_{eff}\frac{\partial j_c(t)}{\partial t}, \quad \text{and in the frequency domain:} \quad E^{FF}_{THz}(\omega) \propto -i\omega Z_{eff}(\omega)j_c(\omega) \tag{1.85}$$

The far-field regime holds for distances longer than $3\lambda_{rel}$. For spintronic THz emitters, the boundary between the near-field and far-field regions is not clearly defined, but it depends on the thickness of the film and the frequency range in consideration. Nenno et al [58] showed that the approximation of $E_{THz} \propto j_c$ holds for low frequencies and in the case of thin films. When the frequency is higher and the film thickness increases (compared to the wavelength), we have to use the other approximation $E_{THz} \propto \partial j_c/\partial t$.

Pump power dependence

There is a clear dependence of the emitted THz electric field with the absorbed laser power, the description of which is similar to the approach given by Preu et al. [59] for a photo-excited electron density in the emitter:

$$\nabla \cdot j_c = -e\theta_{SH}\delta_{rel}\frac{\partial n_e}{\partial t} \quad \text{with} \quad \frac{\partial n_e}{\partial t} = \frac{P_{NIR}}{l_{NIR}\hbar\omega_{NIR}S_{NIR}} \tag{1.86}$$

P_{NIR} is the average pump power corresponding to the pump surface of S_{NIR}, l_{NIR} is the absorption length of the laser at the frequency of ω_{NIR} and λ_{rel} is the spin current relaxation length. Now we obtain the expression for the THz output power as a function of the input pump power:

$$P_{THz} \propto \frac{T^* e^2 \delta_{rel}^4 \pi}{\varepsilon c^3 l_{NIR} h^2}\left(\frac{\omega_{THz}^2}{\omega_{NIR}^2}\right) P_{NIR}^2 \tag{1.87}$$

1.4.2 Ultrafast demagnetization

Understanding the ultrafast electron processes in metals under excitation with a short laser pulse was of fundamental importance in physics in the 80s and 90s of the last century, but little attention was paid to what happens in ferromagnets under such conditions. At that time, the theories predict the demagnetization of the ferromagnet due to the increase of temperature. The first attempt was performed with a 100 nm thick film of Ni [60] with ps to ns long laser pulses. In the ps time range, they did not observe demagnetization while the film was demagnetized after ns. The second experiment was conducted on Fe with 30 ps laser pulses [61] where they observed melting of the metal and concluded that no demagnetization takes place until the melting point. However, the laser pulses were too long so that electrons thermalized to the phonon temperatures and it was not possible to separate electron-spin and spin-lattice relaxation mechanisms. With this hypothesis, Beaurepaire et al [53], conducted a similar experiment with 60 fs and 2.0 eV laser pulses on a 22 nm Ni thin film. The magnetization, that was measured with magneto-optical Kerr effect (MOKE), showed magnetic quenching, though incomplete, in the first ps after the interaction with the pulse, followed by gradual remagnetization (see Fig.1.19a).

Later, it was pointed out that MOKE measurements might have optical artefacts and the results have to be taken with care. A decade after the first demagnetization observation by MOKE, Stamm et al [62] did a similar experiment with 1.5 eV laser pulses on a 15 nm Ni thin film to measure element specific magnetization with X-ray circular magnetic dichroism. From this study they concluded that the relaxation of spin angular momentum into the lattice happens in the time scale of 120 ± 70 fs.

Three temperature model

To exlain their observation, they proposed a three-temperature model (3TM), accounting for the temperatures of electrons, T_e, spins, T_s, and phonons, T_l. To calculate the spin temperature from the hysteresis

loops (after a fixed delay after the laser interaction), they relied on the correspondence between the spontaneous and remanent magnetizations, the electron temperature was taken to be proportional to the relative transmittance.

In the following, I introduce a simple picture of demagnetization process. However, so far, there is not a single way to describe all the processes in all types of magnetic heterostructures. For example, ferrimagnets and antiferromagnets show even more complex dynamics.

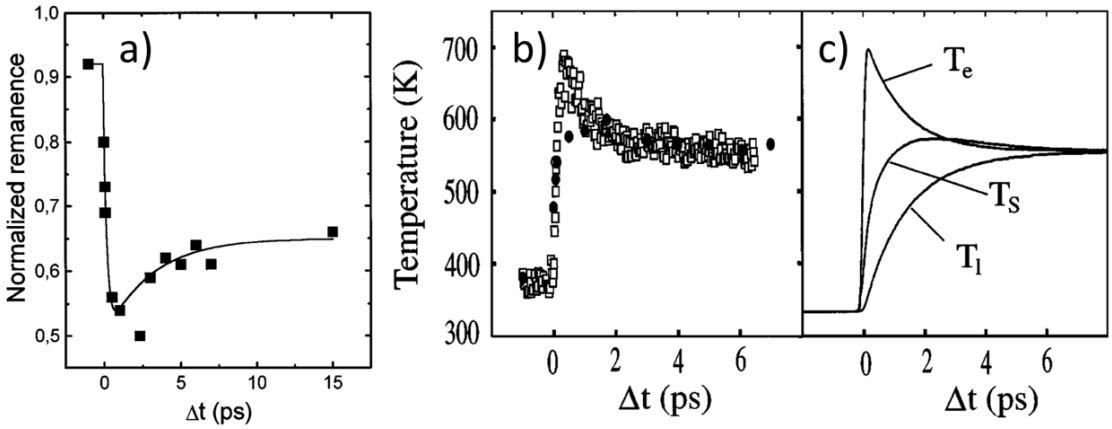

Figure 1.19: The pioneering work on ultrafast demagnetization. a) a rapid decrease in the remanence magnetization after an ultrashort laser excitation, b) the measured electron, spin, and lattice temperatures, c) the modeled electron, spin, and lattice temperatures corresponding to b. Adapted from Beaurepaire et al [53].

When looking at the Fig1.19 b, which shows the experimentally calculated temperatures of the electrons, spins, and lattice, the most remarkable feature is the sudden increase of the electronic temperature in the first picosecond after the laser hits the sample. This changes the density from Fermi-Dirac to an out-of-equilibrium distribution of spin polarized electrons. Since the ferromagnet has electrons with majority and minority spin populations, hot electrons are spin polarized. Due to various scattering events (electron-electron, electron-phonon, electron-impurity, etc.), the electronic system thermalizes into the Fermi-Dirac distribution. The net magnetization decreases due to a redistribution of majority and minority spins in higher energy levels. This can be interpreted as the increase of the spin temperature. The heat to the lattice is transferred through electron-phonon scattering events. On the other hand, the decrease in magnetization due to the redistribution of spin polarized electrons close to the Fermi level means a decrease in the angular momentum of the system. However, due to the conservation laws, the electron angular momentum has to be released into the lattice, which was shown in the works of Einstein and de Haas. Microscopically, the mechanism can be explained with the Elliot-Yafett spin-flip mechanisms. There has been a thorough research on this [63], [64] with controversial proposals [65], [66] [67].

As mentioned above, the thermalization of electrons can occur through various scattering events. An excited electron can also interact with the electrons below the Fermi level. When this happens, due to the energy conservation, it causes another excitation (as the emission of secondary electrons), and this creates a cascade of electrons. Since this mechanism leads to the thermalization of electrons, the electron distribution converges to the Fermi-Dirac one with high characteristic temperature. The multiplication of electrons is accompanied with more electron diffusion. Hence, the electronic system thermalization leads to a multiplication of diffusing electrons.

Due to the high energy of electrons after laser excitation, the three-temperature model implies that there is electronic transport in the ferromagnetic layer. For an amorphous layer, we can claim that this electronic propagation is equal in all the directions and creates an expanding sphere of electronic transport. Moreover,

the electrons in the ferromagnet are spin polarized: there exists majority spins and minority spins. Thus, after the fs excitation, hot electrons are spin polarized as well. Another aspect of ferromagnets is the existence of two transport channels: one for each spin orientation, with different diffusion constant for majority and minority spins. Considering those aspects, we can treat the transport of hot electrons as a spin polarized current. The following subsection is dealing with the generation of the spin current resulting from the fs excitation.

Superdiffusive transport of spins

Battiato et al proposed a model to describe the complex electronic transport after fs excitation [68] [69]. In this model, at the early stages after the excitation, electrons have very high energy, thus their transport can be treated as ballistic. At the later stages, due to electron-electron scatterings, the electronic system thermalizes and the transport can be treated as diffusive. This model is called superdiffusive to capture both extremes, hence, representing more of a transient phenomenon.

Fig. 1.20a) shows a typical geometry of the fs laser excitation experiments consisting of a FM (Ni) and a NM (Al) and the inset shows the geometry used in the calculations [68]. After the laser excitation, hot electrons are generated in the FM layer that start moving in random directions. Battiato et al. calculated the time-dependent magnetization due to the superdiffusive spin currents after the excitation [68].

Once the laser hits the FM layer, the electrons are typically excited from the d-band where they are quasi-localized to sp-like bands with higher velocities. Also, the laser excitation is treated as conserving the electron spin, and the outgoing electron trajectory is considered as a straight line until the first scattering. Those electrons are considered as first-generation electrons, and after the first scattering as second-generation, and so on. The trajectory, $s(t)$, of a first generation electron is given explicitly by the following integration:

$$\int_0^s \frac{ds'}{v(z(s'))} = t \tag{1.88}$$

here, $v(\sigma, E, z)$ is the velocity, $z(s)$ the electron z-coordinate with s being the curvilinear coordinate along the trajectory, and t is the time required to reach s. The probability to reach s without a scattering event is $P(s) = e^{\left[-\int_0^s \frac{ds'}{\tau(z(s'))v(z(s'))}\right]}$, where $\tau(\sigma, E, z)$ is the lifetime.

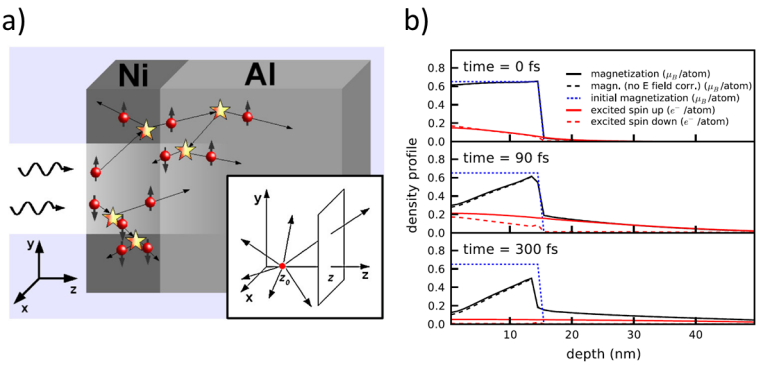

Figure 1.20: Superdiffusive spin current. a) Sketch of the superdiffusive processes after the laser excitation in Ni/Al heterostructure. The excited electrons cause a cascade of electrons, the inset shows the geometry used for the calculations, b) calculation of the spatial magnetization profiles for three different times after the laser excitation. Adapted from Battiato et al [68].

By integrating the emission over all possible angles for an isotropic case, the statistically averaged flux

ϕ at a time t through the infinite plane perpendicular to the z-axis, caused by an electron starting its motion at z_0 at time t_0 (Fig. 1.20a-inset) is given by:

$$\phi(z,t;z_0,t_0) = \frac{[\widetilde{\Delta t}]}{2(t-t_0)^2}\left(e^{\left[-\left[\frac{\widetilde{\Delta t}}{\tau}\right]/[\widetilde{\Delta t}]\right]}\right)^{(t-t_0)} \times \Theta\left[(t-t_0)-|[\widetilde{\Delta t}]|\right], \tag{1.89}$$

here Θ being the unit step function, and:

$$\left[\frac{\widetilde{\Delta t}}{\tau}\right] = \int_{t_0}^{z}\frac{dz'}{\tau(z')v(z')}, [\widetilde{\Delta t}] = \int_{z_0}^{z}\frac{dz'}{v(z')} \tag{1.90}$$

another assumption is that no contribution to the first-generation flux comes from electrons that experienced a scattering event.

On the other hand, if a distributed source of electrons is present instead of exciting a single electron, the total first-generation flux due to all electrons with spin σ and energy E is given by

$$\Phi(z,t) = \int_{-\infty}^{\infty}dz_0\int_{-\infty}^{t}dt_0 S^{ext}(z_0,t_0)\phi(z,t;z_0,t_0) \tag{1.91}$$

Considering the spatial and temporal profile of the laser and absorption probability, we can calculate the electron source term $S^{ext} = S^{ext}(\sigma,E,z,t)$. Now, we define the operator $\hat{\phi}$ as $\hat{\phi}S^{ext} \equiv \Phi$

After the flux expression, we can write the continuity equation for a spin density, $n^{[1]}(\sigma,E,z,t)$:

$$\frac{\partial n^{[1]}}{\partial t} + \frac{n^{[1]}}{\tau} = -\frac{\partial \hat{\phi}S^{ext}}{\partial z} + S^{ext} \tag{1.92}$$

The second term acts as the reaction term removing electrons from the density after scattering. Again, we make the assumption that the electron emission is isotropic after the first scattering and independent of the incoming direction. This assumption is almost exactly true for the case of scattering with phonons, impurities and other large mass particles. Since d-like electrons are more localized than sp-like electrons, also meaning that the former have higher effective mass, the approximation holds since it leads to the diffusive process underestimation. The previous equation describes the second-generation equation well, too, when we use $S^{[2]}(\sigma,E,z,t)$ instead of S^{ext}:

$$S^{[2]} = \Sigma\int p(\sigma,\sigma',E,E',z)\frac{n^{[1]}(\sigma',E',z,t)}{\tau(\sigma',E',z)}dE' \tag{1.93}$$

it corresponds to the scattering term after the first generation with the weighted transition probability of $p(\sigma,\sigma^{prime},E,E',z)$. Note that the second generation emission includes elastic and inelastic scatterings and the generation of cascade electrons. In these calculations, spin-flip events are considered to be negligible. The next operator we define is $\hat{S}$ as $\hat{S}n^{[1]} = S^{[2]}$, and this gives the density of third-generation electrons, $n^{[3]}$. Taking the sum over all possible emission generations, we obtain a set of coupled transport equations:

$$\frac{\partial n^{tot}}{\partial t} + \frac{n^{tot}}{\tau} = \left(-\frac{\partial}{\partial z}\hat{\phi} + \hat{I}\right)(\hat{S}n^{tot} + S^{ext}). \tag{1.94}$$

$\hat{I}$ being the identity operator.

The equation above is different from both ballistic and diffusive transport equations, it explains the fast transport of electrons after laser excitation. The question that comes next is whether this model describes the demagnetization process observed by magneto-optics after laser excitation. In the standard diffusive regime, with the Brownian motion of particles, the variance of the displacement of distribution, σ^2, grows linearly as

a function of time: $\sigma^2(t) \propto t^\gamma$, with $\gamma = 1$ [70], whereas $\gamma = 2$ for a ballistic transport. The model proposed by Battiato et al [68] is that γ is time-dependent and starts from $\gamma = 2$ and slowly decreases down to $\gamma = 1$. Thus, a simple diffusion model cannot fully describe the transport of electrons after a femtosecond laser excitation.

The laser photons excite electrons to *sp* bands which are characterized by high velocity, of the order of 1 nm/fs. On top of that, majority and minority spins have different lifetimes: majority spins have a long mean-free-path and the minority spins are much less mobile. This causes facilitated depletion of majority spins in the ferromagnetic film, thus, it can transfer magnetization away from the surface. Hence, superdiffusive transport can cause demagnetization in the ferromagnet. Another contribution to demagnetization can come from an excited electron experiencing an inelastic scattering with another electron. In this scenario, the excited electron transfers a part of its energy to the other electron, and this generates a cascade of electrons. The newly excited electron now has enough energy to move away quickly, contributing to the demagnetization.

The next step was to assess the amount of demagnetization caused by superdiffusive spin transport, so Battiato et al solved equation (1.94) numerically at three distinct times (t=0 fs, t=90 fs, and t=300 fs) for 15 nm of Ni on an Al substrate, previously studied by Stamm et al. [62]. The details can be found in the original work of Battiato et al [69], and I will only describe Fig. 1.20b) which shows computed profiles at three distinct times as a function of the disctance from the surface of the 15 nm thick Ni layer. Due to the temporal spread of the laser pulse, the effect of laser excitation is already visible at t=0 fs: the magnetization slightly decreased a bit at the Ni surface. The laser excitation is spin conserving, thus the decrease of magnetization is not directly from the laser excitation, but due to the spin-dependent fast transport of electrons. At t=90 fs, when the magnetization at the surface is significantly reduced, and the injection of spin-up electrons in the Al substrate causes the magnetization of Al near the interface with Ni. At t=300 fs, well after the excitation, the spin transport reduces the magnetization even more, while, the density of excited electrons decreased as well. This comes from the inelastic scattering events that lead to the thermalization of the excited electrons. Moreover, a backflow from the Al substrate leads to the accumulation of minority spins on the Ni side of the interface, leading to the demagnetization on this side of Ni as well.

Thermally induced demagnetization

The study on the influence of only energy in the absence of laser excitation and, in consequence, of electric field on the demagnetization process conducted by Eschenlohr et al. added a crucial insight into what contributes to demagnetization[71]. In this work, they used a heterostructures consisting of 30 nm Au/15 nm Ni(FM)/2.5 nm Pt on an Al substrate and 2.5 nm Pt/ 20 nm/2.5 nm on an Al substrate. The samples were pumped by the Au and Pt side of the samples, respectively, and the demagnetization response was measured by XMCD. Since the Au layer on the first sample is thick enough to absorb the laser light and prevent them from reaching the FM layer, the laser-induced demagnetization of the FM can be excluded. In this condition, only the hot electron injection from the Au layer into the FM can lead to demagnetization. They concluded that the laser excitation is not a prerequisite to induce demagnetization and hot electron injection alone can lead to demagnetization, thus the main driving force of demagnetization is ultrafast spin transport. This finding has a significant importance for industrial applications as the miniturazation of a single memory bit and increased density of bits might hinder the use of lasers, as it can be challenging to point the laser onto a single bit, in memory devices.

1.4.3 Spintronic THz emission

Once the existence of superdiffusive spin currents established, it was important to understand its dynamics as it is equally significant for fundamental studies as well as for memory applications at THz frequencies.

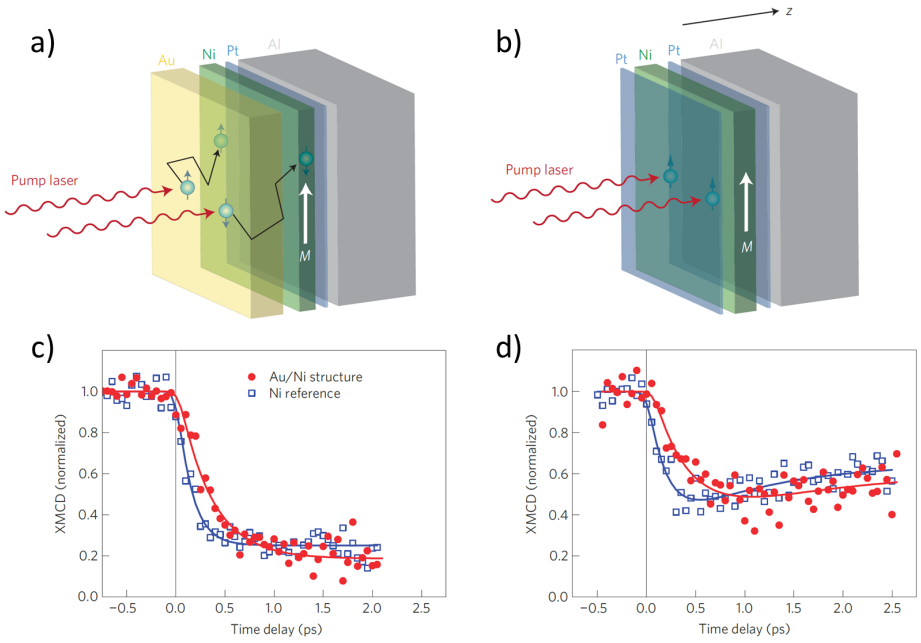

Figure 1.21: Demagnetization induced by spin unpolarized hot electron injection [71].

As discussed in the introduction, existing electronic devices are not fast enough to measure THz dynamics. On the other hand, depositing ferromagnetic electrodes and measuring the spin current through the switching of that ferromagnet could add additional dynamics, complicating the interpretation of the results. Thus, Kampfrath et al showed the possibility to understand superdiffusive spin current dynamics via spin-to-charge conversion in FM/HM heterostructures [55]. The three important stages taking place in this experiment are: (i) *the conversion of a spin current into a charge current by the inverse spin Hall effect* $(ISHE)$, as the existence of ISHE has been shown experimentally earlier by spin pumping experiments [36]; (ii) *the emission of electromagnetic THz radiation by the converted charge current*; (iii) *the detection of THz signal and inversion of the Maxwell equations to obtain the generating current*. The detected signal represents the temporal shape of the charge current that generated it, the propagation outside the sample, and how the detector responds to the electromagnetic radiation. With the knowledge of the detector response function, the attenuation, and distortion during propagation, it is possible to recalculate the temporal shape of the charge current.

Before presenting the findings of Kampfrath et al., it is important to describe the experimental settings of a typical THz time-domain spectroscopy (shown in Fig.1.22)a). The main concept is similar to ultrafast demagnetization experiments: there is a laser source that can deliver 15-100 fs long pulses (the polarity of the light does not seem to play any role in the amplitude of the generated charge current) which hit the FM/NM heterostructure, the NM is preferably a HM with significant SOC, while the sample is inside an in-plane magnetic field, $\mathbf{H}_{DC}$ (grey vertical arrow) to keep the magnetization in-plane (red vertical arrow). The laser pulse causes the demagnetization of the FM, the angular momentum is lost in the form of a superdiffusive spin current injected into the HM along the $+z$ direction. When the NM is a heavy metal with strong SOC or a 2D material with Rashba spin-split states, the superdiffusive (and transient) spin current is converted into a superdiffusive (and transient) charge curent. Due to the charge accumulation on one side of the sample and its transient nature, an oscillating electric-, in turn magnetic-, hence an electro-magnetic field is created. As mentioned earlier, the demagnetization happens within a few ps, corresponding to the THz range in the frequency domain. The optical bench, including the parabolic mirrors to focus the THz radiation and the THz

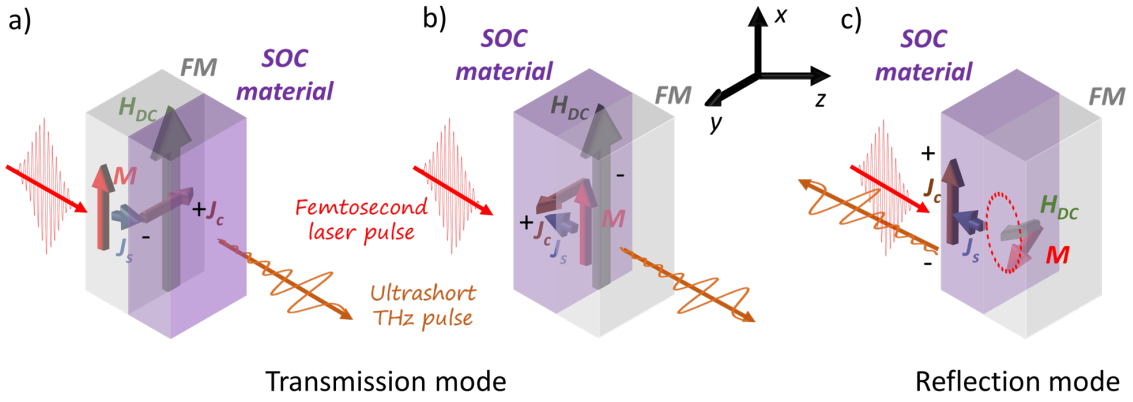

Figure 1.22: Schematics of spintronic THz emission in transmission mode for a) and b), and c) reflection mode.

electromagnetic field detection mechanism (which is based on THz time-domain spectroscopy [72],[73]) is presented in the experimental background chapter. Detecting a THz signal is not sufficient to conclude on its spin-to-charge conversion origin, the same experiment has to be carried out for the opposite magnetization direction: if the polarity of the THz wave packet is opposite, it is a good indication of spintronic THz emission.

The pumping can be performed either from the FM side or the SOC material side: in the former case, as shown in Fig. 1.22a), the superdiffusive spin current is along the $+z$ direction, thus the emitted charge current is along the $-y$ direction, while for the latter case, as shown Fig. 1.22b), the superdiffusive spin current is along the $-z$ direction, thus, the charge current is in $+y$ direction. . This holds for positive a spin Hall angle, it will be the opposite for a negative spin Hall angle. It is essential to carry out THz experiments by pumping from both sides separately to exclude the possibility that the electromagnetic radiation is due to the magnetic dipolar emission, instead of the electric dipolar one.

1.5 Conclusion

In summary, I have presented two distinct techniques to study spin to charge conversion phenomena in FM/SOC material thin film heterostructures. The first one is spin pumping by FMR based on spin current injection in the SOC material at the Fermi level by putting the magnetization in precession. Such technique can provide numerical values of important physical quantities, namely, the spin diffusion length, λ_s, and most importanly the spin Hall angle, θ_{SH}, that describes the spin-to-charge conversion efficiency.

Due to the experimental difficulties in the sample preparation for such experiments and the challenging measurements inside the cavity, which I will describe in the experimental chapter, we have moved to THz-TDS for which we could use as-grown samples without further preparation steps. I have also been familiarized with how powerful THz emission spectroscopy can be to investigate superdiffusive spin current dynamics in FM/NM heterostructures and spin-to-charge conversion phenomena. Moreover, THz emission spectroscopy probes electrons not necessarily at the Fermi level, another contrast to spin pumping by FMR. This property allows to probe spin-to-charge conversion in electronic bands far from the Fermi level in semiconductors like TMDs. Hence, it can be seen as a spectroscopic spin-to-charge conversion detector. Finally, the importance of transport phenomena during the FM demagnetization means that tailoring the electron velocity and the SOC in the SOC material could modulate the demagnetization dynamics. Therefore, THz emission spectroscopy is an ideal tool to study spin-to-charge conversion phenomena in novel materials

bringing them closer to the memory applications thanks to the insights it can provide on the dynamics of electron transport.

Chapter 2

Experimental Background

2.0.1 Introduction

Due to the miniaturization of components, thin films (thicknesses of less than 1000 nm) play a crucial role in microelectronics as they offer advanced functional properties. Various methods of growing thin films can be divided into two main categories: Chemical Vapour Deposition (CVD) and Physical Vapour Deposition (PVD). In CVD, precursors are chemically reacting on the substrate to grow the films. This thesis is about the latter and the two techniques used are sputtering, to grow amorphous or polycrystalline films, and molecular beam epitaxy (MBE), to grow single crystalline films epitaxially on a substrate.

2.1 Molecular Beam Epitaxy and its components

2.1.1 Molecular Beam Epitaxy (MBE)

First, it is necessary to clarify what molecular beam and epitaxy mean. It is a well known fact that gas particles inside a closed chamber move around by Brownian motion, and we can define an average length a gas particle traverses between consecutive collisions, λ_{MFP}, MFP standing for mean-free path. This mean-free path is inversely proportional to the pressure of the chamber. When the pressure is low enough λ_{MFP} can be larger than the dimensions of the chamber, meaning that, on average, a particle does not collide with another particle when crossing the chamber. Such beam of atoms or molecules satisfying this condition is called a (atomic or) molecular beam.

Epitaxy or *epitaxial growth* corresponds to the growth of a crystalline thin film extending the substrate crystal lattice thanks to low lattice mismatch. By using a single crystalline substrate, the grown thin film is also single crystalline with the same in-plane lattice parameter as the substrate one. Homoepitaxy stands for the growth of material A on a substrate A and heteroepitaxy of a material A on a substrate B.

MBE was first used in 1970 to develop thin semiconducting films with high carrier mobility by minimizing the extrinsic effects contributing to the electron scattering, thanks to the single crystalline character of the films. MBE is advantageous over other thin film deposition techniques because of the quality of the films that are grown using ultra-pure sources under low deposition rates in ultra-high vacuum (UHV) conditions which ensures contamination-free thin film growth. The rate can be monitored in real time with a Quartz Crystal Micro-balance and/or with the oscillations of the reflected electron beam intensity off the sample surface using the reflection high-energy electron diffraction (RHEED) setup. The chamber and all the elements inside should be free from contaminants, such as water and organic molecules. Additionally, the targets should be ultra-pure, and for this purpose, they are thermally cleaned after each opening of the MBE chamber to degas H_2O, H_2, CO and CO_2 molecules, as well as organic compounds. The process is monitored using a mass

spectrometer. In UHV conditions, the mean-free path of atoms/molecules becomes larger than the distance between the source and target, hence evaporated atoms do not experience any collision before meeting the substrate, satisfying the condition for molecular beam.

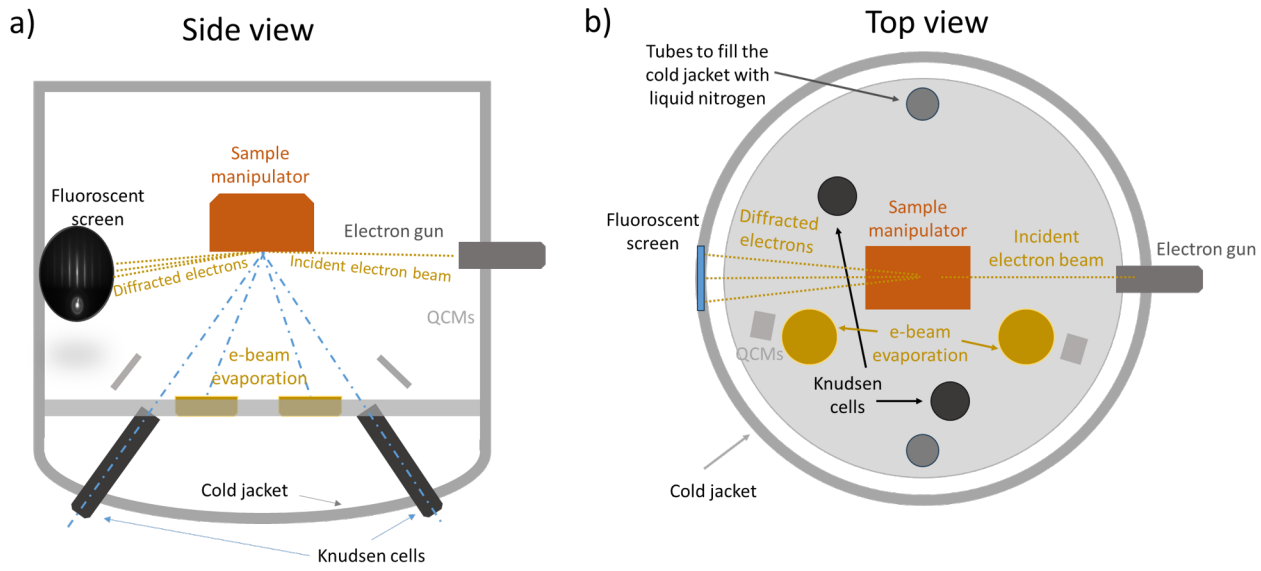

Figure 2.1: MBE chamber and its elements seen from a) side and b) top view.

Once the requirements for the growth chamber are met, the next most important requirement to obtain good quality thin films is the preparation of the substrate surface that can be followed in situ by Reflection High Energy Electron Diffraction (RHEED). The other elements inside the MBE chamber are Knudsen cells (containing Se and Au), electron beam evaporators (for metals), a cold jacket (to be filled with liquid nitrogen to cryopump the chamber), quartz balances to monitor the metal deposition rate and a retractable ionic gauge to read the Se flux rate at the position of the sample. Finally, primary and secondary (turbomolecular) pumps are used, to reach secondary vacuum and when the pressure is low enough (in the $10^{-7} - 10^{-6}$ mbar), the ionic pump is switched on to reach UHV conditions in the low 10^{-10} mbar.

After each opening of the MBE chamber for maintenance, it must be baked for a week and each target should be out-gassed before starting depositions. When heated, the targets usually emit H_2O, H_2, CO_2, N_2 molecules and other organic compounds which could be detrimental for the thin film growth. Samples are introduced from air into a load-lock chamber. They are then transferred into an introduction chamber under UHV in which a four-position carousel allows to store samples. Samples are finally introduced in the deposition chamber from the introduction one. The MBE components that are going to be explained in the following sections are presented in Fig. 2.1a) side view and b) top view sketches of the MBE chamber.

2.1.2 Knudsen cells

The charge is put inside a crucible made of pyrolitic boron nitride (PBN) which is winded with a heating filament which works based on Joule heating. A thermocouple is in contact with the crucible to accurately measure the temperature. A retractable flux gauge gives the vapor pressure of the evaporated element at the position of the sample. There is also water cooling to improve the cell temperature stability. Also Knudsen cells are meant for high vapour pressure elements like Se. A photo of a Knudsen cell is shown in Fig. 2.2a) with various important elements, and b) shows PBN rings that surround the crucible and are used to heat up the charge inside.

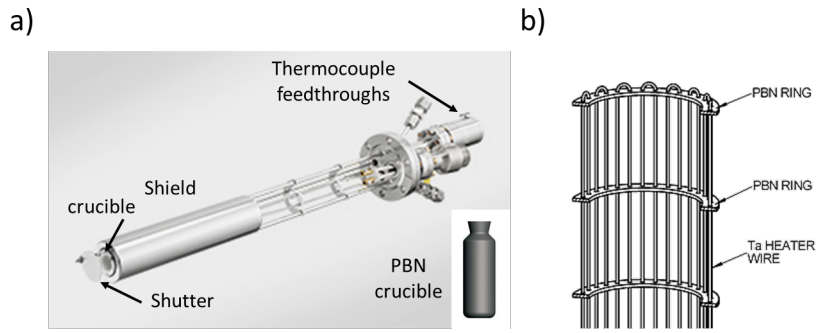

Figure 2.2: Knudsen cell in a) with various components and b) the heating elements surrounding the crucible. Adapted from Reference [74].

2.1.3 e-beam evaporators

Another technique to evaporate targets in MBE is by electron beam. The working mechanism is as follows: a current (around 25 A) is passed through a tungsten filament, with a help of the transverse voltage of 10 kV, electrons from the filament can be extracted with an emission current of about 10-30 mA, depending on the evaporant. The electron beam is directed towards the target using permanent magnets but also electromagnets to be able to sweep the target, as shown in Fig. 2.3. E-beam evaporation is more suitable for elements and compounds with low vapour pressure, requiring high power for sublimation or evaporation like refractory metals (W, Mo, Nb, V...). The deposition rate is measured with a Quartz Crystal Microbalance (QCM). The working principle of QCM is based on the change of the crystal resonance frequency upon deposition of matter on top.

2.1.4 RHEED

Reflection high energy electron diffraction (RHEED) is widely used as a tool for surface analysis, especially with MBEs to follow the film quality in situ and in real time. It gives the electron diffraction pattern of the crystal, only from the top few atomic layers. An electron beam with an energy of 20 keV is incident at grazing angles. The diffracted beam is also at a grazing angle with respect to the sample surface. The RHEED set-up consists of two main components: an electron gun to generate the electron beam and a fluorescence screen to visualize the electron diffraction pattern that can then be recorded with a CCD camera.

Since the sample can be moved up and down inside the growth chamber (also to achieve a preferred electron beam incident angle) the electron beam is directed towards the sample using deflection coils, one for horizontal and one for vertical movement.

The configuration of the electron gun, incident beam, diffracted beam from the sample, and the beam impinging the fluorescent screen is shown in the Figure 2.5.

For elastic scattering, the momentum and energy of electrons are conserved. Considering $\mathbf{k_i}$ and $\mathbf{k_f}$ the initial and final momenta of the electron during the diffraction process, the radius of the Ewald sphere is given by:

$$|\mathbf{k_f}| = |\mathbf{k_i}| \tag{2.1}$$

Hence,

$$\mathbf{k_f} - \mathbf{k_i} = \mathbf{G_m} \tag{2.2}$$

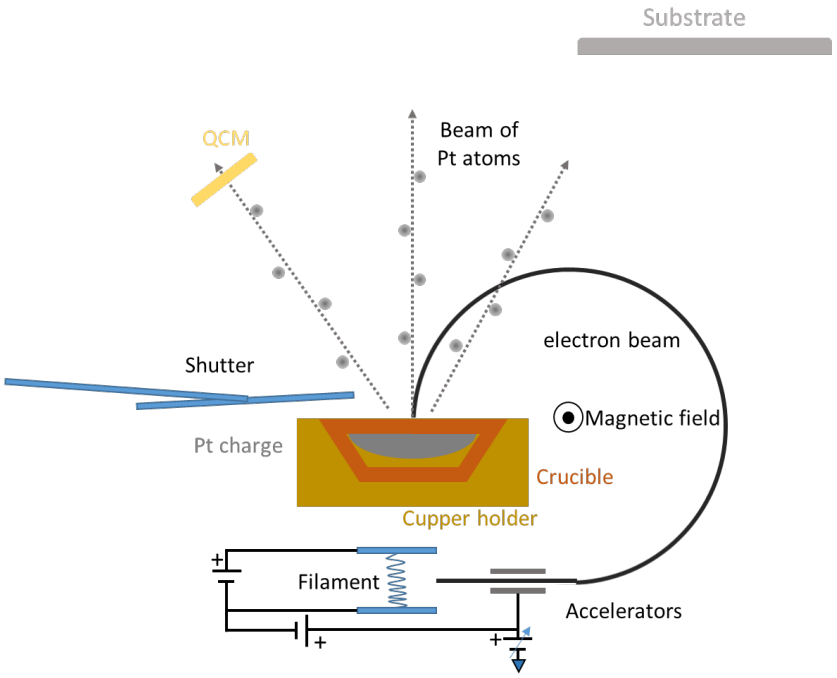

Figure 2.3: A simplified sketch of electron-beam evaporation with the filament used to generate electrons which are accelerated and directed to the metal target using magnetic fields. The evaporated metal atoms/molecules are directed to the substrate and the QCM allows to measure the deposition rate in real time during the growth. The shutter is used to stop the flux reaching the substrate but measuring the flux with the QCM.

the scattering vector is equal to a reciprocal lattice vector $\mathbf{G_m}$ where m refers to the m^{th} diffraction order. The diffraction pattern is thus given by the intersection of the reciprocal space with the Ewald sphere. In theory, this intersection should yield diffraction spots on the fluorescence screen. However, due to the electron energy distribution leading to a finite thickness of the Ewald sphere, due also to the stepped or vicinal surface and the possible presence of defects and limited grain size, the diffraction pattern rather gives diffraction rods [75].

The electron diffraction pattern gives information about the growth process. Fig. 2.6 shows several diffraction patterns that are related to the corresponding surface morphologies [75]. Prior to the growth, the substrate surface quality is evaluated by RHEED to ensure the good epitaxial growth of the film (details are given in the next chapter).

2.1.5 Growth modes

During the growth, we can distinguish three zones inside the MBE chamber as shown in Fig. 2.7 (adapted from Herman et al [76]). In the first zone, the molecular beams are created (either from an e-beam evaporator or a Knudsen cell). The second zone, located close to the substrate and where plumes overlap, is characterized as the mixing zone. In the vicinity of the substrate (up to a few nanometres above the substrate) is situated the third zone where the crystallization (reaction between species A and B + condensation of AB) takes place.

When the atomic/molecular beam reaches the substrate, various processes can happen, as shown in Fig. 2.8, depending on the kinetics and thermodynamics. An atom in a) (either A or B) can be adsorbed on the surface, also referred as adatom, as in b) and diffuse, several atoms can form a nucleus c), an adatom

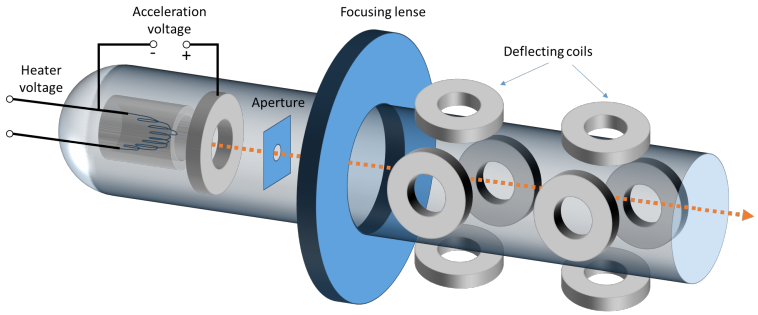

Figure 2.4: E-beam generation by a RHEED electron gun and directing it towards the growing film using magnetic deflectors. Adapted from Hasegawa et al [75].

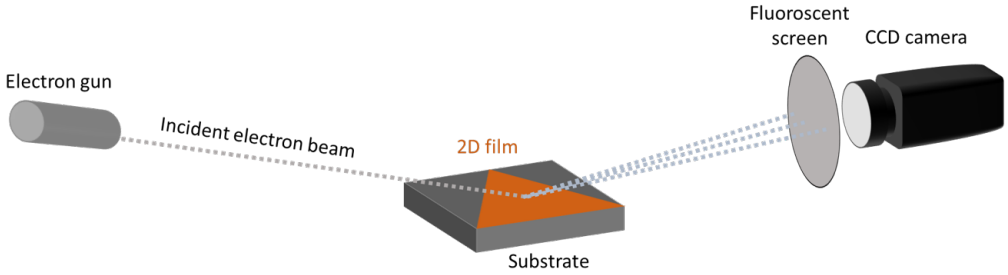

Figure 2.5: Full RHEED setup with the diffraction process and observation of the diffraction pattern with a CCD camera on a fluorescent screen.

can attach to an already existing nucleus, contributing to its growth d), it can diffuse at the crystal edge e), dissociate from the existing crystal f), dimers or trimers can diffuse together g), a second layer can nucleate h), an atom can diffuse to a lower level i), or just desorb j) [77].

The research paper dealing with the three temperature method ([78]) captures the MBE processes for compound thin film growth. This method describes three distinct temperature ranges that give different compositions of the growing film.

During the thin film growth, the three distinct temperature ranges exist where distinct phenomena occur depending on the interactions of the vapour species with each other and with the substrate. More precisely, the method addresses the question: how a substance AB, composed of elements A and B, can grow in thin films. This is based on the vapour pressures of A, B, and AB at various temperatures of A, B, over the substrate and subsequently of AB (here A is less volatile than B). The fraction of condensed A, B, and AB (β_A, β_B, and β_{AB}, β stands for fraction) species on the substrate after adsorption evolves with the substrate temperature (T_S) and the flux of A and B (n_{+A} and n_{+B}). This leads to the conclusion that in a certain temperature range, a stoichiometric AB film can be grown for a specific fluxes of species A and B. There are three points to consider to find the right temperature range for the deposition of this stoichiometric compound AB which deal with the final composition of the films grown at the three temperature ranges (with the phase diagram shown in Fig. 2.9):

i) At low substrate temperatures, total condensation of the species A, B, and AB can be observed ($\beta_A = \beta_B = \beta_{AB} = 1$) and the stoichiometric compound AB is possible only at one value of n_{+B}

ii) At moderate temperatures, the species AB and A are totally condensed ($\beta_A = \beta_{AB} = 1$), certain flux ranges of n_{+B} and n_{+A} exist to obtain a defined composition of AB

iii) At high temperatures, but below the evaporation temperature of AB, AB condenses on the substrate;

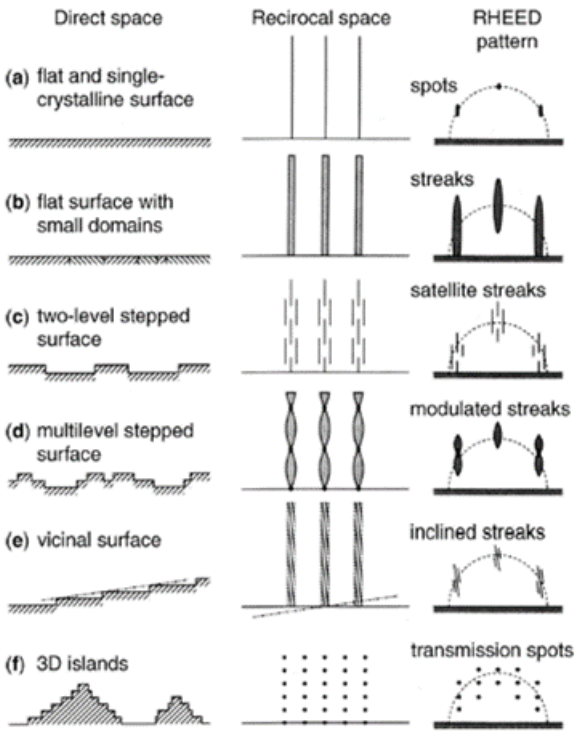

Figure 2.6: RHEED pattern with corresponding surface morphology, highlighting the essential role of RHEED in crystal growth by monitoring in real time the film quality. The ideal surface is depicted in a) with a flat and single crystalline surface. Taken from Hasegawa et al [75].

A and B species cannot ($\beta_{AB} = 1$, β_A, $\beta_B = 0$). A and B can condense only when they react to form AB (A+B$\rightarrow$AB) at the adsorption stage.

Under thermodynamic equilibrium conditions, three modes of growth can be distinguished during a molecular beam epitaxy: Frank-van der Merwe (FvdM, layer-by-layer or step flow, 2D), Stranski-Krastanov (SK, initially 2D, and 3D after a critical thickness) [79], Volmer-Weber (VW, island growth, 3D) [80],[81].

The desired mode we are interested in is the FvdM mode that forms sharp interfaces. In theory, such growth occurs for a lattice mismatch between the epilayer and the susbtrate below a critical value. In the ideal case of this growth mode, each consecutive layer starts growing only after the completion of the preceding one. This requires sufficiently long diffusion lengths for atoms to find a growing nucleus or reaching a descending step, instead of forming a new nucleus on top of an already existing nucleus. This condition can be achieved when the atoms of the growing species have higher affinity to the substrate surface than to their own species. Under these conditions, the layer-by-layer growth mode can be evidenced with the oscillations of the RHEED intensity see Fig. 2.11 [82],[83].

3D growth modes (Stranski-Krastanov or Volmer-Weber modes) are used to grow semiconducting quantum dots. For the former mode, the growth starts in a 2D mode progressively becoming 3D after a critical thickness, while the latter mode already starts with 3D islands. The justification for this transformation is given by the lattice mismatch between the substrate and epilayer. As the layer keeps growing, the mismatch induced strain increases monotonically, leading to a relaxation of the strain in the epilayer in the form of 3D growth. This transition is usually used to grow self-assembled quantum dots [80].

These theories are based on interfacial and surface energies. Bauer developed a theory [81] [84] that unifies the three growth modes considering the energy term: $\Delta = \sigma_f + \sigma_i - \sigma_s$, where σ_f and σ_s are the

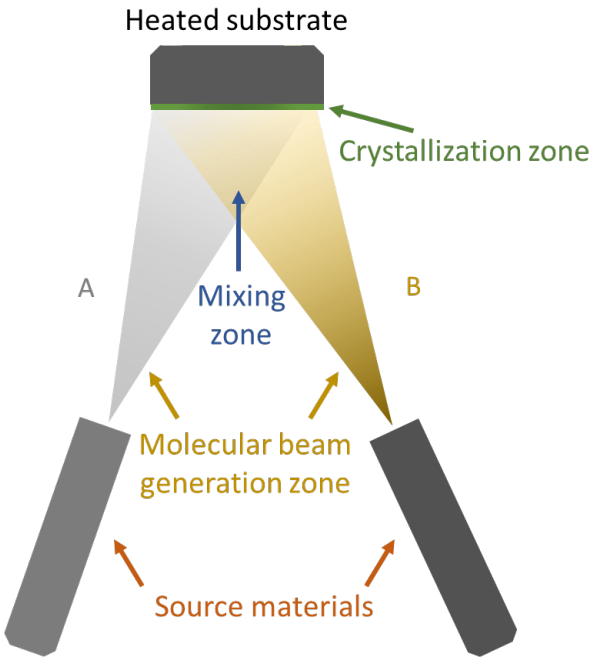

Figure 2.7: The 3 characteristic zones in the MBE chamber: Molecular beam generation, mixing, and crystallization zones. Adapted from Herman et al [76].

specific free surface energy of the film and substrate, respectively, and σ_i is the specific free interfacial energy between the substrate and the film. The VW mode is observed when the thin film surface energy is larger than that of the substrate ($\Delta > 0$); FvdM and SK modes correspond to the opposite scenario with the lower surface energy of the film than that of the substrate ($\Delta \leqslant 0$). This condition must be satisfied for each layer for the growth to be in the FvdM mode, meaning that the film and substrate free surface energies should be similar, $\sigma_f \approx \sigma_s$, and $\sigma_i \approx 0$. When the lattice mismatch between the film and the substrate is low, the elastic energy remains small compared to the film surface energy and the FvdM mode is favoured. In the SK mode, the early monolayers grow in the FvdM mode and, due to the build up of elastic energy, resulting from a large lattice mismatch between the film and the substrate, it transitions to the SK mode. These considerations only apply in the absence of chemical reactions and/or alloying, which is the case for the growth of transition metal dichalcogenides. However, they give solid fundamental understanding of the growth dynamics.

Thermodynamically speaking, epitaxial growth is fundamentally an out-of-equilibrium process since at equilibrium, adsorption and desorption rates would be equal resulting in no net growth. Thus, when considering thin film growth modes, we must give more importance to kinetics than to thermodynamics [85]. MBE exploits out of thermodynamic equilibrium conditions [86], meaning that the film quality (morphology, structure, and stoichiometry) depends on the path the growth takes and the energy barriers that must be overcome along this path. Given the surface and interface energies, the temperature and flux rates usually determine which path is followed for each growth. Hence, MBE results in thermodynamically non-equilibrium crystal structures and morphologies. An important driving force in the MBE growth is the degree of supersaturation. Supersaturation means that the concentration (or vapour pressure) of the vapour species being deposited is higher than the vapour-solid equilibrium value. The term *growth mode* applies to the growth conditions where the supersaturation is low, thus, the approximation of MBE processes to the above described growth modes (FvdM, SK, VW modes) holds when the supersaturation of the vapour pressures is still quite low.

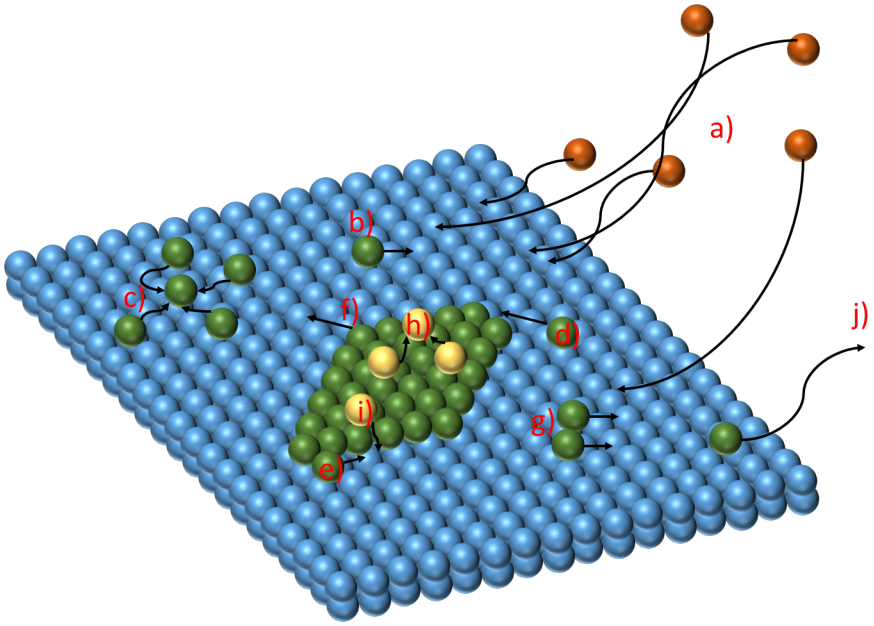

Figure 2.8: Atomic processes during deposition when the molecular/atomic beam reaches the substrate. An atom a) from the chamber can be adsorbed on the surface, also referred as adatom, as in b) and diffuse, c) several atoms can form a nucleus, d) an adatom can attach to an already existing nucleus, contributing to its growth, e) it can diffuse at the crystal edge, f) dissociate from the existing crystal, g) dimers or trimers can diffuse together, h) a second layer can nucleate, i) an atom can diffuse to a lower level, or j) just desorb. Adapted from Rahman et al [77].

When the supersaturation is high, the morphology of crystals is dictated by kinetics, and the term *growth mode* should be replaced by *growth morphology* [86].

2.2 Sputtering

2.2.1 DC magnetron sputtering

Sputtering is a physical phenomenon that involves the removal of atoms or molecules from the surface of a target material through the bombardment of high-energy particles, often heavy ions, like argon. The sputtered atoms are released into the gas phase, creating a vapour of the target material, which can then be condensated onto a substrate. Compared to other vacuum deposition techniques, sputter deposition has several advantages, such as its high deposition rate, high nucleation rate, and smooth surfaces. These properties make it a valuable tool for a variety of applications, including the fabrication of thin films, surface modification, and the production of electronic devices [87].

To sputter the target, we generate ions with sufficient energy and direct them towards the surface of the target material to facilitate the ejection of atoms from its surface, as illustrated in Fig.2.12a). Subsequently, the ejected atoms must travel freely towards the substrate with minimum scattering. This necessitates that sputter deposition has to be carried out under vacuum conditions to maintain low pressures, which serve two purposes: (i) to be able to apply high voltage and sustain high ion energies and (ii) to prevent excessive atom-gas collisions following their release from the target. The concept of mean free path (MFP) is a valuable tool in this context, as it denotes the average distance that atoms can traverse without undergoing collisions with other gas atoms.

We used a custom-built magnetron sputtering apparatus in DC mode to deposit CoFeB (with the com-

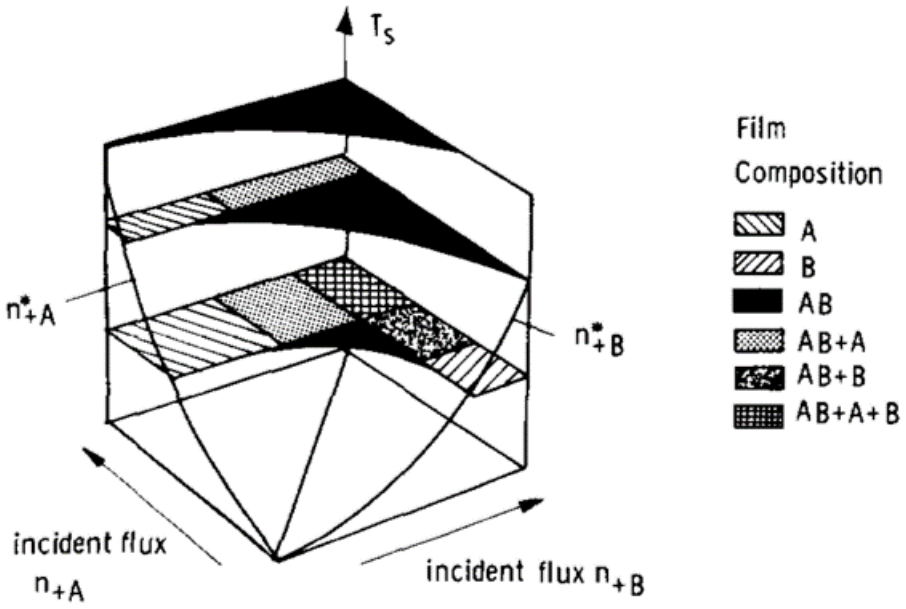

Figure 2.9: A 3D-representation of the relation between the substrate temperature and incident fluxes of the species A and B, showing that at high enough temperatures a stoichiometric compound AB is formed and deposited on the substrate. Obtained from Freller et al [78].

position of $Co_{20}Fe_{60}B_{20}$) onto TMDs and subsequently cap them with Al to prevent the oxidation of the ferromagnetic film when transferred in air. The magnetron [89], as shown in Fig. 2.12a), is made of a cathode element and permanent magnets that create magnetic field lines to confine electrons and ions just above the target material. Electrons are set into motion, and ionize Ar atoms that are then attracted to the cathode by the electric field. Since Ar+ ions possess high energy, they are capable of ejecting atoms or molecules from the target element when they impact it. These sputtered species then form a vapour of the target element, which subsequently gets condensated onto the substrate. This is the fundamental principle of magnetron sputtering. Another crucial aspect during deposition is the distance between the target and the substrate, which significantly influences the film thickness uniformity. The physical principal of atomic (or molecular) ejection off the target using magnetic field to trap charged particles and channel them towards the target imposes a finite distance from the target ensuring a uniform thin film deposition over a limited surface. In the sputtering machine of the 2D spintronics team, the distance between the target and the sample is around 10 cm which gives uniform thickness over a 1 inch wafer.

2.2.2 Calibration with XRR and AFM

The uniformity and thickness of the sputtered films were measured with X-ray reflectivity (XRR, the technique will not be discussed in the manuscript) and/or atomic force microscopy (AFM, the technique will be described later in this chapter) after each opening of the chamber. The basic principle of thickness measurement by XRR lies in the intensity oscillations of the scattered x-ray beam as a function of the incidence angle and the amplitude of the oscillations dependence on the electron density of the material, i.e. the chemical element. For example, Pt and Au have higher electron density than Al, for this reason, it is easier to carry out calibration measurements for Pt than Al using XRR.

Samples for thickness measurements using AFM were prepared on a patterned substrate in the clean-room using a photo-resist with optical lithography. After a development with strongly basic developer, a

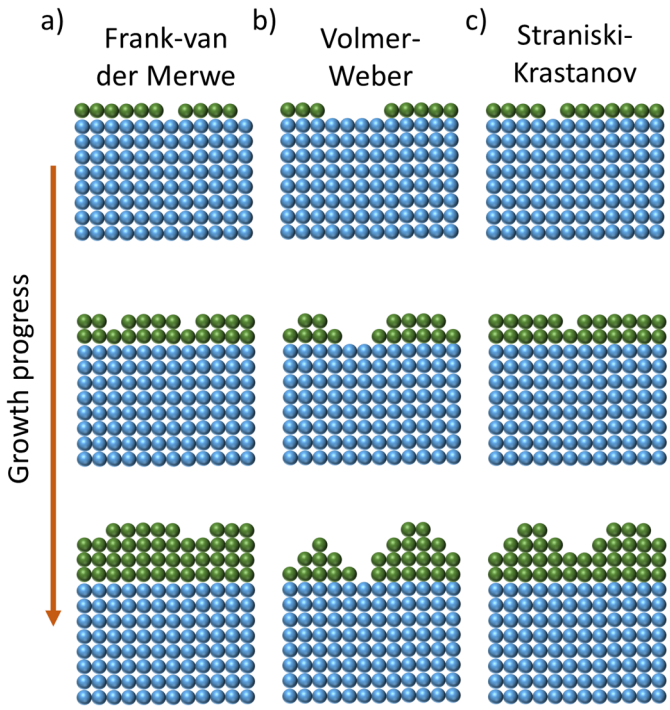

Figure 2.10: Three modes of thin film growth showing the evolution of the surface morphology during the growth.

pattern with grooves is created. Thin films of up to 30 nm were then sputtered on SiO_2/Si substrates, followed by an acetone bath to completely remove the photo-resist, leaving the inverse of the pattern, creating steps which are measurable by AFM.

2.3 Structural characterization of thin films

After the 2D TMD growth by MBE and CoFeB/Al sputtering, we have to assess the quality of the films by various techniques, such as, X-ray diffraction to obtain the lattice parameters, crystallinity, and the mosaic spread (i.e. anisotropy), Atomic Force Microscopy to analyse the topography and morphology of the films, Raman spectroscopy, X-ray photoelectron spectroscopy (XPS) to analyse the chemical state of the elements, and Scanning Transmission Electron Microscopy (STEM) to observe the interfaces at the atomic level. For the study of $PtSe_2$/$MoSe_2$ heterostructures, we also used ARPES at SOLEIL (French synchrotron radiation facility in Paris) and ELETTRA (Italian synchrotron radiation facility in Trieste).

2.3.1 XRD

To obtain a comprehensive structural characterization of the two-dimensional (2D) van der Waals (vdW) layers, we employed the X-ray diffraction (XRD) technique, wherein incident X-rays undergo diffraction by interacting with the electrons. Firstly, let us consider the scenario of a polycrystalline sample consisting of randomly oriented grains in bulk, commonly referred to as powder diffraction. During powder diffraction, the incident angle (θ) and the detection angle (2θ) of the X-rays are varied between 0° and up to 180° in the specular configuration, i.e., along the same vertical plane as the X-ray source. The intensity of the diffracted X-rays, as a function of the incident angle, relies on the periodicities and the electron density characteristics of the species. Subsequently, the experimentally acquired diffractogram is compared to the

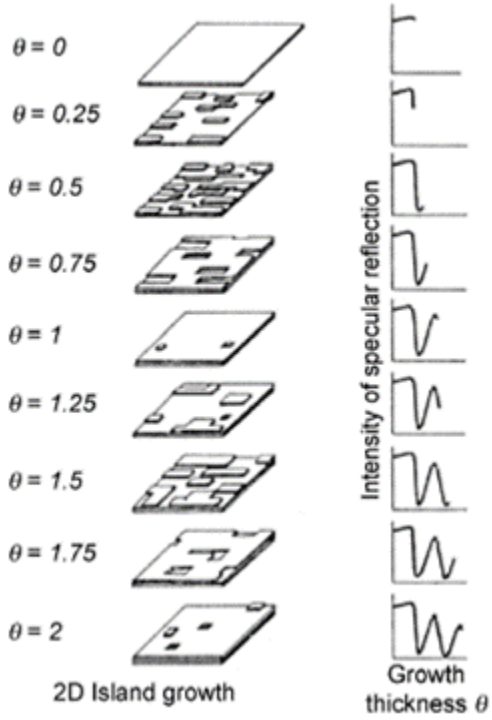

Figure 2.11: The surface morphological explanation behind the oscillations of the RHEED intensity off the surface of the film during growth. Adapted from Hasegawa et al [75].

calculated intensity profiles of anticipated crystals. The remaining peaks are subjected to further analysis, which involves the examination of periodicity in real space and structure factors. Once the quality of the material is confirmed, the subsequent crucial information sought from XRD is the crystal lattice parameter, as the experimental values are not exactly the same with theoretical ones because of the substrate induced strain in the film or thermal effects. Moreover, a distribution of lattice parameters can be observed in real crystals.

The XRD analysis of randomly oriented grains in a bulk sample can yield all the lattice parameters, including the in-plane parameters a and b, as well as the out-of-plane lattice parameter c. However, since the thin films exhibit an epitaxial character, evaluating them solely under one geometric configuration would not provide sufficient insights into their structural quality. Consequently, we employed two types of diffractometers: powder diffraction and SmartLab® , for out-of-plane and in-plane analysis, respectively. In the former case, the aforementioned geometry employed for powder diffraction enables determination of the c-lattice parameter. Furthermore, when thin films with low roughness are examined under this geometry, primary diffraction peaks exhibit fringes with a periodicity that relates to the film thickness.

In the latter case, using SmartLab®, the X-ray incidence angle is fixed only at a few degrees, it is also the case for the detector, except the detector moves in sideways staying on the same horizontal plane with the X-ray source. In-plane XRD measurements are used to estimate the in-plane lattice parameters, a and b. In the case of 2D TMDs, a and b are equal in most of the materials due to the hexagonal geometry. One more information, that proves the single-crystal nature of thin films, is the azimuthal scan where, for a fixed angle between the source and detector, the sample is rotated around the surface normal. For the characterizations, we used a SmartLab Rigaku diffractometer with a copper rotating anode beam tube ($\lambda_{K_\alpha} =$ 1.54 Å), operating at 45 kV and 200 mA. Parallel in-plane collimators of 0.5° of resolution were used both on the source and detector sides. The out-of-plane XRD measurements were performed using a Panalytical

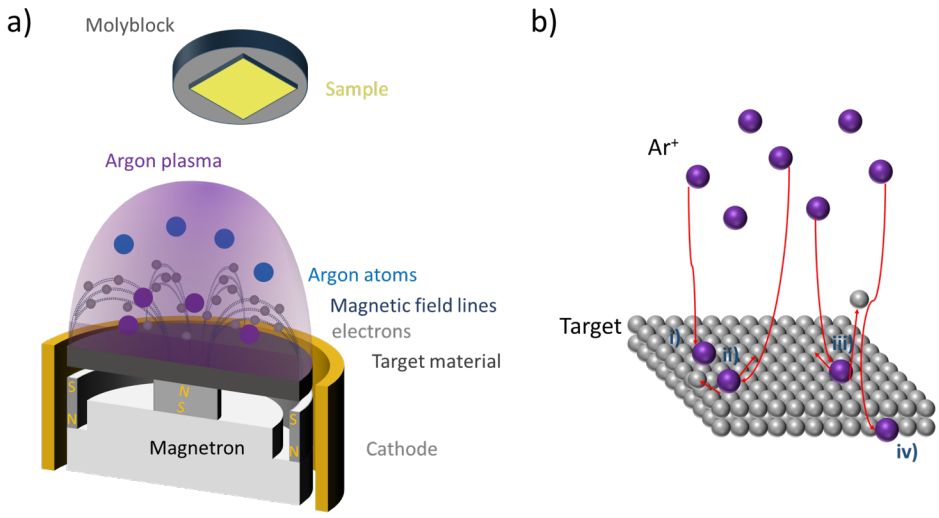

Figure 2.12: a) DC Magnetron sputtering cut-away that reveals its inner components, the plasma is created due the trapped electrons by magnetic field and b) atomic processes during sputtering i) adsorption, ii) momentum transfer, iii) removal of a surface atom, i.e. sputtering or etching, and iv) ion implantation. Adapted from Bohlmark [88].

Empyrean diffractometer operated at 35 kV and 50 mA, with a cobalt source, (λ_{K_α}= 1.79 Å). A PIXcel-3D detector allowed a resolution of 0.02° per pixel, in combination with a divergence slit of 0.125°. Both diffractometers are equipped with a multilayer mirror on the incident beam and K_β filter on the diffracted beam. All the XRD measurements were performed and analysed by Alain Marty.

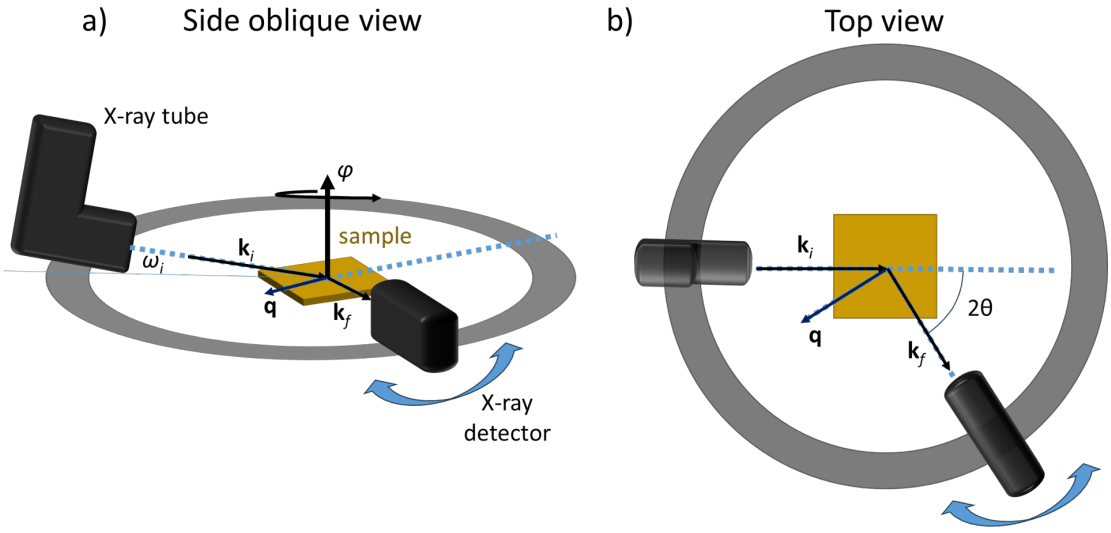

Figure 2.13: Side and top views of the measurement geometry in the SmartLab®.

2.3.2 AFM

Atomic Force Microscopy (AFM) allows non-destructive measurement of sample surface giving insight on the morphology of the film and, under adapted processes as mentioned above about the calibration, their thickness as well. AFM is based on measuring the force in the contact mode between the cantilever tip and the

sample. During this PhD, I used Peak Force Tapping (PFT) AFM. PFT is similar to the TappingMode (TM) in that there is no lateral force on the tip due to short period touching of the sample. However, TM operates at the fundamental resonance frequency of the probe, while PFT operates at much lower frequency of around 1 kHz. A basic working principle of PFT mode is presented in Fig. 4.10. The tip goes down vertically towards the sample surface, as shown in the dashed line of Fig. 4.10a), the feedback signal is maximum or a "peak" force is registered that is applied to the surface (the blue line is when the tip is approaching and the red one is when it is retracting).

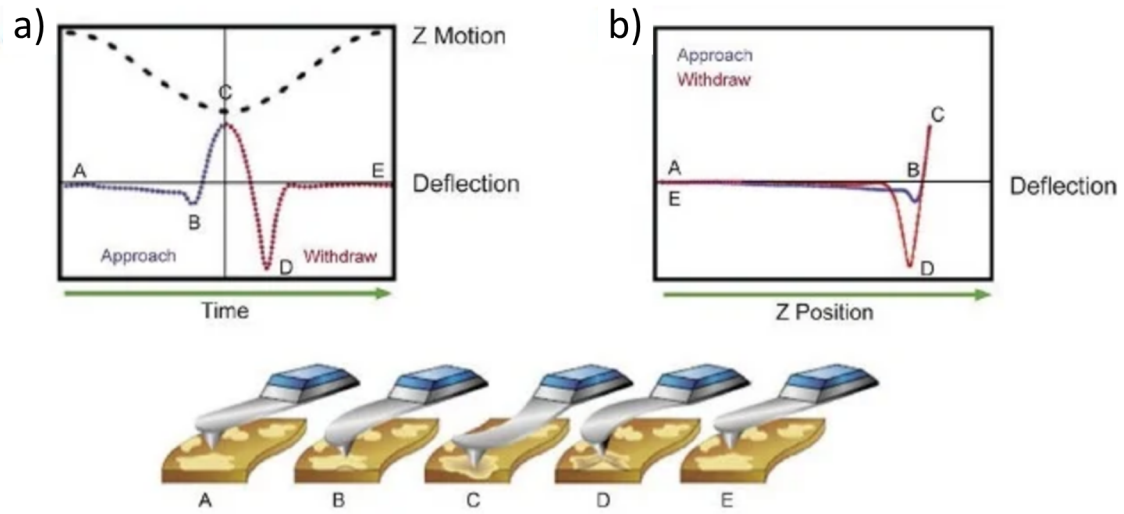

Figure 2.14: Description of the AFM tip trajectory with time (a) and force applied to the surface with Z position of the tip (b) for the Peak Force Tapping (PFT) mode. Adapted from Reference [90].

AFM measurements were carried out by Khasan Abdukayumov, Céline Vergnaud, Oliver Paull, and Isabelle de Gomaes.

2.3.3 Raman Spectroscopy

Raman spectroscopy is a non-destructive tool that is used to characterize materials by studying the vibrational modes. Figure 2.15 summarizes possible light matter interactions. Most of the incident light experiences Rayleigh scattering (elastic) where the energy of the light is conserved. In the case of Raman scattering, the physics is based on inelastic scattering of the incident light off the material. The scattered light can have lower (Stokes scattering) or higher (anti-Stokes scattering) energy than the incident light. The difference between the energies is due to the interaction of the incident light with the vibrational modes of the crystal. Thus, Raman Spectroscopy is widely used in materials science to qualitatively characterize crystals. In 2D materials, Raman Spectroscopy can give complementary information to XRD about the film thickness. Moreover, depending on the deposition method (MBE, CVD, vapour phase transfer, etc.) Raman spectra of 2D materials can differ. Raman spectroscopy experiments were performed by Van-Hoan Le at the PFNC-CEA and Céline Vergnaud.

For Raman measurements, we used a Renishaw INVIA 1 spectrometer with a green laser (532 nm) and a 1800 gr/mm grating. The microscope objective magnification was $\times 100$ and the numerical aperture 0.9. The laser power was <150 mW/μ m^2. All the spectra correspond to the average of at least three spectra recorded at different locations on the samples.

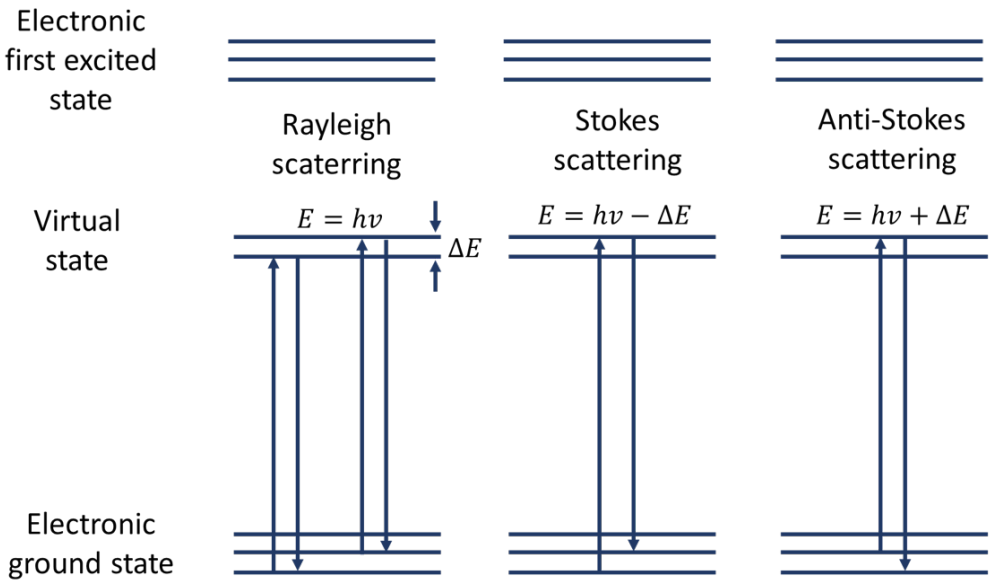

Figure 2.15: Scattering processes of light upon interaction with matter.

2.3.4 XPS

The photoelectric effect, first discovered by Heinrich Hertz and explained by Einstein using quantum mechanics, describes the ejection of an electron from a material by an incident photon with well-defined energy. Since electrons in an atom occupy discreet energy levels, ejecting outermost electrons requires less photon energy than those in the core levels. The energy of core levels depends on the chemical bonds and we can thus access the chemical environment of the elements in the film by measuring precisely the energy position of those levels. To access deep levels, one must use high photon-energy sources, as X-rays. X-ray photoelectron spectroscopy relies on the following equation:

$$E_{hv} = E_k + E_\phi + E_B \tag{2.3}$$

where E_{hv} is the photon energy, around 1300-1500 eV, E_k is electron kinetic energy, E_ϕ is the work function corresponding to the energy required to remove an electron from the material surface to the vacuum, and E_B is the binding energy of emitted electrons. The electron analyser measures the kinetic energy of the ejected electrons, knowing the values of the first energy terms, we can plot the number of electrons detected as a function of E_B.

XPS measurements are carried out under UHV conditions to decrease the probability of electrons to collide with atoms and molecules on their trajectory towards the electron analyser. In XPS, the the measured binding energy of an atom depends on its chemical environment, in other words, a shift of the binding energy from that of the neutral atom gives access to its oxidation state and potential atoms it is bonded to. XPS is thus an important tool to study atomic intermixing, oxidation or contamination.

XPS experiments were performed in situ using a Staib Instruments spectrometer. We used an aluminium anode with K_α (ν=887 pm) emission operating at 300 W. The signal was optimized on the Se LMM Auger spectra at a binding energy of 184 eV. The C^{1s} core level line was used to set the binding energy scale.

2.3.5 Angle resolved photo-electron emission spectroscopy (ARPES)

The physical mechanism of ARPES is similar to that of XPS, also operating under UHV, except there is an additional information on the momentum of the photo-emitted electron and the photon energy is lower compared to XPS, around 20-80 eV. Thus, ARPES is an experimental tool to measure the band structure of materials 0-80 eVs below the Fermi level. A photon source in the range of 20-80 eV energy range corresponds to UV and far UV radiation, a compact size ARPES can be installed in laboratories, however, to achieve high signal-to-noise ratios it is better to use at synchrotron facilities for higher light intensities. A simplified sketch of the ARPES experiments is given in Fig. 4.5.

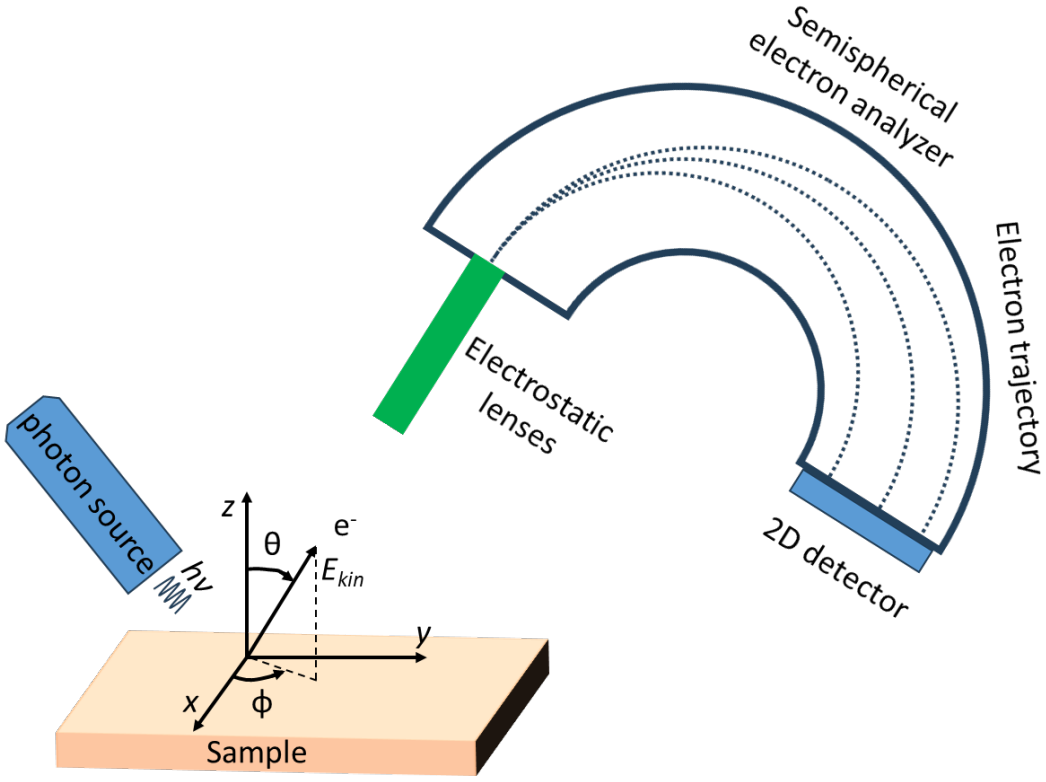

Figure 2.16: Schematics of ARPES measurement showing the photon source (with around 20-80 eV energy), photo-electron emission, semi-spherical analyser that contains the electron trajectory, and 2D detector that detects electron energy and momentum.

To construct the electronic band structure, i.e. the E-k diagram, one has to measure both the energy and momentum of the ejected electrons. The former is done in a similar manner to XPS, whereas the latter is through measuring the emission angle θ of photoemitted electrons using an hemispherical electron detector. Due to the conservation of the in-plane photoelectron momentum, it follows:

$$p_{||} = hk_{||} = \sqrt{2mE_k} sin\theta \tag{2.4}$$

Once E_k and $p_{||}$ values have been obtained, E_B vs $k_{||}$ can be plotted. Later, new techniques were developed for ARPES, such as the spin and time resolutions. The former is essential to study exotic spin textures,

such as spin splitting in the case of the Rashba spin-orbit coupling, and the latter could be used to better understand ultrafast processes from the perspective of the band structure evolution.

2.3.6 STEM

Scanning transmission electron microscopy (STEM) is a combination of scanning electron microscopy (SEM) and transmission electron microscopy (TEM), meaning that the image is obtained through transmission while scanning the sample with the focused electron beam. A special sample preparation is needed to be able to obtain an STEM image using the Focused Ion Beam (FIB) technique [91]. The FIB preparation step thinned the sample down to a few nm thick lamella that allows the transmission of the electron beam.

Scanning transmission electron microscopy (STEM) measurements were performed using a Cs-corrected FEI Themis at 200 kV. HAADF-STEM (high-angle annular dark field) images were acquired using a convergence angle of 20 mrad and collecting electrons scattered at angles higher than 60 mrad. STEM specimens were prepared by the focused ion beam (FIB) lift-out technique using a Zeiss Crossbeam 550. Samples were coated with protective carbon and platinum layers prior to the FIB cut. All the STEM experiments, including the sample preparation step by FIB, were carried out by Djordje Dosenovic and Hanako Okuno of the Laboratoire Modélisation et Exploration des Matériaux (MEM) at IRIG.

2.4 Spin-charge conversion experimental tools

2.4.1 Broadband FMR

As mentioned in the theoretical background chapter, a broadband FMR set-up measures the resonance field at various given microwave frequencies, ranging from 2 to 20 GHz in our case. The frequency dependence of the resonance field and the linewidth gives us essential physical properties of the FM/NM heterostructure, such as, the Landé factor g, the saturation magnetization M_s, and the Gilbert damping α.

The broadband experiments are carried out using an FMR spectrometer based on a coplanar waveguide (CPW) [92] with a schematics shown in Fig. 2.17 (obtained from Seeger et al [93]). The setup was home-built by Bill Bailey et al. in 2010 and it operates at room temperature. A Vector Network analyzer (VNA) is used to inject microwave power (with frequencies in the range of 10 MHz to 24 GHz) to a microstripline (i.e. co-planar waveguide) and the sample is placed on top of the microstripline while an in-plane magnetic field is applied by an electromagnet (which is perpendicular to the microwave field). Then the output microwave power is detected as a function of the applied field. A lock-in amplifier is used to improve the signal-to-noise ratio.

2.4.2 THz-TDS: a tool to study spin-charge conversion

As introduced in Chapter 1, a THz-TDS set-up was adapted to study spin-charge conversion phenomena in FM/SOC material heterostructures. The experiments were carried out at the Physics Laboratory of Ecole Normale Superieure Paris in collaboration with Martin Micica and Sukhdeep Dhillon [94], [4].

As presented in Fig. 2.18, the sample is mounted in a dry air purged box and a permanent magnet is put next to it that provides 20 mT magnetic field. Ultrashort laser pulses with a wavelength of 800 nm were generated by a Ti:Sapphire oscillator (Coherent MIRA, 15-100 fs length and horizontal polarization), with an average repetition rate of 80 MHz. The generated laser pulses are orthogonally split into two by a beam-splitter. The first one is called the pump line that goes to the sample and the second one is called the probe line that goes to the ZnTe crystal. The pump line has an average excitation power of 300 mW (after modulation by a chopper at 2777 Hz) and the average laser spot of 200 μm $\times$ 200 μm. After taking into

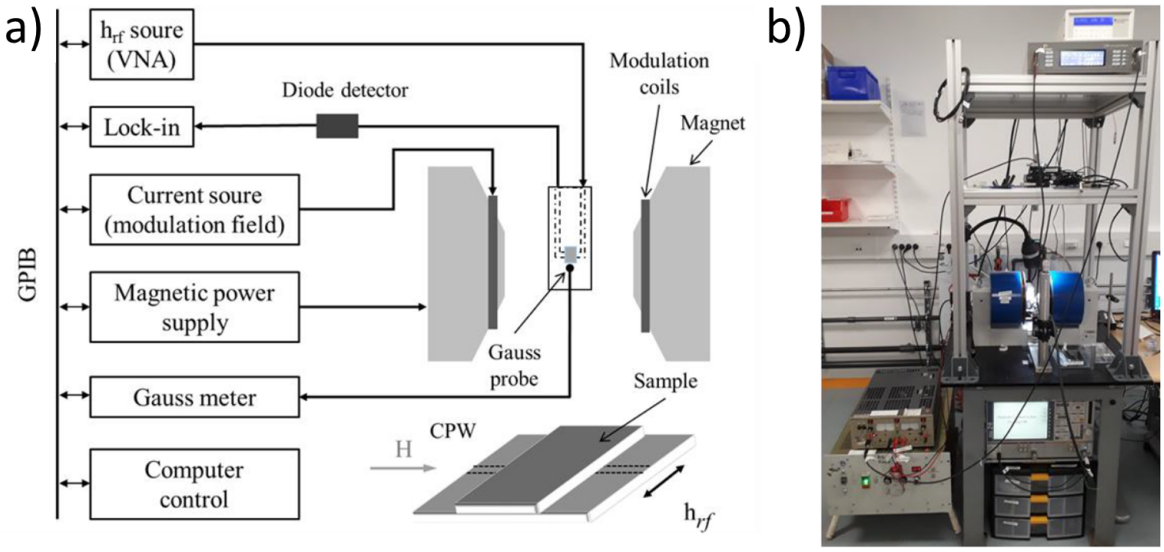

Figure 2.17: a) a schematic of FMR spectrometer based on a coplanar waveguide (CPW) also known as Broadband FMR and b) experimental setup installed at SPINTEC. Adapted from Seeger [93].

account the laser repetition rate, the chopper frequency and some geometrical factors, we obtain that a laser pulse hits the sample every 45 ps, leaving enough time for the remagnetization of the FM layer. The emitted THz pulse is then focused and directed toward the electro-optical sampling (EOS) (more explanation below) crystal with a series of Au-coated parabolic mirrors. A teflon screen (transparent to THz radiation up to ≈ 6 THz) is placed before the ZnTe crystal to filter out residual NIR light.

The probe line is made of a delay line that adds a light path of $2\Delta_L = c\Delta t$, c being the speed of light, Δ_t the time step between the pump and probe pulses on the order of a few picoseconds corresponding to ΔL of a few hundreds μm. The THz pulse and the probe pulse (NIR) are spatially and temporally superposed at the detection crystal. The probe pulse is subjected to a polarization change caused by the change in the refractive index of ZnTe that is induced by the THz electric field. Tuning the delay between the THz and probe pulse using the delay line, allows to construct the THz electric field profile emitted by the sample.

The induced refractive index change comes from the birefringence of the ZnTe<110> crystal and is described by the fact that the propagation of light is dependent of on the crystal axis in anisotropic crystals. Linear birefringence is observed in uniaxial crystals which have two different refractive indices for two different directions perpendicular to the propagating axis by an ordinary refractive index, n_o, and an extraordinary refractive index, n_e. A difference in the wavefront phase originates between the two proper optical axis. This results in the beam polarization variation between the input surface and output surface of the birefringent crystal [56].

Specifically, when an electric field is present in a non-linear (second-order) noncentrosymmetric crystals, the movement of the polarization ellipsoid of light can be described by incorporating the electro-optic tensor $\mathbf{r}_{ij}$, as derived by Yariv [95]:

$$(\frac{1}{n^2})_1 x^2 + (\frac{1}{n^2})_2 y^2 + (\frac{1}{n^2})_3 z^2 + 2(\frac{1}{n^2})_4 yz + 2(\frac{1}{n^2})_5 xz + 2(\frac{1}{n^2})_6 xy = 1 \tag{2.5}$$

where the first three terms correspond to birefringence and the latter three correspond to electro-optic effect and $i = \{1,...6\}$ stand for the six tensor components $\{x^2, y^2, z^2, yz, xz, xy\}$. The first three indices ($i = \{1,2,3\}$) constitute the conventional birefringence term ($1/n_i^2$) in the absence of an electric field while

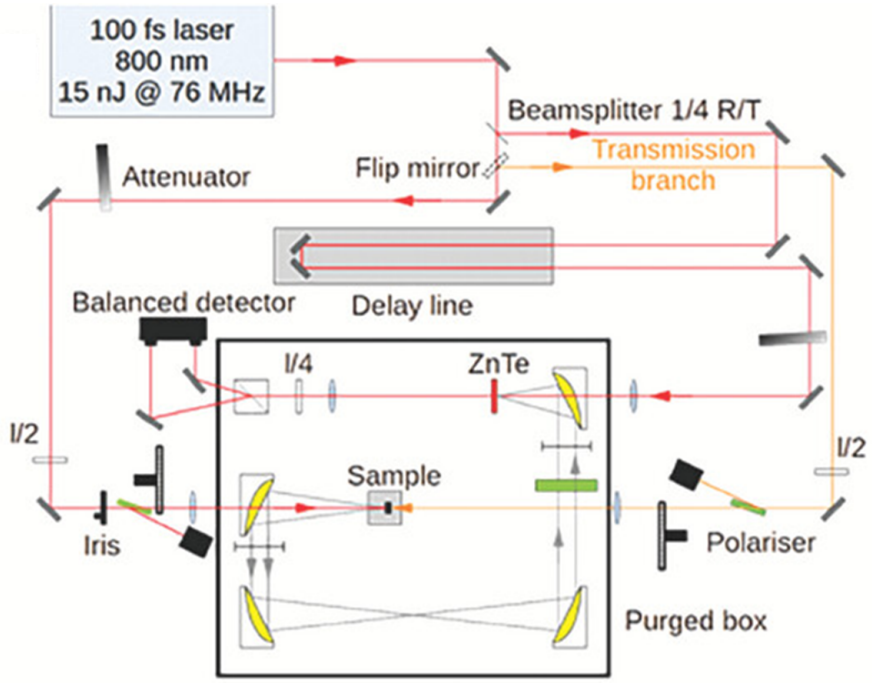

Figure 2.18: Schematics of the THz time domain spectroscopy (THz-TDS) optical bench with the Ti:Sapphire laser, the purged experimental box (inside the black square) that contains the sample, parabolic mirrors, the ZnTe crystal (THz electric field rectifies its refractive index so that the amount of transmitted laser light is modulated), a quarter waveplate, and a prism. The delay line allows to access the time domain of the ultrafast SCC by modulating the time when the laser light reaches the ZnTe crystal. Obtained from Abdukayumov et al [4].

the three mixed terms ($i = \{4,5,6\}$) vanish. The variation of the electric field can be given by:

$$\Delta(\frac{1}{n^2})_i = \Sigma_{j=1}^{3} \mathbf{r}_{ij} E_j \tag{2.6}$$

$\mathbf{r}$ being a 6×3 matrix coding the electro-optic effect. The electro-optic coefficients can potentially become zero due to the symmetry properties of the crystal point group. Yariv has calculated the electro-optic tensor for different symmetries, and in this discussion, we will focus on the specific example of the $\bar{4}3m$ point group, which applies to ZnTe and GaP crystals with a zinc-blende arrangement [96]. In this arrangement, only the coefficients $r_{41} = r_{52} = r_{63}$ are non-zero and are equal. Additionally, the refractive index change Δn can be empirically parameterized using Sellmeier equations, such as in the case of ZnTe and GaP, in order to numerically determine the electro-optic response with frequency [96], [97], [98]. The expression for the phase shift Γ associated with the $\bar{4}3m$ point group is derived from Planken [99] and Schneider [100] and given by:

$$\Gamma = \frac{2\pi e_{cr}}{\lambda NIR}\Delta n = \frac{\omega_{NIR} n_{cr}^3 E_{THz} r_{41} e_{cr}}{2c}(cos\alpha sin2\phi + 2sin\alpha cos2\phi) \tag{2.7}$$

$\lambda = 2\pi c/\omega_{NIR}$ being the free-space NIR wavelength, e_{cr} and n_{cr} the crystal thickness and refractive index at NIR frequency, respectively, α the angle of the THz polarization with respect to the [001] crystal axis and ϕ the angle of the probe-beam polarization with respect to the same crystal axis.

The rotation of the probe polarization can be quantified by two methods: i) separating the polarization using a quarter-wave plate and a Wollaston prism, and ii) generating a photo-current in a balanced photode-

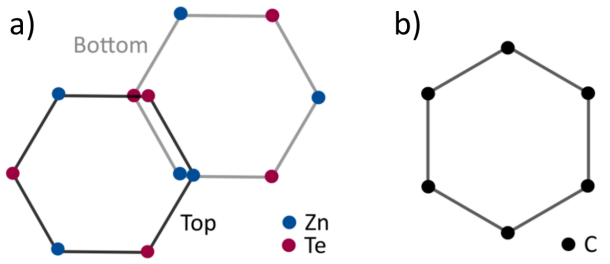

Figure 2.19: The difference between a) non-centrosymmetric (ZnTe) and b) centrosymmetric (graphene) crystals. Adapted from Rongione [56].

tector that is proportional to the difference between the horizontal (P_1) and vertical (P_2) projections of the polarization via:

$$\frac{\Delta P}{P_{NIR}} = \frac{\omega_{NIR} n_{cr}^3 E_{THz} r_{41} e_{cr}}{c} \quad \text{and} \quad V_{RF} = -\Delta P R(\lambda) G \tag{2.8}$$

$\Delta P = P_2 - P_1$ being the power difference between the vertical and horizontal polarizations of the probe pulse, $P_{NIR} = P_2 - P_1$ the probe power going through the nonlinear crystal. In order to accurately measure a minute change in THz-induced polarization rotation, a heterodyne detection technique is employed. This technique utilizes a lock-in amplifier detection scheme, which allows access to the rectified generated bias VRF (assuming impedance matching). The responsivity of the photodiode, denoted as $R(\lambda)$, and the transimpedance gain of the RF output, represented by G, play significant roles in this process.

2.5 Conclusion

In conclusion, I have introduced the MBE technique used to grow 2D transition metal diselenides, its important components and the growth kinetics for simple materials. After the thin film growth, the structural and chemical characterization techniques have been introduced. Lastly, the measurement setups were presented for SCC experiments. The next chapters will be about the results and discussion of 2D materials and their heterostructures.

Chapter 3

Spin-charge conversion in $PtSe_2$

3.0.1 Introduction and Motivation

TMDs can be found in 1T, 1H, 2H, and 3R phases, the number indicated the number of layers per unit cell and the letter means T for trigonal, H for hexagonal, and R for rhombohedral. The most stable crystal structure of $PtSe_2$ is the 1T phase that means a stacking sequence of AAA, as opposed to the metastable 3R phase with ABC sequence. Fig. 3.1 a and b give the crystal structure of $PtSe_2$ from the side and top view, respectively (adapted from reference [101]).

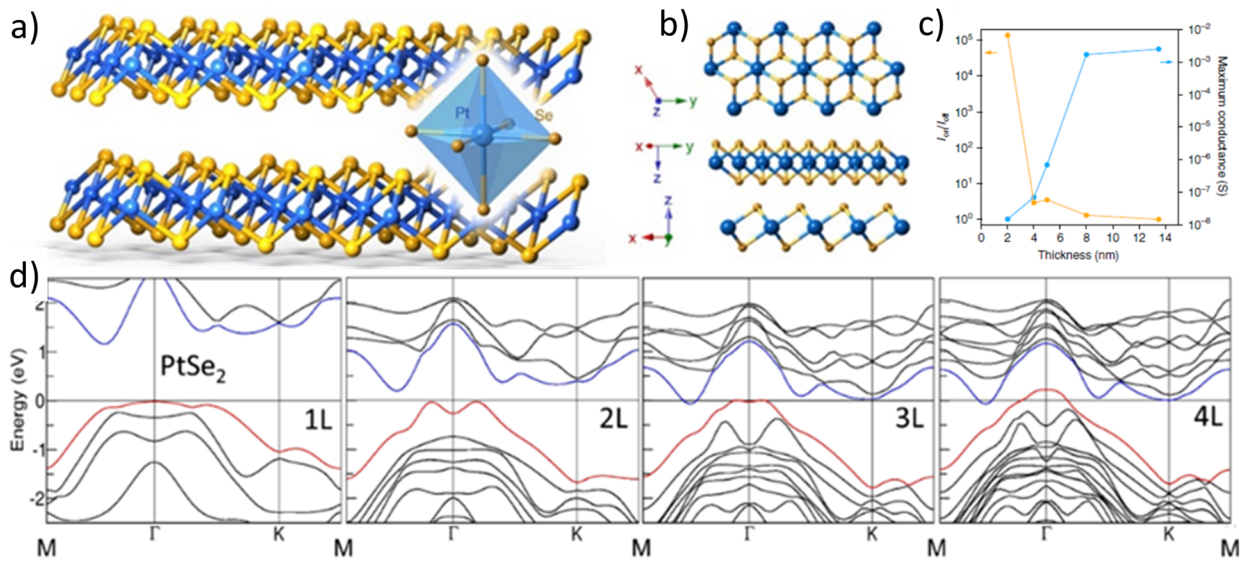

Figure 3.1: Structural and electronic properties of $PtSe_2$. a) side view and b) top and side view sketch of $PtSe_2$ crystals (Xuechao et al [101]), c) conductivity (blue) and on-off current ratio (orange) of $PtSe_2$ indicating the thickness-dependent band gap evolution (Ciarrocchi et al [102]), d) theoretical electronic band structure calculation of $PtSe_2$ confirming the experimental observation on the thickness-dependent band structure evolution with the band gap closing in between 3 ML and 4 ML of $PtSe_2$ (Villaos et al [103]).

Similar to the well-known TMDs based on W and Mo (WS_2, WSe_2, MoS_2, $MoSe_2$), Pt-based dichalcogenides show interlayer interaction, however, it is stronger [102], [104] which becomes obvious when one looks at the thickness dependent band structure: starting with almost a 2 eV band gap in a single layer of $PtSe_2$, the band structure evolves with the thickness and the band gap closes between 3 ML and 4

ML $PtSe_2$, as demonstrated by experimental measurements, Fig. 3.1 c [101], and DFT calculations, Fig. 3.1 d [103]. This interlayer interaction could be utilized in heterostructures, for example with graphene a twist angle dependence of the interlayer coupling between $PtSe_2$ and bilayer graphene has been observed [104]. Yao et al studied the band structure of $PtSe_2$ grown on Pt(111) by spin resolved-ARPES [105]. The experiments yielded a Rashba-like spin texture with time reversal symmetry. This was explained by assigning one chirality to the top Se layer and the opposite chirality to the bottom Se layer. Our calculations do not necessarily agree with this interpretation and this is discussed in the theoretical part of this chapter. However, the interpretation Yao et al [105] gave for the observed spin texture, i.e. the direct evidence for spin-layer locking is of great interest for $PtSe_2$ to be considered as a good candidate for SCC studies.

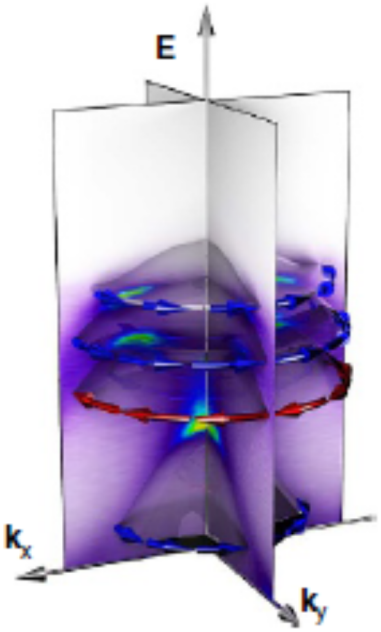

Figure 3.2: Spin texture of $PtSe_2$ observed by spin-resolved ARPES [105].

Among transition metal diselenides, $PtSe_2$ is not the pioneering one that has been shown to emit spintronic THz waves. For example, Fe/$NbSe_2$ and Ni/$NbSe_2$ bilayers showed spintronic THz emission, and the authors could extract a spin Hall angle: $\theta_{SH} \approx 1\%$ ([106]). Unfortunately, this study lacked a thorough material characterization. Another work was performed on exfoliated flakes of WSe_2 covered with FeCo films ([107]), again lacking a detailed material characterization. Without a detailed characterization of the materials and interfaces, it is not possible to conclude about the origin of SCC in ferromagnet/TMD bilayers.

In this chapter, I present the growth of $PtSe_2$ by MBE and van der Waals epitaxy (vdWE) on graphene/SiC, followed by structural and chemical characterizations. Then, CoFeB and Al are sputter deposited on top of $PtSe_2$ to inject a spin current and protect the FM layer against oxidation, respectively. To inject a spin current, two different techniques were explored: spin pumping by FMR and THz-TDS. Spin pumping experiments were very difficult to carry out; the samples have to be cut in 0.4×2.4 mm^2 pieces to be measured by spin pumping FMR. However, during the cutting process, we used a diamond saw with a water solution as a coolant that systematically tended to delaminate the $PtSe_2$ layers. Once this was resolved there was another challenge coming from the FMR machine: most probably it was not sensitive enough to weak signals coming from SCC in $PtSe_2$ mostly due to the very low carrier density

at the Fermi level. One possible contribution is from eddy currents: in an ideal placement of the sample inside the cavity, only the magnetic field component of the h_{rf} penetrates into the film. In the event of a small bend of the sample or trouble in the cavity, the electric field component of the microwave radiation interacts with the heterostructure as well, inducing eddy currents. Only 10 ML $PtSe_2$/CoFeB bilayers gave a measurable signal, for thinner $PtSe_2$ films, the signals were too weak to be detected. We thus started THz-TDS experiments in collaboration with the Laboratoire de Physique of the Ecole Normale Superiéure in Paris to study SCC in $PtSe_2$. The advantage of this technique over the conventional spin pumping by FMR one is that it does not require additional sample preparation step which helps to preserve the 2D materials.

Thus, most of the results presented in this chapter come from THz-TDS experiments. In the particular, the $PtSe_2$-thickness dependence of the emitted THz signal allowed us to establish the mechanism(s) responsible for SCC in $PtSe_2$. The two-step evolution of the latter study suggests two separate effects responsible for SCC: IREE for low thicknesses, ISHE for thicker films after the semiconducting-to-semimetal transition of $PtSe_2$. The spin diffusion model considering this transition fits well the experimental thickness dependence. IREE in the thin film limit is interpreted based on theoretical calculations on the graphene/$PtSe_2$ heterostructure showing the existence of an interface electric field due to a charge transfer from graphene to $PtSe_2$, also evidenced by Scanning Tunneling microscopy (STM) measurements and previously observed in the graphene/WSe_2 bilayer [108].

3.1 Growth and Structural Characterization

3.1.1 vdW epitaxy

As the semiconductor industry is heavily based on the epitaxial growth of commensurate heterostructures for electronic and optoelectronic devices, the lattice-mismatch issue limits the number of possible heterostructure combinations, limiting the number devices with new physical properties, a notable example is III-V materials, such as $In_xGa_{1-x}As$ integration into the Si based fabrication platform [109].

In vdWE, the lattice matching requirement for epitaxy is relaxed due to, by definition, the existence of van der Waals interaction between the epilayer and substrate, instead of much stronger covalent and ionic bonds. This is due to the absence dangling bonds on the substrate and epilayer sides (see Fig. 3.3). vdWE was first demonstrated in 1984 by the group of Koma [110] for the growth of $NbSe_2$ and Se on cleaved faces of 2H-MoS_2 and Te, respectively. Note that in the latter growth, Se has the lattice constant of bulk Se, despite being grown on Te with which it has 20% lattice mismatch. It was later shown that vdWE could be achieved with 3D substrates as well [111], [112], [113] by passivating the dangling bonds, in this case, it is referred as quasi-vdWE. On the other hand, when the dangling bonds are not passivated, the interface between the film and substrate forms a so-called 'sacrificial layer' [114]. This can be observed in the RHEED pattern, for example, that it shows diffuse pattern for the initial stages of growth, and once there is enough matter on the surface, the RHEED pattern shows thin rods.

The conventional epitaxial growth modes described in the previous chapter do not fully capture characteristics of vdWE. For example, as each layer is bonded with the previous one by vdW interaction during the growth, we can not really say that lattice-mismatch-induced strain is transferred to the growing layer (the case of Stranski-Krastanov mode). The explanation given by conventional VW mode in terms of interactions between the materials does not really fit when multilayer island growth is observed with vdW materials. Because VW mode dictates that due to the presence of strong covalent bonds and lattice mismatch between the growing film and substrate, elastic energy builds up, leading to dislocations in the film. Although, there is a lattice mismatch between the growing film and substrate in vdWE, the absence of strong bond between them, prevents the build-up of the elastic energy, thus, dislocations in the film. However, any type of TMD can possess various crystal symmetries defined by their respective energy levels, some are more stable than

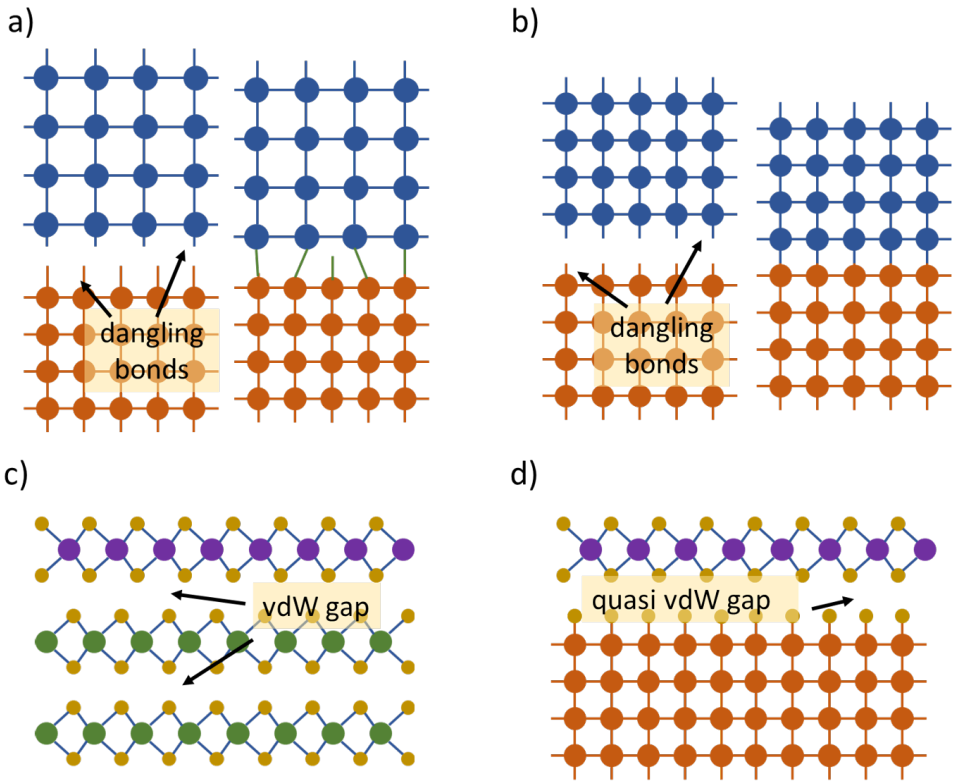

Figure 3.3: Various epitaxy mechanisms. a) commensurate and b) incommensurate epitaxy during conventional 3D epitaxial growth; c) vdWE of layered materials; d) by saturating the dangling bonds at the surface of a 3D substrate, vdWE is possible.

the others and can be grown in either layer-by-layer or island growth, meaning that there is probably a small window in the growth parameters (temperature, flux rate, surface treatment that modifies the atomic mobility, for example) that can give a layer-by-layer growth mode. This is not necessarily true for all the TMDs on all the substrates, the best matches can be explored by theoretical calculations or experimental trials.

Now, we can discuss the origin of triangular grains that are indicative of high crystal quality. The limiting flux in the epitaxy of TMDs is that of the chalcogen as it has higher vapour pressure. Usual flux ratio of C:M (chalcogen-to-metal) is around 20:1. For such high ratios, the observation of triangular grains can be explained due to the varying reactivities of different edges (for example zigzag and armchair, as shown in Fig. 3.4 a.), thus, resulting in different growth rates. In the small window of growth parameters, this could yield a triangular grain, as shown Fig. 3.4 b).

Even though, as mentioned before, vdWE relaxes lattice matching criterion for the epitaxy and vdW materials do not show lattice-mismatch-induced strain, there are some experimental demonstrations that the growth of vdW materials on lattice matched substrates could yield higher crystal quality, for example, the MBE growth of Bi_2Se_3 on InP(111) leads to a better orientation of the grains than on Si(111) [114], therefore, we cannot completely ignore the role of the substrate lattice parameters on the epitaxy.

An important distinction of vdWE from the conventional epitaxy during the growth is that due to the weak nature of vdW forces, according to Vergnaud et al [115] the growing grains are not fixed on the surface, but have degrees of freedom to rotate and translate on the substrate surface. That assumption is valid up to a critical size of the grains, then they cannot move any more: the energy cost to rotate or translate is too high in comparison with k_BT. The relative loose nature of the interaction between the grains and the substrate

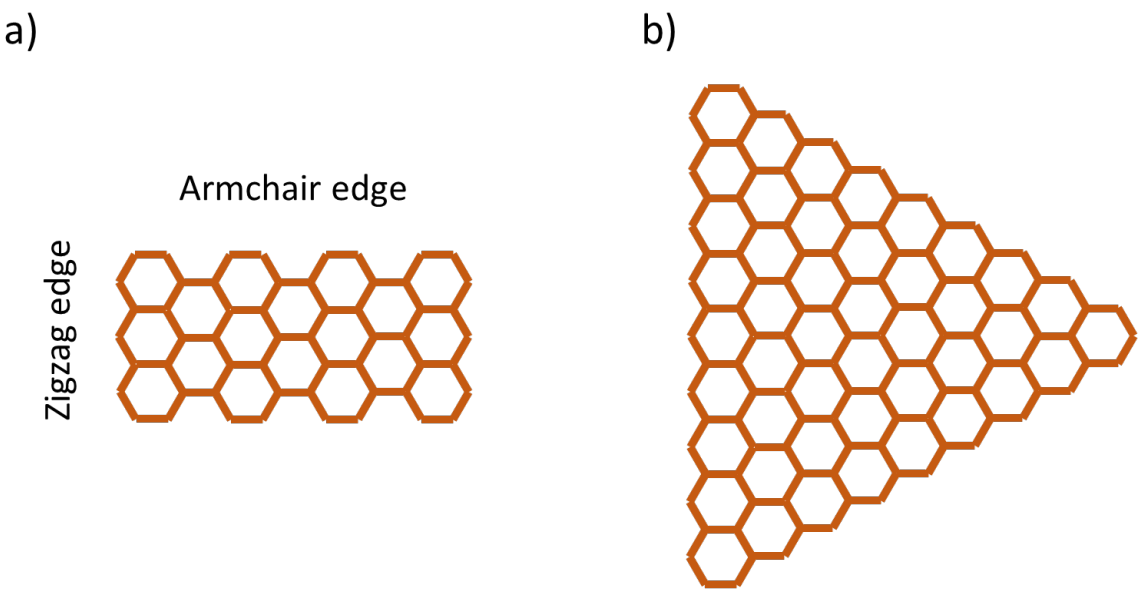

Figure 3.4: a) Zigzag vs armchair edge; b) two distinct edges can have different thermodynamics in terms of growth, finally resulting in thermodynamically stable triangular shape of the crystal. In this example, the zigzag edge is more stable than the armchair one.

could be taken advantage of to improve the crystal anisotropy and the overall quality during the early stages of the growth.

In the lab, we use co-evaporation van der Waals epitaxy to deposity vdW materials by MBE where the metal and chalcogen atoms are evaporated simultaneously and the vapours are pointed towards the substrate. The two species then react on the substrate.

3.1.2 MBE growth and characterization

In this section, I describe the growth parameters and RHEED patterns of $PtSe_2$ on graphene/SiC. The graphene layer was epitaxially grown on the Si-rich face of SiC (for the growth of the substrate see References [116] and [117]). This substrate was chosen due to low SOC and graphene does not have dangling bonds, which is required for vdWE. The substrate is thermally treated at 800 °C for 30 minutes inside the MBE chamber under UHV as it was introduced directly from the air, to remove organic matter as well as water molecules on the surface. Then the substrate is cooled down to 300 °C to start the growth of $PtSe_2$. For THz-TDS experiments, $PtSe_2$ thin films of 1, 3, 6, 10, and 15 ML (0.5, 1.5, 3, 5, and 7.5 nm, respectively) were grown by co-evaporation of Pt and Se. For spin-pumping by FMR, only one 10 ML sample was prepared. The deposition rate of Pt was 0.003125 Å/s for the 1 ML sample and 0.00625 Å/s for the other samples. 1 ML and 3 ML samples were grown in one step and annealed for 15 minutes at 700 °C under Se flux. The other samples were grown alternating deposition and annealing to flatten the surface and avoid 3D growth, all the growths were ended with an annealing step. The growth was carefully monitored using RHEED during the deposition, RHEED patterns of 10 ML $PtSe_2$ taken at room temperature after the final annealing step are presented in Fig. 3.5. The RHEED images were taken along two distinct crystal orientations as sketched in Fig. 3.5 a) and RHEED patterns are shown in Fig. 3.5 b). As the images are different from each other, the films have preferential crystal orientation and aligned with the graphene layer below.

Structural and chemical characterizations were first carried out. For example, to establish the amount of

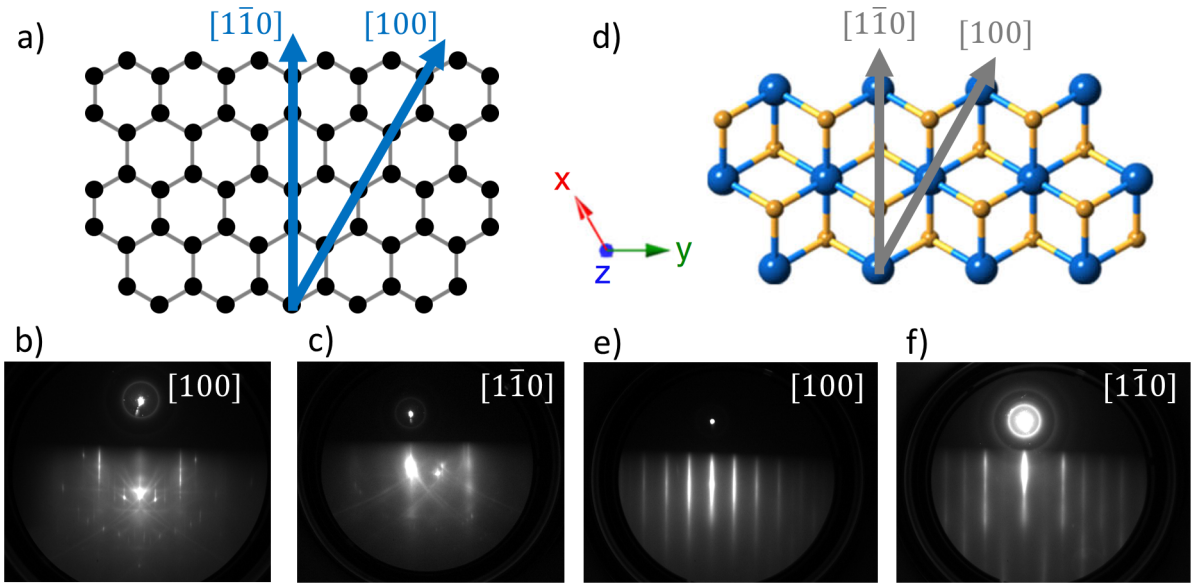

Figure 3.5: RHEED of graphene/SiC and 10 ML $PtSe_2$. a) (d)) shows the top view crystal structure of graphene ($PtSe_2$) with the two high symmetry crystal directions along which the RHEED pattern is recorded; b) and c) (respectively e) and f)) are the two distinct crystal direction shown in a) and d) for graphene and $PtSe_2$, respectively. The streaky aspect and anisotropic character of the RHEED patterns indicate the flatness and high crystal quality of the films.

Pt to cover the substrate with one $PtSe_2$ layer, we deposited less than 1 ML of the film and performed AFM measurements. As we can see in Fig.3.6 a), the growth is in the layer-by-layer mode and the height profile is around 0.51 nm, corresponding to the *c* lattice parameter of $PtSe_2$.

Next, a nominal thickness of 1 ML sample was prepared for STM and spectroscopy (STS) on bilayer graphene (BLG). The STM/STS is based on a qunatum mechanical effect of electron tunneling through an energy barrier [118]. The experiments were carried out and analysed by P. Mallet and J-Y. Veuillen at Institut Néel, CNRS Grenoble. The actual topography showed mostly 1 ML with average grain size of around ten nanometers (Fig. 3.6 b), with some small islands of the second layer and missing $PtSe_2$, i.e. the bare substrate. The inset shows the spectra on two different grains of 1 ML $PtSe_2$ (marked with light and dark blue dots). The spectra overlap with each other, indicating the good homogeneity of the layers, with an estimated band gap of 1.93 eV. The Fermi level (0 eV) is not in the center, but located closer to the conduction band minimum (CBM). We can see that the CBM is at +0.25 eV and Valence band maximum is at -1.68 eV. After a series of experiments, we find the average gap to be 1.95$\pm$0.05 eV with the CBM and VBM at +0.24$\pm$0.03 eV and -1.75$\pm$0.05 eV, respectively. The obtained band gap value is in agreement with the previous experimental findings on $PtSe_2$ grown on highly pyrolytic graphite (HOPG) ([119], [120], [121]) where the CBM is typically at +0.55 eV which is greater than what we observed in our experiments. The shift is, however, almost equal to the work function difference between BLG and HOPG (around 0.20 eV [122]). Continuing this line of reasoning to the single layer graphene (SLG) on SiC(0001) case, as was observed experimentally on WSe_2 grown on SLG and BLG ([108]), we estimate the CBM to be around +0.1 eV to +0.15 eV, due to the decrease of the substrate work function from 100 eV to 135 meV.

To conclude about STS observations, we observe that the Fermi level of 1 ML $PtSe_2$ is shifted towards the CBM as a consequence of the charge transfer from graphene layer underneath to $PtSe_2$. I will discuss the effect of this charge transfer on SCC later in this chapter with theoretical calculations. The out-of-plane XRD measurements on a 6 ML sample showed a c-parameter of 5.14 Å corresponding to an expansion of

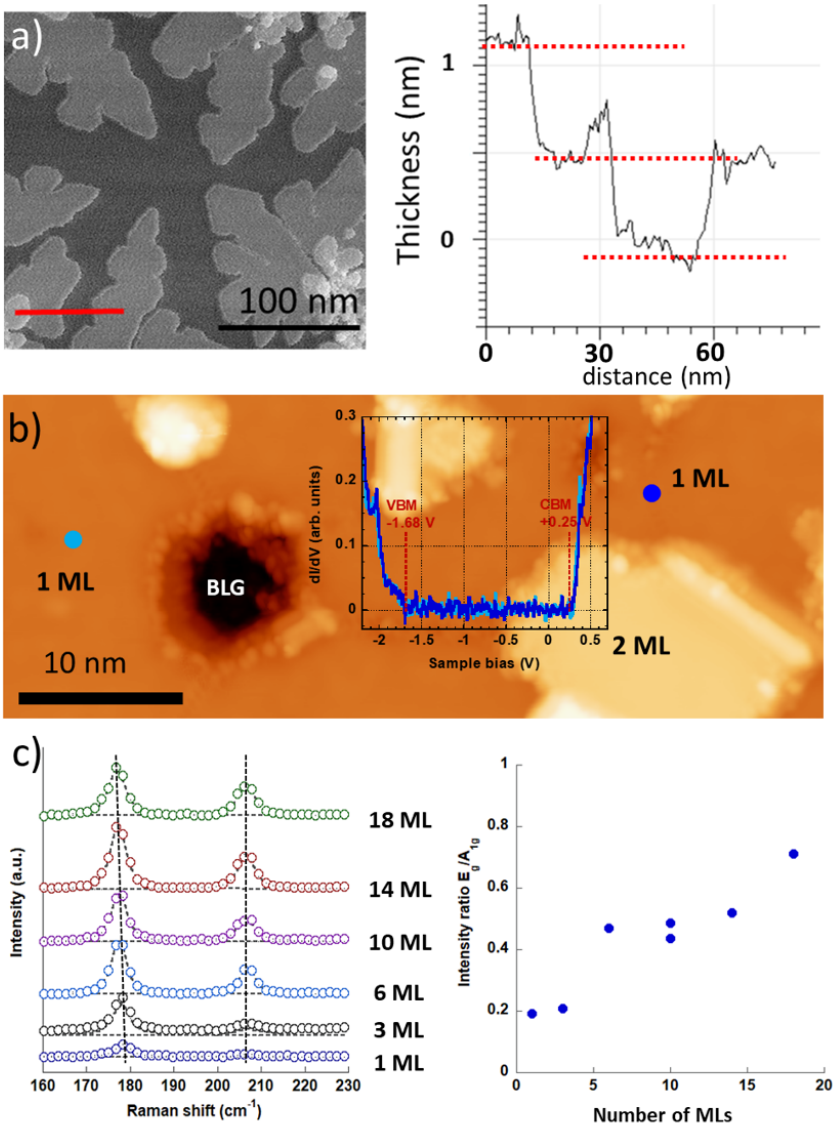

Figure 3.6: Structural characterizations of $PtSe_2$. a) sub-monolayer AFM image showing the layer-by-layer growth with a step-height of around 0.5 nm, as expected for the c lattice parameter of $PtSe_2$, b) STM and STS of 1 ML sample on bilayer graphene/SiC with islands of 2 ML and some holes that allows to access the substrate, the inset shows a couple of STS measured on the points highlighted with light and dark blue, showing a band gap of around 1.93 eV, c) Raman spectra of $PtSe_2$ with various thicknesses after CoFeB/Al deposition and the ratio of E_g/A_{1g} intensities as a function of $PtSe_2$ thickness. Adapted from Abdukayumov et al [4].

2.2% compared to the bulk value [123].

To study SCC by THz-TDS (resp. spin pumping and broadband FMR), the epitaxial growth of $PtSe_2$ is followed by the growth of a 3 nm (resp. 15 nm) thick CoFeB layer on top by magnetron sputtering. The magnetic layers were then capped with 4 nm Al which gradually transforms into AlO_x. The difference of FM thickness for spin pumping by FMR and THz-TDS is due to the fact that we need to keep the layers transparent enough for the laser to pass through and fully demagnetize the FM in THz-TDS, while we need a large enough resonance signal in FMR experiments for spin pumping. After MBE deposition, the

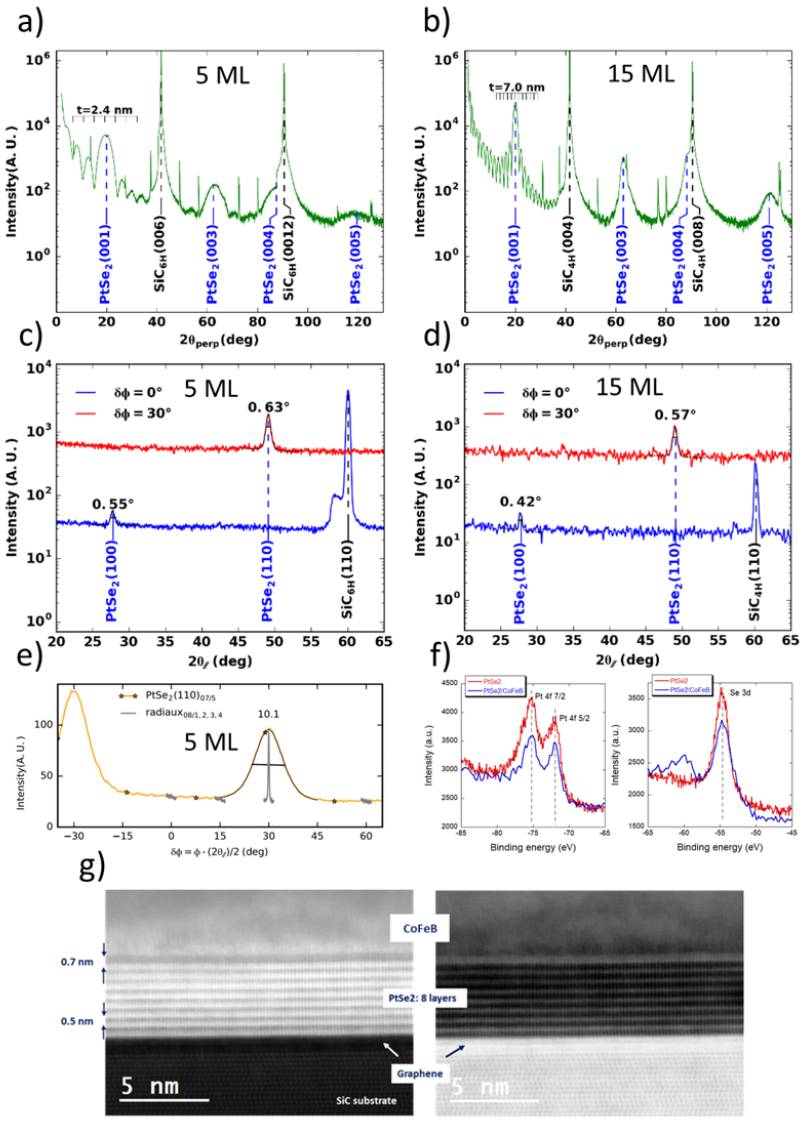

Figure 3.7: Structural and chemical characterization of $PtSe_2$ after CoFeB deposition. a) and b) (c) and d)) out-of-plane (in-plane) X-ray diffractogram of 5 ML and 15 ML $PtSe_2$ after CoFeB deposition, respectively. The fringes around the (001) Bragg peak are indicative of the low roughness of the TMD films and can be used to estimate the thickness. The high quality of the films is confirmed by the small FWHM of the Bragg peaks in in-plane scans. e) azimuthal scan of 5 ML $PtSe_2$/CoFeB recorded on the (110) Bragg peak. It gives a crystal azimuthal spread of $\pm$ 5°. f) XPS spectra of 3 ML $PtSe_2$ before (red) and after (blue) deposition of 1 nm CoFeB. The peaks for Pt and Se show no altering (shift or broadening) after the FM deposition, only a decrease in the intensity because XPS is highly surface sensitive and $PtSe_2$ is now buried under 1 nm of CoFeB. g) STEM cross-sectional image of 8 ML $PtSe_2$ after 15 nm CoFeB deposition highlighting the absence of intermixing. Adapted from Abdukayumov et al [4].

samples were transferred to the sputtering chamber without breaking the UHV thanks to a UHV connection with the main MBE reactor. This allows to keep the TMD layers pristine and free from water and organic contaminants. The sputter deposition rate of the FM was 0.319 Å/s for CoFeB and 0.265 Å/s for Al under the Ar pressure of 1.25 10^{-2} mbar. The coercive field of the magnetic layer was less than 10 mT. After the deposition of 3 nm of CoFeB and 4 nm of Al, we studied the films by Raman spectroscopy first, as

presented in Fig. 3.6 c), on the samples from 1 ML to 18 ML to see if the TMD films are preserved. We can see that all the films have E_g and A_{1g} peaks, meaning that the films quality is not lost after the sputter deposition of CoFeB and Al. Moreover, the peak positions are the same for the layers with and without CoFeB deposition. Lastly, from Raman spectroscopy, we can see that the ratio E_g/A_{1g} is increasing with increasing the film thickness, in agreement with previous observations [124]. This observation was further backed by XRD measurements on 5 ML and 15 ML samples after CoFeB deposition (Fig. 3.7 a and Fig. 3.7d). In the specular or out-of-plane measurements, we can observe Laue oscillations around the (001) Bragg peaks, characteristic of an atomically flat surface which can also be used to estimate the film thickness. The estimated thicknesses are 2.4 nm (instead of 2.5) and 7.0 nm (instead of 7.5), respectively, the c-lattice parameters are 5.18 Å and 5.14 Å, in agreement with bulk $PtSe_2$. In-plane XRD experiments on the same samples (Fig. 3.7 c and Fig. 3.7) show in-plane lattice parameters of 3.709 Å and 3.713 Å, respectively, without additional peaks, for example that of Pt in the presence of unreacted Pt. The azimuthal scan on the 5 ML sample (Fig. 3.7 e) was carried out to estimate the mosaic spread of the crystal giving $\pm 5°$. This is relatively larger than the growths I present in the next chapters which can be explained by the relatively higher atomic mobility on the surface of graphene, allowing more rotation of the growing grains.

Following these structural characterizations, we carried out the chemical analysis on a 3 ML $PtSe_2$ sample before and after the depositon of 1 nm of CoFeB by XPS (Fig. 3.7 f) which did not show any shift of the Pt 4f 7/2, Pt 4f 5/2, and Se 3d peaks, nor additional peaks. This is another evidence that the sputtering process does not deteriorate the TMD films. (The appeared blue peak at -60 eV belongs to Co 3p). Finally, a more visual evidence of the claim is given by STEM in the high angular annular dark field (HAADF) mode on an 8 ML sample after 15 nm CoFeB deposition (Fig. 3.7 g). We can clearly see the layered structure of $PtSe_2$ with a vdW gap in between the layers

In conclusion, high quality films of $PtSe_2$ were grown by MBE, CoFeB and Al were deposited by magnetron sputtering. Post-growth advanced structural and chemical characterizations confirmed the high quality and showed that the sputter deposition of CoFeB does not affect the quality of vdW layers beneath.

3.2 Electrical measurements with the van der Pauw method

First demonstrated by L. J. van der Pauw (vdP) [125], this method offers quick resistivity measurement of discs or arbitrary shapes without requiring any advanced sample preparation steps. The basic principle is similar to four-point resistance measurements, for example, by injecting the current between contacts 1 and 2 as shown in Fig. 3.8 b and detecting the potential difference between contacts 3 and 4. This corresponds to the resistance: $R_{12,34} = \frac{V_{34}}{I_{12}}$. The main assumption in this method is that the contact size is much smaller than the size of the sample. Using the method, $R_{vertical}$ and $R_{horizontal}$ are calculated as shown in Fig.3.8 c on square samples with dimensions of 5 mm$\times$5 mm and varying thicknesses of 3, 6, and 10 ML $PtSe_2$. The samples were electrically connected to a printed circuit board (PCB) using Au wires and silver paste. Four resistance measurements were carried out for each of them (vertical and horizontal) and the average value was calculated. Fig. 3.8 d summarizes the obtained results as a function of $PtSe_2$ with 0 ML indicating the measurement on bare graphene/SiC. The resistance and resistivity show a sudden drop from 3 ML to 6 ML $PtSe_2$, in agreement with the semiconducting to semimetallic transition, as previously reported [102]. The sheet resistance values were then calculated using the following equation:

$$e^{-\pi R_{vertical}/R_s} + e^{-\pi R_{horizontal}/R_s} = 1 \tag{3.1}$$

where R_s is the sheet resistance. Moreover, a clear disparity can be seen between the resistance (and sheet resistance) values for the vertical and horizontal measurements. This can be explained by the vicinal surface of the substrate that is shown in this AFM image in Fig. 3.8 a. This anisotropic behaviour of the

electrical resistance was previously reported and explained by the presence of steps (and hence, terraces) on the substrate and the resistance is smaller when electrons flow along the terrace than perpendicular to the terraces [126]. Because of the unique topography of the samples originating from the substrate preparation process, it is not physically meaningful to just insert $R_{vertical}$ and $R_{horizontal}$ into equation 3.1. Thus, to calculate the sheet resistance, R_S, we have to make the distinction between them, $R_{S,vertical}$ and $R_{S,horizontal}$: we insert $R_{vertical}$ ($R_{horizontal}$) twice. This was done to obtain a more realistic value as we do not exactly know the relative orientation of the steps with respect to the resistance measurement direction. Finally, the sheet resistance values for the reference sample (AlO_x/CoFeB) were 224 Ohm/sq and 538 Ohm/sq for the vertical and horizontal configurations, respectively.

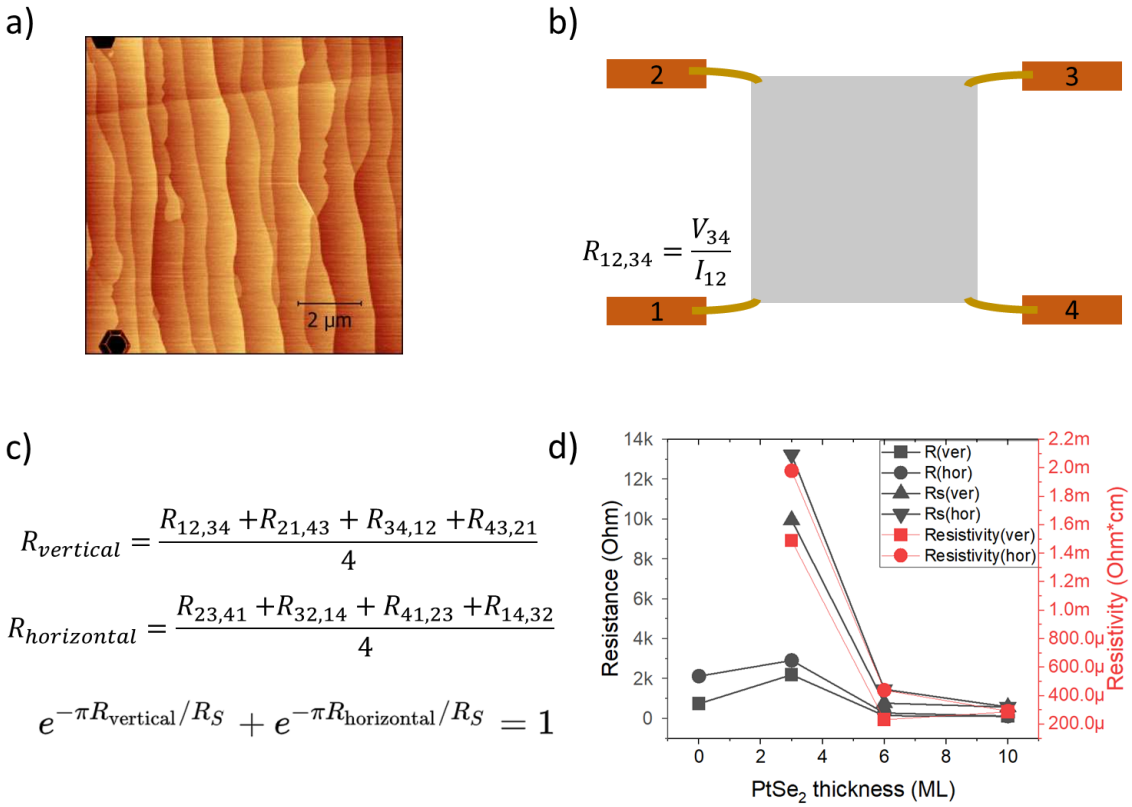

Figure 3.8: van der Pauw (vdP) measurements. a) AFM image of graphene/SiC showing the steps originating from the small miscut angle. b) a sketch of sample geometry for vdP measurements and the explanation of resistance $R_{12,34}$ corresponding to the current injection between contacts 1 and 2 and measuring the potential drop between contacts 3 and 4. c) Equation to estimate $R_{vertical}$ and $R_{horizontal}$ from the measured resistance values and, from the two, the equation to calculate the sheet resistance. Estimated $R_{vertical}$, $R_{horizontal}$, $R_{S,vertical}$, $R_{S,horizontal}$, $Resistivity_{vertical}$, $Resistivity_{horizontal}$. For the last four values, the contribution from the substrate is subtracted.

3.3 SCC experiments

The high quality of the films has been established and we can now discuss THz-TDS experiments. No additional sample preparation steps were performed. The sample was placed in a mount to apply in-plane magnetic field of around 20 mT. The mount allowed us to independently rotate the magnetic field and sample.

For the first run of experiments with 10 ML TMDs, we used the reflection mode with 15 fs laser pulses, for the thickness dependence on $PtSe_2$ and Pt, we used the transmission mode pumped from the substrate side and 100 fs laser pulses (the former setup was down).

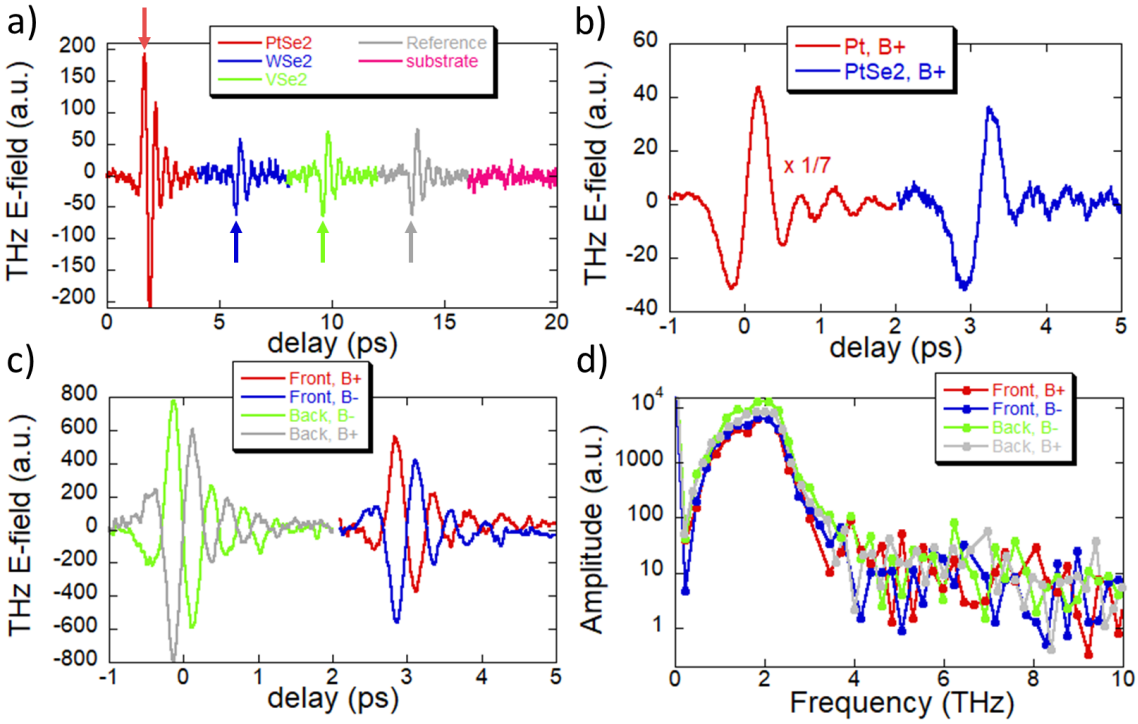

Figure 3.9: Preliminary results of THz-TDS experiments. a) THz spectra of $PtSe_2$, WSe_2, VSe_2 (10 ML each and 3 nm CoFeB/AlO_x sputtered on top), and reference sample (AlO_x/CoFeB) and the bare substrate. The $PtSe_2$ sample exhibits the highest THz voltage. b) Comparison of the THz spectra of CoFeB/5 nm Pt and CoFeB/10 ML $PtSe_2$, To make the comparison easier, the signal of Pt was divided by a factor 7. c) THz spectra of CoFeB/10 ML $PtSe_2$ with pumping from the front (FM side) and back (substrate side) for two opposite magnetic field directions. The sign changes indicate that the THz pulse is of spin origin and due to SCC, and the corresponding fast Fourier transform (FFT) of the spectra is given in c). Adapted from Abdukayumov et al [4].

The first experiments were carried out on Al/CoFeB covered 10 ML $PtSe_2$, 10 ML WSe_2 [127], 10 ML VSe_2 [128], graphene/SiC (reference sample), and bare substrate graphene/SiC, as presented in Fig. 3.9 a. The ferromagnetic nature of VSe_2 with room temperature T_c has been long debated. However, this was later debunked by many follow-up experimental observations, one is for example from the team of 2D spintronics [128]. The preliminary experiments on various TMDs showed the THz emission from 10 ML $PtSe_2$ was the highest, whereas WSe_2 and VSe_2 did not show an obvious increase in the THz signal, leading to the conclusion that the origin of THz emission in all the three samples is the same and the common aspect on these structures being the AlO_x/CoFeB bilayer, possibly the SCC is from this interface or due to self-conversion in the FM layer. SCC in graphene/SiC, VSe_2, and WSe_2 can be considered negligible. The first two have low SOC, thus, no strong SCC is expected, whereas 2H-WSe_2 has spin-valley locking that favours out-of-plane spin polarization at the K-points of the Brillouin zone while in SCC experiments in-plane polarized spins are injected.

After showing that $PtSe_2$ shows enhanced THz emission, the next step is to compare it with SCC in known materials, such as Pt, verify that the emission is indeed due to SCC, and identify the nature of the

conversion. First, I compared it with 5 nm Pt sputtered on graphene/SiC, and we see that Pt emits seven times higher THz field compared to 10 ML $PtSe_2$ in Fig. 3.9 b. To establish the magnetic (also known as spintronic origin in the field of THz emission) origin of the emission, we first inverted the field direction (B-) that gave equal in magnitude but opposite in polarity emission. As discussed in the Theoretical background chapter, there could be THz emission originating from the magnetic dipole which is not related to SCC and it does not change polarity when pumped from the front (FM side) or back (substrate side), on the other hand, THz fields originating from electric dipole do. We confirm in Fig. 3.9 c that the THz field comes from the electric dipole. The fast Fourier transform (FFT) is shown in Fig. 3.9 d, that shows an emission in the range of 0-4 THz, comparable to other spintronic THz emitters [129]. The emission spectrum was not affected by changing the FM deposition technique, e-beam evaporated 3 nm Co on 10 ML $PtSe_2$, shown in 3.10f.

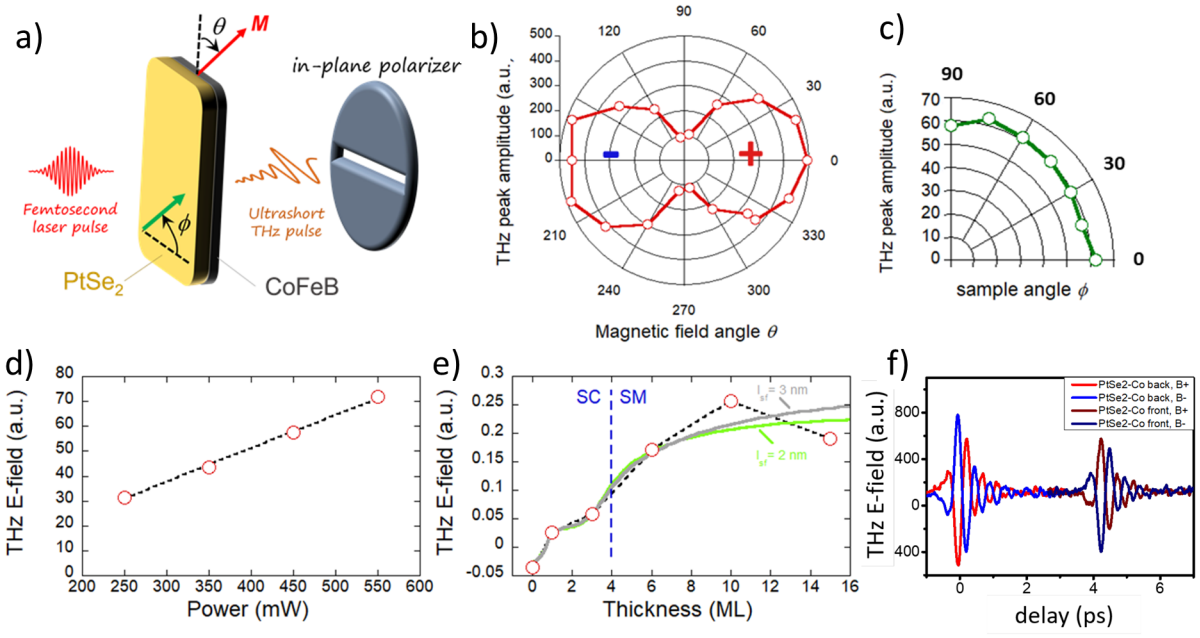

Figure 3.10: Study of the nature of the detected THz pulse. a) Geometry of the measurement, a horizontal analyzer is used to filter out the THz component originating from SCC, modulating the magnetic field direction θ alters the polarization of the emitted THz pulse. It is also possible to rotate the sample around the surface normal by an angle ϕ and b) result of the full magnetic field-angle dependence of the THz pulse, confirming the expected dipolar emission , c) magnetic field direction is fixed and the THz emission is recorded as a function of the sample angle. Rotating the sample, (ϕ), showing no crystal direction dependence of the emission. d) laser power dependence confirming the SCC as the mechanism of THz emission. e) $PtSe_2$ thickness dependence of the THz signal with a two-step-like feature (after normalization by the laser absorption and the THz emission from the CoFeB/5 nm Pt sample), f) THz emission by SCC from AlO_x/3 nm of Co (e-beam evaporated)/10 ML of $PtSe_2$ showing the same result as in with CoFeB instead Co. Adapted from Abdukayumov et al [4].

The THz electric field, E, emitted by SCC conversion should obey the geometry given by $E \propto \mathbf{M} \times \sigma$, $\mathbf{M}$ and σ being the magnetization and spin vectors. Thus, it is imperative to establish if the electric field is polarized. For this we put an in-plane analyzer before the detector in Fig. 3.10 a only passes through the electric field component obeying the geometry. Fixing the analyser while rotating the external magnetic field by θ (θ(B+)=0° and θ(B-)=180°), thus rotating the polarization of the electric field shown in Fig.3.10 b establishes the dipolar nature of the emission. In this figure, the measured voltage is proportional to the absolute value of the electric field and the right lobe is taken to be positive while the left one is negative, giving rise to a typical dipolar emission defined by a $cos(\theta)$ dependence. Now, all the geometrical studies

of the THz emission point towards SCC as the mechanism responsible for the emission, the next step is to study any crystal orientation dependence. While fixing the external field direction, the sample is rotated, by ϕ, (due to easy plane anisotropy of CoFeB, the in-plane magnetization follows easily the applied field) that shows no dependence on the crystal orientation, in other words, an isotropic emission, as shown in Fig. 3.10 c. Note that the 1T structure is six-fold symmetric. Finally, the laser power dependence of the THz field was linear (average E is shown which is equal to $(|E_{B+}| + |E_{B-}|)/2$) as expected for SCC to be responsible for the THz emission.

3.3.1 Thickness dependence of THz signal amplitude

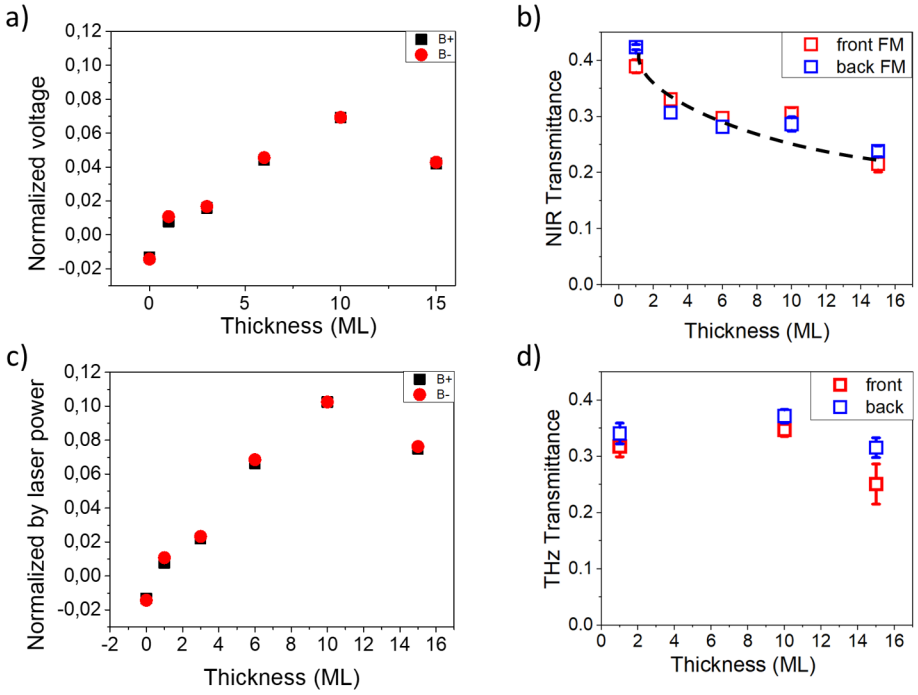

Figure 3.11: Normalization of the THz signal from AlO_x/CoFeB/$PtSe_2$ for various thicknesses of $PtSe_2$. a) as-measured emitted THz signal. The absolute values are given for B+ and B-. b) NIR transmittance of the AlO_x/CoFeB/$PtSe_2$ samples to normalize the NIR power absorbed by the FM layer: an assumption was made that A=1-T, where A is the absorbance and T is the transmittance and the maximum power absorbed by FM corresponds to the 1 ML $PtSe_2$ sample, and the decrease in transmittance is assigned to the absorption by $PtSe_2$, hence, decreasing the laser power reaching the FM layer. The dashed line is a guide for the eye. c) The normalized figure of a by the NIR absorption by the FM calculated using the data points in b. THz transmittance for various $PtSe_2$ thicknesses shows a constant behaviour, for this reason, we did not consider THz absorption in the normalization. Adapted from Abdukayumov et al [4].

After establishing the SCC origin of the THz emission in CoFeB/$PtSe_2$ heterostructures, we investigate the nature of SCC. For this, we conducted thickness dependent measurements as shown in Fig. 3.10e. In this experiment, we used 100 fs laser pulses and pumping from the substrate side as higher THz voltage was measured in this configuration than the one pumped from the FM side, possibly due to THz absorption by the substrate. The electric field polarity was opposite in the reference sample to that of CoFeB/$PtSe_2$, justifying the negative electric field for 0 ML $PtSe_2$ in Fig.3.10e.

The injected spin current from the FM to the TMD dependens on the absorbed laser power. Thus, in

order to obtain an accurate estimate of the thickness dependence of the emitted THz radiation, we need to normalize the emission by the absorbed laser power. The $PtSe_2$ thickness dependence of the THz emission is presented in Fig. 3.11 a, showing a maximum at 10 ML of $PtSe_2$. Fig. 3.11 b shows the transmittance of NIR light for AlO_x/CoFeB/$PtSe_2$ samples with varying thickness of $PtSe_2$ in the configuration of pumping from the front (red squares) and back (blue squares). To normalize the results presented in Fig. 3.11 a, we assumed that A=1-T, where A is the absorbance and T is the transmittance and the maximum amount of laser power absorbed by the FM layer corresponds to the sample with 1 ML $PtSe_2$. The decrease in the transmittance of NIR as the thickness increases corresponds to the absorption by the TMD layers, hence, decreasing the laser power reaching to the FM. This is summarized in 3.1. Applying this correction on Fig. 3.11 a, we obtain Fig. 3.11 c where we see an increased THz signal. The transmittance of the THz electro-magnetic radiation in the range of 0.7-3 THz does not show as strong $PtSe_2$ thickness dependence, thus the absorption of THz radiation was not included in the final normalization of the emitted THz signal.

$PtSe_2$ **thickness, ML**	**Laser transmittance**	**Laser power fraction absorbed by FM**
1	0.434	1
3	0.307	0.72
6	0.282	0.665
10	0.286	0.676
15	0.238	0.562

Table 3.1: Transmittance of NIR laser and the absorbed power fraction for the five samples. Adapted from Abdukayumov et al [4].

Fig. 3.10 e displays the normalized (with respect to the laser power absorption and the emission from CoFeB/5 nm Pt) THz voltage values taking the laser power and THz waves absorption into account. The thickness dependence of the THz voltage shows two steps: the first one is from 0 ML (i.e. the reference sample) to 1 ML, the second is after 3 ML. The band structure of $PtSe_2$ evolves with its thickness: starting from a semiconductor for 1 ML, the bandgap gradually decreases with the increasing thickness. The bandgap closes between 3 and 4 ML $PtSe_2$ and becomes semimetallic. This was previously shown experimentally, also our vdP measurements are in agreement with this observation as presented in the previous section. The second step coincides with this transition. In the thick and semimetallic regime, ISHE can give rise to SCC as there are states at the Fermi level and $PtSe_2$ exhibits strong SOC. Another effect that can give rise to SCC is IREE in the regime. Following the STM/STS results, there exists a charge transfer from graphene to $PtSe_2$ monoloyer that creates an out-of-plane electric field. In the semimetallic regime, this electric field is screened, hence cannot affect the layers more than a couple of ML thick.

3.3.2 SCC measured by FMR techniques

FMR is a well-established technique to study SCC in FM/SOC material heterostructures. In this sections, I present SCC measurements conducted by spin pumping FMR and broadband FMR on AlO_x/CoFeB/10 ML $PtSe_2$, AlO_x/CoFeB/5 nm Pt, and AlO_x/CoFeB (all were deposited on graphene/SiC) samples. Only the first two samples were measured by spin pumping FMR and all were measured by broadband FMR.

Spin pumping FMR

Spin pumping FMR measures a DC voltage in the sample, under optimized conditions, mostly originating from SCC in the SOC material. This voltage is proportional to the strength of the excited and then injected spins from the FM to the SOC material, for this reason, the DC voltage shows a Lorentzian shape as a function

of the applied field, as described in Chapter 1. Due to the geometrical relation between the magnetization direction, spin polarization of the injected spin current, and then the converted charge current, the reversal of the magnetization direction, reverses the direction of the charge current. This means that the Lorentzian shape of the measured DC voltage (as a function of the applied magnetic field) reverses if SCC conversion is the sole cause of the DC voltage. On the other hand, there could be other contributions as well, for example, anomalous Nernst effect [130], or spin Seebeck effect [131].

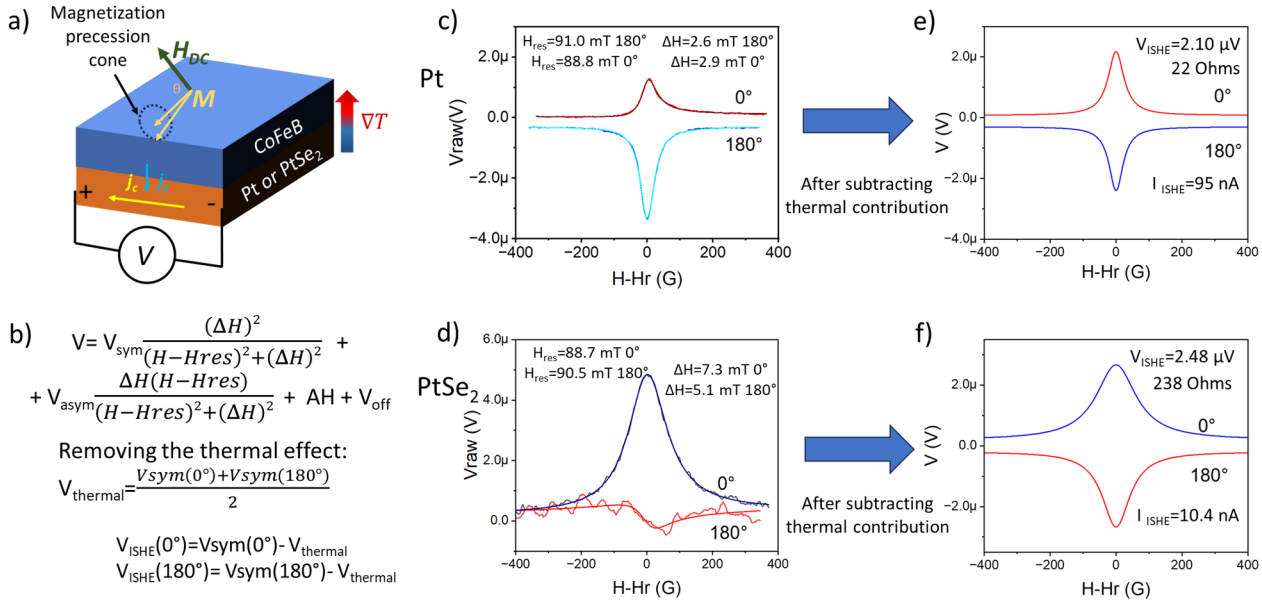

Figure 3.12: a) Sketch of SP-FMR on b) equation of measured DC voltage that is made up of symmetric, V_{sym}, asymmetric, V_{asym}, and linear, A, components, and an offset, V_{off}. Moreover, how to disentangle thermal contributions in V_{sym}. c) 15 nm CoFeB/5 nm Pt and d) 15 nm CoFeB/10 ML $PtSe_2$. The raw signals in c and d contain thermal effects that is even in magnetic field direction, compared to V_{ISHE} which is odd in the magnetic field direction. The thermal contribution was subtracted from the raw signals and V_{ISHE} was extracted in e and f for the figures in c and d, respectively. Adapted from Abdukayumov et al[4].

As shown in Fig. 3.12 a, the thermal gradient is perpendicular to the sample surface and independent of the applied magnetic field direction. Fig. 3.12 b summarizes the necessary equations to disentangle the contributions from SCC and thermal effects. The first equation:

$$V_{DC} = V_{sym}\frac{(\Delta H)^2}{(H-H_{res})^2+(\Delta H)^2} + V_{asym}\frac{(\Delta H)(H-H_{res})}{(H-H_{res})^2+(\Delta H)^2} + AH + V_{off} \tag{3.2}$$

includes a symmetric, V_{sym}, and an asymmetric, V_{asym}, Lorentzian contributions, a linear contribution with the slope equal to A, and an offset voltage, V_{off}. Using this equation, the obtained DC voltage from CoFeB/5 nm Pt and CoFeB/10 ML $PtSe_2$ samples for magnetic field directions of θ=0° and θ=180° were fitted, (see Fig. 3.12 c and d). Only the symmetric contributions are of interest for SCC studies. As the thermal contributions are independent of the apllied magentic field direction, we can estimate it using the equation:

$$V_{thermal} = \frac{V_{sym}(0)+V_{sym}(180)}{2} \tag{3.3}$$

Then, to extract the spin pumping voltage originating from ISHE, V_{ISHE}, $V_{sp}(\theta)$, $V_{thermal}$ was subtracted

and we obtained the results shown in Fig. 3.12 e and f: 2.10 μV for the Pt sample and 2.48 μV for the $PtSe_2$ samples. Although, the voltages are very similar, the former sample has an electrical resistance of 22 Ohms, while the latter has 238 Ohms, which represents an order of magnitude difference. This makes the generated charge current in the Pt 10 times larger than in $PtSe_2$, 95 nA vs 10.4 nA. On the other hand, the FWHM of the $PtSe_2$ spectrum is larger than that of Pt, not necessarily attributed to larger conversion, but just larger damping. Probably, there is larger spin-memory loss at the $PtSe_2$/CoFeB interface.

Broadband FMR

Broadband FMR measurements, in the 4-22 GHz frequency range, allow to estimate the damping parameter, α, in FM/SOC material heterostructures. The measurements were performed on a microstripline at room temperature with the sample directly in contact with the stripline, as depicted in Fig. 3.13 a. A typical spectrum is presented in Fig. 3.13 b for the sample with $PtSe_2$. The resonance fields at a given microwave frequency are plotted in Fig. 3.13 c, and Fig. 3.13 d summarizes the peak-to-peak bandwidths as a function of the frequency for the three samples.

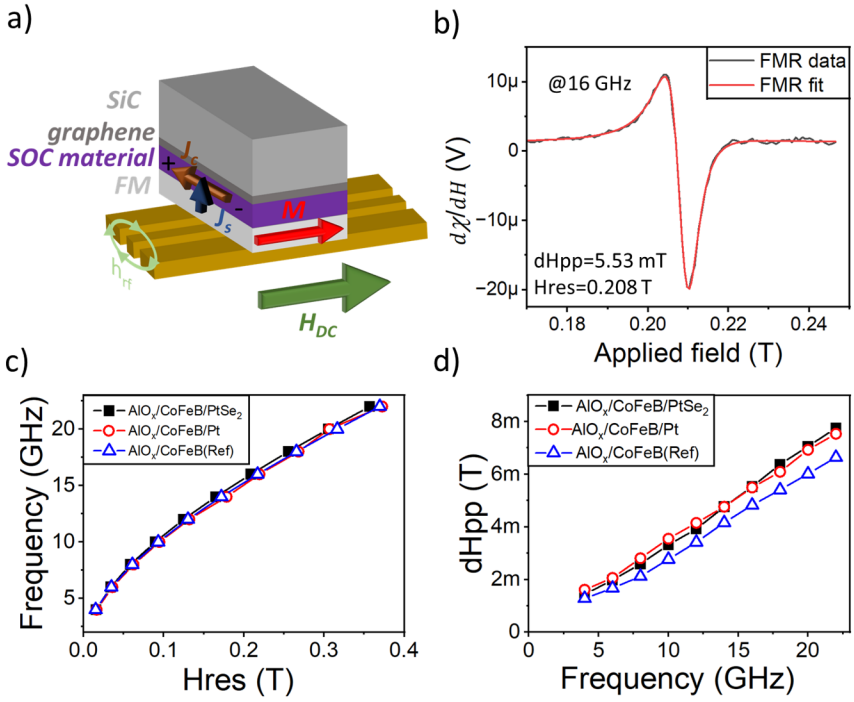

Figure 3.13: Results obtained from broadband FMR. a) the measurement geometry with the sample on top of the co-planar waveguide,) an exemplary linashape of the raw data and the corresponding fit. Dependence of c) resonance magnetic field of the FM and d) the dHpp on the applied microwave frequency.

The plot in Fig. 3.13c) can be fitted with the Kittel equation [132]:

$$f = \frac{\gamma}{2\pi}\sqrt{H_{res}(H_{res}+4\pi M_{eff})} \tag{3.4}$$

f is the microwave frequency, γ is the gyromagnetic ratio, and M_{eff} is the effective magnetization. The slope of the ΔH_{pp} vs Frequency plot in Fig. 3.13d) is directly proportional to the damping parameter, α, via the following equation:

$$\Delta H_{pp} = \Delta H_o + \frac{4\pi}{\sqrt{3}\gamma}\alpha f \tag{3.5}$$

ΔH_o is the inhomogeneous broadening. Thus, we can fit the data and extract the slopes for the three samples, which were $3.60 \times 10^{-4} \pm 6.60 \times 10^{-6}$ for AlO_x/CoFeB/10 ML $PtSe_2$, $3.34 \times 10^{-4} \pm 4.22 \times 10^{-6}$ for AlO_x/CoFeB/5 nm Pt, and $3.09 \times 10^{-4} \pm 6.66 \times 10^{-6}$ for AlO_x/CoFeB. The slope is the largest for the first sample, qualitatively in agreement with the spin pumping results presented above.

3.3.3 Modeling the thickness dependent behaviour of THz emission: IREE to ISHE transition

Starting from the assumption that the two-step function of Fig. 3.10e corresponds to the occurrence of two different SCC mechanisms, a simple spin diffusion model was developed to fit the data. Firstly, it was assumed that all the spin current generated by laser excitation is entirely absorbed in the $PtSe_2$ layer (i.e. in the spin sink model). The equations to describe the spin current $j_s(z)$ at a depth z (from the interface of CoFeB/$PtSe_2$) and the layer integrated spin current in $PtSe_2$, $J_N(d_N)$ are given by:

$$\begin{aligned} \frac{j_s(z)}{j_s(0)} &= e^{-\frac{z}{\lambda_s}} \\ \frac{J_N(d_N)}{j_s(0)} &= \int_0^{d_N} \frac{j_s(z)}{j_s(0)} dz = \lambda_s(1 - e^{-\frac{d_N}{\lambda_s}}) \end{aligned} \tag{3.6}$$

d_N being the thickness of $PtSe_2$, λ_s the spin diffusion length in $PtSe_2$, j_{s0} the spin current at the interface of CoFeB/$PtSe_2$, θ_N the spin Hall angle of $PtSe_2$, θ_I the spin Hall angle at the $PtSe_2$/graphene interface. Figures 3.14 a and 3.14 b represent the profile of $j_s(z)$ for 1 ML (or semiconducting) and 10 ML (or semimetallic) $PtSe_2$, respectively. We can write down the total generated charge current by the interface (IREE) and bulk (ISHE) with: $I_c = H(z - d_N^I)\theta_I j_s(d_N) d_N^I + H(z - d_N^C)\theta_N J_N(d_N)$ with H being a step function and d_N^I and d_N^C the $PtSe_2$ thickness at which IREE and ISHE arises, respectively. We can then define the inverse Rashba-Edelstein length for this model as $\lambda_{IREE} = \theta_I d_N^I$, assuming θ_I is independent on d_N. From the best fits to the thickness dependence in Fig. 3.10 e, we extracted the following results: d_N^I=0.35 nm, d_N^C=1.7 nm, λ_s is in between 2 and 3 nm (green and grey fitted curves in Fig. 3.14b) and, finally, $\frac{\theta_I}{\theta_N} \approx 2$. d_N^I is comparable to 1 ML $PtSe_2$, as expected for IREE, and d_N^C falls in between 3 ML and 4 ML, corresponding to the semiconducting-to-semimetallic transition in $PtSe_2$, as expected for the onset of ISHE. The calculated spin diffusion length is in between 2 nm and 3 nm which corresponds to 4 ML and 6 ML of $PtSe_2$. The equivalent Pt thickness in this amount of $PtSe_2$ is around 0.65 nm and 0.975 nm meaning that the spin flip rate along the normal to the film plane is larger in $PtSe_2$ than in Pt. This results highlights the spin diffusion that flows along the surface normal in layered materials, thus the role of the van der Waals gap has to be considered, which demands additional theoretical studies that was beyond the study in focus. The final important result is that IREE and ISHE have the same sign with IREE being twice as efficient as ISHE.

Unlike spin pumping by FMR, it is not as straightforward to extract the absolute value of the spin Hall angle θ_{SH} by THz-TDS. To do so, we compare the THz signal from $PtSe_2$ with the one of Pt: a well-known SCC material, under identical conditions (pumping from the substrate side in the transmission mode). Fig. 3.9 b shows that the peak-to-peak amplitude of the THz signal from 5 nm Pt/3 nm CoFeB sample is slightly more than 7 times stronger than 10 ML $PtSe_2$/ 3 nm CoFeB sample. When the absorption length of the laser at 800 nm is taken into account (10 nm for Pt [133] and 5 nm for $PtSe_2$ [134],[135]), we can derive the ratio $\theta_{SH}(Pt)/\theta_{SH}(PtSe_2) \approx 3.5$. However, Fig. 3.12 shows the ISHE current is almost 9 times larger

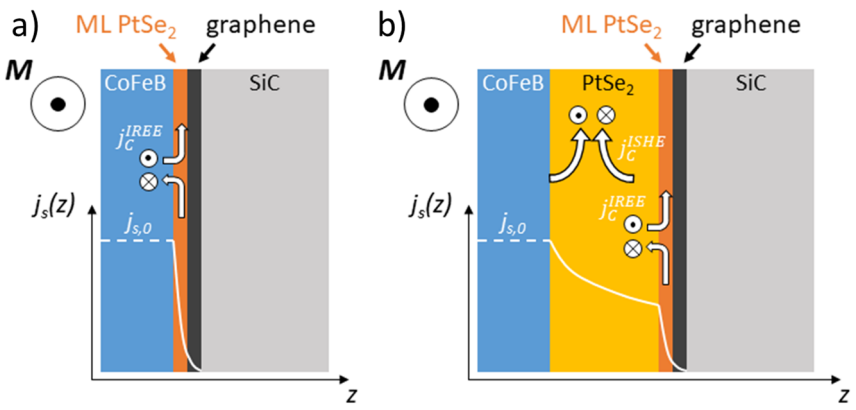

Figure 3.14: Spin-charge conversion mechanism sketched for semiconducting (1-3 ML) and semimetallic (more than 3 ML) $PtSe_2$, arising from IREE and IREE+ISHE, respectively. $j_z(z)$ represents the spin current profile (white curve) and $j_s(0)$ the amount of injected spin current from CoFeB after the optical excitation. Adapted from Abdukayumov et al [4].

for Pt than for $PtSe_2$. This difference between the ratios obtained by two different measurement techniques can be explained with the energy levels they probe: THz-TDS is based on the injection of hot electrons with a maximum energy corresponding to the laser one, moreover, due to thermalisation processes in the FM, carriers with varying energies (in the energy window defined by the photon energy) are injected as well. On the other side, spin pumping by FMR probes states at the Fermi level, and are not sensitive to states with probably stronger Rashba SOC. Another explanation can be the transparency of the Co/Pt interface for the majority electrons that decreases above the Fermi level [73]. With the assumption of $\theta_{SH}(Pt) \approx 10\%$, we can estimate $\theta_{SH}(PtSe_2) \approx 3\%$, and with the fitting parameters obtained from the thickness dependence of the spintronic THz signal, the estimated value of the inverse Rashba-Edelstein length, $\lambda_{IREE}(PtSe_2)$, is around 20 pm. This is a low value which can be detected by THz-TDS.

3.4 ab-initio calculations

In order to support our interpretation and understand the mechanisms behind the spintronic THz emission, Fatima Ibrahim, Libor Vojacek, and Mairbek Chshiev of the Theory and Simulation team at SPINTEC conducted first principles calculations using the projector-augmented wave (PAW) method. These calculations were performed with the VASP package [136],[137], [138], employing the Perdew-Burke-Ernzerhof (PBE)[139] generalized gradient approximation and including spin-orbit coupling.

It should be noted that our calculations, which go beyond standard density functional theory (DFT) with the generalized gradient PBE approximation, underestimate the band gap of monolayer $PtSe_2$ by approximately 0.5 eV compared to experimental values. However, recent research by Guan et al. [140] has shown that using the PBE and HSE06 hybrid functionals to calculate the band structure of the 1 ML $PtSe_2$/Gr heterostructure results in a shift of the $PtSe_2$ valence bands by around -0.5 eV, with minimal impact on the conduction bands. This suggests that the use of hybrid functionals primarily causes a "rigid-band" shift without significantly affecting the character of the $PtSe_2$ bands. Consequently, while the number of bands within a specific energy window may change, the Rashba splittings induced by spin-orbit interaction remain intact. We have confirmed this through spin-projected band structure calculations of the 1 ML $PtSe_2$/Gr system using both PBE and HSE06 functionals, as shown in Fig. 3.15. The spin texture remains remarkably similar, with only the aforementioned -0.5 eV shift in the valence bands. Therefore, we believe that PBE functionals

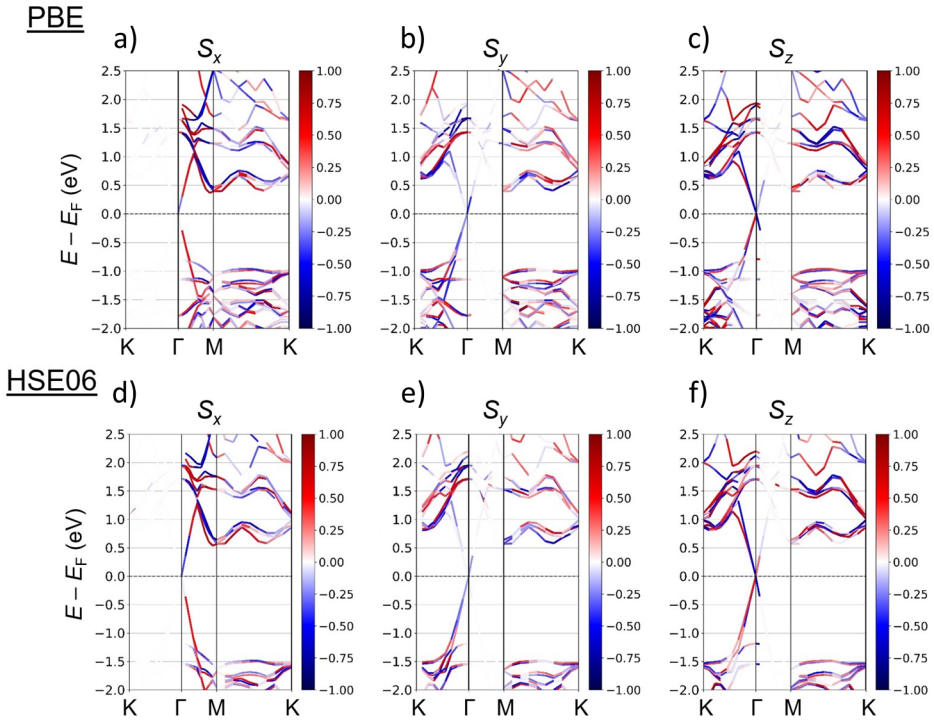

Figure 3.15: Comparison of PBE and HSE06 methods to calculate the band structure of $PtSe_2$/graphene heterostructure in a, b, c) and d, e, f), respectively. a) and d) for the *x*-axis, b) and e) for the *y*-axis, c) and f) for the *z*-axis. The overall features of the band structures calculated by the two methods look very similar with the same spin texture. Differences are in the width of the band gap, closer to the experimental observation, and larger group velocity in graphene, compared to PBE. Adapted from Abdukayumov et al [4].

provide reliable spin textures and Rashba splittings at the $PtSe_2$/Gr interface.

The $PtSe_2$/Gr heterostructure was constructed by matching a 2×2 supercell of 1T-$PtSe_2$ with a 3×3 supercell of graphene, minimizing the lattice mismatch to less than 1.5%. A vacuum layer with a thickness of 20 Å was included. The atomic coordinates were relaxed until the forces reached a magnitude smaller than 1 meV/Å. A kinetic energy cutoff of 550 eV was utilized for the plane-wave basis set, and a Γ-centered 15×15×1 k-mesh was employed to sample the first Brillouin zone. To accurately describe the interaction across the interface, van der Waals forces were incorporated using the Grimme type dispersion-corrected density functional theory-D2 method [141]. Two-dimensional spin textures were calculated using a 10×10 Γ-centered 2D k-mesh, and the PyProcar package was employed for plotting purposes [142].

We can see in Figures 3.16a and 3.16d the differences in the band structure of freestanding $PtSe_2$ and $PtSe_2$/graphene heterostructure. The relaxed interlayer distance between $PtSe_2$ and graphene is estimated to be around 3.29 Å, and induces a charge transfer across the interface, as shown by the charge clouds in the inset of Fig. 3.16d. The amount of charge transfer is calculated to be around 0.04 e from the graphene to $PtSe_2$, a rather small value and it is consistent with the vdW interaction type. This is also supported by the preserved band features of $PtSe_2$ and graphene even after they form the heterostructure, in agreement with previous theoretical findings [143]. The next step is to assess the supposed Rashba effect at the interface of $PtSe_2$/graphene. Thus the calculated spin textures of the free standing monolayer $PtSe_2$ and $PtSe_2$/graphene are compared with two of their representive bands in the CB and VB, emphasized in blue and red, in Fig. 3.16 a and d, respectively. At constant energies in the CB and VB of the freestanding $PtSe_2$ monolayer, the corresponding spin textures show the two opposite, but degenerate contours. This was expected from

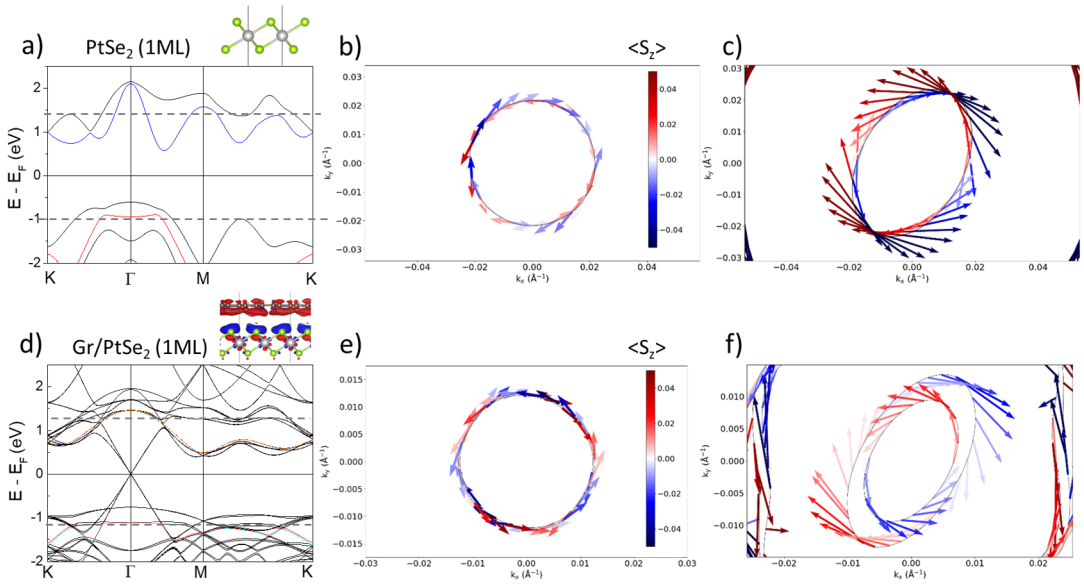

Figure 3.16: Calculated band structures of a) free-standing $PtSe_2$ including spin-orbit coupling, the grey (green) balls represent Pt (Se) atoms . The most representative bands in CB (blue) and VB (red) are selected to calculate their spin textures in b ($E = E_F + 1.4$ eV) and c ($E = E_F - 1$ eV) for the free-standing $PtSe_2$. The arrows represent the S_x and S_y projections, and the color code represents the S_z component. d) Calculated band structures of the $PtSe_2$/graphene heterostructure including spin-orbit coupling. The charge transfer from graphene to $PtSe_2$ is presented as the charge depletion in red and accumulation in blue. The most representative bands in CB (blue) and VB (red) are selected to calculate their spin textures e ($E = E_F + 1.25$ eV) and f ($E = E_F - 1.1$ eV) for the heterostructure, a Rashba splitting is observed in the VB. Adapted from Abdukayumov et al [4].

the absence of any inversion symmetry breaking in this structure. Therefore, in this regard the earlier experimentally reported spin textures [124],[105] in $PtSe_2$ can be attributed to the interfacial electrical field. Graphene-interfaced $PtSe_2$ has now broken inversion symmetry coming from the interface electric dipole which in turn induces a Rashba splitting of the bands, as presented in Fig. 3.16 e and f. The band splitting is larger in the VB compared to that in the CB, with an estimated Rashba splitting of $\alpha_R \approx$-195 meV.Å. This can be explained by the orbital character that is mainly contributed by the p-orbitals of Se. On the other hand, CB is dominated by Pt d-orbitals and regardless of the fact that Pt has larger spin-orbit strength, Se atoms are positioned at the interface and more affected by the interfacial dipole effect. SCC in the VB of transition metals is often neglected as the hole velocity is small, however, in the current system it plays a crucial role and certainly the first step in the thickness dependence of spintronic THz emission comes from IREE in the valence bands. It is not easy to estimate the fraction of hot holes that can reach this band due to the lack of knowledge on the exact position of the Fermi level as CoFeB deposition on top is expected to alter it. Now, if we discuss the origin of ISHE in the semimetallic regime, it can be of either intrinsic or extrinsic origin, it is not possible to conclude at this point as more calculations are required. However, regarding 3 ML $PtSe_2$, we observe avoided band crossings in the VB in Fig. 3.17b (highlighted by grey discs) which are hot spots for the Berry curvature and could be at the origin of large intrinsic ISHE.

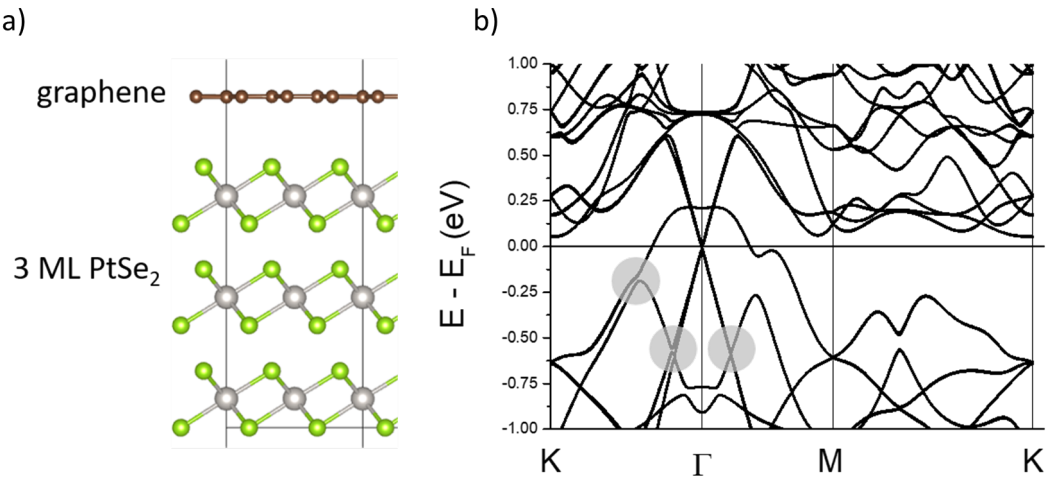

Figure 3.17: Band structure calculation of 3 ML $PtSe_2$/ graphene heterostructure. a) graphical presentation of the heterostructure and b) the calculated band structure with three grey discs pointing out avoidance of the band crossings that would contribute to the intrinsic spin Hall effect. Adapted from Abdukayumov et al [4].

3.5 Conclusion

In summary, in this chapter, I presented the SCC in three-distinct CoFeB/TMD heterostructures probed by THz-TDS. CoFeB/VSe_2 and CoFeB/WSe_2 heterostructures did not show additional THz emission to AlO_x/CoFeB reference sample, only CoFeB/$PtSe_2$ showed enhanced THz emission. All the geometrical dependences for SCC mechanism as the source of the THz emission were satisfied and the $PtSe_2$-thickness dependence showed a two-step evolution. This can be explained by the thickness-dependent band structure of $PtSe_2$: for 1-3 ML it is a semiconductor with a bandgap of around 2.0 eV (for 1 ML $PtSe_2$), as the thickness increases the bandgap closes and it becomes a semimetal between 3 ML and 4 ML. This was also indeed reflected in the spintronic THz emission mechanisms: for the first 3 ML IREE is responsible for SCC and the Rashba spin structure was created by the charge transfer from graphene to $PtSe_2$. In the semimetallic regime, the transferred charge is screened and the importance IREE in SCC diminishes; now the responsible mechanism for SCC is suggested to be ISHE. Due to the avoided of band crossings in 3 ML $PtSe_2$, ISHE is probably of intrinsic nature due to strong Berry curvature. The unique band structure evolution of $PtSe_2$ makes it a good candidate for the fundamental spintronics research, for example by gating to access deeper levels with possibly stronger Rashba splitting.

Chapter 4

Inverse Rashba-Edelstein effect in $PtSe_2$-$MoSe_2$ bilayer

4.0.1 Introduction and Motivation

As discussed in the previous chapter, $PtSe_2$ has an in-plane spin texture when the inversion symmetry is broken and exceptional degree of interlayer coupling and can be used in heterostructures to obtain materials with new physical properties. Using first principles calculations Xiang et al [5] predicted that the 1 ML $PtSe_2$/1 ML $MoSe_2$ bilayer should host a giant Rashba-type spin splitting. The reported value of spin-splitting around the Γ point was 110 meV at the momentum offset of k_0=0.23 Å^{-1} due to the strong interfacial spin-orbit coupling caused by the hybridization of the transition metal diselenides. $MoSe_2$ has a peculiar thickness dependence of the band structure that in 1 ML it has a direct band gap of $\approx$2.15 eV [144] with out-of-plane oriented spins at K-points in the Brillouin zone [145] and in 2 ML the band gap is indirect and experimentally observed to be $\approx$1.58 eV and the spin-splitting vanishes with no more out-of-plane spin texture due to restored inversion symmetry in the 2H stacking [145].

Xiang et al performed the calculations using the density functional theory (DFT) with the PAW method implemented in VASP. They first present the band structures of 1 ML $MoSe_2$ and 1 ML $PtSe_2$ with (green) and without (purple) SOC in Fig. 4.1 a and b, with the Fermi level assigned at the VBM, showing direct and indirect bandgaps, respectively. Since $MoSe_2$ exhibits inversion symmetry breaking and $PtSe_2$ does not, the bands with SOC are spin-split in $MoSe_2$, but not in $PtSe_2$ along the the path M-K- Γ. Finally, since the interaction between $MoSe_2$ and $PtSe_2$ is van der Waals, which is weaker than, for example, covalent bonding, the band structure of the bilayer should exhibit the main features as the one of the pristine constituent layers, as shown in Fig 4.1 c. In this heterostructure, one can see the indirect band gap of around 0.9 eV with SOC. Moreover, the heterostructure preserves the spin-splitting of 181 meV at the K points originating from $MoSe_2$, though slightly reduced from 186 meV in Fig. 4.1 a.

The most interesting additional feature of this heterostructure is the emergence of spin splitting around the Γ point, which is absent in $MoSe_2$ and $PtSe_2$. In order to understand the origins of this spin splitting, Xiang et al investigate the layer projected band structure for $MoSe_2$ (red) and $PtSe_2$ (blue). They find a hybridization of the two constituent monolayers at the valence band edge (VBE) in the vicinity of the Γ point. This hybridization is mostly contributed by Mo-d orbitals in $MoSe_2$ and Se-p orbitals in $PtSe_2$, unlike reported in the previous studies on $MoSe_2$/MoS_2 that was mainly due to the Mo-d orbitals. The plotted charge densities in Fig. 4.1 e-g help to understand the details of the bands around the Γ point. For pristine $MoSe_2$ (Fig. 4.1 e) and $PtSe_2$ (Fig. 4.1 f) the charge density around the Γ point is equally contributed by the top and bottom Se layers, thus, the total vertical electric field acting on the electrons vanishes and a spin splitting due to the Rashba effect is not expected. In the case of the $PtSe_2$/$MoSe_2$ heterostructure in Fig.

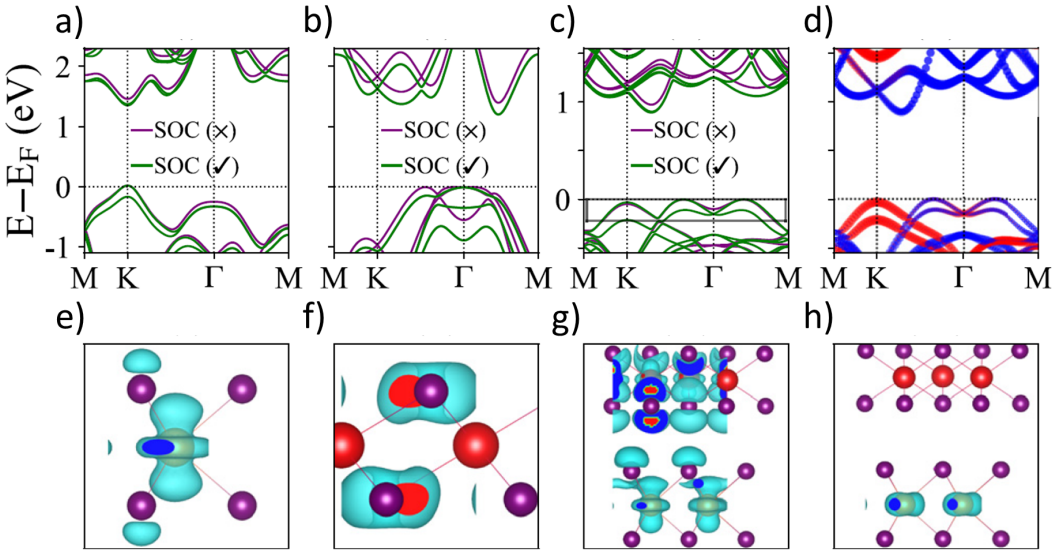

Figure 4.1: Calculated band structures of a) 1 ML $MoSe_2$, b) 1 ML $PtSe_2$, and c) 1 ML $PtSe_2$/1 ML $MoSe_2$ with (green) and without (purple) SOC; d) projected bands where blue (red) shows the contribution from $PtSe_2$ ($MoSe_2$). The charge densities at the VBE are shown in e-g) around the Γ point corresponding to the band structures shown in a-c) respectively. h) corresponds to the charge densities at the K point of the $PtSe_2$/$MoSe_2$ bilayer. Adapted from Xiang et al [**?**].

4.1 g, the charge density, mostly coming from Mo-d_{z^2} in $MoSe_2$ and Se-p_z in $PtSe_2$, is asymmetric due to the interlayer hybridization, inducing an effective vertical electric field leading to strong interfacial SOC. On the other hand, at the *K*-point, the hybridization between the layers is negligible and Mo-d_{xy/x^2-y^2} orbitals contribute the most, as shown in Fig. 4.1 d and h.

The zoomed-in figures of the highest energies in the valence bands of the heterostructure show in Fig. 4.2 a that the bands around the Γ point look similar to Rashba-type spin splitting, also observed at the surface of heavy metals [40]. The spin components of s_x, s_y, and s_z are calculated at constant energy cuts (blue dashed line). Figs. 4.2 b-d show that the spin polarization is mainly in-plane (s_x and s_y) with a small out-of-plane component (s_z). The inner and outer contours show identical spin textures in Figs. 4.2 b-d, which is expected for the Rashba effect. Hence, Xiang et al proposed a generalized Rashba Hamiltonian, $\mathscr{H}_{Rashba}$, to understand the band structure near the VBE around the Γ point for the energy ranging from -0.1 to 0 eV, highlighted by the red dashed line.

The shape of the VBE near the Γ point in Figs. 4.2 can be closely approximated by a parabola and the spin texture is very close to the one given by the original Rashba Hamiltonian.

$$\mathscr{H}_{Rashba}(k_{||}) = -\frac{\hbar^2 k_{||}^2}{2m} + ck_{||} + \alpha_R \sigma \cdot (\mathbf{k}_{||} \times \mathbf{z}) \tag{4.1}$$

here, the first two terms give the dispersion curve known as "mexican hat", c is the strength of spin-independent interaction with the crystal field and α_R is the strength of the Rashba-type SOC.

Based on these theoretical predictions, we study experimentally this system. We first expect to observe the spin polarized bands by spin polarized ARPES and then SCC by THz spintronic emission. As Xiang et al report the tunability of the generalized Rashba constant η_R (η_R=c+α_R, c being the strength of the spin-independent interaction with crystal field), with the position of the Fermi level, it could be studied

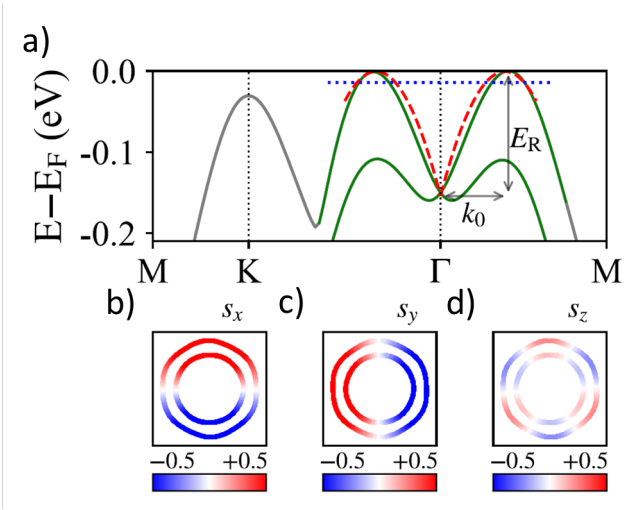

Figure 4.2: a) Zoom-in plot of the two highest valence bands around Γ point. The top one is fitted with a generalized Rashba Hamiltonian (red dashed line). b-d) at a constant energy (highlighted by the blue dotted line), spin components of the band [5].

experimentally as well, for example, by gating the system vertically.

4.1 On graphene/SiC substrate

The study was divided in two parts based on the substrate used for the epitaxy: *i*) graphene/SiC to measure the band structure by spin polarized ARPES and preliminary SCC experiments by THz-TDS, and *ii*) mica to be able to transfer the vdW layers on a SiO_2/Si to apply a gate voltage that allows to access levels with higher Rashba spin-splitting. The direct growth of TMD on SiO_2 by MBE does not give high quality crystals, the layers consist of small grains with random crystal orientation in plane. The growth and transfer of $MoSe_2$ has been well established in the 2D spintronics team, and here we also developed the transfer of $PtSe_2$/$MoSe_2$ bilayers. Moreover, ARPES measurements are not possible on mica due to its insulating character and the resulting charging effects.

4.1.1 MBE growth on graphene/SiC and characterization

The preparation of the substrate was exactly the same as described in the previous chapter and the RHEED patterns show the good crystalline quality of the layers as shown in Fig 4.3 a. The substrate was then cooled down to 340 °C to start the vdWE of $MoSe_2$ with a Mo deposition rate of 0.001875 Å/s and a Se flux of 1×10^{-6} mbar. In total, 1.2 ML of $MoSe_2$ was deposited to ensure sufficient coverage of the substrate. The crystals were mostly anisotropic, as can be seen in Fig. 4.3 b and c. Although, a nominal 1.2 ML was deposited, the substrate could still be observed in the RHEED images, this could be due to the non-layer-by-layer growth of the film. Then, the film was annealed for 20 minutes at 820 °C under a Se flux of 1×10^{-6} mbar.

After the annealing step, the sample was cooled down back to 340 °C to deposit 1.2 ML of $PtSe_2$ at a Pt deposition rate of 0.005 Å/s under a Se flux of 1×10^{-6} mbar. The growth of $PtSe_2$ was epitaxial on $MoSe_2$ as can be seen in Fig. 4.3 d showing 0.25 ML of $PtSe_2$, and the RHEED profile in Fig. 4.3 g (olive) shows the peaks corresponding to the two diselenides. The epitaxial bilayer was then annealed at 720 °C for 15 minutes under Se flux, the RHEED images of 1.2 ML $PtSe_2$ in Fig. 4.3 e ([100]) and f ([1$\bar{1}$0]), recorded

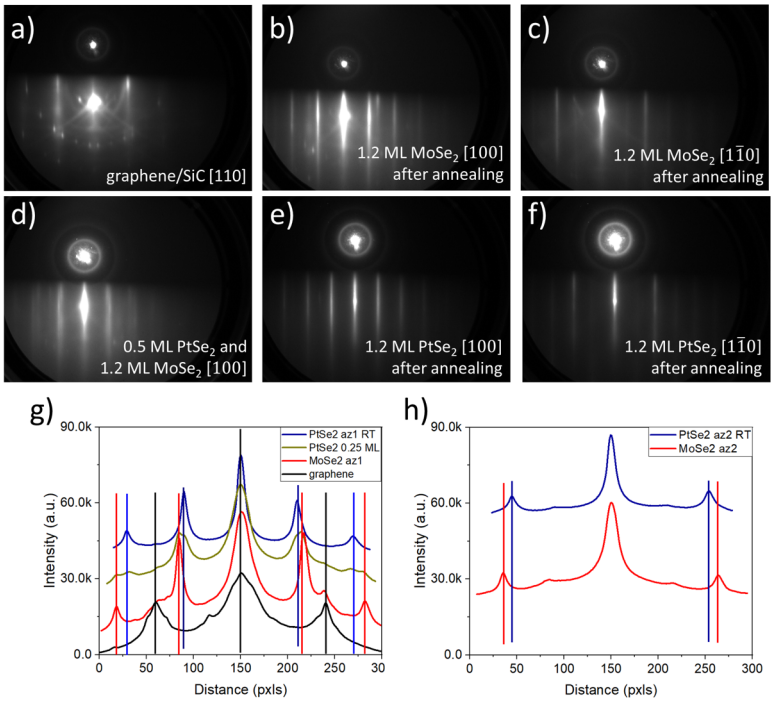

Figure 4.3: Electron diffraction of $PtSe_2$/$MoSe_2$ on graphene/SiC. RHEED pattern of a) graphene/SiC after 30 minutes at 800 °C, b) [100] and c)[1$\bar{1}$0] of nominal 1.2 ML $MoSe_2$, d) [100] of 0.5 ML $PtSe_2$ on $MoSe_2$ (recorded during the growth), e) [100] and f) [1$\bar{1}$0] of 1.2 ML $PtSe_2$ (recorded at room temperature). g) and h) profiles of the RHEED patterns in a-f along [100] and [1$\bar{1}$0] directions, respectively.

at room temperature, show the very high quality of the growth with thin rods without modulation and clear anisotropy.

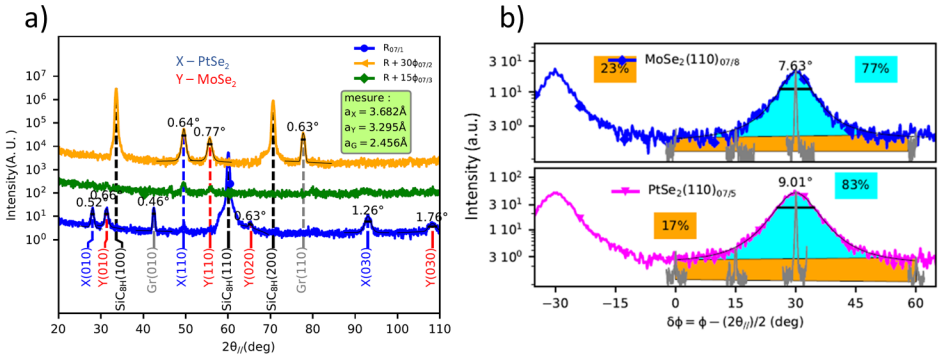

Figure 4.4: a) in-plane XRD of 1.2 ML $PtSe_2$/1.2 ML $MoSe_2$ on graphene/SiC and b) azimuthal scans of $MoSe_2$ and $PtSe_2$ at the (110) Bragg peak.

The high crystal quality of the bilayer was confirmed by in-plane XRD measurements, as presented in Fig. 4.4 a. The obtained lattice parameters of $PtSe_2$ and $MoSe_2$ are 3.682 Å and 3.295 Å, respectively, in a good agreement with the literature values [123], [146]. The FWHM of the (010) Bragg peaks of $PtSe_2$ and $MoSe_2$ being equal to 0.52° and 0.66°. The mosaic spread of the crystals was ±4.5° and ±4°. The

anisotropic part, measured on the (110) Bragg peak, was 83% and 77% for $PtSe_2$ and $MoSe_2$, respectively.

4.1.2 ARPES

To measure the bilayer band structure and study the spin polarization of the bands by spin-ARPES, a separate sample was prepared without the ferromagnetic layer. Instead, 10 nm of Se capping layer was deposited to preserve the bilayer against degradation during air transfer. The measurements were carried out by Oliver Paull, Céline Vergnaud, Matthieu Jamet, Vincent Polewzyk, and Federico Mazzola at the APE beamline of the ELETTRA synchrotron facility in Trieste, Italy.

The Se capping layer was removed by slowly heating up the sample up to 300 °C. The six-fold LEED pattern corresponding to $PtSe_2$ was obtained, indicating the complete removal of the Se cap layer. The heating was then stopped and the sample was moved to the ARPES chamber, then cooled down to 30K. ARPES was performed with a photon energy of $h\nu = 25eV$ along the $\Gamma - K$ directions. The measured band structure is shown in Fig. 4.5 a. The most important feature of this figure is the hybridized band just below the Fermi level, with the "mexican hat" spcific shape, as predicted by Xiang et al [5] and presented in Fig. 4.1 c. The spin-plarization of the bands was measured by scanning at constant angles of $\pm 8°$, $\pm 4.5°$, and $\pm\ 3°$ and recording the spin components. The obtained results were compared, as presented in Fig. 4.5 c-e, with the previous measurements of 1 ML $PtSe_2$ on Pt(111) [105] and 2ML $PtSe_2$ on graphene/SiC [124]. The bands in the 1 ML $PtSe_2$ study show the top-most band, located at around $E - E_F$ =1.5 eV, possesses counter-clockwise spin-texture around the Γ point. The band below, at around $E - E_F$ = 2eV has a clock-wise spin-texture. Those two bands with the exact same spin-textures can be recognized in the 2 ML $PtSe_2$ as well, on top of that, the ARPES data show an additional band with counter-clockwise spin-texture. As the thickness of $PtSe_2$ increases, this band later moves up closer to the Fermi level and evolves to a three-dimensional Dirac cone as in topological Dirac semimetals [124]. The previously mentioned two bands are observed in the 1 ML $PtSe_2$/1 ML $MoSe_2$ bilayer as well with the same spin-texture, and the hybridized band resembles the early stage of the Dirac cone, however, it has an opposite spin-texture near the Γ point, indicating it has a different origin than the Dirac cone.

4.1.3 THz-TDS experiments to study SCC

In order to verify the theoretical findings on the 1 ML $PtSe_2$/1 ML $MoSe_2$ bilayer structure which predicted strong Rashba-type spin-splitting, THz-TDS experiments were carried out, and compared with 1 ML $PtSe_2$ (single layer). Similar to the previous chapter, 3 nm of CoFeB and 4 nm of Al were deposited which naturally oxidizes into AlO_x. The experiments were carried in a setup that allows the modulation of the photon energy that enables probing wider energy ranges that could potentially host larger spin-split states.

The first measurement was made at the same laser wavelength as in the previous chapter, i.e. λ=800 nm (1.5 eV), then at 700 nm (1.77) and 940 nm (1.32 eV) wavelengths for both samples in the transmission mode. The sample was pumped from the substrate side as it showed stronger measured THz field in the previous chapter. As presented in Fig. 4.6 a and b, the bilayer samples shows around 3.5 times stronger THz electric field than 1 ML of $PtSe_2$ for the wavelength of 800 nm. The magnetic field angle dependence in Fig. 4.6 d-f shows no non-magnetic contribution in the THz emission. We notice that the two samples show opposite THz electric field polarities. In the previous chapter, the reference sample (AlO_x/CoFeB/graphene/SiC) had the opposite polarity to the AlO_x/CoFeB/$PtSe_2$/graphene/SiC one, and the THz emission from the reference sample was attributed to the AlO_x/CoFeB interface or self-conversion in the FM. Thus, it is important to separate the contribution from the AlO_x/CoFeB interface. However, in this set of measurements, the reference sample was not included. Looking at the results of the previous chapter,

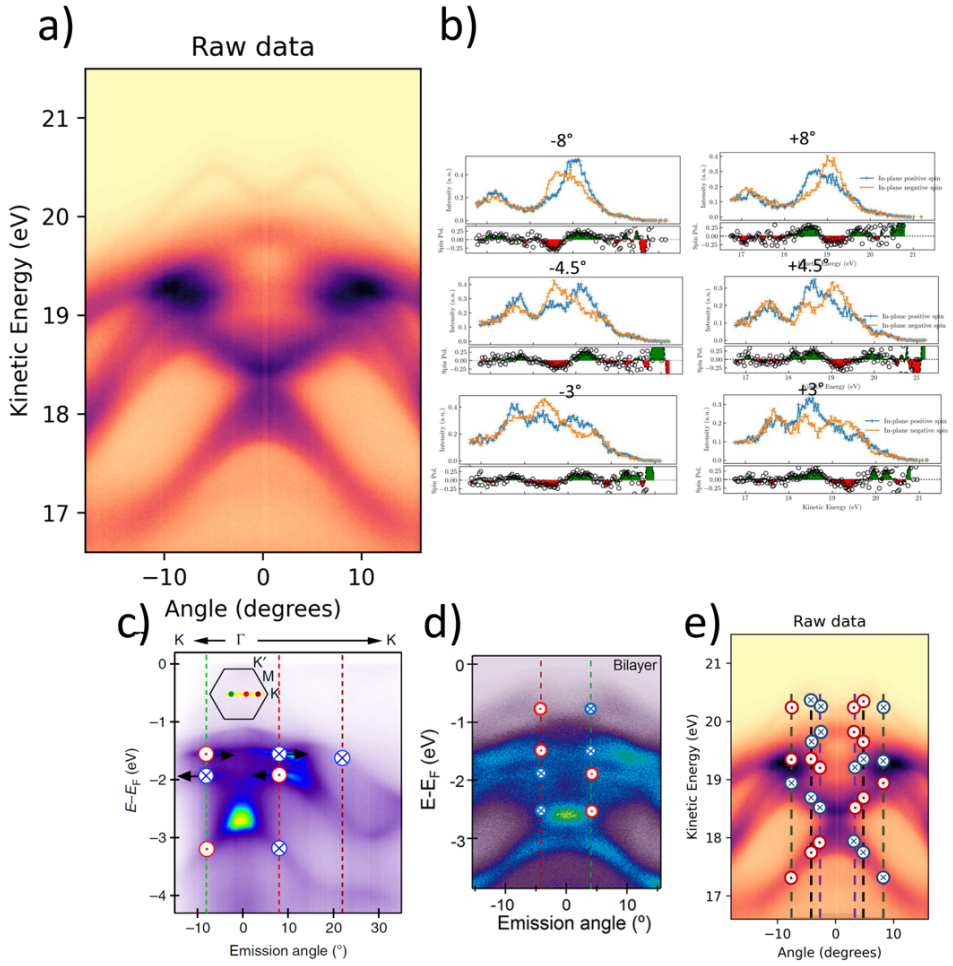

Figure 4.5: Measured band structures of a) 1.2 ML $PtSe_2$/$MoSe_2$ on graphene/SiC (b) with Energy scans at constant incidence angles of ±3°, ±4.5°, and ±8°), c) 1 ML $PtSe_2$ on Pt(111) [105] and d) 2 ML $PtSe_2$ on graphene/SiC [124], e) corresponding spin polarization extracted from b.

we obtained: $\frac{E^{THz,B+}_{1MLPtSe_2} - E^{THz,B+}_{1MLPtSe_2}}{2} / \frac{E^{THz,B+}_{ref} - E^{THz,B+}_{ref}}{2} \approx$-0.61 at λ=800 nm, and we add this data point as a blue triangle in the plot of Fig. 4.6 c.

Note that the THz voltage (normalized with respect to the Pt/Co/W spintronic trilayer THz emitter) of the bilayer sample is negative. The black double arrow shows the contribution of single layer $PtSe_2$ (with respect to the reference sample THz voltage), while the red double arrow shows the contribution from the TMD bilayer. As can be seen, it is not stronger than for the single layer sample, even 25 % less. However, we have to carefully analyze this taking into account the results obtained from spin-ARPES measurements presented in the previous paragraph. First of all, we have to address the polarity reversal in the case of the bilayer sample with respect to the single layer one. The sign reversal means the reversal of the sign of the spin Hall angle, θ_{SH}, in the case of the ISHE, and in the case of the IREE, it is due to an opposite spin texture chirality in the band structure. In Fig. 4.5 (and as discussed before) the comparison between the two band structures show that the new band appearing due to the hybridization in the bilayer has the opposite spin texture with respect to the highest valence band of the single layer. Considering the similarity of the bands at lower energy than the hybridized band, we can say that they can also contribute to the SCC in the

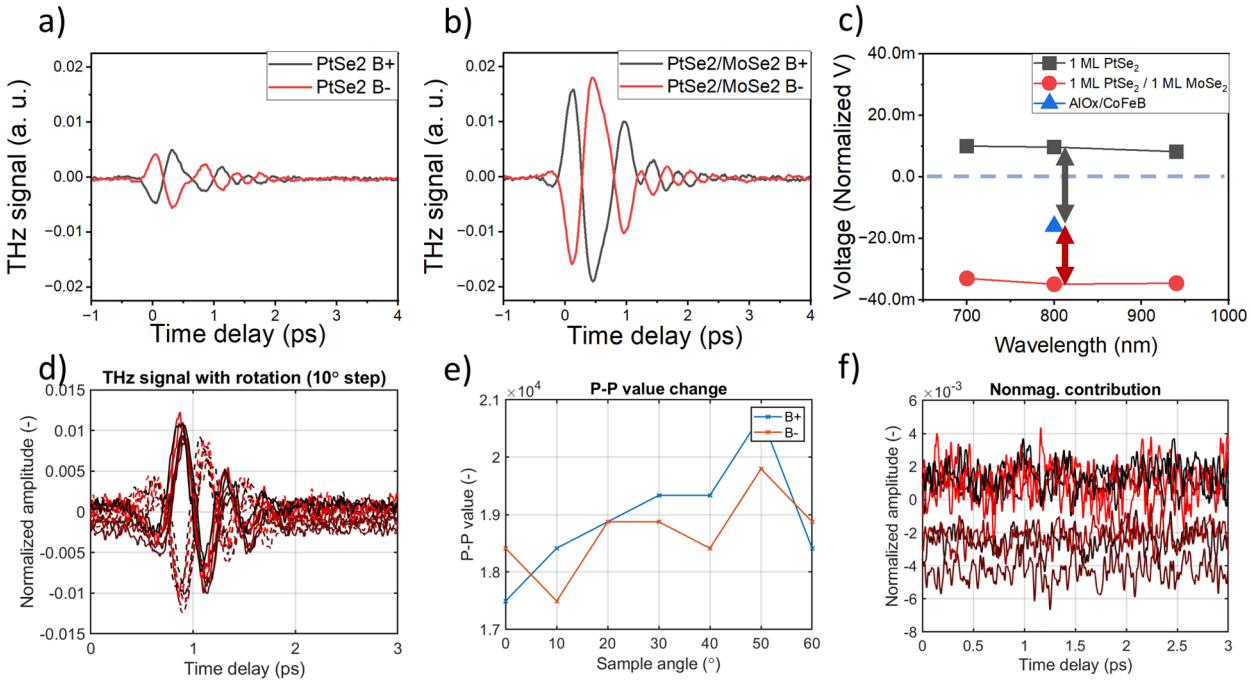

Figure 4.6: SCC studies of a) AlO_x/CoFeB/1 ML $PtSe_2$ and b)AlO_x/CoFeB/1.2 ML $PtSe_2$/1.2 ML $MoSe_2$ by THz-TDS at a photon wavelength of 800 nm. Both samples are epitaxially grown on graphene/SiC. c) photon-energy dependence of the THz signals. The blue triangle corresponds to the emission of AlO_x/CoFeB, obtained from the experiments in the previous chapter. d-f) the angular dependence experiments on b shows isotropic emission with no obvious non-magnetic contribution.

bilayer which should give equally strong THz field with the same polarity as in the case of the single layer $PtSe_2$. Therefore, the SCC by the hybridized band overrides the contribution from the single layer bands (making the total THz field of opposite sign but with smaller intensity than the single layer case). These considerations lead to a 75% stronger THz field in the case of the bilayer compared to the single layer. It means that if one could *isolate* the hybridized band in the SCC by using higher wavelength (lower photon energy), even higher THz signal would be detected. However, in the range of wavelengths we used here, we could not observe this enhancement effect, probably because the photon energy was not low enough. Another method could be using a gate voltage to move the Fermi level within the band structure and moving the single layer bands out of the energy window. This is the focus of the next paragraph where the sample preparation steps will be presented as the substrate of graphene/SiC does not allow to carry out such experiments. The THz experiments are in the perspectives of this work as it was challenging to process the 2D layers in the cleanroom due to the weak nature of the vdW interactions.

4.2 On mica substrate

Wei et al [147] reported that the crystal phase of $MoSe_2$ depends on the substrate temperature on mica. 2D films grown at temperatures below 500 °C show the metallic 1T phase, the fraction of which decreases with increasing temperature. To avoid the formation of 1T crystal structure (as a whole or in a multiphase structure), it is important to carry out the growth at high temperatures.

4.2.1 MBE growth on mica

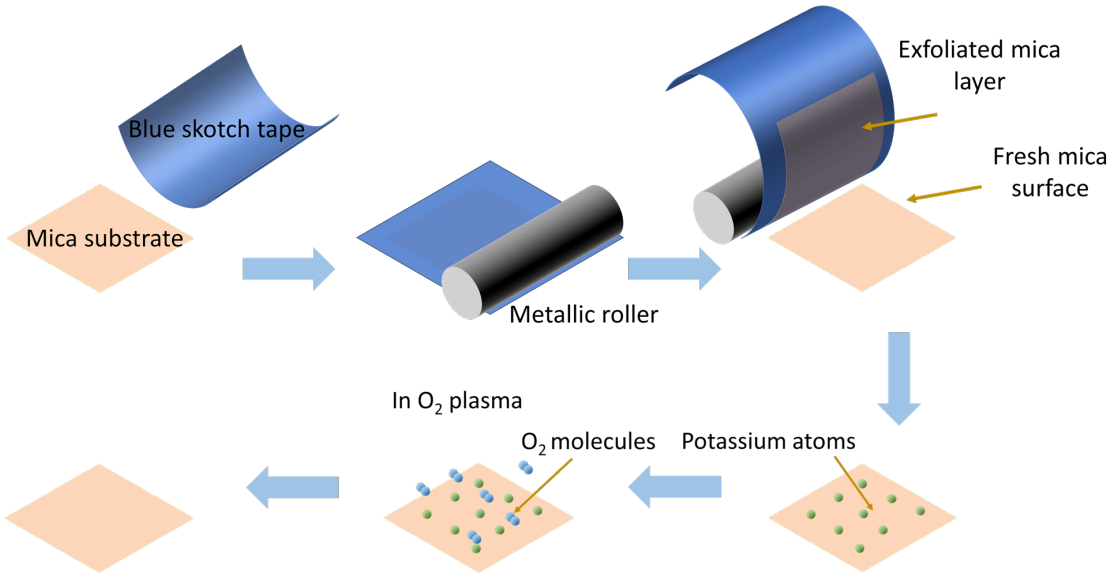

Figure 4.7: Flowchart of mica exfoliation using blue scotch tape. The blue tape should be applied on top of mica without any trapped bubbles inside. A small metallic cylinder is rolled gently but firmly enough to ensure better adhesion of the scotch tape on mica. The scotch tape is then rolled up carefully from one side to the other so that no 'old' layer remains on the freshly exposed surface. Due to the natural formation of mica layers, K atoms are intercalated between the layers and they are removed in an O_2 plasma. The fresh and K-free mica is immediately introduced into the load-lock chamber of the MBE.

Muscovite mica is a naturally occurring mineral that consists of layers of aluminosilicate with intercalated potassium atoms, with the chemical formula $[KAl_2(AlSi_3O_{10}(OH)_2]$ [148]. The preparation of 15 $\times$ 15 mm^2 mica substrates, provided by Ted Pella Inc, included the exfoliation of the top most layer mechanically with a scotch tape, as presented in Fig. 4.7. After exposing a fresh mica surface, a part of potassium atoms stay on the surface, the other part go with the exfoliated out layer. Vergnaud et al. reported on the effect of the intercalated K atoms on the increased crystalline isotropy of the flakes [115], thus, the potassium atoms are removed in an O_2 plasma during 3 minutes and the substrate is immediately introduced into the loadlock chamber of the MBE. Mica was then outgassed for 30 minutes at 800 °C in the UHV chamber before the growth, with the RHEED pattern shown Fig. 4.8 a. The epitaxy of 1.2 ML $MoSe_2$ was carried out at the same temperature with a Mo deposition rate of 0.00125 Å/s and Se flux of 1×10^{-6}, followed by an annealing step under the same Se flux at 800 °C and a flash annealing at 820 °C. Fig. 4.8 b and c show the RHEED pattern of the annealed 1.2 ML $MoSe_2$.

1.2 ML $PtSe_2$ was then grown on $MoSe_2$ at 400 °C with a Pt deposition rate of 0.003125 Å/s and Se flux of 1×10^{-6} mbar and annealed at 700 °C for 15 minutes under the same Se flux, the room temperature RHEED pattern of 1.2 ML $PtSe_2$, in Fig. 4.8 e and f, exhibits an anisotropic behaviour, with more diffuse streaks than the one observed for $MoSe_2$ at 400 °C which can be explained by the insulating character of mica leading to defocusing due to charging effects at low temperature. The corresponding profiles of the RHEED patterns are presented in Figs 4.8 g and h for the [100] and $[1\bar{1}0]$ crystal directions, respectively. A nominal 1 ML $PtSe_2$/1 ML $MoSe_2$ heterostructure was prepared to observe the coverage and the AFM image shows incomplete coverage in Fig. 4.8 i. However, we observe that the step height of $MoSe_2$ on mica was 6 Å, it is then not easy to conclude whether the layer on top is $PtSe_2$ or $MoSe_2$ that shows a step height of 7 Å.

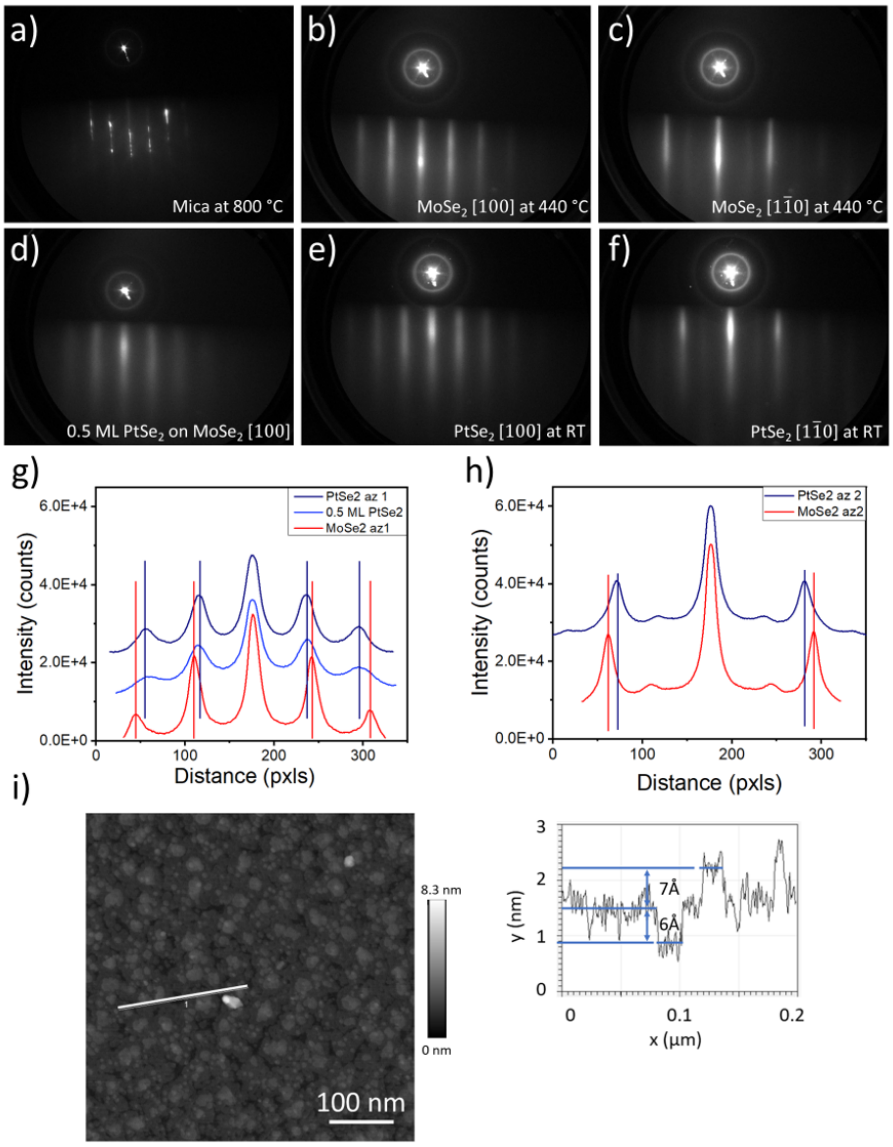

Figure 4.8: Electron diffraction of $PtSe_2/MoSe_2$ on mica. RHEED pattern of a) mica after 30 minutes at 830 °C, along b) [100] and c) [1$\bar{1}$0] of nominal 1.2 ML $MoSe_2$, d) azimuth 1 [100]of 0.5 ML $PtSe_2$ on $MoSe_2$ (taken during the growth), e) [100] and f) [1$\bar{1}$0] of 1.2 ML $PtSe_2$ (taken at room temperature). Profiles of the RHEED patterns along g) [100] and h) [1$\bar{1}$0] in a-f. i) AFM image of 1 ML $PtSe_2$/1 ML $MoSe_2$ with the height profile showing the first step of ≈6 Å and the second one ≈ 7 Å.

4.2.2 Transfer of vdW layers onto SiO_2/Si

To be able carry out the THz-TDS experiments applying a back gate voltage, the heterostructure of $PtSe_2/MoSe_2$ was transferred onto a SiO_2/Si substrate in the following manner: polystyrene was spin coated on the sample on mica and left to dry overnight. The hardened polystyrene provides sufficient mechanical support to prevent the rolling up of the vdW layers. The next day, it was put inside a deionized water bath. Since mica is hydrophilic, the water molecules can penetrate in between the 2D film and mica lifting off the 2D film with polystyrene to the surface of water. The floating film could then be fished up with the SiO_2/Si substrate. The optical images of the samples 1.2 ML $PtSe_2$/1.2 ML $MoSe_2$ and 2.4 ML $PtSe_2$/1.2 ML $MoSe_2$

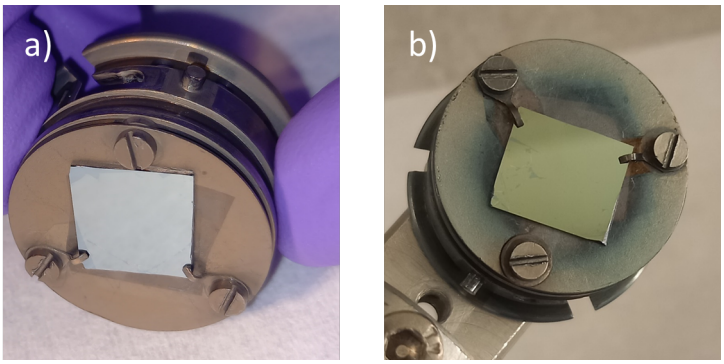

Figure 4.9: Optical images of transferred a) 1.2 ML $PtSe_2$/1.2 ML $MoSe_2$ and b) 2.4 ML $PtSe_2$/1.2 ML $MoSe_2$ onto SiO_2/Si and then fixed on the molyblock.

after the transfer onto SiO_2/Si are shown in Fig. 4.9 a) and b), respectively. The AFM images of before and after transfer and cleaning in IsoparG and toluene onto SiO_2/Si are displayed in Fig. 4.10 and show that the film flatness is preserved.

Fig. 4.10e) and g) show in-plane and azimuthal XRD scans of 3.4 ML $PtSe_2$/1.2 ML $MoSe_2$ on mica with the two main peaks named as X and Y, corresponding to $PtSe_2$ and $MoSe_2$ Bragg peaks, respectively. (110) Bragg peaks show the highest intensity with FWHM of 0.82° and 0.77°, respectively. These values are comparable to the ones of the films grown on graphene/SiC. The highly intense and narrow peaks of mica can only be seen before transfer. The difference of deposition rates on graphene/SiC and mica is justified by the higher atomic mobility on graphene that requires higher deposition rates to favor nucleation.

The azimuthal scans of the (110) peaks for $PtSe_2$ and $MoSe_2$ show narrow FWHM of 3.19° and 2.26°, respectively, which is around three times smaller than the growth on graphene/SiC. As mentioned earlier, atomic mobility on the mica surface is lower than on graphene, indicating stronger interaction of the growing film with the substrate, this could result in the better crystal alignment with the substrate. Another important aspect of this measurement is the clear alignment of the $PtSe_2$ crystal lattice on the one of $MoSe_2$ below, the vdWE nature of the growth.

The post-transfer in-plane and azimuthal XRD scans of 2.4 ML $PtSe_2$/1.2 ML $MoSe_2$ are shown in Fig. 4.10f) and h), respectively. Comparing these results with Fig. 4.10e) and g), one can notice that the Bragg peaks FWHMs are similar and the mosaic spreads of the crystals are also in the same order of magnitude which are the evidence of successful transfer of large area vdW layers onto another substrate.

Post-transfer heat treatment

Three batches of 1.2 ML $PtSe_2$/1.2 ML $MoSe_2$ and 2.4 ML $PtSe_2$/1.2 ML $MoSe_2$ samples were processed into Hall bars and square patches. The Hall bars of length 100 μm and width 10 μm were aimed at performing out magnetotransport measurements and the square patches for THz-TDS experiments. The patches were chosen to isolate regions from the rest of the sample for two main reasons: to be able to apply the gate voltage on the exact same region where the laser beam hits the sample and to avoid short circuit where the oxide layer is not enough insulating and losing the gate voltage effect.

The heat treatment, as shown in Fig. 4.11a), consisted of two main stages: (i) ramping up to 170 °C in one hour and dwell for 3 hours, this step was meant to remove water molecules and residual polystyrene (that might not have been removed by the chemical cleaning) (ii) improving the flatness of the transferred films by annealing at steps of temperatures under Se flux of 5×10^{-7} mbar starting from 250 °C to avoid the creation of Se vacancies.

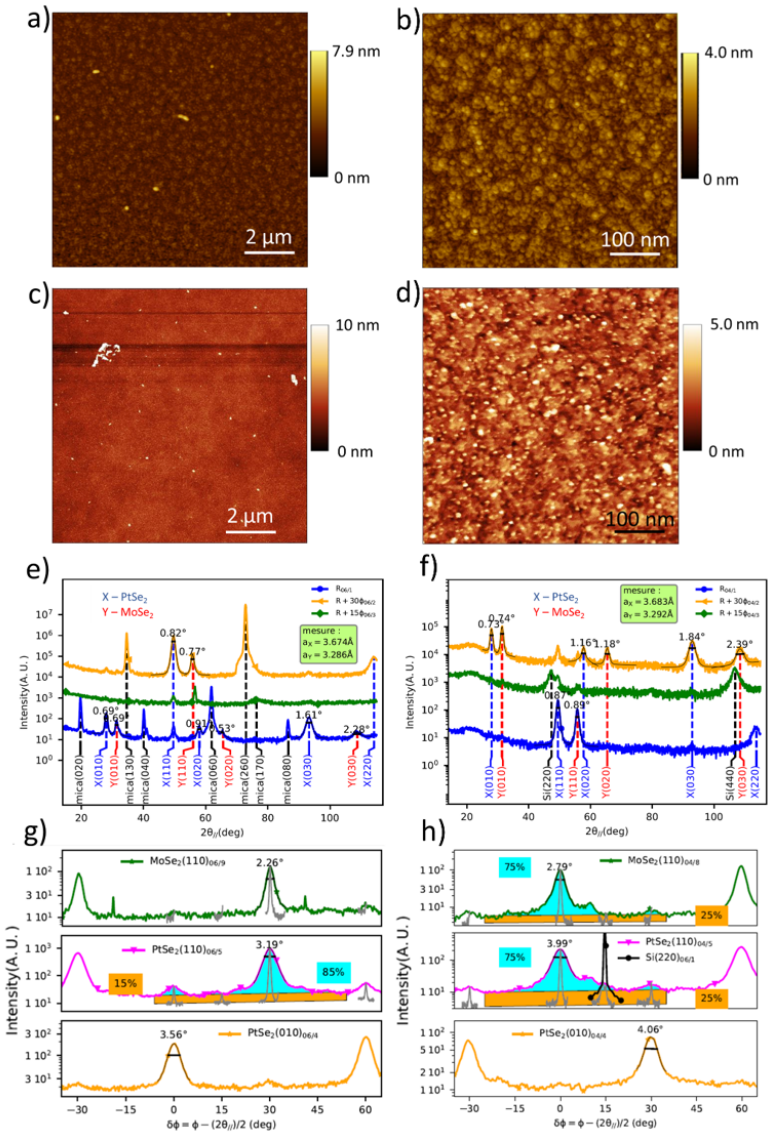

Figure 4.10: AFM images of 1.2 ML $PtSe_2$/1.2 ML $MoSe_2$ a) and b) before transfer and c) and d) after transfer. In-plane XRD of e) 3.4 ML $PtSe_2$/1.2 ML $MoSe_2$on mica before the transfer and f) 2.4 ML $PtSe_2$/1.2 ML $MoSe_2$ on SiO_2/Si after the transfer. g) and h) show the azimuthal scans recorded on Bragg peaks defined in a and b, respectively.

The first batch of samples, after the transfer and chemical cleaning, showed rings and streaks in the RHEED image just after introduction into the vacuum chamber. As the crystalline surface was already visible by RHEED, it was decided not to go too high in temperature to avoid damaging the SiO_2 oxide layer of the substrate under Se flux. However, processing those two samples in the cleanroom was unsuccessful: the whole film was lifted off and the bare substrate was recovered. The next batch of two samples were annealed up to 720 °C and the process was better: most of the film and devices stayed on the substrate, only some were lifted-off. We can conclude that high temperature treatment is essential to ensure that the vdW layer sticks on the substrate after a wet transfer.

This second batch of processed samples was sufficient to test our setup built for the gate dependent THz-TDS experiments, though it was not possible to carry out the full gate-dependence. Thus, a third batch was

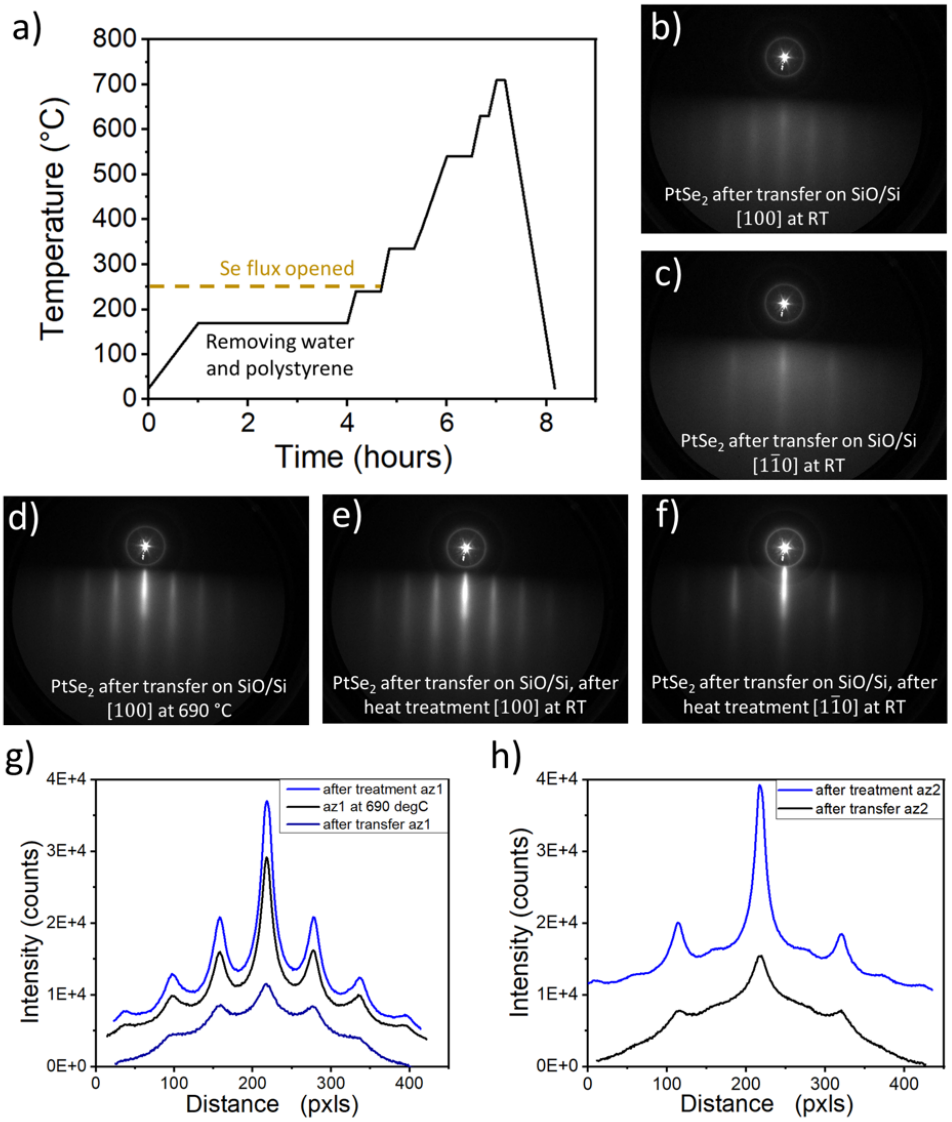

Figure 4.11: a) Thermal cycle of the post-transfer heat treatment of the transferred $PtSe_2$/$MoSe_2$ heterostructures. Electron diffraction of $PtSe_2$/$MoSe_2$ after the transfer onto SiO_2/Si. RHEED pattern of b) [100] and c) [1$\bar{1}$0] after the transfer and chemical cleaning, at room temperature, d) [100] after 6 hours of thermal treatment (recorded at 690 °C), e) [100] and f) [1$\bar{1}$0] after the heat treatment (recorded at room temperature). Profiles of the RHEED patterns along g) [100] and h) [1$\bar{1}$0] in a-e, respectvely.

prepared and the process and the measurements are part of the prospectives of this study.

The evolution of the RHEED pattern of the transferred 1.2 ML $PtSe_2$/1.2 ML $MoSe_2$ from the third batch is shown in Fig.4.11 with the profiles in g) and h) for the crystal directions [100] and [1$\bar{1}$0], respectively. The RHEED pattern after chemical cleaning in Fig. 4.11b) and c) for the two azimuths, shows a diffuse background that decreases drastically by increasing the sample temperature, as shown for example in Fig. 4.11d) at 690 °C.

To conclude, slowly ramping up the temperature during the post-transfer annealing ensures the contaminants can be removed from the surface and opens up the expected RHEED pattern. This should be finished

by a sufficiently high temperature of annealing to guarantee the good bonding with the new substrate.

4.2.3 Cleanroom processing

To define the Hall bars conduction channel and isolate square patches for THz experiments, etching and contact pad deposition were realized in a cleanroom facility. The adhesion of vdW films to the substrate is very weak due to the weak vdW interaction: it cannot be directly dipped into water (at the development step) which makes the cleanroom process challenging. A special two-resist process was developed to solve this issue. First, we start with the deposition of an electron-beam lithography resist (PMMA 4% 950K), a uniform 300 nm-thick resist is obtained by spin coating at 4000 rpm and 2000 rpm/s for 60 s, followed by annealing at 120 °C for 120 s.

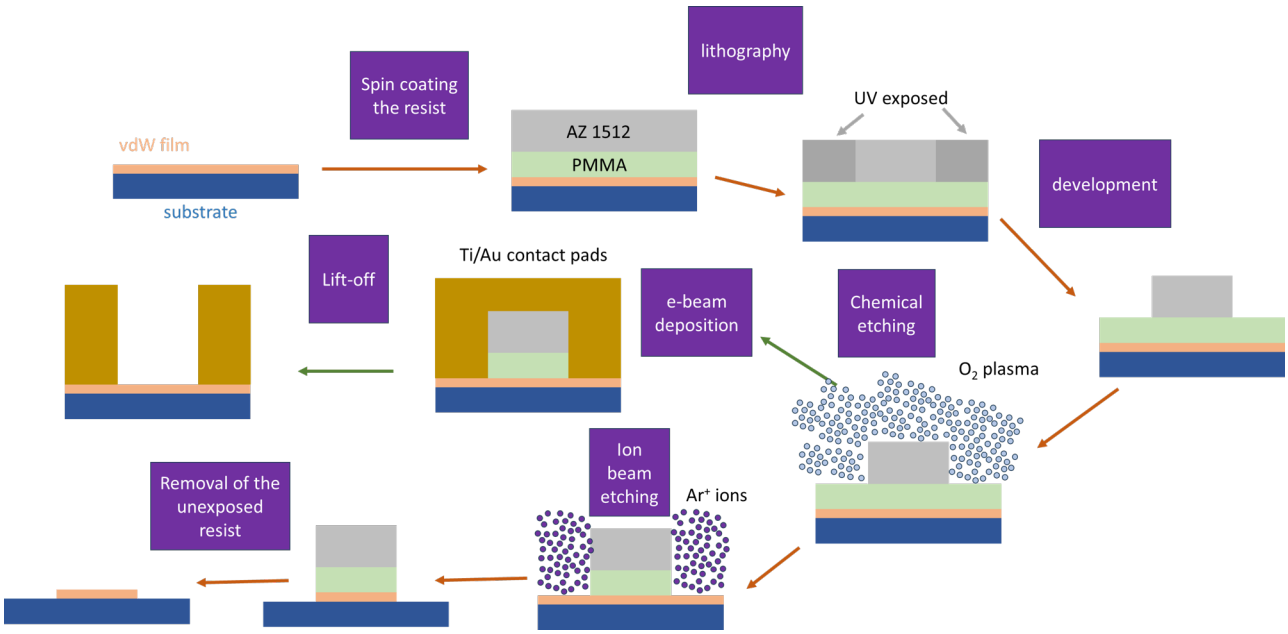

Figure 4.12: Flowchart of the cleanroom process. The orange (green) arrow shows the flow corresponding to the first and third (second) lithography processes.

The flowchart of a cleanroom process involving various stages is presented in Fig. 4.12. This first layer of resist protects the vdW films from being lifted off when dipped in water. Afterwards, a 1.2 μm-thick optical resist (AZ 1512HS) was also deposited using the same spin coating parameters and annealed at 100°C for 90 s. Now the sample is ready for lithography. Laser lithography (LL) is employed to expose the resist and draw the pattern, the machine consists in x-y-z stages moving below a focused UV laser beam (λ=380 nm). Several write-heads are available, characterized by different spatial resolutions and exposure times. In our case, we use the so-called write-head V, which gives a resolution of about 3 μm and takes approximately 1 min to expose a 1 cm^2–large sample. We are using a positive resist that becomes dissolvable [in the basic solution called 'developer'] when exposed to the UV light source. The complete device preparation requires three lithography-etching-deposition steps which necessitate precise alignment of the patterns in each cycle using alignment crosses as shown in Fig. 4.13 a. The patterns are exposed to the UV light and developed. As we aim at protecting the Hall bar channel from the etching process, we expose the negative pattern (i.e. areas where there is no pattern in the layout). After the exposure, the parts of the photoresist that were exposed to the laser beam are removed with the developer. The AZ developer solution is diluted with DI water in a 1:1

ratio, the development lasts for 25 seconds. After the development, the sample is cleaned with water. The PMMA resist acts as a protective layer for the vdW layers during this step avoiding its removal.

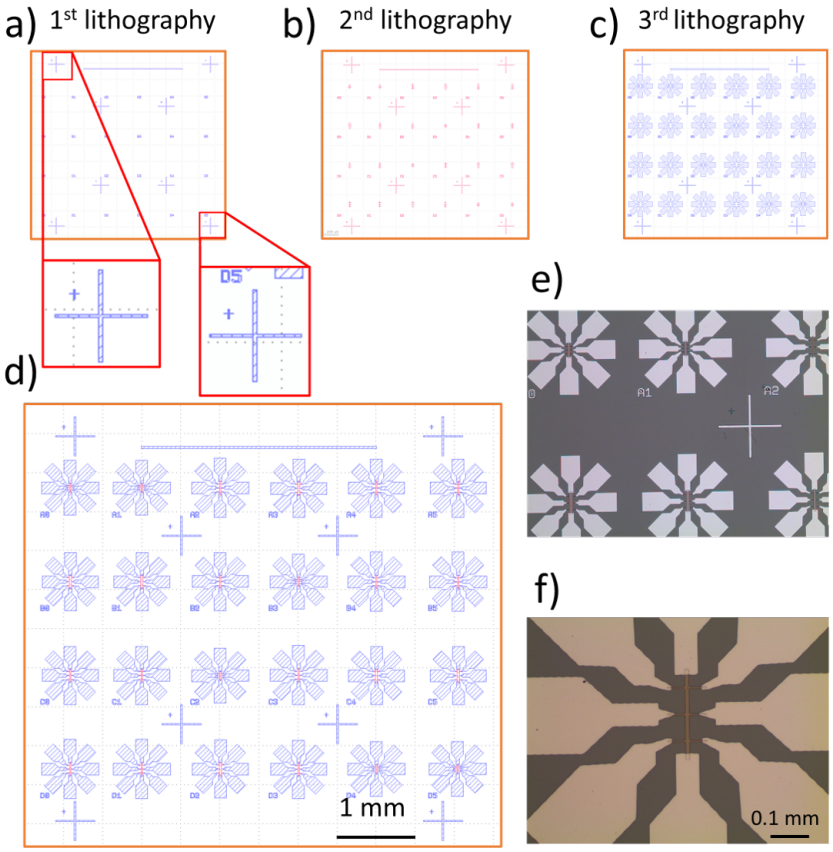

Figure 4.13: a-c) layouts corresponding to the first, second, and third lithography processes, respectively. d) The merging of all the layouts. e) and f) the final state of the processed 2.5 nm permalloy/5 nm Pt thin films. This sample was processed as a part of my training in the cleanroom as it consists of conventional 3D materials.

Once the pattern is developed, the PMMA film is removed using ion-coupled plasma etching with an STS machine. O_2 is used as the gas source with a flow of 45 sccm. The etching was controlled by monitoring the resist thickness using a laser interference pattern, the total etching time was around 2 mins. At the end of this step, the vdW layers or substrate are exposed to air and is ready to be etched or for the e-beam deposition of metallic electrodes, as shown by the two diverging arrows in Fig. 4.12. 10 nm of Ti/100 nm of Au are deposited by e-beam evaporation, followed up by the lift-off. Starting with this stage ensures that we have the alignment crosses. In the second step, the inverted layout is exposed to the UV leaving the pattern unexposed, as shown in Fig. 4.13 b. Thus, the development stage removes everything outside the pattern. The second step does not include e-beam evaporation, but ion-beam etching that etches away the TMD/FM layers outside the pattern. Finally, the unexposed resist is removed in an acetone bath. In the last third step, we again do the alignment using alignment crosses, the direct pattern (as opposed to the inverted pattern in the previous step) is exposed to the UV light. Again, after the development and the chemical etching, 10 nm of Ti/100 nm of Au is deposited (direct deposition of Au is not desirable as it may dewet from the sample, which not observed when Au is deposited on Ti), and followed by the lift-off in an acetone bath. The final layout that includes all the layouts is shown in Fig 4.13 d, with optical microscope images of the fully processed 2.5 nm of permalloy/5 nm of Pt sample in Fig4.13 e and f.

The film is then either removed by ion beam etching; or 5 nm Ti and 80 nm Au are deposited with a pre-deposition etching to remove the possible contaminants during air transfer from the chemical etching chamber to the e-beam deposition chamber. The parts of the 2D material which are exposed will be removed. The incident ion beam was perpendicular to the sample surface and lasted for 30 s with an energy of 250 eV. The sample was rotated on its own axis to achieve uniform etching. Finally, the sample was put in O_2 plasma etching again to partly remove the resist to ease the final cleaning with aceton, it also removed PMMA.

4.3 THz-TDS experiments conceptualization

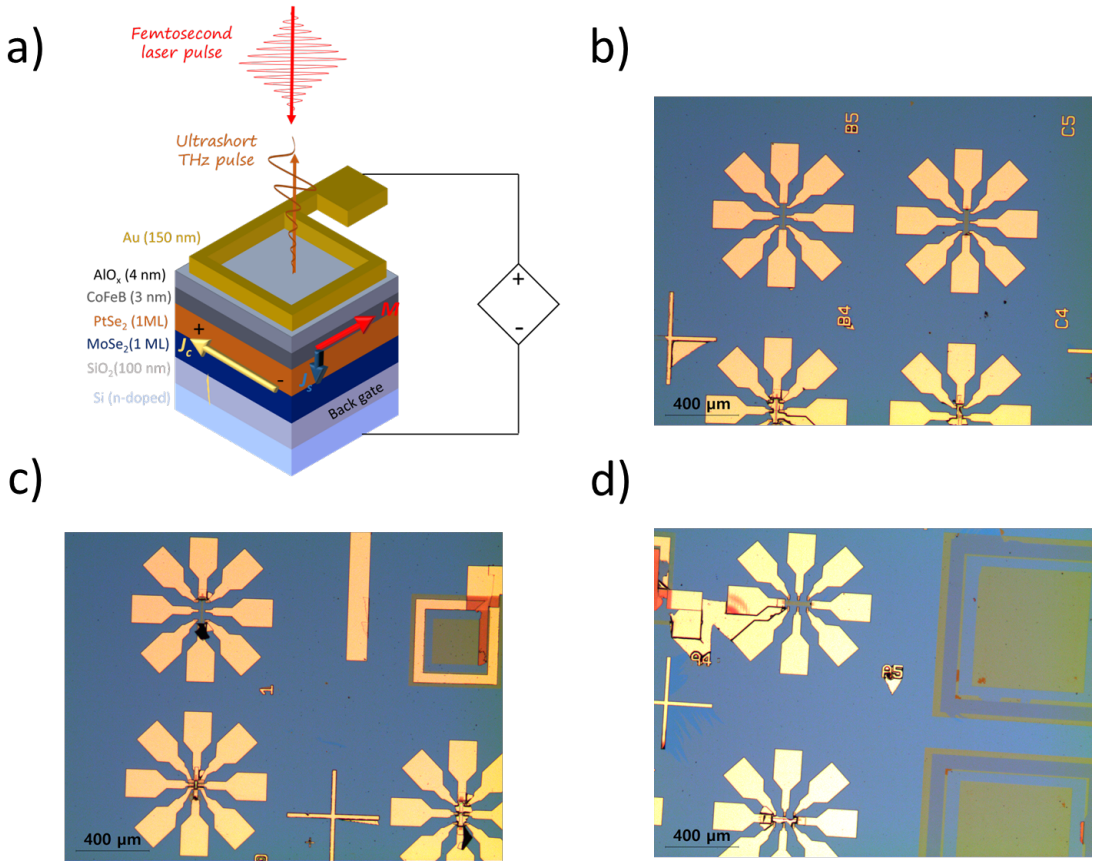

Figure 4.14: a) skecth of the square patched device and geometry of the gate-voltage application b-d) first cleanroom process attempt on sample AlO_x/CoFeB/ 1.2 ML $PtSe_2$/ 1.2 ML $MoSe_2$ for gate-voltage-dependent THz-TDS experiments.

As mentioned in the post-transfer heat treatment, there have been three batches of two samples prepared for the study of the gate-dependence of SCC probed by THz-TDS. The first batch was lost due to complete lift-off of the layers during the cleanroom process. The second batch was partially good. Fig. 4.14 a shows a sketch of the device in the shape of a square patch and the geometry of gate-voltage application. In Fig. 4.14 b-d corresponding to the sample AlO_x/CoFeB/ 1.2 ML $PtSe_2$/ 1.2 ML $MoSe_2$, we can see that a few Hall bars were processed well, while some show contacts that are shorted, and some others show that the lift-off did not work and the thick Au layer stayed on top of the Hall bar. It is possible to carry-out magnetotransport measurements on these devices in the future. However, we faced clear issues with the patches: the Au contacts that are used to apply the gate-voltage are either completely lifted-off or with

discontinuities, not viable to apply the gate-voltage. It was still possible to obtain THz signal from the square patches with pointing the laser exactly inside the square, the gate-voltage dependence experiments had failed though.

4.4 Conclusion

In conclusion, anisotropic 1.2 ML $PtSe_2$/ 1.2 ML $MoSe_2$ bilayer was grown by vdWE on graphene/SiC, and CoFeB and Al were sputtered on top. Photon-energy dependent SCC conversion experiments probed by THz-TDS showed the polarization of the THz electric is opposite to that of only $PtSe_2$ measured in the previous chapter, indicating an opposite θ_{SH} This was later verified by spin resolved ARPES measurements that the spin texture of the topmost valence in the bilayer is opposite to that of $PtSe_2$ layer previously measured.

To able to access deeper bands by the THz-TDS experiments by the electric gating, the bilayer was first grown on mica, then transferred on SiO_2/Si. Following XRD studies show that the transfer process does not affect the quality of the crystals. The first of cleanroom processing was not very successful, the next round of the experiments are in preparation.

Chapter 5

Perspectives

5.0.1 Introduction

5.1 2 ML $PtSe_2$/ 1 ML $MoSe_2$ transferred on Ferroelectric substrate

5.1.1 Motivation and 2D/3D ferroelectric heterostructure state-of-the-art

The previous chapter described for the application of a gate-voltage to modulate the SCC efficiency by moving the Fermi level within the Rashba spin-split states of the band structure in vdW heterostructures. The current chapter focuses on similar physical principles, except the gate-voltage is replaced with the remanent electric field produced by a ferroelectric substrate. The 2D spintronics team has gained enough experience and published one of the pioneering works on 2D vdW/3D ferroelectric heterostructures [149].

In the reported experimental work [149], a direct measurement of the electronic band structure modulation of WSe_2 by the ferroelectric polarization of the substrate was demonstrated by ARPES. High-quality and large-area (≈ 1 cm^2) WSe_2 was epitaxially grown on a mica substrate by MBE, as shown in Fig. 5.1 a and b. The growth conditions of WSe_2 on mica are similar to the ones of $MoSe_2$ on mica, as presented in the previous chapter. The grown layers are then transferred onto $BiFeO_3$ (BFO) following the same method as the one presented in the previous chapter. BFO films are prepared using Pulsed Laser Deposition (PLD) by Oliver Paull at the Laboratoire Albert Fert (Palaiseau) in the team of Manuel Bibes and their UP or DOWN polarization state is defined during the growth: the BiO^+ termination results in a UP polarization state and the FeO_2^- termination results in a DOWN polarization state, as shown in Fig. 5.1 c. The XPS analysis of 3 ML WSe_2 after being transferred on DOWN (DN, in blue) and UP (in red) polarized BFO films shows a rigid shift of 0.6 eV of the peaks $4f_{7/2}$ and $4f_{5/2}$ of W and $3d_{5/2}$ and $3d_{3/2}$ of Se without any additional phases of WO_x or SeO_x. The rigid energy shift indicates electrostatic doping.

The ARPES results on 3 ML WSe_2 transferred on DOWN (UP) BFO are given in Fig.5.1 f and h (g and i) where Fig.5.1 f and g show the Γ-K as-measured cuts from the Fermi level down to 4 eV below. The spin-orbit splitting can be observed at K points. Those bands merge and then split into 3 bands at Γ. Fig. 5.1 h and i show the same band structure after Laplacian normalization that sharpens the bands. The band splittings at K and Γ are consistent with the literature [150], [151], [152], [153]. The VBM can be measured to be located at -0.215 and -0.985 eV below the Fermi level for DOWN and UP polarization states, respectively. This is equal to a rigid band shift of 750 meV of the bands between DOWN and UP polarization states which is higher than previously measured value of 450 meV by Kelvin probe microscopy [154], indicating better coupling between the TMD and the ferroelectric material in the current samples.

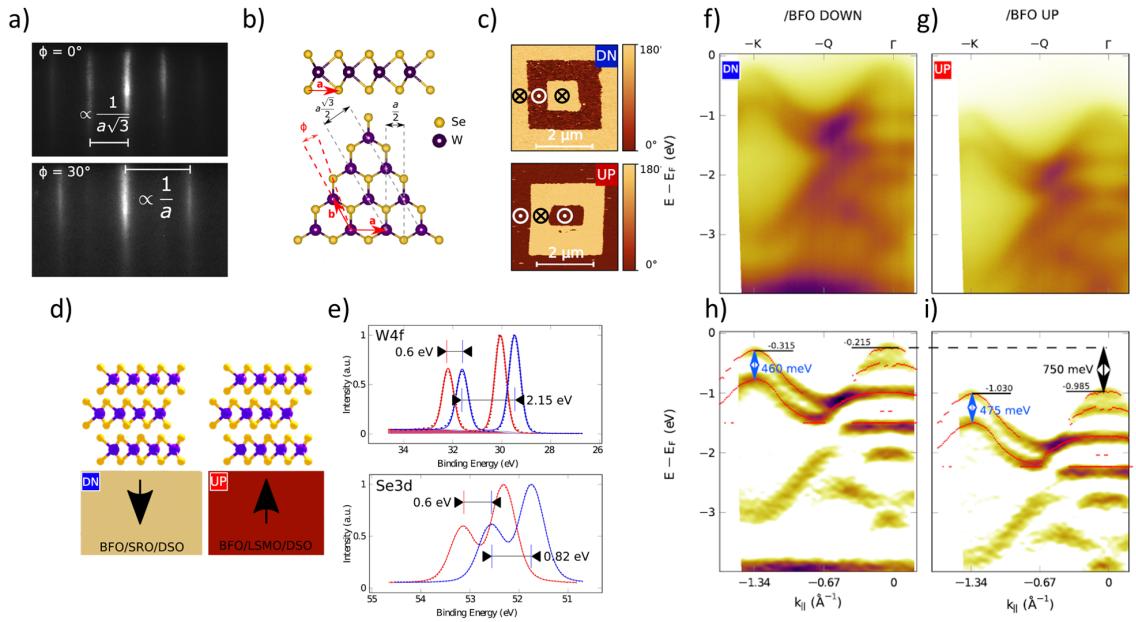

Figure 5.1: Experimental study on ferroelectric substrate polarization dependence of the electronic band structure of 3 ML WSe_2. a) RHEED pattern along two distinct azimuths of 3 ML WSe_2, b) side and top views of WSe_2 showing the two crystalline directions giving the RHEED patterns in a. c) Piezo Force Microscopy (PFM) image of DOWN and UP polarized BFO grown on LSMO, d) 3 ML WSe_2 on DOWN and UP polarized BFO, e) XPS spectra of WSe_2 of W^{4f} and Se^{3d} peaks on DOWN (blue) and UP (red) polarized BFO, f) and g) ARPES raw data of WSe_2 on top of DOWN and UP polarized BFO, respectively. h) and i) are the second derivatives of the raw data in f) and g), respectively.

LNO substrate

The $LiNbO_3$ (LNO) substrates were obtained from a supplier and the z-cut substrate's electric polarization was reported to be in the order of $\approx 80\ \mu C/cm^2$ [155]. The electric polarization of LNO is parallel to the c-axis of the crystal. When a semiconducting film is placed on top of that surface (either with UP or DOWN polarization), the electric field at the surface of the ferroelectric LNO will naturally gate the adjacent film, shifting the Fermi level and enhancing the Rashba coefficient since this depends linearly on the electric field E_0. As strong polarization has been reported on z-cut LNO crystals, we expect a strong modulation of the magnetic component of the THz signal (coming from SCC) for UP and DOWN polarizations. At this point in time, we only had access to x-cut LNO substrates which have a polarisation in the plane of the substrate. After measuring the piezoresponse force microscopy (PFM) of these substrates, as presented in 5.2c) and), it was found that they have a clear component of the polarisation out-of-plane which can still gate an adjacent 2D material. We therefore decided to perform a THz study on the x-cut LNO substrates whilst waiting for an order of z-cut LNO to arrive.

5.1.2 Growth and Transfer

The growth and transfer stages for this set of experiments were exactly the same as described in the previous chapter, the only difference was the substrate on which they were transferred which were UP and DOWN electrically polarized ferroelectric LNO substrates with dimensions of 5 mm × 5 mm. Fig. 5.2e) and g) show the optical microscopy images of the transferred films on DOWNN and UP polarized LNO. The corresponding AFM images are shown in Fig. 5.2g) and h). After these experiments, the samples were

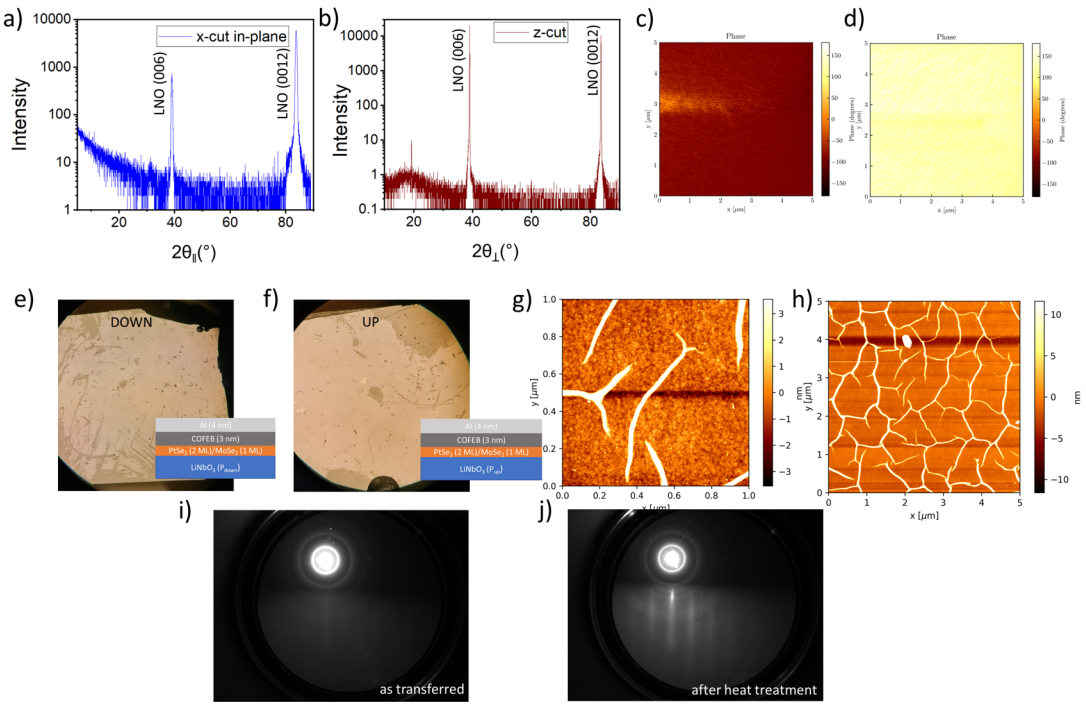

Figure 5.2: a) In-plane and b) out-of-plane XRD spectra of LNO substrates. Electric polarization measurements by PFM for c) UP and d) DOWN polarizations. Optical images of the transferred layer on e) DOWN and f) UP polarized LNO. g) and h) AFM images of a transferred layers on LNO i) RHEED pattern of 2.4 ML $PtSe_2$/1.2 ML $MoSe_2$ transferred on LNO substrate and j) the same sample after heat treatment at 540 °C.

introduced into the MBE chamber and the RHEED pattern of the as transferred films with very low intensity of the diffraction rods, probably due to the surface contamination, as can be seen in Fig. 5.2i) and j). Upon slowly heating up the sample up to 600 °C, the diffraction intensity improved and rings can also be observed. These rings can be attributed to ripples on the TMD film, as shown in AFM images in Fig. 5.2 g and h, that form during the drying step of the films after the fishing.

5.1.3 THz results

Preliminary results

This set of THz-TDS experiments was, similar to the ones in the previous chapters, also carried out using the Ti:Sapphire laser at 800 nm wavelength. The measurements were done with UP and DOWN polarizations at θ=0°, 90°, 180°, and 270° for positive and negative magnetic fields, θ being the sample rotation for a fixed field direction. As shown in Fig. 5.3 a-d, we can clearly see the variations of the THz lineshape with the angle θ. The measurements at θ=90° and 270° show almost one order of magnitude higher THz electric field strength than that at θ=0° and 180° for both samples. For the former two angles, the electric field polarity did not reverse upon magnetic field reversal, but only the strength of the electric field changed. This effect which is not expected for magnetic emission, means that only the small change in the field strength can be attributed to magnetic emission. For the latter two angles, we see polarity reversal upon magnetic field reversal, though with a much weaker field strength compared to the former two angles and there is a small non-magnetic contribution as well. At this stage, it was not straightforward to interpret the results and more complete angular dependence studies were required.

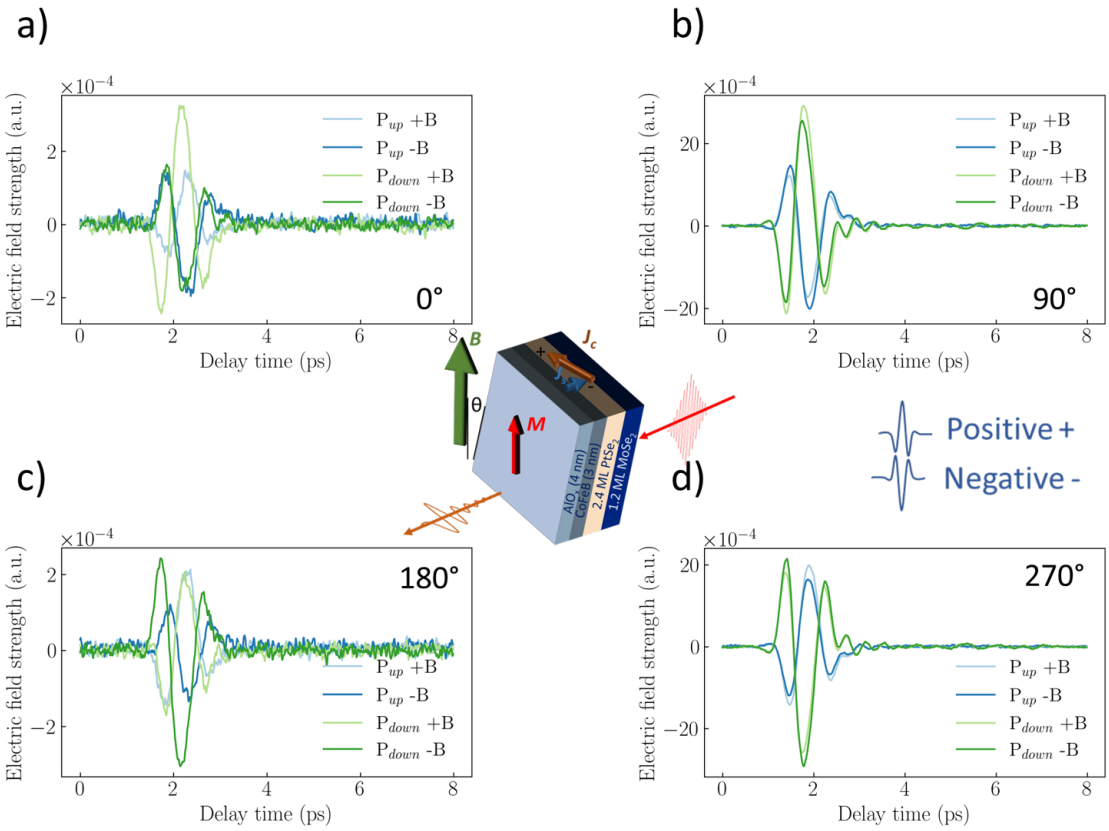

Figure 5.3: Preliminary results on THz emission in 2.4 ML $PtSe_2$/1.2 ML $MoSe_2$ for B+ and B- magnetic field on DOWN and UP polarized LNO substrates at a) θ=0°, b) θ=90°, c) θ=180°, and d) θ=270°.

Full angular dependence

The full angular dependence of the THz electric field strength, was performed with the sample rotated by 360° with steps of 3° for both magnetic field directions. The obtained result consisted of two lobes, one bigger than the other for both samples, as shown in Fig: 5.4 a and b. Such an anisotropic behaviour was already expected from the previous figure. The magnetic and non-magnetic contributions from the angular dependence experiments, were separated using the formulas:

$$\begin{aligned} S_{mag} &= \frac{S_{B+} - S_{B-}}{2} \\ S_{non-mag} &= \frac{S_{B+} + S_{B-}}{2} \end{aligned} \tag{5.1}$$

S_{mag} ($S_{non-mag}$) is the magnetic (non-magnetic) contribution, S_{B+} (S_{B-}) is the THz electric field strength for positive (negative) magnetic field direction. The obtained angular dependence for the magnetic contribution is almost one order of magnitude smaller than the non-magnetic one and is four-fold symmetric, the origin of such symmetry is under study. The two samples were not exactly aligned as can be seen in Fig. 5.4 d in the tilt angle. DOWN polarized sample showed around 50% stronger magnetic and non-magnetic signals than UP polarized sample. On the other hand, on the non-magnetic contribution of our study, previous

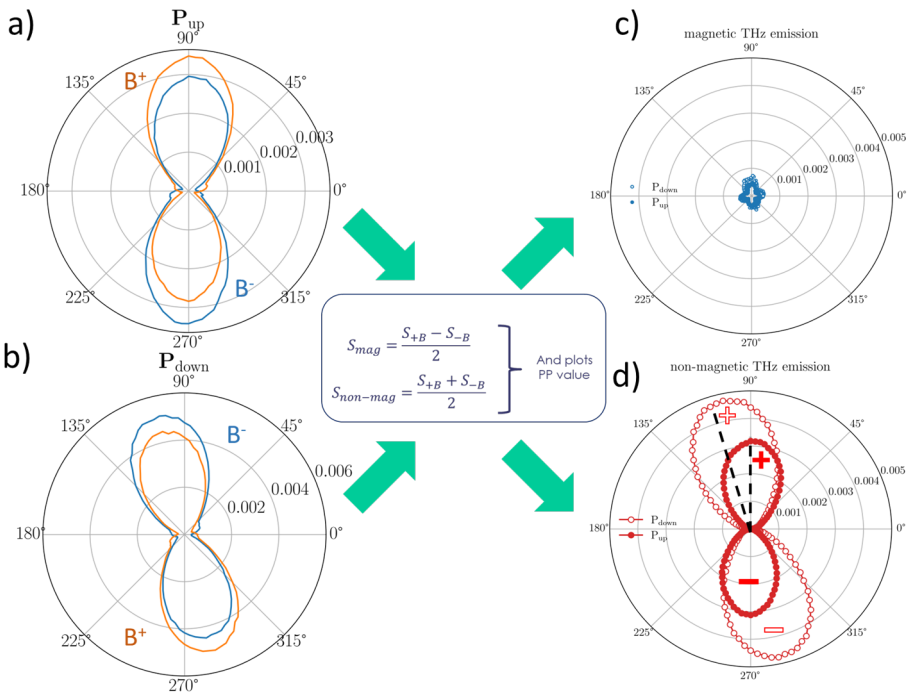

Figure 5.4: Full angular dependence on a) UP and b) DOWN polarized LNO substrates for B+ and and B- magnetic field directions. After applying the formula in equation 5.1 we obtain the c) magnetic and d) non-magnetic contributions of the THz signals in a and b.

finding reported that LNO is a good material to generate THz pulses by optical rectifications [156], [157], [158].

Post-experiment XRD analysis showed that the LNO crystals were in fact x-cut, not z-cut which is the polarization direction. This can explain the observed small difference in the THz emission in samples with UP and DOWN polarization LNO substrates. As the surface normal of the substrate is not perfectly aligned with the c-axis of the crystal due to the surface polishing process, but has a small tilt angle of α (see Fig. 5.5a), the difference of the effective polarization would be smaller in x-cut case than z-cut case. Thus, the x-component of the electric field at the interface between LNO and the 2D materials would also be smaller. This explains the rather small difference we observe in the magnetic contributions to the THz signal (Fig. 5.5b).

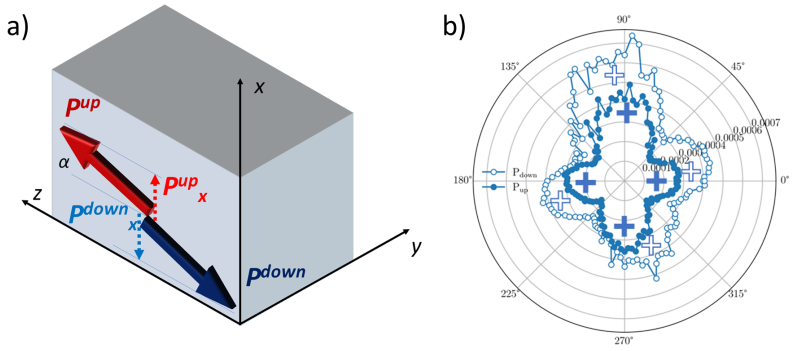

Figure 5.5: a) Sketch of the ferroelectric polarization with the respect to the crystal axis. Due to the tilt of the polarization away from the z-axis, there can be smaller polarization on the x-axis. b) enlarged angular dependence of the THz signal for DOWN (open circles) and UP polarizations (closed circles).

5.2 $PtSe_2/Bi_2Se_3$ heterostructures

5.2.1 Motivation

As discussed in the previous chapter, vdW heterostructures can host novel spintronic properties due to the emergence of hybridized bands. Sattar et al [6] calculated the band structure of $PtSe_2/Bi_2Se_3$ heterostructures. One layer of Bi_2Se_3 is made of five atomic layers of Se-Bi-Se-Bi-Se, as shown in Fig. 5.6 b, referred to as a quintuple layer. Bi_2Se_3 is known for thickness dependent electronic structure: in the few layer limit (<6 QL) it is semiconducting, as the thickness increases above 6 QL topological insulating properties appear [159], [160]. In DFT calculations, the optimized lattice parameters of 4.14 Å for Bi_2Se_3 and 3.74 Å for $PtSe_2$ were used for the 2 QL and 2 ML case. The distance between Bi_2Se_3 ($PtSe_2$) layers was 2.91 Å] (2.63 Å) while the interlayer distance between Bi_2Se_3 and $PtSe_2$ was 3.20 Å, as shown in Fig. 5.6 a. To obtain minimal lattice mismatch, a $\sqrt{7}\times\sqrt{7}\times 1R19.1°$ supercell of Bi_2Se_3 was matched with a $3\times3\times1$ supercell of $PtSe_2$ to obtain a lattice parameter of 11.05 Å which resulted in a mismatch of less than 1 %.

In their calculations, Sattar et al [6] took 1 ML and 2 ML of Bi_2Se_3 and $PtSe_2$ each to build four distinct heterostructures in total. The bonding between $PtSe_2$ and Bi_2Se_3 layers was found to be physisorption, thus the heterostructure is of vdW nature. They summarized their results in the table of Fig. 5.6 b for each configuration. The most important parameter here is the Rashba-splitting, α_R. The first two heterostructures with 1 QL of Bi_2Se_3 show spin-splitting only in the valence band, the heterostructures with 2 QL of Bi_2Se_3 show the coexistence Rashba-type spin-splitting in the valence and conduction bands. The highest α_R in the 2 QL Bi_2Se_3 heterostructures is almost 17 eV.Å in the valence band.

5.2.2 MBE growth and characterization

The double-side polished sapphire substrates were provided by the Laboratoire Albert Fert in Palaiseau and thermal annealing in air was carried before the growth which consisted of a preparation stage at 300 °C for 30 minutes that removes the surface contamination, and a second one at 1000 °C for 60 minutes to improve the surface crystal quality. After the substrate cooled down, it was introduced into the MBE chamber, then heated up to 780 °C for 30 minutes in UHV with the RHEED patterns for two crystalline directions shown in Fig. 5.7 a and b. The substrate was then cooled down to 280 °C to co-deposit Bi and Se atoms to form Bi_2Se_3. The flux rate of Bi was 0.075 Å/s and partial pressure of Se was 1×10^{-6} mbar. 2 QL and 10 QL Bi_2Se_3 were prepared, without the annealing step. Fig. 5.7 c and d show the RHEED patterns of as-grown 10 QL Bi_2Se_3. Next, 2 ML or 5 ML $PtSe_2$ were deposited at 322 °C with a Pt deposition rate

a)

Table 2. Rashba Spin-Splitting Parameters of Few-Layer $Bi_2Se_3/PtSe_2$ vdW Heterostructures[a]

heterostructure	E_R (meV)	k_0 ($Å^{-1}$)	α_R (eV Å)
1QL Bi_2Se_3/1L $PtSe_2$	4.8	0.002	4.80 (CB)
2QL Bi_2Se_3/1L $PtSe_2$	4.0	0.002	4.00 (CB)
2QL Bi_2Se_3/1L $PtSe_2$	15	0.006	5.00 (CB)
	275	0.033	16.66 (VB)
2QL Bi_2Se_3/2L $PtSe_2$	11	0.005	4.40 (CB)
	278	0.033	16.84 (VB)

b)

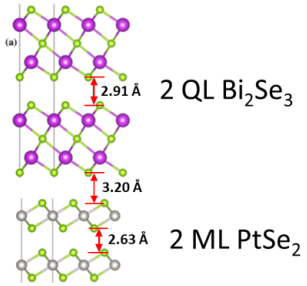

c)

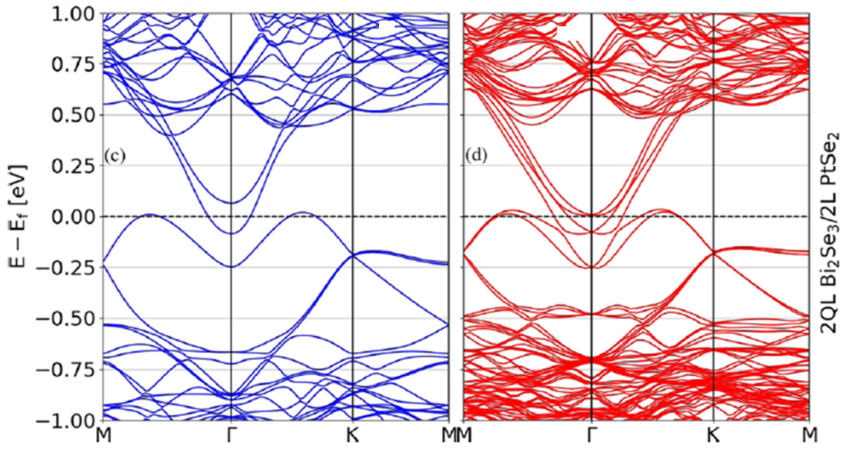

Figure 5.6: a) Summary of the band structure calculations carried out by Sattar et al [6](ref Sattar) showing the Rashba spin-splitting parameters for a couple of thicknesses of $PtSe_2$ and Bi_2Se_3 in their heterostructures. b) side view of the crystal structure of 2 QL Bi_2Se_3 and 2 ML $PtSe_2$ with the interlayer thickness and c) electronic band structure calculation of 2 QL Bi_2Se_3/2 ML $PtSe_2$ without (blue) and with (red) SOC showing Rashba-type band splitting.

of 0.001875 Å/s and a Se flux of 1×10^{-6} mbar. Anisotropic RHEED patterns were obtained with diffuse streaks as shown in Fig. 5.7 e and f. To improve the crystalline quality, the annealing consisted of a first step at 330 °C for 5 minutes and a second step at 510 °C for 5 minutes followed up by a flash annealing up to 550 °C. The crystal quality improvement can be clearly seen in Fig. 5.7 g and h. Unlike the epitaxy on graphene/SiC or mica, $PtSe_2$ could not be annealed at high temperature on Sapphire since Bi_2Se_3 might evaporate or degrade.

As discussed for the FM/$PtSe_2$ system, CoFeB and Co gave the same THz emission. Thus, in the current $PtSe_2/Bi_2Se_3$ heterostructure, 3 nm of Co were deposited by e-beam evaporation in the same MBE chamber, so were 3 nm Al as a capping layer.

XRD characterization was performed on the 5 ML $PtSe_2$/ 10 QL Bi_2Se_3 with the in-plane configuration with the Rigaku SmartLab. The results are presented in Fig. 5.8 where we can identify several Bragg peaks of Bi_2Se_3 (in red denoted by X) and $PtSe_2$ (in green denoted by Y). From the 2θ analysis in 5.8 a, the in-plane parameters are estimated to be 4.15 Å for Bi_2Se_3 and 3.71 Å for $PtSe_2$, in good agreement with the literature value of 4.14 Å [161] (0.22% expansion) and 3.72 Å [123] (0.37% compression), respectively. The azimuthal scans at several Bragg peaks shows that the crystals are highly anisotropic with a mosaic spread in the range of $\pm0.40°$ for Bi_2Se_3 and $\pm0.75°$ and $\pm0.80°$ for $PtSe_2$, which is remarkably narrow for $PtSe_2$ and the lowest value observed in MBE grown $PtSe_2$ films. The growth on sapphire is not fully by vdWE due

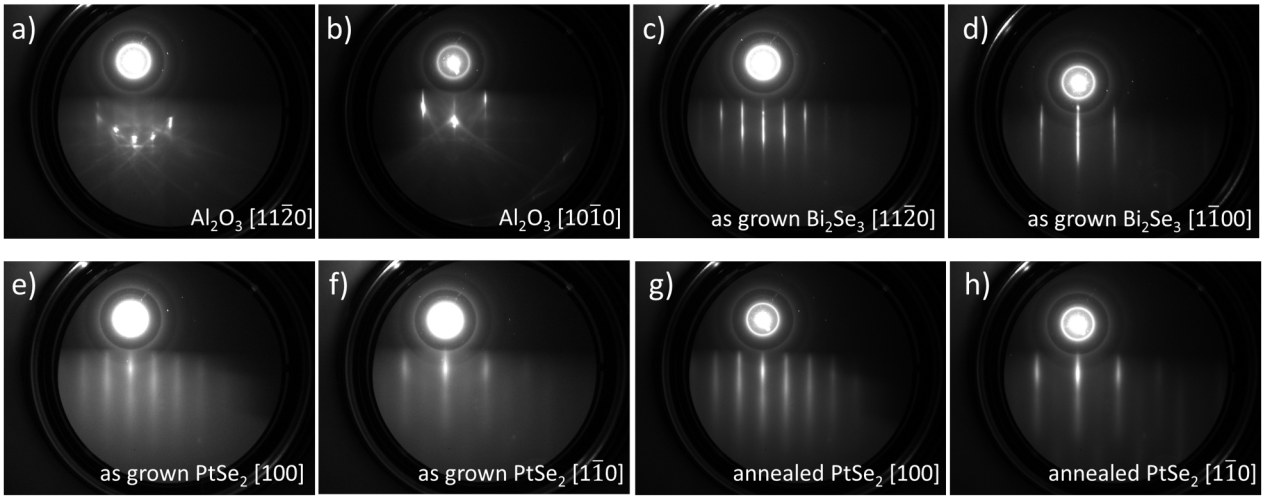

Figure 5.7: RHEED patterns of a) and b) sapphire (substrate), c) and d) 10 QL Bi_2Se_3, e) and f) of as-grown 2 ML $PtSe_2$, and g) and h) of annealed 2 ML $PtSe_2$.

to the surface dangling bonds which gives a little freedom for the grains to rotate during the growth. Thus, Bi_2Se_3 shows very little mosaic spread, which then ensures highly anisotropic epitaxy of $PtSe_2$ on top.

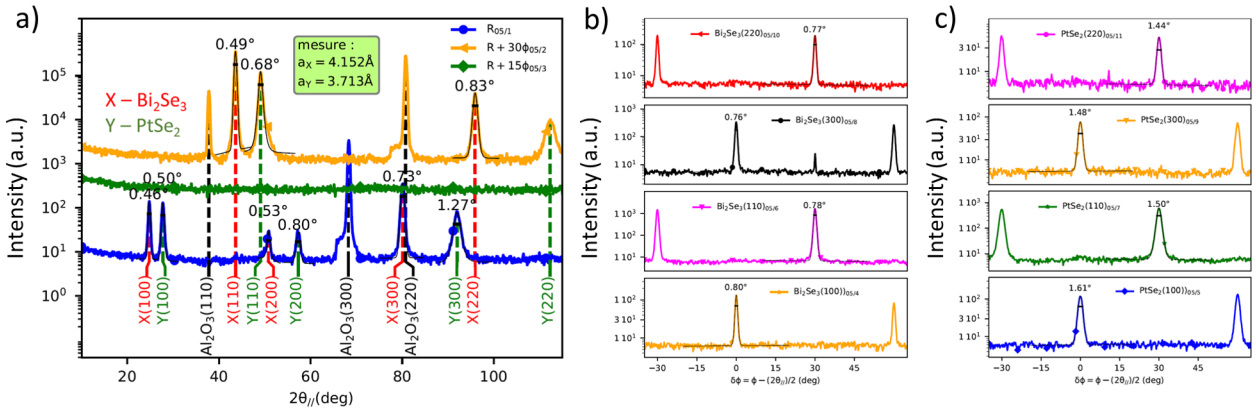

Figure 5.8: In-plane XRD of a) 5 ML $PtSe_2$/10 ML Bi_2Se_3 on sapphire and b) and c) azimuthal scans of Bi_2Se_3 and $PtSe_2$,respectively, showing very little mosaic spread. This high anisotropy is attributed to the strong interaction with the substrate that does not give much degree of freedom for the growing grains to rotate.

5.2.3 SCC conversion studies by THz-TDS

To test the theoretical results of by Sattar et al [6], THz-TDS experiments were then carried out to investigate SCC in the $PtSe_2/Bi_2Se_3$ heterostructures with varying thicknesses. In addition, heterostructures of $PtSe_2$ with the topological insulating phase of Bi_2Se_3 (10 QL) were tested. Each sample was measured at three distinct laser energies corresponding to 670 nm, 780 nm, 940 nm wavelengths in the transmission mode from the FM side. For fixed positive and negative field directions, the sample was rotated around the axis of the surface normal. The raw signal was then separated into magnetic and non-magnetic constituents using equation 5.1.

$PtSe_2$/semiconducting Bi_2Se_3 heterostructure

Since the calculations predict the largest Rashba-like spin splitting for the 2 ML $PtSe_2$/2 QL Bi_2Se_3 heterostructure (see table in Fig. 1.6a), we selected this structure to test the validity of the model by Sattar et al. [6]. First of all, we tested the 2 QL Bi_2Se_3 and 2 ML $PtSe_2$/2 QL Bi_2Se_3 samples. Fig. 5.9 a and b show the angular dependence of the magnetic contributions at three distinct photon energies. First, we can notice the isotropic character of SCC in both samples. The former has a slight photon energy dependence (Fig. 5.11 h) and higher THz emission than the latter in all the photon energies. This observation is not in agreement with the theoretical predictions by Sattar et al [6]. On one hand, the lowest photon energy used to pump was 1.32 eV, (corresponding to a wavelength of 940 nm), and it already covers multiple spin-split bands with possibly opposite spin-textures, leading to a reduction of the overall THz electric field strength and making it difficult to probe SCC efficiency precisely. On the other hand, the theoretical model used to calculate the band structure underestimates the band-gap, thus it is not straightforward to conclude if low photon energy is better to access bands resulting in higher THz electric field strength. A more careful approach to estimate SCC efficiency would be to narrow down the photon energy window and apply a gate voltage. However, this involves highly advanced and complicated sample preparation steps. Finally, the non-magnetic contribution is negligible in both samples with isotropic character in the former, and a slight elongated shape in the latter. The origins of those contributions are unknown at the moment.

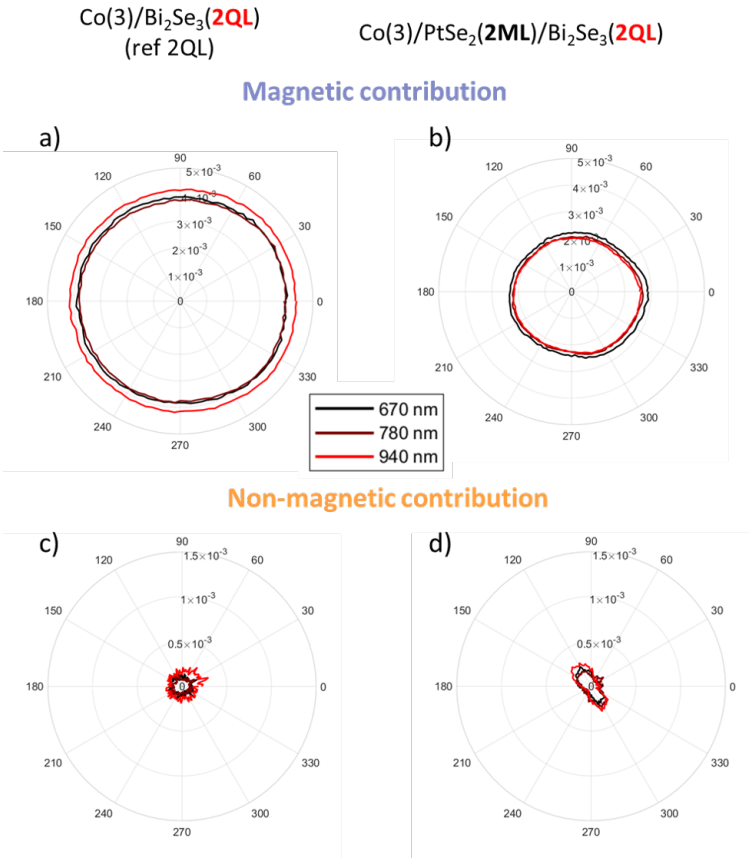

Figure 5.9: Full angular dependence of the magnetic contribution in a) 3 nm Co/2 QL Bi_2Se_3 and b) 3 nm Co/2 ML $PtSe_2$/2 QL Bi_2Se_3, and non-magnetic contributions in c and d, respectively.

$PtSe_2$/TI Bi_2Se_3 heterostructure

To explore new heterostructures with distinct physical properties, the $PtSe_2$/TI Bi_2Se_3 system was studied by THz-TDS. Three samples were selected for this study: 10 QL Bi_2Se_3, 2 ML $PtSe_2$/10 QL Bi_2Se_3, and 5 ML $PtSe_2$/10 QL Bi_2Se_3. From the band structure point of view, the heterostructure consisting of semiconducting (2 ML) $PtSe_2$ and TI ($\approx$10 QL) Bi_2Se_3 can be the most interesting among the three. At 2 ML thickness, topological semi-metal Dirac cones start to appear in $PtSe_2$, thus, the expected hybridization of this feature with the TI surface states could exhibit exotic physics. The first experiment on this sample showed three-fold symmetry in the angular dependence of the THz emission with the opposite triangles for the positive (solid line) and negative (dashed line) field directions at all three photon energies as presented in Fig. 5.10 c.

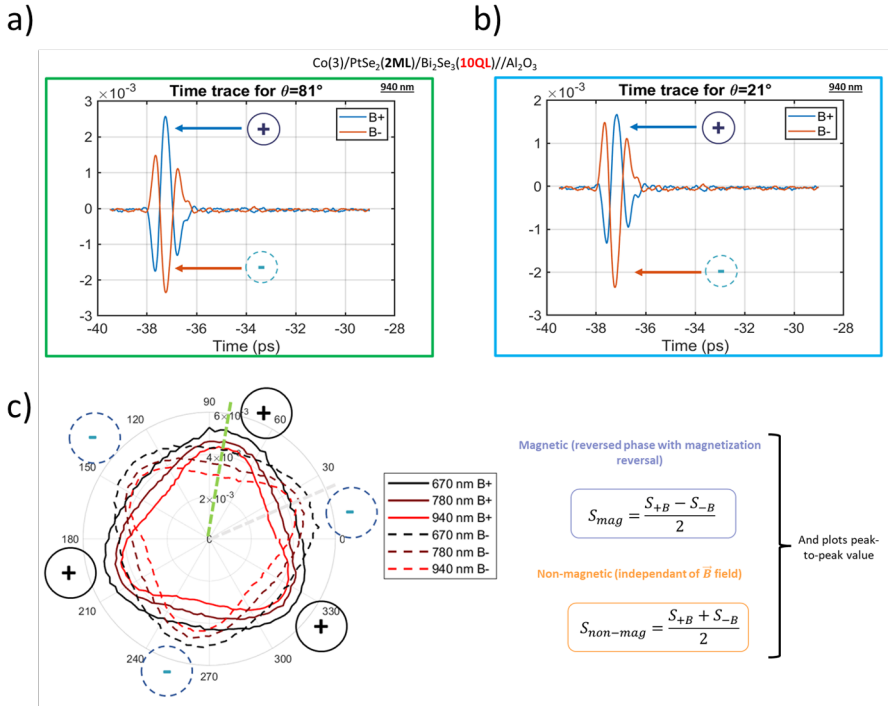

Figure 5.10: Raw THz signal emitted from 3 nm Co/2 ML $PtSe_2$/10 QL Bi_2Se_3 at a photon wavelength of ν940 nm at a) θ=81° and b) θ=21°, corresponding to a maximum measured in B+ and B- magnetic field directions, respectively. c) full angular dependence of the emitted THz signal of the corresponding sample for B+ (full lines) and B- (dashed lines) magnetic field directions.

Applying equation 5.1 to the obtained angular dependence results gives an isotropic character of the magnetic contribution for all three samples, and among them, 10 QL Bi_2Se_3 presented the strongest photon-energy-dependence. The exact same system was previously studied by Wang et al. [162] with the fastest spin-to-charge conversion dynamics ever recorded due to the presence of TI surface states. The sample made of 2 ML $PtSe_2$/10 QL Bi_2Se_3 shows a weaker magnetic contribution than 10 QL Bi_2Se_3 for the two highest photon energies, however, the signal from both samples is equal for the lowest photon energy of 1.32 eV, as can be seen in Fig. 5.11 h. The extrapolated prediction shows that at lower photon energies 2 ML $PtSe_2$/10 QL Bi_2Se_3 is expected to show stronger magnetic contribution than 10 QL Bi_2Se_3. The case of 5 ML $PtSe_2$/10 QL Bi_2Se_3 is a bit different: it shows an even smaller magnetic contribution than 2 ML $PtSe_2$/10 QL Bi_2Se_3, and this contribution decreases sharply when decreasing the photon energy. Note that,

when grown on graphene/SiC, $PtSe_2$ exhibited an opposite thickness dependent behaviour: there was only magnetic contribution and it was enhanced with increasing the thickness. In the current case, however, there is also Bi_2Se_3 which has much larger atomic mass than graphene and more hybridized bands are expected due to the larger charge density of Bi.

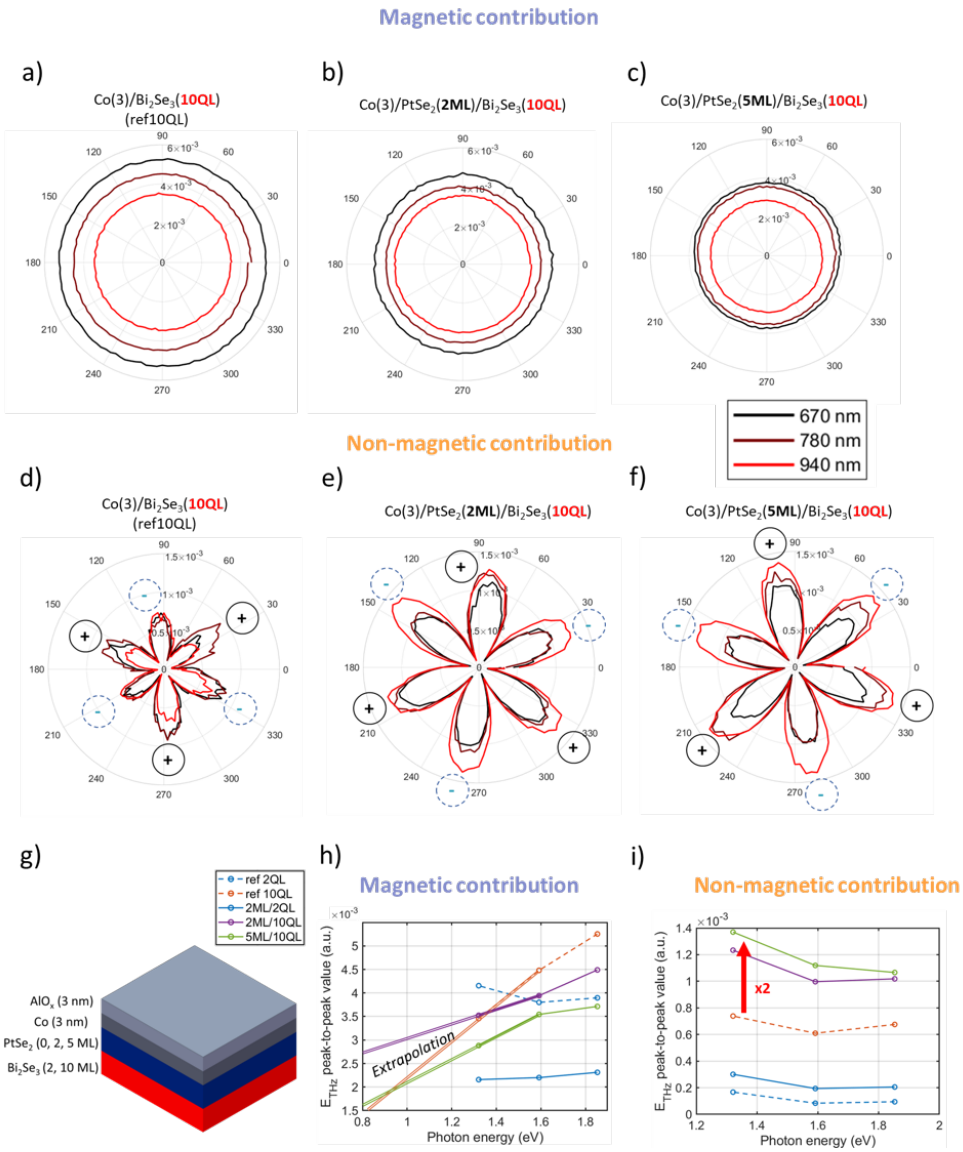

Figure 5.11: Full angular dependence of the magnetic contribution of the emitted THz signal from 3 nm Co/10 QL Bi_2Se_3, b) 3 nm Co/2 ML $PtSe_2$/10 QL Bi_2Se_3, c) 3 nm Co/5 ML $PtSe_2$/10 QL Bi_2Se_3, all the samples show isotropic behaviour. d-f) the corresponding non-magnetic contributions from the samples in a-c showing three-fold symmetry. g) simple sketch summarizing the different stacks with varying thickness of $PtSe_2$ and Bi_2Se_3. Photon energy dependence of the emitted THz signal coming from h) magnetic and i) non-magnetic contributions, extracted from a-f.

The previous studies on SCC in Bi_2Se_3 did not focus on the non-magnetic contribution. The results are drastically different regarding the non-magnetic contribution. It has a clear six-fold symmetry in all the samples. The addition of $PtSe_2$ consistently increased the non-magnetic signal in Bi_2Se_3, with the strongest signal in 5 ML $PtSe_2$/10 QL Bi_2Se_3 that increases when decreasing the photon energy, as shown in Fig.

5.11 i, and reaching twice the THz emission from 10 QL Bi_2Se_3 at the photon energy of 1.32 eV. A deeper discussion of this behaviour is outside the scope of this thesis as it does not involve spin-charge conversion phenomena.

5.3 Conclusion

As a conclusion, this chapter covered a discussion on SCC in FM/vdW heterostructures in two different configurations probed by THz-TDS, both with the aim of accessing deeper levels in the electronic band structure. The first one was 2 ML $PtSe_2$/ 1 ML $MoSe_2$ transferred on top of LNO substrates with UP and DOWN electric polarizations. Due to the limited access to z-cut of the substrate, we tested the vdW heterostructures on x-cut LNO that showed much lower electric polarization. Thus, the effect of the polarization direction on the SCC was not as much enhanced. This is an ongoing research and more experiments will follow in the future with z-cut LNO that has stronger electric polarization.

The second system covered $PtSe_2$/Bi_2Se_3 heterostructures and it was based on theoretical band structure calculations by Sattar et al [6]. In this experiment, we used three distinct photon energies to excite the system. There was a clear photon-energy dependence of the emitted THz signal, however, the predictions of the enhancement of SCC in the heterostructures was not confirmed using those three photon-energies. A strong enhancement of THz emission of non-magnetic origin was observed which is out of the scope of the study.

Conclusion and Perspectives

The ongoing rise of the power consumption by data processing and storage necessitates the search for materials with novel physical properties that do not require as much energy as conventional 3D materials. One class of materials that has been proposed is 2D materials and vsW heterostructures because of the relaxed lattice-matching criteria for the epitaxy and tunability of the electronic band structure by thickness and stacking with other vdW materials.

To be able to integrate 2D materials into memory applications, large-area and high quality growth and materials with large spin Hall angle, θ_{SH}, have to be developed. The first part has been demonstrated to be possible by MBE in this manuscript, with even transfer onto an oxide layer. The second part requires more studies as $PtSe_2$ has smaller θ_{SH} than Pt which is a well-established SCC element. Gating the vdW layers is postulated to allow to access bands with larger spin-splitting which is in the prospect of this study in the team of 2D Spintronics.

To study SCC in FM/vdW heterostructures, we first used spin pumping by FMR, however, instabilities of the machine pushed us to explore other measurements techniques. THz-TDS has proved itself to be a reliable tool that is based on the measurement of THz electric field which could have spintronic or other origins. We first studied thickness dependent spintronic THz emission from a FM (sputtered or e-beam deposited)/$PtSe_2$ (vdWE) that showed transition from IREE in the semiconducting regime of $PtSe_2$ to ISHE in the semimetallic regime. The theoretical calculations resulted in that the charge transfer from the graphene layer underneath breaks the inversion symmetry of $PtSe_2$ giving rise to the Rashba-type spin-splitting.

Using the same technique, we then moved on to the bilayer of $PtSe_2/MoSe_2$ which was predicted to host large Rashba-type spin-splitting of the hybridized band. The bilayer was epitaxially grown on graphene/SiC. Experimental studies by spin-resolved ARPES and THz-TDS showed that the bilayer hosts a band with the opposite spin-texture to that of $PtSe_2$. This is the first demonstration of reversing the sign of θ_{SH} in 2D materials. Further experiments have been planned on this system, for example, they have been transferred onto SiO_2/Si to investigate the gate-voltage dependence of SCC.

Based on the previous work of the team of 2D spintronics on 2D material/3D ferroelectric that showed the modulation of the electronic band structure, the next study covered the effect of the electric polarization of the ferroelectric on the SCC in $PtSe_2/MoSe_2$ heterostructures. Due to the small polarization of the ferroelectric, the effect was also small. The advancing study is on ferroelectric with stronger electric polarization.

The other ongoing work focuses on the $PtSe_2/Bi_2Se_3$ vdW heterostructures that was predicted to host large Rashba-type spin-split states. High quality of vdW films were grown on sapphire that showest the highest anisotropy of the $PtSe_2$ crystal. However, the THz-TDS experiments did not show as high SCC. There was enhancement of THz emission of non-magnetic origin which was not the aim of the study.

To conclude, this work presented that tunable SCC phenomena can be observed in 2D materials and their vdW nature relaxes the lattice-matching requirement, allowing the growth and transfer of vdW materials on different substrates. This opens new areas of research in spintronics, such as spintronic THz emission and SOT-MRAMs, with 2D materials.

Bibliography

[1] J. Inoue and S. Maekawa. Theory of tunneling magnetoresistance in granular magnetic films. *Physical Review B*, 53(18):R11927(R), 1996.

[2] E. Hall. On a new action of the magnet on electric currents. *American Journal of Mathematics*, 2(3):287–292, 1879.

[3] K. Novoselov et al. Electric field effect in atomically thin carbon films. *Science*, 306(5696):666–669, 2004.

[4] K. Abdukayumov et al. Atomic-layer controlled transition from inverse rashba–edelstein effect to inverse spin hall effect in 2d PtSe2 probed by thz spintronic emission. *Advanced Materials*, page 2304243, 2024.

[5] L. Xiang et al. Tunable giant rashba-type spin splitting in PtSe2/MoSe2 heterostructure. *Applied Physics Letters*, 115(20):203501, 2019.

[6] Shahid Sattar and J. Andreas Larsson. Tunable electronic properties and large rashba splittings found in few-layer Bi2Se3-PtSe2 van der waals heterostructures. *ACS Applied Electronic Materials*, 2(11):3585–3592, 2020.

[7] N. W. Ashcroft and N. D. Merin. *Solid State Physics*.

[8] Vincent Baltz. *The basics of electron transport in spintronics : textbook with lectures, exercises and solutions*. Current Natural Sciences. edp sciences, 2023.

[9] E. C. Stoner. Collective electron ferromagnetism. *The Royal Society*, 165(922):372–414, 1938.

[10] M. Gibertini et al. Magnetic 2d materials and heterostructures. *Nature Nanotechnology*, 14:408–419, 2019.

[11] K. S. Novoselov et al. Electronic properties of graphene. *phys. stat. sol. (b)*, 244(11):4106–4111, 2007.

[12] R. Peierls. On ising's model of ferromagnetism. *Proc. Camb. Philos. Soc.*, 32:477–481, 1936.

[13] N. D. Mermin and H. Wagner. Absence of ferromagnetism or antiferromagnetism in the one- or two-dimensional isotropic heisenberg models. *Physical Review Letters*, 17:1133–1136, 1966.

[14] P. C. Hohenberg. Existence of long-range order in one and two dimensions. *Physical Review*, 158:383–386, 1966.

[15] W. Heisenberg. On the theory of ferromagnetism. *Z. Phys*, 49:619–636, 1928.

[16] B. Huang et al. Layer-dependent ferromagnetism in a van der waals crystal down to the monolayer limit. *Nature*, 546:270–273, 2017.

[17] Z. Fei et al. Two-dimensional itinerant ferromagnetism in atomically thin Fe3GeTe2. *Nature Materials*, 17(10):778–782, 2018.

[18] M. Ribeiro et al. Large-scale epitaxy of two-dimensional van der waals room-temperature ferromagnet Fe5GeTe2. *npj 2D Materials and Applications*, 6(10), 2022.

[19] X. Zhang et al. Room-temperature intrinsic ferromagnetism in epitaxial CrTe2 ultrathin films. *Nature Communications*, 12:2492, 2021.

[20] Jack Bass and William P Pratt. Spin-diffusion lengths in metals and alloys, and spin-flipping at metal/metal interfaces: an experimentalist's critical review. *Journal of Physics: Condensed Matter*, 19(18):183201, 2007.

[21] A. Fert. Two-current conduction in ferromagnetic metals and spin wave-electron collisions. *Journal of Physics C: Solid State Physics*, 2:1784–1788, 1969.

[22] S. Sangiao. Anomalous hall effect in Fe (001) epitaxial thin films over a wide range in conductivity. *Phys. Rev. B*, 79(1):014431, 2019-01.

[23] R. Karplus. Hall effect in ferromagnets. *Phys. Rev*, 95(5):1154–1160, 1954.

[24] J. Smit. The spontaneous hall effect in ferromagnetics i. *Physica*, 21(6):877–887, 1955.

[25] J. Smit. The spontaneous hall effect in ferromagnetics II. *Physica*, 24(1):39–51, 1958.

[26] L. Berger. Side-jump mechanism for the hall effect of ferromagnets. *Phys. Rev. B*, 2(11):4559–4566, 1970.

[27] W.-K. Tse et al. Spin accumulation in the extrinsic spin hall effect. *Physical Review B*, 72(24):241303(R), 2005.

[28] Shuichi Murakami. Intrinsic spin hall effect. *arXiv:cond-mat/0504353, 45:197–209, 2005*, 2005.

[29] Shuichi Murakami et al. Dissipationless quantum spin current at room temperature. *Science*, 301(5638):1348–1351, 2003.

[30] Edurne Sagasta et al. Tuning the spin hall effect of pt from the moderately dirty to the superclean regime. *Physical Review B*, 94(6):060412(R), 2016.

[31] L. Berger. Side-jump mechanism for the hall effect of ferromagnets. *Physical Review B*, 2(11):4559, 1970.

[32] S. Smit. The spontaneous hall effect in ferromagnetics i. *Physica*, 21(6):877–887, 1955.

[33] P. Noel. Dynamical spin injection and spin to charge current conversion in oxide-based rashba interfaces and topological insulators, 2019.

[34] A. Fert and P. M. Levy. Spin hall effect induced by resonant scattering on impurities in metals. *Physical Review Letters*, 106(15):157208, 2011.

[35] A. Magni et al. Spin hall magnetoresistance and spin–orbit torque efficiency in pt/fecob bilayers. *IEEE Transactions on Magnetics*, 58(2):1–5, 2022.

[36] E. Saitoh et al. Conversion of spin current into charge current at room temperature: Inverse spin-hall effect. *Applied Physics Letters*, 88(18):182509, 2006.

[37] M. N. Baibich. Giant magnetoresistance of (001)Fe/(001)Cr magnetic superlattices. *Phys. Rev. Lett*, 61(21):2472–2475, 1988.

[38] T. McGuire. Anisotropic magnetoresistance in ferromagnetic 3d alloys. *IEEE Transactions on Magnetics*, 11(4):1018–1038, 1975.

[39] H. Lu and Sh. Shen. Weak localization and weak anti-localization in topological insulators. *Proc. SPIE*, page 9167, 2014.

[40] Ch. Tusche et al. Spin resolvedbandstructureimagingwithahighresolution momentum microscope. *Ultramicroscopy*, 159(3):520–529, 2015.

[41] T. Guillet. Tuning the spin-orbit coupling in ge for spin generation, detection and manipulation, 2020.

[42] J. C. Rojas Sánchez et al. Spin-to-charge conversion using rashba coupling at the interface between non-magnetic materials. *Nature Communications*, 4:2944, 2013.

[43] L. Landau and E. Lifshits. On the theory of the dispersion of magnetic permeability in ferromagnetic bodies. *Phys. Zeitsch. der Sow*, 8:153–169, 1935.

[44] T. Gilbert. A phenomenological theory of damping in ferromagnetic materials. *IEEE Transactions on Magnetics*, 40(6):3443–3449, 1955.

[45] C. Kittel. On the theory of ferromagnetic resonance absorption. *Physical Review Journals Archive*, 73(2):155, 1948.

[46] H. Hurdequint. Fmr studies of ultrathin permalloy layers sandwiched by Al2O3. *Journal of Magnetism and Magnetic Materials*, 242-245:521–524, 2002.

[47] H. Puszkarski and M. Kasperski. On the interpretation of the angular dependence of the main fmr/swr line in ferromagnetic thin films. *Acta Physica Polonica A*, 121(5-6):1165–1168, 2012.

[48] J.-C. Rojas-Sánchez et al. Spin pumping and inverse spin hall effect in germanium. *Physical Review B*, 88(6):064403, 2013.

[49] M. Johnson and R. H. Silsbee. Spin-injection experiment. *Physical Review B*, 37(10):5326–5335, 1988.

[50] Y. Tserkovnyak et al. Spin pumping and magnetization dynamics in metallic multilayers. *Physical Review B*, 6(22):224403, 2002.

[51] J. C. Slonczewski. Current-driven excitation of magnetic multilayers. *Journal of Magnetism and Magnetic Materials*, 159(1):L1–L7, 1996.

[52] J.-C. Rojas-Sánchez et al. Spin pumping and inverse spin hall effect in platinum: The essential role of spin-memory loss at metallic interfaces. *Physical Review Letters*, 112(10):106602, 2014.

[53] E. Beaurepaire et al. Ultrafast spin dynamics in ferromagnetic nickel. *Physical Review Letters*, 76(22):4250, 1996.

[54] M. Battiato. Superdiffusive spin transportand ultrafast magnetization dynamics, 2013.

[55] T. Kampfrath et al. Engineering ultrafast spin currents and terahertz transients by magnetic heterostructures. *Nature Nanotechnology*, 8:256–260, 2013.

[56] E. Rongione. Ultrafast spin-currents mediated by spin-orbit coupling: towards new concepts for thz emitters, 2022.

[57] C. Cohen et al. Photons et atomes: introduction à l'électrodynamique quantique. *Savoirs actuels, EDP Sciences, cnrs editions*, 36:230–231, 1987.

[58] D. M. Nenno et al. Simulation of hot-carrier dynamics and terahertz emission in laser-excited metallic bilayers. *Physical Review Applied*, 11(5):054083, 2019.

[59] S. Preu et al. Tunable, continuous-wave terahertz photomixer sources and applications. *Journal of Apllied Physics*, 109:061301, 2011.

[60] M. B. Agranat et al. Interaction of picosecond laser pulses with the electron, spin, and phonon subsystems of nickel. *Zh. Eksp. Teor. Fiz.*, 86:1376–1379, 1984.

[61] A. Vaterlaus et al. Different spin and lattice temperatures observed by spin-polarized photoemission with picosecond laser pulses. *Journal of Applied Physics*, 67:5661–5663, 1990.

[62] C. Stamm et al. Femtosecond modification of electron localization and transfer of angular momentum in nickel. *Nature Materials*, 6:740–743, 2007.

[63] B. Koopmans et al. Microscopic model for femtosecond magnetization dynamics. *Journal of Magnetism and Magnetic Materials*, 286:271–275, 2005.

[64] B. Koopmans et al. Explaining the paradoxical diversity of ultrafast laser-induced demagnetization. *Nature Materials*, 9:259–265, 2010.

[65] I. Radu et al. Laser-induced magnetization dynamics of lanthanide-doped permalloy thin films. *Physical Review Letters*, 102:117201, 2009.

[66] J. Walowski et al. Energy equilibration processes of electrons, magnons, and phonons at the femtosecond time scale. *Physical Review Letters*, 101:237401, 2008.

[67] K. Carva et al. Ab initio investigation of the elliott-yafet electron-phonon mechanism in laser-induced ultrafast demagnetization. *Physical Review Letters*, 107:207201, 2011.

[68] M. Battiato et al. Superdiffusive spin transport as a mechanism of ultrafast demagnetization. *Physical Review Letters*, 105(2):027203, 2010.

[69] M. Battiato et al. Theory of laser-induced ultrafast superdiffusive spin transport in layered heterostructures. *Physical Review B*, 86:024404, 2012.

[70] R. Metzler and J. Klafter. The random walk's guide to anomalous diffusion: a fractional dynamics approach. *Physics Reports*, 339(1):1–77, 2000.

[71] A. Eschenlohr. Ultrafast spin transport as key to femtosecond demagnetization. *Nature Materials*, 12(1):332–336, 2013.

[72] Ch. Fattinger; D. Grischkowsky. Terahertz beams. *Applied Physics Letters*, 54(6):490–492, 1989.

[73] T. H. Dang et al. Ultrafast spin-currents and charge conversion at 3d-5d interfaces probed by time-domain terahertz spectroscopy. *Appl. Phys. Rev.*, 7:041409, 2020.

[74] Mbe componenten knudsen cell description.

[75] S. Hasegawa. Reflection high-energy electron diffraction. *In Characterization of Materials, E.N. Kaufmann (Ed.).*, 2012.

[76] M. A. Herman and H. Sitter. *Molecular beam epitaxy: fundamentals and current status*. Number 7 in Springer series in materials science. Springer, 2nd, rev. and updated ed edition, 1996.

[77] T. S. Rahman et al. Atomistic studies of thin film growth. page 1, 2004-08-02.

[78] H. Freller and G. Gunther. Three-temperature method as an origin of molecular beam epitaxy. *Thin Solid Films*, 88:291–307, 1982.

[79] B. Daudin et al. Stranski-krastanov growth mode during the molecular beam epitaxy of highly strained GaN. *Physical Review B*, 56(12):R7069–R7072, 1997.

[80] K. A. Lozovoy et al. Kinetics of epitaxial formation of nanostructures by frank–van der merwe, volmer–weber and stranski–krastanow growth modes. *Surface and Coatings Technology*, 384:125289, 2020.

[81] E. Bauer and H. Poppa. Recent advances in epitaxy. *Thin Solid Films*, 12(1):167–185, 1972.

[82] W. Braun. Origin of electron diffraction oscillations during crystal growth. *Physical Review Letters*, 80(22):4935–4938, 1998.

[83] H. N. Yang et al. Quantitative study of the decay of intensity oscillations in transient layer-by-layer growth. *Physical Review B*, 51(24):17932–17945, 1995.

[84] E. Bauer. Epitaxy of metals on metals. *Applications of Surface Science*, 11-12:479–494, 1982.

[85] A. Madhukar. Far from equilibrium vapour phase growth of lattice matched III-v compound semiconductor interfaces: some basic concepts and monte-carlo computer simulations*. *Surface Science*, 132(1):344–374, 1983.

[86] H. Brune. Growth modes. In *Encyclopedia of Materials : Science and Technology*, pages 3683–3693. Pergamon, 2001.

[87] S. Swann. Magnetron sputtering. *Physics in Technology*, 19(2):67, 1988.

[88] Johan Bohlmark. Fundamentals of high power impulse magnetron sputtering, 2005.

[89] P.J Kelly and R.D Arnell. Magnetron sputtering: a review of recent developments and applications. *Vacuum*, 56(3):159–172, 2000.

[90] Azo materials using peakforce tapping mode atomic force microscopy to image the dna double helix.

[91] J. Melngailis. Focused ion beam technology and applications. *Journal of Vacuum Science and Technology B*, 5(2):469–495, 1987.

[92] S. S. Kalarickal et al. Ferromagnetic resonance linewidth in metallic thin films: Comparison of measurement methods. *Journal of Applied Physics*, 99(9):093909, 2006.

[93] R. L. Seeger. Etude de nouveaux mécanismes de transport de spin et de charge dans des structures et textures de spin ferromagnétiques et antiferromagnétiques, 2021.

[94] T. H. et al Dang. Ultrafast spin-currents and charge conversion at 3d-5d interfaces probed by time-domain terahertz spectroscopy. *Applied Physics Reviews*, 7(4):041409, 2020.

[95] A. Yariv. *Quantum Electronics*. Wiley, third edition edition, 1989.

[96] S. Casalbuoni et al. Numerical studies on the electro-optic detection of femtosecond electron bunches. *Physical Review Special Topics - Accelerators and Beams*, 11(7):072802, 2008.

[97] B. Pradarutti et al. Highly efficient terahertz electro-optic sampling by material optimization at 1060nm. *Optics Communications*, 281:5031–5035, 2008.

[98] G. Gallot et al. Electro-optic detection of terahertz radiation. *Journal of the Optical Society of America B*, 16:1204, 1999.

[99] G. Gallot et al. Measurement and calculation of the orientation dependence of terahertz pulse detection in znte. *Journal of the Optical Society of America B*, 18:313, 2001.

[100] A. Schneider et al. Measurement of the terahertz-induced phase shift in electro-optic sampling for an arbitrary biasing phase. *Applied Optics*, 45:6598, 2006.

[101] Y. Xuechao et al. Atomically thin noble metal dichalcogenide: a broadband mid-infrared semiconductor. *Nature Communications*, 9(1545), 2018.

[102] A. Ciarrocchi et al. Thickness-modulated metal-to-semiconductor transformation in a transition metal dichalcogenide. *Nature Communications*, 9(919), 2018.

[103] B. Villaos et al. Thickness dependent electronic properties of pt dichalcogenides. *npj 2D Materials and Applications*, 3(2), 2019.

[104] P. Mallet et al. Angular dependence of the interlayer coupling at the interface between two-dimensional materials 1t-PtSe2 and graphene. *Physical Review Materials*, 7(12):L121001, 2023.

[105] W. Yao et al. Direct observation of spin-layer locking by local rashba effect in monolayer semiconducting PtSe2 film. *Nature Communications*, 8(14216), 2017.

[106] L Nádvorník et al. Terahertz spin-to-charge current conversion in stacks of ferromagnets and the transition-metal dichalcogenide NbSe2. *Advanced Materials Interfaces*, 9(2201675), 2022.

[107] D Khusyainov et al. Increasing the efficiency of a spintronic thz emitter based on WSe2/FeCo. *Materials*, 14(6479), 2021.

[108] T. Le Quang et al. Scanning tunneling spectroscopy of van der waals graphene/semiconductor interfaces: absence of fermi level pinning. *2D Materials*, 4(3):035019, 2017.

[109] Lee A. Walsh and Christopher L. Hinkle. van der waals epitaxy: 2d materials and topological insulators. *Applied Materials Today*, 9:504–515, 2017.

[110] A. Koma et al. Fabrication and characterization of heterostructures with subnanometer thickness. *Microelectronic Engineering*, 2(1):129–136, 1984.

[111] A. Koma et al. Heteroepitaxy of a two-dimensional material on a three-dimensional material. *Applied Surface Science*, 41-42(1):451–456, 1990.

[112] K. Ueno et al. Heteroepitaxial growth of layered transition metal dichalcogenides on sulfur-terminated GaAs(111) surfaces. *Appl. Phys. Lett.*, 56:327–329, 1990.

[113] K. Liu et al. Heteroepitaxial growth of layered semiconductor GaSe on a hydrogen-terminated Si(111) surface. *Jpn. J. Appl. Phys*, 32(32):L434, 1993.

[114] N. V. Tarakina et al. Comparative study of the microstructure of Bi2Se3 thin films grown on Si(111) and InP(111) substrates. *Cryst. Growth Des*, 12(4):1913–1918, 2012.

[115] C. Vergnaud et al. New approach for the molecular beam epitaxy growth of scalable WSe2 monolayers. *Nanotechnology*, 31(255602), 2020.

[116] Kumar et al. Growth protocols and characterization of epitaxial graphene on SiC elaborated in a graphite enclosure. *Physica E: Low-dimensional systems and nanostructures*, 75:7–14, 2016.

[117] Palecchi et al. High electron mobility in epitaxial graphene on 4H-SiC(0001) via post-growth annealing under hydrogen. *Scientific Reports*, 4(4558), 2014.

[118] G. Binnig and H. Rohrer. Scanning tunneling microscopy—from birth to adolescence. *Rev. Mod. Phys.*, 59:615, 1987.

[119] J. Li et al. Layer-dependent band gaps of platinum dichalcogenides. *ACS Nano*, 15(8):13249–13259, 2021.

[120] L. Zhang et al. Precise layer-dependent electronic structure of mbe-grown PtSe2. *Advanced Electronic Materials*, 7(11):2100559, 2021.

[121] L. Zhang et al. Shallowing interfacial carrier trap in transition metal dichalcogenide heterostructures with interlayer hybridization. *Nano Res*, 14:1390–1396, 2021.

[122] H. Hibino et al. Dependence of electronic properties of epitaxial few-layer graphene on the number of layers investigated by photoelectron emission microscopy. *Phys. Rev. B*, 79(12):125437, 2009.

[123] A. Kjekshus S. Furuseth, K. Selte. Redetermined crystal structures of NiTe2, PdTe2, PtS2, PtSe2, and PtTe2. *Acta Chemica Scandinavica*, 19:257–258, 1965.

[124] M. Yan E. Wang X. Zhou G. Zhang. High quality atomically thin PtSe2 films grown by molecular beam epitaxy. *2D Materials*, 4(4):045015, 2017.

[125] L. J. van der Pauw. A method of measuring specific resistivity and hall effect of discs of arbitrary shape. *Philips Research Reports*, 13(1):1–9, 1958.

[126] F. Giannazzo et al. Origin of the current transport anisotropy in epitaxial graphene grown on vicinal 4H-SiC (0001) surfaces. *Materials Science Forum*, 806:103–107, 2015.

[127] M. T. Dau et al. The valley nernst effect in WSe2. *Nature Communications*, 10(5796), 2019.

[128] E. Velez-Fort et al. Ferromagnetism and rashba spin–orbit coupling in the two-dimensional (V,Pt)Se2 alloy. *ACS Appl. Electron. Mater.*, 4(1):259–268, 2022.

[129] M. Wang et al. Spintronics based terahertz sources. *Crystals*, 12(11):1661, 2022.

[130] M. Ikhlas et al. Large anomalous nernst effect at room temperature in a chiral antiferromagnet. *Nature Physics*, 13:1085–1099, 2017.

[131] K. Uchida et al. Observation of longitudinal spin-seebeck effect in magnetic insulators. *Applied Physics Letetrs*, 97:172505, 2010.

[132] C. Kittel. Ferromagnetic resonance. *Le Journal de Physique et le Radium*, 12:291, 1951.

[133] E. D. Palik. Handbook of optical constants of solids. *Academic press*, 3, 1998.

[134] M. Hemmat et al. Layer-controlled nonlinear terahertz valleytronics in two-dimensional semimetal and semiconductor PtSe2. *InfoMat*, 5(11):e12468, 2023.

[135] X. Zhao et al. Thickness-dependent ultrafast nonlinear absorption properties of PtSe2 films with both semiconducting and semimetallic phases. *Appl. Phys. Lett.*, 115:263102, 2019.

[136] G. Kresse and J. Hafner. Ab initio molecular dynamics for liquid metals. *Phys. Rev. B*, 47:558(R), 1993.

[137] G. Kresse and J. Furthmuller. Efficient iterative schemes for ab initio total-energy calculations using a plane-wave basis set. *Phys. Rev. B*, 54:11169, 1996.

[138] J. Furthmuller G. Kresse. Efficiency of ab-initio total energy calculations for metals and semiconductors using a plane-wave basis set. *Phys. Rev. B*, 6(1):15–50, 1996.

[139] M. Ernzerhof J. P. Perdew, K. Burke. Generalized gradient approximation made simple. *Phys. Rev. Lett.*, 77:3865, 1996.

[140] Z. Guanet al. Band gap opening of graphene by forming a graphene/PtSe2 van der waals heterojunction. *RSC Advances*, 7(72):45393–45399, 2017.

[141] T. Bucko et al. Improved description of the structure of molecular and layered crystals: ab initio dft calculations with van der waals corrections. . *Phys. Chem. A*, 43(114):11814–11824, 2010.

[142] U. Herath et al. Pyprocar: A python library for electronic structure pre/post-processing. *Computer Physics Communications*, 251(107080), 2010.

[143] U. Schwingenschlogl S. Sattar. Electronic properties of graphene–PtSe2 contacts. *ACS Appl. Mater. Interfaces*, 9(18):15809–15813, 2017.

[144] Q. Zhang et al. Bandgap renormalization and work function tuning in MoSe2/hBN/Ru(0001) heterostructures. *Nature Communications*, 7:13843, 2016.

[145] Y. Zhang et al. Direct observation of the transition from indirect to direct bandgap in atomically thin epitaxial MoSe2. *Nature Nanotechnology*, 9:111–115, 2014.

[146] P. James and M. Lavik. The crystal structure of MoSe2. *Acta Crsyt.*, 16:1183, 1963.

[147] Y.Wei et al. Initial stage of mbe growth of MoSe2 monolayer. *Nanotechnology*, 31(31):315710, 2020.

[148] K. Muller and C. Chang. Electrical dipoles on clean mica surfaces. *Surface Science*, 14:39–51, 1969.

[149] R. Salazar et al. Visualizing giant ferroelectric gating effects in large-scale WSe2/BiFeO3 heterostructures. *Nano Letters*, 22(23):9260–9267, 2022.

[150] P. V. Nguyen et al. Visualizing electrostatic gating effects in two-dimensional heterostructures. *Nature*, 572:220–223, 2019.

[151] Y. Zhang et al. Electronic structure, surface doping, and optical response in epitaxial WSe2 thin films. *Nano Lett*, 16(572):2485–2491, 2016.

[152] H. Nakamura et al. Spin-splitting and strain in epitaxial monolayer WSe2 on graphene. *Physical Review B*, 101:165103, 2020.

[153] J. M. Riley et al. Direct observation of spin-polarized bulk bands in an inversion-symmetric semiconductor. *Nature Physics*, 10:835–839, 2014.

[154] J.W. Chen et al. A gate-free monolayer WSe2 pn diode. *Nature Communicqtions*, 9:3143, 2018.

[155] V. Gopalana and T. E. Mitchell. The role of nonstoichiometry in 180° domain switching of LiNbO3 crystals. *Applied Physics Letters*, 72(16):1981–1983, 1998.

[156] J. Hebling et al. Tunable thz pulse generation by optical rectification of ultrashort laser pulses with tilted pulse fronts. *Applied Physics B*, 78:593–599, 2004.

[157] H. Hirori et al. Single-cycle terahertz pulses with amplitudes exceeding 1 mv/cm generated by optical rectification in LiNbO3. *Applied Physical Letters*, 98:091106, 2011.

[158] L. Guiramand et al. Near-optimal intense and powerful terahertz source by optical rectification in lithium niobate crystal. *Applied Physics B*, 10(2):340–346, 2022.

[159] H. ZhangLiu et al. Topological insulators in Bi2Se3, Bi2Te3 and Sb2Te3 with a single dirac cone on the surface. *Nat. Phys.*, 5(6):438–442, 2009.

[160] D. Hsieh et al. A tunable topological insulator in the spin helical dirac transport regime. *Nature*, 460:1101–1105, 2009.

[161] S. Nakajima. The crystal structure of Bi2Te3xSex. *Journal of Physics and Chemistry of Solids*, 24(3):479485, 1963.

[162] X. Wang et al. Ultrafast spin-to-charge conversion at the surface of topological insulator thin films. *Advanced Materials*, 30:1802356, 2018.